UNIVERSIDADE D
COIMBRA

João Pedro dos Reis Luís

TARGETING NEUROINFLAMMATION

FROM TARGET VALIDATION TO RATIONAL DESIGN OF SELECTIVE MODULATORS

Tese no âmbito do doutoramento em Química, ramo de Química Médica, orientada pelo Professor Doutor Rui Manuel Pontes Meireles Ferreira de Brito, coorientada pela Professora Doutora Dora Maria Tuna Oliveira Brites e Doutor Carlos José Vieira Simões e apresentada ao Departamento de Química da Faculdade de Ciências e Tecnologia da Universidade de Coimbra.

Dezembro de 2021

UNIVERSIDADE D
COIMBRA

TARGETING NEUROINFLAMMATION

FROM TARGET VALIDATION TO RATIONAL DESIGN OF SELECTIVE MODULATORS

João Pedro dos Reis Luís

Doctoral Thesis in Chemistry, specialization in Medicinal Chemistry, supervised by Professor Doctor Rui Manuel Pontes Meireles Ferreira de Brito, Professor Doctor Dora Maria Tuna Oliveira Brites and Doctor Carlos José Vieira Simões, and submitted to the Faculty of Sciences and Technology of the University of Coimbra.

December 2021

The research work presented in this thesis was developed under the supervision of Professor Doctor Rui Brito and co-supervision of Doctor Carlos Simões, at the Structural and Computational Biology group, Coimbra Chemistry Center, University of Coimbra, and under the co-supervision of Professor Doctor Dora Brites at the Neuroinflammation, Signaling and Neuroregeneration group, The Research Institute for Medicines (iMed.ULisboa), Faculty of Pharmacy, University of Lisbon.

O trabalho de investigação apresentado nesta tese foi desenvolvido sob a orientação do Professor Doutor Rui Brito e coorientação do Doutor Carlos Simões no grupo de Biologia Estrutural e Computacional do Centro de Química de Coimbra da Universidade de Coimbra, e sob a coorientação da Professora Doutora Dora Brites no grupo de Neuroinflamação, Sinalização e Neuroregeneração do Instituto de Investigação do Medicamento (iMed.ULisboa), Faculdade de Lisboa, Universidade de Lisboa.

The research presented in this thesis was supported by Ph.D. fellowship PD/BD/135292/2017 from FCT Doctoral Programme "MedChemTrain" (PD/00147/2013) in Medicinal Chemistry — Ministry of Science, Technology, and Higher Education (MCTES), Portugal. The work performed at the Coimbra Chemistry Center, University of Coimbra, coordinated by Professor Doctor Rui Brito and Doctor Carlos Simões was funded in part by Fundação para a Ciência e a Tecnologia (FCT), grant CPCA/A0/7316/2020 for the High Performance Computing (HPC) resources provided, and grant UID/QUI/00313/2019 (to Coimbra Chemistry Centre). The work developed in the Neuroinflammation, Signaling and Neuroregeneration lab (NeuroSignal) coordinated by Professor Doctor Dora Brites at the Research Institute for Medicines (iMed.ULisboa), Faculty of Pharmacy, University of Lisbon, was funded by Santa Casa da Misericórdia de Lisboa (SCML), project ref. ALS-Research Grant ELA-2015-002, by Fundação para a Ciência e a Tecnologia (FCT), project PTDC/MED-NEU/31395/2017 and LISBOA-01-0145-FEDER-031395 to Dora Brites, as well as in part by FCT: UIDB/04138/2020 and UIDP/04138/2020, to iMed.ULisboa.

Dedicated to my Parents & Brother

Dedico este trabalho aos meus pais e irmão

“Wax on, right hand. Wax off, left hand. Wax on, wax off. Breathe in through nose, out the mouth. Wax on, wax off. Don't forget to breathe, very important.”

Mr Miyagi, “The Karate Kid”

ACKNOWLEDGEMENTS

First and foremost, I want to express my deepest gratitude to my supervisor Prof. Dr. Rui M. M. Brito for all the scientific advice and support. His vision and know-how to see things in an orderly manner, critical supervision, leadership and broad awareness are a source of inspiration. I also acknowledge the fact that he gave me the freedom to experiment, to take the paths of my own choosing through the vicissitudes of the scientific and creative process. I am honoured he has been my Ph.D. supervisor, and I am grateful to him for guiding me throughout this work.

I am particularly indebted to my co-supervisor Dr. Carlos Simões. He has been a fantastic mentor throughout the years. I thank him for his invaluable guidance on the craft of writing, his discerning ideas and insightful discussions in the field of science that refined my thinking and guided my research. With him, I learned to see the big picture, being reminded all the time to *first make it work, then make it perfect*.

I thank Prof. Dr. Dora Brites for providing me the opportunity to perform the experimental part of this work myself at the Neuroinflammation, Signaling and Neuroregeneration group, for her guidance, kindness and wise words. I also thank her for the critical supervision, scientific rigor and vast experience in the neuroimmune landscape, which was crucial to choose the right direction and successfully complete my experimental work.

I am thankful also to all members of the Structural and Computational Biology group, who provided significant help and constant support for this project, and the basis of a friendly environment where I found myself welcome. Special thanks to Ana Mata, Andreia Cunha, Daniela Vaz, Nícia Ferreira, Nuno Alves, Pedro Cruz, Rui Loureiro and Zaida Almeida. In particular, I am deeply grateful to Ana Mata and Nuno Alves, with whom I shared the office during most of the time. To Ana Mata for her devoted and exceptional troubleshooting skills and excellent illustrations, and to Nuno Alves for his outstanding research insights and ideas. Thank you for the scientific discussions that greatly contributed to improve the quality of this work. Thank you for your friendship.

Also, I thank the dedicated team at iMed.ULisboa for all their thoughtful expertise, thorough advice, empathy and positive environment, including Prof. Dr. Ana Rita Vaz, Prof. Dr. Adelaide Fernandes, Dr. Gecioni Loch-Neckel, Alexandre Neto, Catarina Barros, Gonçalo Garcia, Helena Coutinho, Dr. Hélio Crespo, Isabel Maurício, Laura Prezado, Maria Vaz Pinto, Marta Barbosa, Paulo Faria and Rita Ribeiro. Prof. Dr. Ana Rita Vaz and Dr. Gecioni Loch-Neckel deserve a special mention for the valuable expert advice, continuous support during the experimental work, and most of all for being generous, kind persons. Also, I would like to mention my dear friends Alexandre Neto, Catarina Barros, Gonçalo Garcia, Maria Vaz Pinto,

Paulo Faria and Rita “Chefinha” Ribeiro for the nice times we have been spending together, memories that will stay with me for the rest of my life, for your support and for our unforgettable friendship. You guys will be great scientific thinkers and an inspiration for generations to come. I am proud for sharing this journey with you. I miss you all and am grateful to have known you.

I thank all my friends for the emotional support and encouragement, for the invaluable moments and memories over the years, and for playing a part in keeping me sane during the more difficult times. Without you this work would not have been possible.

I thank my family for all their support and willingness to listen, and for allowing me the freedom to discover my own path in life. For their love and inspiration.

Last but not least, I thank the Portuguese Foundation for Science and the MedChemTrain Ph.D. programme (PD/00147/2013) in Medicinal Chemistry for the financial support (PD/BD/135292/2017), as well as PTDC/MED-NEU/31395/2017 in iMedULisboa, and all the institutions involved in this project.

CONTENTS

PART I GENERAL INTRODUCTION

EPILOGUE

ABSTRACT

The modulation of neuroinflammation has been increasingly recognized as a viable approach to slow down or even halt the progression of several disorders of the central nervous system (CNS), such as Alzheimer's disease, Parkinson's disease, amyotrophic lateral sclerosis, multiple sclerosis, among others. The search for therapeutic molecules targeting microglia – the immune cells of the CNS – has been gaining momentum in the field of neurodegeneration, not only to decipher the molecular mechanisms of microglia-mediated neurotoxicity but also to find promising targets to reach the limelight of clinical research. One of the most important group of cytokines implicated in neuroinflammation is the interleukin 1 (IL-1) family, a well-characterized cluster that plays a critical role in inflammatory responses. Importantly, a growing body of evidence is showing that blocking the IL-1 signalling pathway via interleukin-1 receptor type 1 (IL-1R1) reduces neuroinflammation and delays disease progression. Notably, while there is a substantial body of research on the effects of IL-1R1 in such pathological processes, no small molecule modulators of this receptor have been reported to date.

This project focused on the modulation of harmful neuroinflammatory responses associated with specific microglia subtypes, using IL-1R1 as a model target, via small molecules discovered through computational techniques and tested in human CHME3 microglial cell lines. The first goal was to identify and prioritize regions in the IL-1R1 ectodomain (ECD) surface prone to small-molecule binding, using three binding site prediction algorithms. The predictive druggability landscape analysis of IL-1R1 led to the identification of two potential druggable regions that may disturb pro-inflammatory cytokine binding.

Given that IL-1R1 regulates IL-1 signalling in two forms - as a membrane-bound form and as a soluble ECD – the conformational dynamics of these two forms, with particular focus on a particular predicted binding site, was studied and compared by long timescale all-atom molecular dynamics (MD) simulations. These simulations revealed that major differences between the two IL-1R1 forms appear to be mainly governed by rearrangements of the linker connecting the D2 and D3 domains of the ECD, leading to different structure-dynamics behaviours. Representative protein conformations of both forms were extracted from the MD runs based on physicochemical features of the IL-1R1 binding site.

The amount of structural data generated by the MD simulations coupled with experimental data motivated the implementation of an integrated structure-based virtual screening (VS) protocol targeting the ECD of IL-1R1, combining (i) three-dimensional (3D) pharmacophore modelling, (ii) clustering by maximum common substructures (MCS), (iii) molecular docking, and (iv) 3D shape similarity. Six receptor-based pharmacophore hypotheses were generated

on the IL-1R1 binding site, which allowed the retrieval of 27.206 virtual hit compounds from a CNS-tailored virtual screening deck of 19.3 million compounds. As a post-screening filter, said screening hits were docked into IL-1R1, with the best candidates ranked via quantitative analysis of protein-ligand interactions and pharmacophore fitness levels. Twenty-one commercially available compounds were selected based on the best docking results and 3D shape similarity to a dataset of compounds exhibiting relevant bioactivity data, and taking in consideration chemical diversity. Compounds were acquired from their respective chemical vendors for *in vitro* evaluation.

The selected compounds sought out by the VS campaign were evaluated *in vitro* in terms of aqueous solubility and cytotoxic activity in human HepG2 cancer cell lines and CHME3 microglial cell lines. Thereupon, microglia-based phenotypic screenings were employed to search for small molecules able to modulate the effects of microglial pro-inflammatory activation. Three compounds displaying the best solubility and toxicity profiles were tested at 20 μM in human CHME3 microglia after activation with a pro-inflammatory cytokine interferon-γ (IFN-γ). Two compounds were able to prevent upregulation of the inflammatory axis IL-1R1/IL-1β/IL-6/NRLP3/iNOS in microglia upon incubation with IFN-γ, as well as to reduce IFN-γ-induced activation of nuclear factor-kappa B (NF-κB). Our findings point out that these compounds exert regulatory effects in microglia polarization by potentially inhibiting the IL-1R1/Myd88/NF-κB signalling pathway.

To sum up, this project was pioneer in discovering small molecule modulators of microglia-induced neuroinflammation, via an integrated medicinal chemistry approach encompassing the utilisation of computational methods and *in vitro* studies in human microglia. As a result, two molecular entities that modulate microglial pro-inflammatory markers and autocrine/paracrine signalling mediators have been discovered. Considering the current advanced state of this project, we firmly believe that the results achieved herein gathers conditions to "hit-the-ground running" for modulating microglia pro-inflammatory phenotypes and uncontrolled neuroinflammatory processes.

RESUMO

A modulação da neuroinflamação tem sido cada vez mais reconhecida como uma abordagem viável para retardar ou mesmo parar a progressão de várias doenças do sistema nervoso central (SNC), como a doença de Alzheimer, doença de Parkinson, esclerose lateral amiotrófica, esclerose múltipla, entre outras. A procura de moléculas com potencial terapêutico direcionadas à microglia - as células imunes do SNC – tem vindo a despertar atenção no campo da neurodegeneração, não apenas para decifrar os mecanismos moleculares de neurotoxicidade mediados pela microglia, mas também para encontrar alvos terapêuticos que possam alcançar a prática clínica. Um dos grupos de citocinas mais importantes implicado na neuroinflamação é a família da interleucina-1 (IL-1), um conjunto que desempenha um papel fundamental nas respostas inflamatórias. Vários estudos têm vindo a demonstrar que o bloqueio da via de sinalização da IL-1 através do recetor tipo 1 da interleucina-1 (IL-1R1) leva à redução da neuroinflamação e retarda a progressão de doença. Curiosamente, embora exista um grande conjunto de estudos sobre o IL-1R1, até ao momento não foram reportadas pequenas moléculas moduladoras da sua atividade biológica.

O propósito subjacente a este projeto centra-se na modulação de respostas neuroinflamatórias prejudiciais devidas a fenótipos polarizados da microglia, usando o IL-1R1 como modelo de estudo principal, através de pequenas moléculas identificadas com o auxílio de métodos computacionais de descoberta de fármacos e testadas em linhas celulares de microglia humana CHME3. O primeiro objetivo consistiu em identificar e priorizar regiões à superfície do domínio extracelular (ECD) do IL-1R1 com tendência para ligarem pequenas moléculas, usando três algoritmos de previsão de locais de ligação. A análise preditiva de locais de ligação no IL-1R1 levou à identificação de duas regiões propensas à interação com pequenas moléculas, que após a ligação, podem perturbar a interação das citocinas pro-inflamatórias.

Dado que o IL-1R1 regula a sinalização da IL-1 sob duas formas – como uma forma transmembranar e como um ECD solúvel – a variabilidade conformacional destas duas formas, com particular foco num local de ligação previsto, foi estudada e comparada através de simulações de dinâmica molecular (DM). Estas simulações revelaram que as principais diferenças entre as duas formas do IL-1R1 parecem ser devidas, em grande parte, a rearranjos conformacionais do "linker" localizado entre os domínios D2 e D3 do ECD, o que por sua vez leva a diferentes comportamentos estrutura-dinâmica. Conformações proteicas representativas de ambas as formas foram extraídas das corridas de DM com base em características físico-químicas do local de ligação do IL-1R1.

A quantidade de estruturais gerados pelas simulações de DM juntamente com dados experimentais motivou a implementação de um protocolo de rastreio virtual (VS), baseado na

estrutura, direcionado ao ECD do IL-1R1, que integra (i) modelação tridimensional (3D) de farmacóforos, (ii) agrupamento de estruturas químicas com base na máxima subestrutura comum (MCS), (iii) acoplamento molecular, e (iv) pesquisas de similaridade tridimensionais baseadas na forma. Inicialmente, 6 hipóteses de farmacóforo foram construídas usando o local de ligação previsto do IL-1R1, o que permitiu identificar 27,206 compostos a partir de uma biblioteca virtual personalizada de 19,3 milhões de moléculas previstas passarem a barreira hemato-encefálica e chegarem ao SNC. Este conjunto de compostos foi sujeito a estudos de acoplamento molecular, e filtrados por meio de análise quantitativa de interações proteína-ligando e níveis de complementaridade com o farmacóforo. Foram selecionados 21 compostos disponíveis comercialmente com base nos melhores resultados de acoplamento molecular e pesquisas de similaridade 3D contra um conjunto de compostos com dados de bioatividade relevantes, tendo em consideração a diversidade química. Para validar o trabalho computacional executado, os compostos foram adquiridos aos respetivos fornecedores para avaliação *in vitro*.

Os compostos selecionados através do protocolo de VS foram testados experimentalmente *in vitro* para averiguar a sua solubilidade aquosa e atividade citotóxica em linhas celulares de hepatoma humano (HepG2) e de microglia humana CHME3. Em seguida, foram realizados ensaios fenotípicos na microglia a fim de identificar compostos capazes de modular os efeitos da ativação pro-inflamatória da microglia. Os três compostos com melhores perfis de solubilidade e toxicidade foram testados na concentração de 20 μM na microglia CHME3 após ativação com a citocina pró-inflamatória interferão-gama (IFN-γ). Destes, dois compostos demonstraram capacidade para reverter a indução de mediadores pro-inflamatórios IL-1R1/IL-1β/IL-6/NRLP3/iNOS juntamente com uma redução de ativação do NF-κB na microglia após incubação com IFN-γ. Os nossos resultados indicam que estes compostos exercem efeitos reguladores na polarização da microglia possivelmente através da inibição da via de sinalização IL-1R1/Myd88/NF-κB.

Em suma, este projeto foi pioneiro em descobrir compostos moduladores da neuroinflamação mediada pela microglia, através uma abordagem integrada de química medicinal que incorpora a utilização de métodos computacionais e estudos *in vitro* em microglia humana. Como resultado, foram descobertas duas entidades moleculares que modulam os marcadores pro-inflamatórios da microglia e mediadores para sinalização parácrina e autócrina. Considerando o atual estado avançado deste projeto, acreditamos que os resultados aqui mencionados reúnem condições para o desenvolvimento de novas moléculas moduladoras da fenótipos pro-inflamatórios da microglia e neuroinflamação descontrolada.

LIST OF ABBREVIATIONS

AB/AM	Antibiotic-antimycotic
Ar	Aromatic ring
BBB	Blood-brain barrier
CADD	Computer-aided drug design
CNS	Central nervous system
DMEM	Dulbecco's modified eagle's medium
DMSO	Dimethyl sulfoxide
D1	Domain 1
D2	Domain 2
D3	Domain 3
ECD	Extracellular domain
FBS	Foetal bovine serum
H	Hydrophobic group
HBA	Hydrogen bond acceptor
HBintra	Intramolecular hydrogen bonds
HDB	Hydrogen bond donor
HEPES	4-(2-hydroxyethyl)-1-piperazineethanesulfonic acid
ICC	Immunocytochemistry
IFN-γ	Interferon-γ
IL	Interleukin
IL-1R1	Interleukin-1 receptor type 1
IL-1R1-ECD	Extracellular domain of interleukin-1 receptor type 1
iNOS	inducible nitric oxide synthase
MCS	Maximum common substructure
MD	Molecular dynamics
NF-κB	Nuclear factor-kappa B

N	Negatively charged group
NLRP3	NLR family pyrin domain containing 3
PAINS	Pan-assay interference compounds
PAM	Partitioning around medoids
PBS	Phosphate-buffer saline
PCA	Principal component analysis
PDB	Protein Data Bank
P	Positively charged group
POPC	1-palmitoyl-2-oleoyl-sn-glycero-3-phosphocholine
RT-qPCR	Real-Time Quantitative PCR
Rg	Radius of gyration
RMSD	Root mean square deviation
RMSF	Root mean square fluctuation
ROS	Reactive oxygen species
SASA	Solvent-accessible surface area
SBDD	Structure-based drug design
TIR	Toll/interleukin-1 receptor homology domain
TM	Transmembrane domain
VS	Virtual screening

THESIS OUTLINE

The research described in this thesis entails the application of *in silico* and experimental methodologies towards the identification of novel, neuroinflammatory small molecule modulators, via targeting strategies focused on an essential cytokine receptor involved in the inflammatory landscape. This thesis is organized in six main chapters – including a general introduction and the core results divided into five chapters - along-with an epilogue, an appendix, a section with references and a last page containing the relevant publications ensuing from this PhD project.

Part I starts with a brief overview on the role of neuroinflammation in neurodegenerative diseases, with special emphasis on microglial activation and its implications in neuroinflammatory responses. The relevance of microglial modulation in the context of neurodegeneration is discussed, along with some promising compounds and targets proposed to modulate microglial functions in the central nervous system (CNS). Interleukin-1 receptor type 1 (IL-1R1) is introduced as a potential target in neuroinflammation, in view of its involvement in the neuroinflammatory complex landscape. A short review of currently known IL-1R1 therapeutics is also provided. The second half of the chapter focus on the Medicinal Chemistry of neuroinflammation via computer-aided drug design (CADD) approaches. These facets represent the engine of this project, and an introduction to the basic principles and fundamental techniques in molecular modelling is provided, with special attention to the main methodologies employed throughout the project. The application of CADD approaches for designing and discovering neuroinflammatory modulators is also included in this review. Phenotypic screening strategies for the discovery of small molecule modulators under the light of their potential implementation in the neuroinflammation field is discussed. The final section of this chapter outlines the objectives of this thesis.

Part II focuses on the application of structure-based approaches to predict and evaluate IL-1R1 putative binding sites and interactions for the design of IL-1R1 small molecule modulators. The analysis of the available structural data on IL-1R1 is provided, with an emphasis on the interactions of IL-1R1 with other molecules, and the results of structural quality evaluations are reported. The chapter also presents a summary of the different methods used to predict druggable binding sites. A thorough examination comprising three different binding site prediction methods is conducted to map and prioritize suitable binding regions on the surface of IL-1R1.

Part III deals with the results of molecular dynamics (MD) simulation studies performed on two biologically active IL-1R1 forms. An exhaustive comparative analysis of the conformational dynamics between the soluble and membrane-bound IL-1R1 ectodomains

(ECDs) is presented, focusing on the conformational stability and flexibility of ligand binding sites predicted in Part II. For each IL-1R1 form, representative binding site conformations are extracted from the MD simulations for virtual screening (VS) purposes.

Part IV reveals the implementation of a multi-layered VS approach towards the identification of novel, small molecule neuroinflammatory modulators of pharmaceutical interest. Amongst the techniques employed at different steps of the VS workflow are: (i) receptor-based pharmacophore modelling; (ii) pharmacophore-based VS; (iii) molecular docking; and (iv) three-dimensional (3D) shape similarity methods. The filtering of virtual libraries of chemical compounds using molecular descriptors predicted for blood-brain barrier (BBB) permeability is approached. From the VS procedure, 21 compounds, predicted as promising starting points in the development of novel and selective IL-1R1 modulators are identified and acquired from their respective chemical vendors for *in vitro* evaluation.

Part V reports the results of a setup array of experimental assays designed to assess the solubility and toxicity profiles of the compounds carefully chosen via the VS protocol. A brief review is provided on the human cell lines selected for cytotoxicity and cell viability assays in this chapter. The utilisation of *in silico* methods for the prediction of compound promiscuity is also carried out.

Part VI describes the implementation of an *in vitro* phenotypic-based screening assay for interrogating the ability of three VS selected compounds to modulate microglial pro-inflammatory activation. Considerations about the interleukin-1 (IL-1) signalling pathways in microglia are discussed as well as the expression of IL-1R1 in this cell type. The experimental validation of the *in silico* results allowed the identification of promising modulators of microglia-mediated neuroinflammation.

The **Epilogue** reflects on the findings and future perspectives of this project and provides a brief overview of my own perspectives in the field of neurodegeneration drug discovery.

PART I

General Introduction

"Shaped a little like a loaf of French country bread, our brain is a crowded chemistry lab, bustling with nonstop neural conversations. Imagine the brain, that shiny mound of being, that mouse-gray parliament of cells, that dream factory, that petit tyrant inside a ball of bone, that huddle of neurons calling all the plays, that little everywhere, that fickle pleasuredome, that wrinkled wardrobe of selves stuffed into the skull like too many clothes into a gym bag."

Diane Ackerman, in *An Alchemy of Mind: The Marvel and Mystery of the Brain*

1.1. Targeting Neuroinflammation: The Common Thread in Neurodegenerative Diseases

The usage and meaning of "neuroinflammation", a word deriving from the combination of the Greek neuron (for nerve, sinew, tendon) with the Latin noun *inflammatio*, has been in constant evolution and remodelling. The name has been wrongly associated with encephalitis, a type of acute brain inflammation with tissue-infiltrating blood-borne immune cells (Graeber et al., 2011). Neuroinflammation actually refers to the response of the central nervous system (CNS) to injury and disease sparked by complex immune networks, coordinated by the activation of glial cells (microglia, astrocytes and oligodendrocytes) and neuron-glia interactions. The increasing awareness of the involvement of the immune system, not only in the progression but also directly related to the onset of CNS diseases, fuelled a renewed interest in the field in recent years (Craft et al., 2005; Brambilla, 2019; Guzman-Martinez et al., 2019). Indeed, neuroinflammation has been linked to Parkinson's disease (PD) (Troncoso-Escudero et al., 2018), Alzheimer's disease (AD) (Heppner et al., 2015; Ardura-Fabregat et al., 2017), amyotrophic lateral sclerosis (ALS) (McCauley and Baloh, 2019) and other CNS disorders, such as multiple sclerosis (Bjelobaba et al., 2017), traumatic brain injury (Simon et al., 2017), depression (Brites and Fernandes, 2015) and schizophrenia (Müller et al., 2015), among others.

Despite the involvement of different molecular triggering mechanisms in the above-mentioned diseases, a common feature of all is the activation of glial cells to a state that prompts an exacerbated secretion of pro-inflammatory factors. Importantly, microglia and astrocytes are the glial cell types responsible for mediating neuroinflammation in response to various stimuli, polarizing into pro-inflammatory and anti-inflammatory states with the release of multiple cytokines and chemokines, modulating the function of the neighbouring neurons. These dynamic behaviours are crucial for maintaining homeostasis of the brain microenvironment. However, in neurodegenerative diseases and aging, changes in the immune system triggers an amplification of the initial immune response and consequently a shift towards a pro-inflammatory immune microenvironment resulting in neuronal cell death and ultimately chronic neurodegeneration (Hickman et al., 2018).

Within this context, modulation of neuroinflammatory cytokine networks has emerged as an appealing strategy aiming to halt, or at least slow down, the induction and progression of neurodegenerative diseases. The identification of target macromolecules and the search for drugs able to modulate neuroinflammation is of central importance in the development of therapeutics for neuroinflammation-associated neurodegenerative diseases. To date, however, few small molecules with promising *in vivo* efficacy to modulate neuroinflammation-associated effects were developed. This is mainly due to unexpected side effects by targeting

peripheral inflammation responses rather than being selective to glia-associated mediators and pathways that prevail in CNS-inflammation.

1.1.1. Neuroinflammation: a Yin and Yang (dys)harmony

Traditionally, the brain has been considered an immuno-privileged system, derived from the presence of the blood-brain barrier (BBB) and the apparent inability to elicit immune responses against danger signals originating within the CNS. However, throughout the years, it has become clear that this immune-privileged status of the CNS is not as solid as it might be, as it is deeply interconnected with the peripheral inflammatory responses, towards the ultimate goal of protecting and preserving the integrity of the CNS (Lucin and Wyss-Coray, 2009). Importantly, the complex web of molecular connections and interactions that prevail between the BBB cellular machinery (astrocytes, pericytes, and endothelial cells), the CNS "housekeeping" cells (microglia, astrocytes and oligodendrocytes) and the peripheral immune cells, are critical for the regulation of neuroinflammatory responses. In this sense, neuroinflammation is a coordinated cell-mediated immune response to damaged nervous tissues, stimulated by factors such as the normal aging process, environmental factors, trauma, stroke, diabetes, infections, toxins and drugs. This process is driven primarily by microglia activation, leading to an increased expression of inflammation-related miRNAs (inflamma-miRs), secretion of pro-inflammatory mediators such as interleukin (IL)-1β, IL-6, tumour necrosis factor (TNF)-α, the high mobility group box protein 1 (HMGB1), free radicals and reactive oxygen species (ROS), and release of small extracellular vesicles, usually designated as exosomes. To re-establish normal levels, microglia also releases several anti-inflammatory and neuroprotective agents such as IL-4, IL-13, IL-10 and transforming growth factor (TGF)-β (Sochocka et al., 2017; Guzman-Martinez et al., 2019). Notably, all these components summon, amplify, spark, calm, and transform one another, endowing CNS with an absurdly intricate network of cells and molecules able to promote and maintain homeostasis.

However, just as the CNS immunity holds the "tools" to repair and protect the brain, glial cells can also become overstimulated. When that happens, there is a shift toward more reactive glia phenotypes, resulting in an elevated expression and release of pro-inflammatory cytokines and ROS, together with reduced expression and release of molecules involved in reparative processes, such anti-inflammatory cytokines. In fact, this persistent activation of the immune system, mediated by microglia and astrocytes, alongside the periphery-to-CNS inflammatory crosstalk, has been implicated in a wide range of CNS diseases, including classic neuroinflammatory disorders like multiple sclerosis and neurodegenerative diseases such as AD, PD or ALS, and neuropsychiatric disorders, as depression and schizophrenia (Brambilla, 2019). A summary of the most well-known neuroinflammation-associated diseases and related conditions is provided in **Table I.1**.

Table I. 1 - Aetiology and immune profile of representative examples of neuroinflammatory conditions.

Disease	Aetiology-based proposal	Innate immune response	Adaptive immune response	References
AD	β-amyloid (amyloid plaques) Tau (neurofibrillary tangles)	↑ microgliosis and astrogliosis ↑TNF-α ↑IL-1β ↑IL-6 ↑IFN-γ ↑IL-10 ↑complement ↑chemokines ↑NLRP3 ↑TLRs	↑antibody and T-cell response	(Blum-Degena et al., 1995; Monsonego et al., 2003; Heneka et al., 2013; Brosseron et al., 2014; Wu et al., 2015; D'Anna et al., 2017)
PD	α-synuclein intra-neuronal inclusions	↑microgliosis and astrogliosis ↑TNF-α ↑IL-1β ↑IL-6 ↑IFN-γ ↑IL-10 ↑complement ↑chemokines ↑NLRP3 ↑TLRs	↑antibody and T-cell response	(Reale et al., 2009; Qin et al., 2016; Li et al., 2018; Tansey and Romero-Ramos, 2018; Anderson et al., 2021)
ALS	Genetic mutations Sporadic nature	↑microgliosis and astrogliosis ↑TNF-α ↑IL-1β ↑IL-6 ↑IL-8 ↑IFN-γ ↑S100B ↑NLRP3 ↑chemokines ↑ROS	↑CD4+, ↑CD8+ T-cells	(Kamo et al., 1987; Migheli et al., 1999; Johann et al., 2015; Gustafson et al., 2017; Hu et al., 2017; Jin et al., 2020)
MS	Autoimmune Viral	↑microgliosis and astrogliosis ↑TNF-α ↑IL-1β ↑IL-6 ↑S100B ↑NLRP3 ↑ROS	↑Heat Shock Proteins ↑neurotrophins ↑antibody and T-cell response	(Stelmasiak et al., 2000; Barateiro et al., 2016; Burm et al., 2016; Barros and Fernandes, 2021)
HD	Huntingtin	↑microgliosis ↑TNF-α ↑IL-1β and ↑IL-6 ↑IL-10 ↑chemokines ↑ROS	Not reported	(Björkqvist et al., 2008; Silvestroni et al., 2009; Labadorf et al., 2015)
Depression	Multifactorial	↑microgliosis ↑TNF-α ↑IL-1β and ↑IL-6 ↑chemokines ↑ROS	↑T-regulatory cell response	(Liu et al., 2012; Brites and Fernandes, 2015; Ng et al., 2018; Patas et al., 2018)
Ageing	Natural event	↑glia senescence ↑pro-inflammatory cytokines ↑ROS ↓Natural Killer cell response	↓T-cells	(Brites, 2015; Whiting et al., 2015; Lee et al., 2017)

Table abbreviations: Alzheimer's disease (AD); Parkinson's disease (PD); amyotrophic lateral sclerosis (ALS); multiple sclerosis (MS); Huntington's disease (HD); interleukin-1β (IL-1β); interleukin-6 (IL-6); tumour necrosis factor-α (TNF-α); interleukin-8 (IL-8); interleukin-10 (IL-10); S100 calcium-binding protein B (S100B); interferon-γ (IFN-γ); NLR family pyrin domain containing 3 (NLRP3); reactive oxygen species (ROS); toll-like receptors (TLRs).

Adapted from Stephenson et al., 2018

One of the most well-known examples of a disease featuring neuroinflammation is AD, a progressive neurodegenerative age-associated condition accounting for 60 to 70% of the estimated 50 million people globally who suffer with dementia (Livingston et al., 2020). The pathogenesis of AD requires the contribution of multiple factors, of which two have been considered the main hallmarks: the presence of amyloid-β-peptide (Aβ) plaques and neurofibrillary tangles (aggregates of hyperphosphorylated tau protein) in the brain. However, it has been reported for decades that the brains of AD patients present signs of a persistent inflammation response, leading people to question whether AD leads to inflammation or inflammation leads to AD. Only more recently, in parallel with the exponential growth of epidemiological and genetic linkage data regarding microglial and astrocytic neurobiology, it was recognized that the immunological mechanisms are active players in the onset and progression of AD pathophysiology (Metcalfe and Figueiredo-Pereira, 2010; Heneka et al., 2015; Heppner et al., 2015). Essentially, activated microglia and astrocytes (albeit in a lower fashion) secrete a variety of inflammatory mediators (pro-inflammatory cytokines, prostaglandins, free radicals and complement system), but do it so in an exaggerated and chronic manner, leading to neuroinflammation and neurodegeneration in a vicious cycle, which drives AD pathogenesis. Indeed, these cells surround amyloid plaques and react to Aβ with a pro-inflammatory phenotype endowed by cytokine expression (e.g., IL-1β, IL-6, TNF-α) that may initially limit amyloidosis but ultimately becomes exacerbated and neurotoxic. The presence of activated microglia near amyloid plaques suggests that Aβ accumulation may trigger a persistent microglial activation (Mizuno, 2012; Heppner et al., 2015; Leng and Edison, 2020). Recently, a statistical analysis of human post-mortem cortex conducted by Felski et al. estimated that activated microglia interaction with Aβ plaques leads to increased accumulation of tau pathology and subsequent cognitive decline, positioning tangle pathology downstream of morphologically activated microglia (Felsky et al., 2019).

Among the many inflammatory pathways implicated in the disease, signalling through IL-1β reportedly worsens AD pathogenesis (Sciacca et al., 2003; Kitazawa et al., 2011). At the molecular level, IL-1β is regulated by the NLR family pyrin domain containing 3 (NLRP3) inflammasome, a central hub for cytokine production that initiates downstream inflammatory cascades in response to endogenous danger signals (**Figure I.1**). Upon stimulation, this inflammasome assembles into a multiprotein complex, activating the proteolytic processing of precursor proteins, leading to the biological active forms of IL-1β and IL-18, two important pro-inflammatory mediators which are significantly increased in AD brains (Licastro et al., 2000; Heneka et al., 2013; Italiani et al., 2018; Paik et al., 2021).

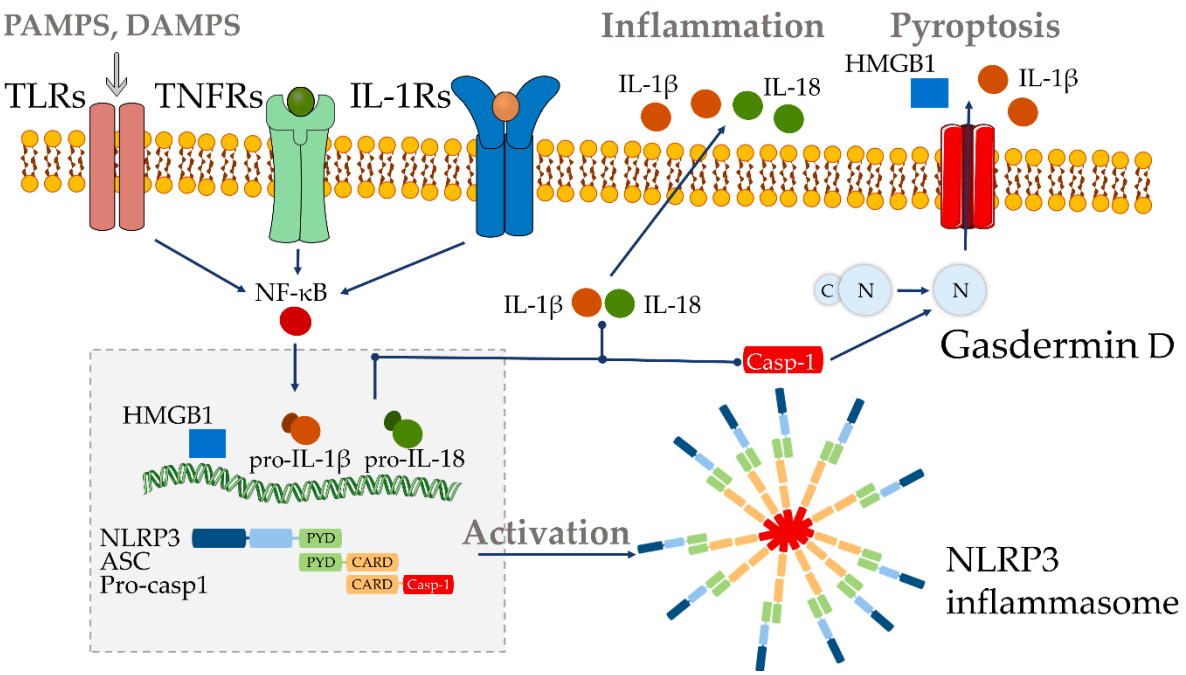

Figure I. 1 - Mechanism of NLRP3 activation upon cellular stress. First a priming signal, i.e., pathogen- or damage-associated molecular patterns (PAMPs/DAMPs) are recognized by tumour necrosis factor receptors (TNFRs), interleukin-1 receptor family members (ILRs) or toll-like receptors (TLRs), leading to the activation of the transcription factor nuclear factor-kappa B (NF-κB) and subsequent upregulation of NLR family pyrin domain containing 3 (NLRP3), pro-interleukin-1β (pro-IL-1β) and pro-interleukin-18 (pro-IL-18). Structurally, the NLRP3 protein contains a pyrin domain (PYD), and the ASC (the adaptor molecule apoptosis-associated speck-like protein) is formed by PYD and caspase recruitment domain (CARD) domains. Upon activation, the NLRP3 protein interacts with ASC via PYD, and the CARD domain of ASC recruits the CARD domain of pro-caspase-1 to form NLRP3–ASC–pro-caspase-1 complex. This assembly leads to the activation of caspase-1 (casp-1), which cleaves inactive pro-IL-1β and pro-IL-18 into active pro-inflammatory IL-1β and IL-18 cytokines, thereby activating inflammatory pathways. The activated inflammasome is also involved in an inflammatory form of cell death termed pyroptosis, as casp-1 is implicated in the cleavage of the C-terminal domain of Gasdermin D, which forms pores in the plasma membrane, releasing the cellular content into the extracellular environment and, consequently, increasing inflammation (Adapted from Zhou et al., 2016; Paik et al., 2021).

In parallel, other studies have been undertaken to understand the complex immune mechanisms and identify potential neuroinflammatory biomarkers or novel therapeutic targets in AD. For instance, Heneka et al. observed a significant reduction in AD symptom severity *in vivo* upon *NLRP3* gene deficiency in APP/PS1 mice, and concluded that Aβ-induced activation of the microglial NLRP3 inflammasome may boost AD progression (Heneka et al., 2013). More recently, the authors demonstrated a direct link between NLRP3 inflammasome activation and tau aggregation and pathology (Ising et al., 2019). In addition to the *NLRP3* gene, genome-wide association studies (GWAS) have identified rare structural variants of key protein-coding genes relevant to microglial function and inflammation, including *TREM2*, *PLCG2*, *ABI3*, *CD33* and *CR1*, considered to be risk factors for AD (Guerreiro et al., 2013; Durrenberger et al., 2015; Jansen et al., 2019).

Chronic neuroinflammation is also implicated in PD, the second most common progressive neurodegenerative disorder. The core of PD is characteristically ascribed to the accumulation of aggregated forms of misfolded α-synuclein (Lewy bodies) in the *substantia nigra* area of the brain. These abnormal protein aggregates have been deemed as a critical factor responsible for cellular homeostasis imbalance and progressive degeneration of dopaminergic neurons. However, although these molecular mechanisms underlying α-synuclein propagation in PD still remain elusive, the involvement of numerous innate and adaptive inflammatory processes in the brain and in the periphery of PD patients is increasingly recognized (Hirsch and Hunot, 2009; Troncoso-Escudero et al., 2018). McGeer et al. first reported the presence of large numbers of activated microglial cells in the brains of patients with PD, at post-mortem (McGeer et al., 1988). Hereafter, further post-mortem and *in vivo* imaging studies have confirmed the involvement of microglia in PD (Barkholt et al., 2012; Béraud et al., 2013). Also, a relationship between neuroinflammation and α-synuclein has been observed, as the overexpression of this peptide promote microglia polarization toward pro-inflammatory phenotypes. More recently, some studies have established a link between α-synuclein-specific T cells and cytotoxic immune responses in preclinical and early motor PD (Sulzer et al., 2017; Lindestam Arlehamn et al., 2020). Importantly, several reports have described up-regulated expression of major histocompatibility complex (MHC), T-lymphocyte infiltration and increased levels of inflammatory factors such as TNF-α, interferon-γ (IFN-γ), epidermal growth factor (EGF), TGF-α, TGF-β, IL-1β, IL-6, IL-2, inducible nitric oxide synthase (iNOS) and free radicals in the striatum and *substantia nigra* of PD patients (Mogi et al., 1994; Vawter et al., 1996; Vroon et al., 2007; Karpenko et al., 2018).

This tangled network of cytokines and immune molecules, microglial activation and sustained neuroinflammation emerge also as a prominent feature in ALS. Fundamentally, this non-cell-autonomous disease is characterized by motor neuron degeneration leading to progressive muscle weakness, paralysis and ultimately death (Lobsiger and Cleveland, 2007; McCauley and Baloh, 2019). Mutations in about a dozen of genes had already been identified as risk factors for ALS in humans. Of these, the main ones are the *Cu, Zn superoxide dismutase 1* (SOD1), *TAR DNA binding protein* (TDP-43), *fused in sarcoma* (FUS) and *chromosome 9 open reading frame 72* (C9orf72), responsible for 5-10% of ALS cases. The remaining 90–95% of ALS are sporadic in nature meaning there is no known cause or mechanism for the disease. Amongst the several intrinsic mechanisms proposed for neuronal death in ALS, the involvement of microgliosis and astrogliosis is now believed to be essential in the disease onset and/or progression (Yamanaka et al., 2008; Geloso et al., 2017). Indeed, a complex pathological interplay subsists between motor neurons and neighbouring glia at an early stage of the disease, long before neuronal cell death, and the degree of inflammatory responses correlates with disease progression (McCauley and Baloh, 2019). For instance, in SOD1 transgenic mouse models,

activated microglia were shown to increase their number in the spinal cord over the course of ALS, moving between protective (clearance) and damaging (persistent neuroinflammation) roles (Gerber et al., 2012). The activation of astrocytes and microglia is heterogeneous and brain-region-specific, still, it is plausible that both cells shift at a pre-onset phase to a more neuroprotective profile, to help mitigate tissue damage and restore homeostasis (Zhao et al., 2013). In contrast, during ALS slowly progressing phase, persistent microglial expression and secretion of pro-inflammatory markers such as IL-1β, IL-6, TNF-α, iNOS, cyclooxygenase-2 (COX-2) (Maihofner et al., 2003), as well as NLRP3 inflammasome (Deora et al., 2020), leads to neuronal dysfunction, contributing to disease progression. Several studies have reported dysregulated cytokine profiles in the cerebrospinal fluid (CSF) and serum of ALS patients during disease progression (Martínez et al., 2017; Mishra et al., 2017). In parallel, the dysregulation of miRNAs, namely miR-124, miR-146a and miR-155, has also been shown to influence the pathobiology of ALS (Parisi et al., 2013; Cunha et al., 2017; Barbosa et al., 2021; Vaz et al., 2021).

Collectively, the neuroinflammatory landscape in these CNS diseases holds up the notion that the overstimulation of the immune response is a major determinant in the pathophysiology of these diseases. Three main factors appear to be key across all the cited diseases, in many respects complementary in nature: i) cytokines, whether in a damaging or protective capacity (or both) are involved in the different disease stages, holding pleiotropic and systemic effects, and displaying variations in number and phenotypic features on all cell types; ii) glial cell activation is an early and persistent feature in the course of the disease, whose phenotype and function may change over time; iii) a whole constellation of neuron-glia interactions sustain and propagate the neuroinflammatory cascade (Brambilla, 2019).

Although our full understanding on the contribution of the immune system to neurodegenerative disorders still remain to be elucidated, several reviews can be found in the literature providing a thorough overview of neuroinflammation molecular pathophysiology (Brites and Vaz, 2014; Heppner et al., 2015; Troncoso-Escudero et al., 2018).

1.1.2. Microglia: the key immune cells at the crux of neuroinflammation

For a tiny cell type comprising approximately 5 to 15% of the total cells in the brain, currently there seems to be no room for doubt that microglia have an outsize impact on neuroinflammation and neurodegeneration (Frost and Schafer, 2016; Tavares-Gomes et al., 2021). These cells are found ubiquitously throughout the brain and spinal cord, and are thought to have hematopoietic origin, being derived from myeloid precursor cells from yolk sac, seeding the CNS very early during embryonic development (Butovsky and Weiner, 2018). Interestingly, the first mentions of this type of glial cells can be traced back to Frank Nissl in

1899, who used the term *stäbchenzellen* or rod cells to describe them (Nissl, 1899), and Alois Alzheimer in 1907, reporting the presence of large deposits of glia cells in the vicinity of the Aβ plaques (Alzheimer, 1907). Nonetheless, Río-Hortega was the first to provide a clear identification of microglia in the brain, alongside a description of some of their functional features such as migration and phagocytosis (Rio-Hortega, 1939). From then on, it was recognized that microglia function extends beyond its scavenger role onto a highly dynamic and multipurpose immune cell population, playing a fundamental role in the maintenance of CNS homeostasis.

Importantly, the idiosyncrasies and peculiarities that characterize microglia as the most prominent players in maintaining normal CNS function are owed to their phenotypical and functional versatility (**Figure I.2**). Indeed, in a non-stimulated state (resting or surveillance) microglia are constantly sensing their close environment with their long ramifications, whereas upon activation by an immune challenge, they undergo morphological changes to an amoeboid shape, shifting their gene expression pattern. Notably, this remarkable plasticity allows microglia to maintain and/or restore homeostasis, held by a carefully orchestrated ballet of processes like phagocytosis, cytokine production, antigen presentation and cell proliferation. Simultaneously, microglia are an important component in the protection and remodelling of synapse plasticity, and modulation of the activity and/or viability of astrocytes, oligodendrocytes, endothelial cells, and neurons (De Schepper et al., 2020).

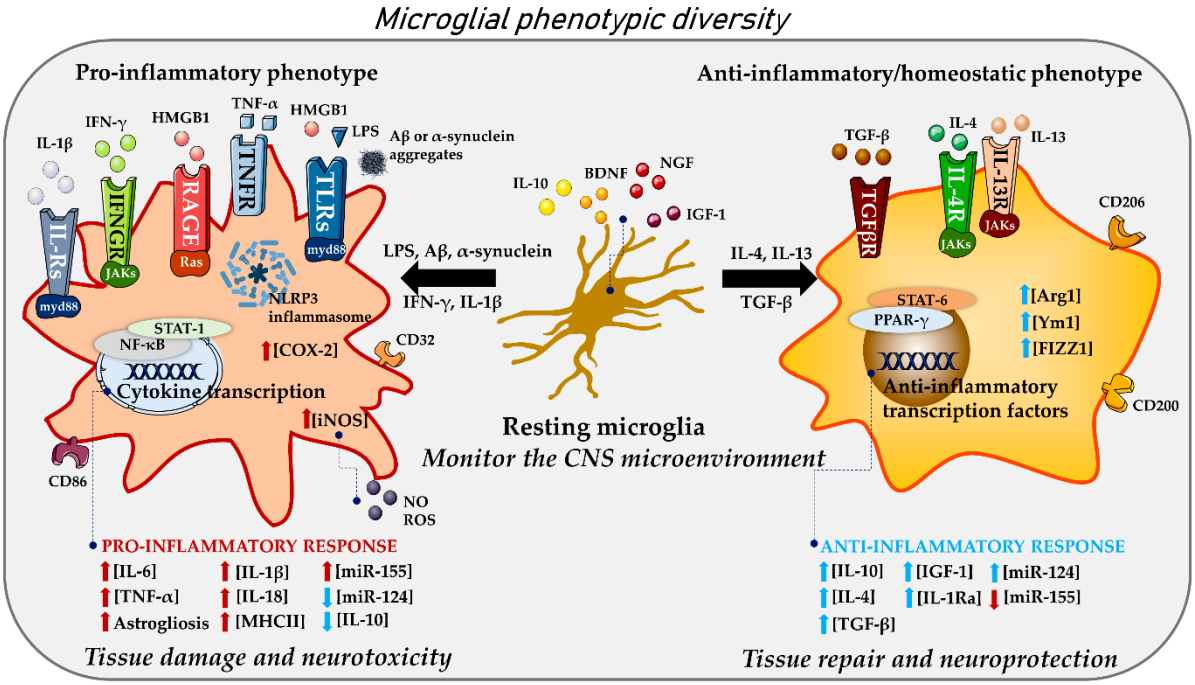

Figure I. 2 - Activation and polarization of microglia during neuroinflammation. In the steady-state, the amazingly mobile fine branches of ramified microglia provide extensive surveillance and show a rapid chemotactic response to immune challenges. Microglia interact with neurons and astrocytes and secrete neuroprotective factors such as brain-derived neurotrophic factor (BDNF), insulin-like growth factor 1 (IGF-1), nerve growth factor (NGF)

and interleukin (IL)-10. However, these cells can acquire different activation states in response to specific stimuli. Following recognition of lipopolysaccharides (LPS), interferon-γ (IFN-γ), IL-1, aggregated amyloid-β or α-synuclein, microglia shift to a pro-inflammatory phenotype, characterized by the upregulation of the major histocompatibility complex (MHC) class II, the release of pro-inflammatory cytokines, i.e., IL-1β, IL-18, IL-6, tumour necrosis factor (TNF)-α, transcription of pro-oxidant molecules including inducible nitric oxide synthase (iNOS) and cyclooxygenase-2 (COX-2), increased levels of miRNA (miR)-155 and downregulation of miR-124 and IL-10. The IFN-γ receptor (IFNGR) signalling increases iNOS expression. Activated microglia release both nitric oxide (NO) and reactive oxygen species (ROS) targeting damaged neurons or cells undergoing apoptosis. Toll-like receptors (TLRs), via high mobility group box protein 1 (HMGB1), LPS or misfolded proteins, tumour necrosis factor receptors (TNFRs) and interleukin-1 receptor family members (ILRs) signalling pathways drive nuclear factor-kappa B (NF-κB) activation, resulting in the expression of cytokines as well as of the NLR family pyrin domain containing 3 (NLRP3). Activation of the NLRP3 inflammasome in microglia induces IL-1β and IL-18 maturation. In turn, the release of these cytokines promotes astrogliosis and neuronal dysfunction, creating a positive feedback loop that drives additional cytokine production and primes local microglia for inflammasome activation. When activated alternatively by IL-4, transforming growth factor (TGF)-β, or IL-13 microglia attain anti-inflammatory/homeostatic states prompting neuroprotection through secretion of IL-4, IL-10 and TGF-β, as well as upregulation of IGF-1, arginase 1 (Arg1), chitinase 3-like protein 3 (Ym1), found in inflammatory zone (Fizz1) and interleukin-1 receptor antagonist (IL-1Ra). These phenotypes also show a downregulation of the pro-inflammatory miR-155 expression and an upregulation of miR-124. All the above-mentioned mediators are differently expressed in microglia in accordance with their phenotype upon activation, which in turn exhibit a wide spectrum of possibilities depending on stimuli. (*The two represented microglia phenotypes are a simplified view of the different activation profiles*)

However, microglia can also promote neuronal dysfunction and degeneration in case of prolonged or chronic stimulation, losing gradually their functionality. Under pathologic conditions, such as exposure to misfolded proteins (as occurs in many neurodegenerative disorders), infections, or CNS injury, an uncontrolled and amplified neuroinflammatory response can lead to detrimental outcomes. Indeed, persistent neuroinflammation can impair the ability of microglia to clear debris, contributing to synaptic loss and neuronal degeneration, in a vicious cycle (Hickman et al., 2018).

In recent years, a dramatic increase in our understanding of the crosstalk between microglia and other cell types in the CNS and periphery has been witnessed, revealing their potential as therapeutic targets. As such, targeting the dark side of microglia have been gaining momentum for the modulation of neuroinflammation (Priller and Prinz, 2019).

1.1.2.1. Microglia homeostasis: a finely tuned mechanism

Microglia have been firmly established as a key cellular component in brain development and homeostasis. Microglia-driven neuroimmune responses are shaped by a whole array of interactions within the CNS cellular microenvironment. These communications involve a plethora of ligand (commonly termed signals) and receptor interactions, resulting in tightly regulated biological functions, including cell migration, phagocytosis, the induction of

acquired immunity, and secretion of factors including cytokines, prostaglandins, ROS and growth factors. Fundamentally, the multifunctional roles of microglia are designed to sense disturbances and elicit appropriate microglial responses to maintain homeostasis (De Schepper et al., 2020).

Gene expression profiling of microglia showcased diverse phenotypes exhibiting multifaceted roles and significant spatiotemporal variation, dependent on specific brain environments, in development and immune modulation (Grabert et al., 2016). Indeed, these cells seem to display a spectrum of cellular forms that express a homeostatic core signature and others that appear to assume a more pro-inflammatory profile. Overlying this diversity, microglia are also dynamic, and may switch between different states (physical and/or biochemical changes) in response to different stimuli. Several phenotypes have been already characterized in conditions such as aging or disease (Caldeira et al., 2014; Keren-Shaul et al., 2017; Olah et al., 2020).

Under normal circumstances, microglia display a more uniformly quiescent and "silent" phenotype, spaced throughout the brain, processes extended, actively patrolling their microenvironment for subtle changes or the presence of pathogens. In this state, microglial cells strongly sense and regulate the proper function of the neuronal networks, ensuring CNS homeostasis and function (Nimmerjahn, 2005). Microglia produce physiological levels of pro- and anti-inflammatory cytokines such as IL-1β, IL-10 and TNF-α, and various trophic factors and synaptogenic signals, which are involved in synaptic plasticity, learning and memory (Blank and Prinz, 2013; Donzis and Tronson, 2014). Interestingly, several reports suggest that the chemokine C-X3-C motif ligand 1 (CX3CL1) and CD200, expressed by neurons, interact with microglia CX3C chemokine receptor 1 (CX3CR1) and CD200 receptor, respectively, keeping microglia in this steady-state, acting also as fundamental players in synaptic pruning, synaptic plasticity and adult neurogenesis (Cardona et al., 2006; Shrivastava et al., 2012). Additionally, microglia secrete TGF-β, insulin growth factor 1 (IGF-1) and brain-derived neurotrophic factor (BDNF), promoting the differentiation and survival of neurons. Besides these beneficial roles on neuronal activity, microglia also promote neuronal death via soluble factors, such as nerve growth factor (NGF) and ROS (Butovsky and Weiner, 2018).

Microglia ability to detect potential stimuli that disturb CNS homeostasis is intimately linked to the expression of a hallmark cluster of genes (*sensome*) and their corresponding proteins, known as pattern recognition receptors (PRRs) (Hickman et al., 2013). These include toll-like receptors (TLRs), inflammasome-forming nucleotide-binding oligomerization domain (nod)-like receptors (NLRs), and triggering receptor expressed on myeloid cells (TREMs), among others. Importantly, they recognize and bind danger-associated molecular patterns (DAMPs, e.g., Aβ or α-synuclein) and pathogen-associated molecular patterns (PAMPs, e.g., virus or

bacteria, such as lipopolysaccharides), sparking microglial activation. As a result, a cascade of molecular events occurs, leading to either a pro- or anti-inflammatory response, promoting either neuroprotection or neuronal damage. Moreover, microglia suffer visible morphological changes, with a clear increase in amoeboid microglial density, acquiring specific functions, including phagocytosis, and secretion of cytokines, chemokines, ROS and trophic factors (De Schepper et al., 2020). In the brain, this neuroinflammatory response is of paramount importance to protect the CNS.

The binary M1/M2 classification of pro-inflammatory and anti-inflammatory microglia have classically been used to distinguish and characterize the phenotypic predilections of such cells. The implication of such dichotomy was that the physiological roles of macrophages were sufficiently well understood to extrapolate it to microglia, without respect to the dissimilarities between these two myeloid populations. Currently, there is a broad consensus on the oversimplification and limited nature of this classification scheme (Ransohoff, 2016). Accordingly, microglia exist in a continuum of transcriptional states combined with tightly packed networks of separate expression profiles, likely based on their exposure to different stimuli. Activation of microglia results in increased expression and production of pro-inflammatory cytokines (e.g. IL-12, IL-6, IL-1β, TNF-α), oxidative metabolites (ROS and iNOS) and inflammatory-related microRNAs (miRNA-155, miRNA-27b, miRNA-326). Moreover, there is also increased production of chemokines such as IL-8 and monocyte chemoattractant protein 1 (MCP-1), which can recruit other microglia and peripheral macrophages to the injury site. Oppositely, it is now known that microglia adopt a more anti-inflammatory/homeostatic phenotype that counterbalances and resolves the preceding pro-inflammatory response. This shift toward an anti-inflammatory milieu is characterized by the expression of anti-inflammatory markers such as IL-4, IL-10, IL-13, IL-1Ra, TGF-β, arginase 1 (Arg1), IGF-1, chitinase 3-like protein 3 (Ym1), and anti-inflammatory miRNA-124, miRNA-146a, miRNA-21 and miRNA-223 (Lee et al., 2002; Graeber et al., 2011; Brites, 2020). Their function is deeply involved in dampening neuroinflammation, by counteracting pro-inflammatory signalling pathways and inducing a regenerative/repairing polarization.

These chameleon-like behaviours of microglia are inherently synchronized with astrogliosis, as astrocytes are activated by a multitude of molecules (e.g., inflammatory cytokines) released by CNS damaged cells, neighbouring glia and infiltrating immune cells, particularly T-cells (Vainchtein and Molofsky, 2020). While the exact mechanisms by which astrocytes operates in the brain remain elusive, it is clear that these cells also release cytokines and chemokines, modulating the neuroinflammatory response and supporting homeostatic neuronal function. Recently, Damisah et al. revealed, through photochemically induced neuronal apoptosis, a precisely and complementary phagocytic response of both microglia and astrocytes in the

removal of apoptotic cells, that may be critical for maintaining brain homeostasis (Damisah et al., 2020).

1.1.2.2. Microglial dysregulation in chronic neuroinflammation

Under healthy conditions, microglia can deal with small deviations in homeostasis. However, under more severe and chronic conditions, an uncontrolled and sustained activation of microglia may lead to neurodegeneration. Indeed, microglia chronic activation by abnormal protein aggregates, such as Aβ and α-synuclein aggregates, or by lipopolysaccharide (LPS), or even injury, can drive microglial dysregulation, responding exaggeratedly to stimuli generating a strong pro-inflammatory microenvironment. In other words, activated microglia may act as a double-edged sword being either protective or detrimental, either by reducing in early phases the stimuli through increased phagocytosis, clearance and degradation, though the progressive accumulation of such immune challenge may promote a chronic stimulation of microglia, resulting in a low-grade pro-inflammatory status (Craft et al., 2005; Hickman et al., 2018).

Aging and aging-related neurodegenerative diseases are associated with signs of chronic neuroinflammation. In such conditions, microglia display reduced motility and impaired phagocytosis, thereby altering their ability to mount a normal response to injury, releasing dysregulated quantities of pro-inflammatory cytokines and ROS. For instance, *in vitro* administration of Aβ to cultured CHME3 microglial cell line influenced their phagocytic properties, inducing an increased expression of key innate-associated and pro-inflammatory markers such as IL-1R1 and iNOS, microglial cell death, and reduced secretion of BDNF (Hjorth et al., 2010). In microglia, TLRs bind fibrillary Aβ and are essential for microglial activation, resulting in the generation of archetypical pro-inflammatory cytokines (TNF-α, IL-1β, IL-6, IL-12, IL-23), chemokines and stress-associated neurotoxic factors (ROS, iNOS) (Jana et al., 2008; Reed-Geaghan et al., 2009). These inflammatory mediators may further enhance their production by acting in an autocrine manner or by paracrine signalling and activation of astrocytes.

Irrefutably, chronic neuroinflammation mediated by microglial cells is a major pathophysiological contributor to neuronal dysfunction. Activated microglia, together with reactive astrocytes, pump out tons of inflammatory products sparking widespread neuroinflammation and neurodegeneration. Importantly, a key central regulator of immunity has been postulated to play a central role in these microglia-mediated neuroinflammatory responses, the pro-inflammatory transcription factor nuclear factor-kappa B (NF-κB) p65/p50 heterodimer. Multiple receptors converge on the canonical NF-κB signalling activation such as tumour necrosis factor receptors (TNFRs) and interleukin-1 receptor family members

(ILRs), TLRs or ROS. This process is known to trigger the translocation of NF-κB into the nucleus and the expression of pro-inflammatory genes, involving the activation of the NLRP3 inflammasome. Noteworthy, enhanced microglial NF-κB inflammatory activity have been linked to neuroinflammation-related neurodegeneration in ALS, AD and PD (Frakes et al., 2014; Ju Hwang et al., 2019; Bellucci et al., 2020). Zhang et al. reported in mice that the hypothalamic NF-κB activity changed over their lifespan. In this work, while activation of NF-κB in hypothalamic neurons by IκB kinase-β (IκK-β) shortened the lifespan of mice alongside an accelerated aging status, delivery of IkBα, an NF-κB negative regulator, revealed a neuroprotective effect. The number of microglia exhibiting activated NF-κB was enhanced with age in the hypothalamus, overproducing pro-inflammatory cytokines such as TNF-α. In contrast, inhibiting microglial NF-κB activation abolished the age-induced increase of hypothalamic microglia and also prevented microglial TNF-α expression (Zhang et al., 2013). With such example in mind, it is clear that the aberrant activation of the NF-κB cascade amplify pro-inflammatory signals and contribute to chronic and progressive neuronal loss.

Importantly, understanding the homeostatic balance of molecular interactions between microglia, neurons and astrocytes, as well as establishing correlations between certain microglial phenotypes and some diseases is of utmost significance to get a more detailed foundation of the roles of microglia in neurodegeneration. Moreover, the elucidation and characterization of microglial activation profiles can also shed light on the "best/ideal" *windows of opportunity* to slow neuroinflammation-associated neurodegeneration processes.

1.1.2.3. Microglial modulation as a pharmacological strategy in neurodegenerative diseases

Microglia are positioned at the “epicentre” of neuroinflammation and consequently, neurodegeneration and aging processes. In the past few years, in parallel with an increased understanding of microglial biology, a major focus and effort has shifted to microglia, and in particular to disease-associated microglia (DAM) phenotype as a major perpetrator of neurodegenerative diseases (Keren-Shaul et al., 2017; Deczkowska et al., 2018). In this regard, the therapeutic modulation of microglia-induced inflammation in the CNS is right in the spotlight of the pharmaceutical research field, being widely pursued. Multiple strategies have been employed to find new druggable targets and active compounds for microglia modulation and, consequently neuroinflammation, creating a pipeline of potential therapeutics. In **Table I.2** it is highlighted ten candidates that are object of various drug discovery stages, ranging from early discovery to Phase 3 studies.

Table I. 2 - Neuroinflammation-targeted pipeline of potential therapeutics.

Representative compound	Type	Phase of development	Discovery method	MOA/Target	Activity
ALZT-OP1 (cromolyn with ibuprofen) (Zhang et al., 2018)	Combination Small Molecule	Repurposed - Phase 3	Phenotypic	Unknown, possibly via histamine. COX-2	Cromolyn inhibits Aβ and supress cytokine release; ibuprofen dampens the neuroinflammatory response
AL002 (Wang et al., 2020)	Monoclonal antibody	Phase 1	Target-based	TREM2 receptors	Promote microglial clearance of amyloid and other toxic proteins
Dapansutrile (Lonnemann et al., 2020)	Small molecule	Preclinical	Phenotypic	NLRP3 inflammasome	Prevents the activation of caspase-1 and the maturation and release of IL-1β
DAPPD (Park et al., 2019)	Small molecule	Preclinical	Phenotypic	Unknown, possibly NLRP3 inflammasome	Promote microglial phagocytosis, lowering pro-inflammatory signalling
GV-971 (Xiao et al., 2021)	Small molecule	Phase 3	Phenotypic	Unknown	Restore the gut microbial profile; Reduced microglial activation and decreased cytokine release
Inzomelid (MCC950-related compound) (Coll et al., 2015)	Small molecule	Phase 1	Phenotypic	NLRP3 inflammasome	Inhibits NLRP3-dependent ASC oligomerization
Montelukast (Lai et al., 2014)	Small molecule	Repurposed - Phase 2	Target-based	Leukotriene D4 receptor antagonist	Attenuation of microglial activation and p38 MAPK expression.
MW-189 (Van Eldik et al., 2020)	Small molecule	Phase 1	Phenotypic	Unknown	Reduction of glial pro-inflammatory cytokine overproduction
Neflamapimod (Duffy et al., 2011)	Small molecule	Phase 2a	Target-based	p38 mitogen activated protein kinase alpha	Shifts microglial activation from a pro-inflammatory to a phagocytic state. Inhibition of key inflammatory mediators IL-1β and TNFα.

Table abbreviations: amyloid-β (Aβ); cyclooxygenase-2 (COX-2); interleukin-1β (IL-1β); NLR family pyrin domain containing 3 (NLRP3); the adaptor molecule apoptosis-associated speck-like protein (ASC); p38 mitogen-activated protein kinases (p38 MAPK); Triggering receptor expressed on myeloid cells 2 (TREM2); tumour necrosis factor-α (TNF-α).

As mentioned above, microglia, once activated, can acquire a wide repertoire of immune profiles, ranging from a pro-inflammatory to a homeostatic signature, and from an increased phagocytic phenotype to an anti-inflammatory polarized state. Several reports have shown that small molecules, through interaction with microglial proteins, can modulate microglial functional polarization or molecular signatures. These molecules can be categorized based on their target and microglial response, according to the following features: (i) compounds that decrease pro-inflammatory microglial responses; (ii) compounds that enhance reparative and anti-inflammatory microglial phenotypes; (iii) compounds that promote the transition of microglia from a pro-inflammatory to more homoeostatic/phagocytic phenotypes (Lan et al., 2017). Interestingly, in these three categories two fundamentally different treatment strategies are being considered: searching of new molecules (novel chemical scaffolds) and repurposing existing drugs.

Effective molecules that act on microglia to selectively turn down the pro-inflammatory microenvironment have been widely described (**Figure I.3**). Amongst them are fingolimod (approved for multiple sclerosis) (Aytan et al., 2016), deferoxamine (Zhang and He, 2017), minocycline (Kobayashi et al., 2013), pinocembrin (Zhou et al., 2015), resveratrol (Wiedemann et al., 2018), rifampicin (Acuña et al., 2019) and bioactive compounds extracted from various plants such as curcumin (Ghasemi et al., 2019) and rosmarinic acid (Lv et al., 2019). Waterson's group developed a CNS-penetrant small molecule, MW-189, which selectively targets microglia supressing pro-inflammatory cytokine overproduction and their long-term neurotoxic effects (James et al., 2012). MW-189 just completed phase 1b trials and will enrol in phase 2 clinical trials for the treatment of patients with acute brain injuries such as traumatic brain injury or haemorrhagic stroke (Van Eldik et al., 2020). Meanwhile, Coll et al. reported that a sulfonylurea-containing compound, MCC950, was able to specifically inhibit NLRP3 activation, in multiple NLRP3-dependent mouse models and in *ex vivo* samples from individuals with Muckle-Wells syndrome (Coll et al., 2015, 2019). More recently, Gordon et al. have shown that this compound, in multiple rodent PD models, reduced α-synuclein-mediated microglial NLRP3 activation and downstream neuroinflammation, improving motor performance (Gordon et al., 2018). Together with other observations, this work supports the hypothesis that the modulation of the NLRP3 signalling network may represent a valuable therapeutic strategy for neurodegeneration.

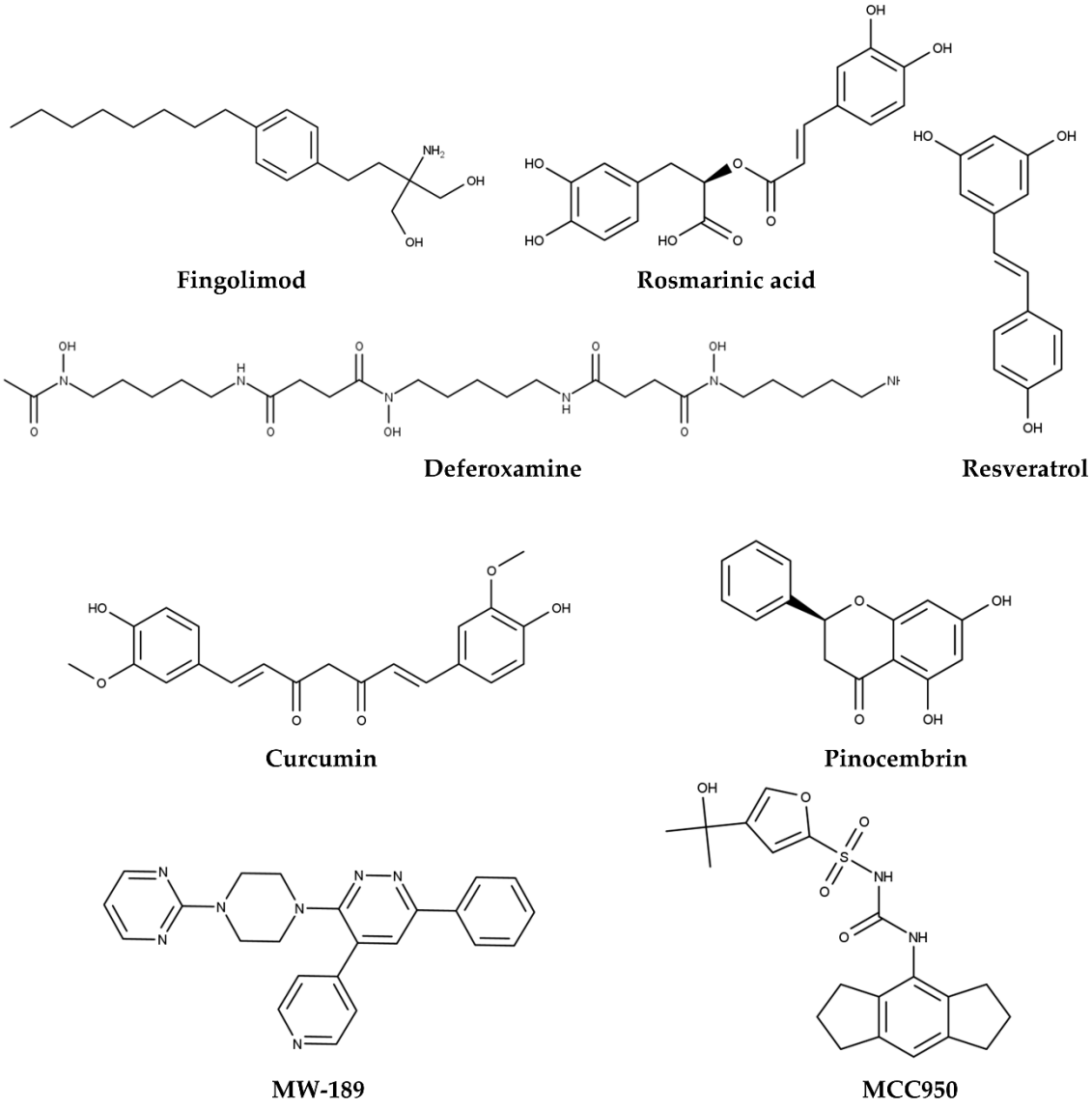

Figure I. 3 - Chemical formulae of eight compounds that decrease the pro-inflammatory microglial response.

Some molecules holding the ability of enhancing microglial anti-inflammatory phenotypes or inducing a microglial phenotype switching from pro-inflammatory to anti-inflammatory have also been reported (**Figure I.4**). Sinomenine, a compound found in a Chinese medicinal plant, *Sinomenium acutum*, was shown to reduce the levels of pro-inflammatory IL-1β, IL-6, TNF-α, and ROS, released by BV-2 microglia *in vitro*, and to increase the levels of the anti-inflammatory mediators IL-10 and Arg1 in primary microglia exposed to erythrocyte lysate (Yang et al., 2014; Shi et al., 2016). Likewise, the loop diuretic drug, furosemide, inhibited the production of multiple pro-inflammatory biomarkers, including TNF-α, IL-6, NO, COX-2, and iNOS, in LPS-stimulated SIM-A9 mouse microglial cell line and promoted microglial phagocytosis and the expression of anti-inflammatory IL-1Ra and Arg1 (Wang et al., 2020). In a recent study, Park et al. described that N,N'-Diacetyl-p-phenylenediamine (DAPPD), a

simple synthetic molecule composed by a benzene ring with 2 acetamide groups at the *para* position, decreased inflammatory cytokine expression and promoted microglial Aβ phagocytosis in two mouse models of amyloidosis, by inhibiting the NF-κB pathway-mediated activation of microglia through Aβ. Moreover, this acetaminophen derivative decreased the expression of NLRP3 and ASC, two members of the NLRP3 inflammasome complex. According to the authors, in the presence of DAPPD, microglia expressed more homeostatic and anti-inflammatory genes, such as *IL-4*, *TGFB1*, and *ARG1*, and less pro-inflammatory markers, including IL-6, TNF-α and IL-1β (Park et al., 2019). Importantly, the examples here mentioned denote that instead of having different and specific targets, most compounds share common pathways and players involved in microglial activation and neuronal dysfunction.

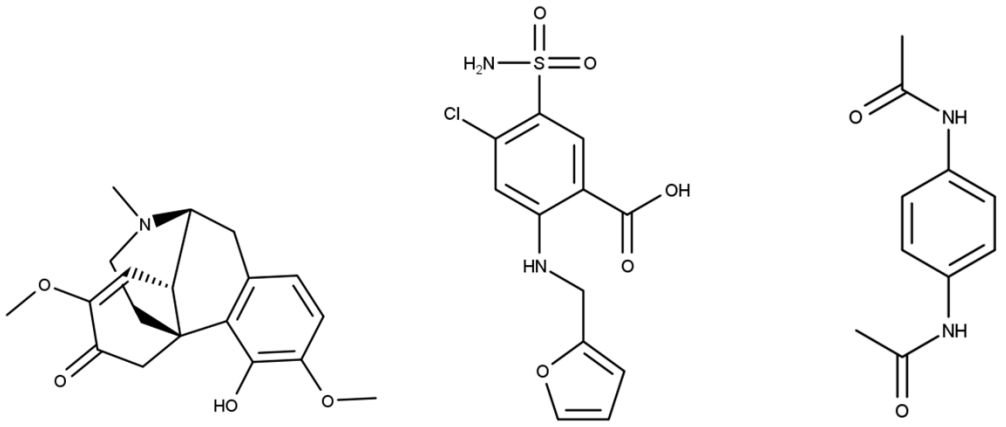

Figure I. 4 - Chemical formulae of three compounds that promote the transition of microglia from a pro-inflammatory to a more homoeostatic/phagocytic state.

From the pharmacological point of view, a critical aspect of potential microglia modulators is indeed the need to specifically target the DAM cells showing exacerbated pro-inflammatory states without downregulating homeostatic microglia or peripheral tissue macrophage populations. Unfortunately, microglia cannot be easily accessed in the CNS. The BBB, formed by a closely packed network of blood vessels, endothelial cells and pericytes, regulates the influx and efflux of molecules in the CNS compartment (Chow and Gu, 2015). This system constitutes an efficient barrier not only for toxins but also a wide range of therapeutic agents falling outside of the preferred zones for molecular weight, lipophilicity, and polar surface area (Mikitsh and Chacko, 2014). Hence, the intersection between selective small molecules targeting microglial neurotoxic phenotypes and the physicochemical properties required for CNS penetration is critical for development of efficacious strategies to modulate microglia-induced neuroinflammation.

1.1.3. Target fishing within the neuroinflammation haystack

The impetus for targeting neuroinflammation in neurodegenerative conditions arose as a result of epidemiological observations showing that individuals given some non-steroidal anti-inflammatory drugs (NSAIDs) seemed to be at a lower risk of developing AD than the general population (Breitner et al., 2011). Even though randomized clinical trials have failed to establish the efficacy of NSAIDs in either the primary prevention or the treatment of AD, they paved the way for several drug programs targeting harmful neuroinflammation and new discoveries emerging on promising drug targets. Indeed, as the neurodegeneration field branches out its therapeutics search beyond Aβ, tau, α-synuclein, some neuroinflammation players are showing glimmers of promise. Over the last decade, a number of quite plausible targets for immunomodulation emerged from the shadows: (i) NLRP3, a cytosolic protein complex that assembles in response to cellular damage or infection, prompting the secretion of pro-inflammatory cytokines that can damage the CNS (Heneka et al., 2013); (ii) triggering receptor expressed in myeloid cells 2 (TREM2), a microglial surface receptor which promotes microglial phenotype switching and sustains microglial response to pathology (Shi and Holtzman, 2018); (iii) HMGB1 protein, an inflammatory factor released by astrocytes, microglia, and neurons that triggers neuroinflammation by stimulating multiple receptors, specifically TLR4 and receptor for advanced glycation end products (RAGE) (Takata et al., 2004; Yang et al., 2020); and (iv) glycogen synthase kinase-3β (GSK-3β), expressed in astrocytes and microglia that regulates the production of inflammatory molecules and has been found at high levels in the brains of AD patients (Yuskaitis and Jope, 2009). These pathways may represent important targets to develop novel and effective disease-modifying treatments for the neuroinflammation-associated neurodegeneration processes. Unfortunately, to date, no effective therapeutics achieved approval, despite many studies showing their efficacy in mouse models.

Neuroinflammation is an early feature of almost all neurodegenerative diseases, driven by many events apparently different but strongly dependent one on the other. Given the sheer complexity of neuroinflammation signalling networks, it is of utmost importance to compile evidence linking certain protein or peptide "players" to neuroinflammation, and that modulating the target would result in therapeutic benefit. Importantly, properties of a promising candidate target might include: (i) altered expression in neuroinflammatory-associated diseases; (ii) confirmed role in the pathophysiology and exacerbation of neuroinflammation and/or is disease-modifying; (iii) genetic link between the target and inflammation; (iv) having a mechanistic link between dysregulated immune responses and neuronal dysfunction; and (v) demonstration of beneficial effects when modulated in an *in vitro* or (preferably) *in vivo* models of neuroinflammation (Biber et al., 2019).

One crucial aspect of target fishing is the druggability of the target (Owens, 2007). The concept of "druggability", disclosing the intrinsic ability of a given genome/proteome to be targeted by a drug, is closely linked with the presence of a group of features sitting in a more or less concealed region of a protein target. The spatial arrangement of these (polar) features in a characteristic fashion is both required and responsible for the specific and strong (non-covalent) binding of a ligand endowed with an appropriate arrangement of complementary features. When these features are lacking or are mostly nonpolar/hydrophobic, the target is often considered "undruggable". Thus, an undruggable protein lacks potential binding sites in which a small molecule can bind, thereby meaning that a small molecule intervention with the protein would be extremely difficult if not impossible (Moll and Carotta, 2019).

Considering the inherent risks of target fishing, in this project while seeking to identify key proteins involved in the neuroinflammatory landscape, suitable for targeting, specific criteria was considered:

- Upstream/downstream position of the proteins in the neuroinflammatory signalling networks;
- Availability of 3D structural data of the target, deposited in the Protein Data Bank (PDB) (Berman et al., 2000);
- Known target modulators and its propensity to bind small organic molecules.
- Correlations between the target and neuroinflammation highlighted and confirmed by experimental data.

1.1.4. Interleukin-1 receptor type 1 (IL-1R1): the question-mark-shaped target

One of the most well-established group of cytokines capable of orchestrating inflammatory responses, by inducing the expression of pro-inflammatory molecules in both peripheral (PNS) and CNS environments is the IL-1 family. Within this group, the first interleukin ever purified, IL-1, is found in two distinct isoforms: IL-1α and IL-1β. It stands as a pleiotropic cytokine with multiple biological activities, far from restricted to promoting inflammation, including (i) development and maturation of immune cells, (ii) fever, (iii) regulation of insulin levels and lipid metabolism; (iv) and regulation of stress response through modulation of the hypothalamic-pituitary-adrenal (HPA) axis (Sims and Smith, 2010; Mantovani et al., 2019). The biological effects of IL-1α and IL-1β are mediated by binding to the IL-1 receptor type 1 (IL-1R1). The IL-1/IL-1R1 signalling axis is essential to the activation and regulation of the immune response against PAMPS or DAMPS. Importantly, the IL-1 inflammatory cytokine has been shown to be upregulated in a wide range of human pathologies, ranging from monogenic

autoinflammatory diseases such as cryopyrin-associated periodic syndrome (CAPS) and familial Mediterranean fever (FMF), to rheumatoid arthritis, type 2 diabetes mellitus and neurodegenerative diseases (Dinarello and van der Meer, 2013). Hence, the regulatory role of IL-1R1 in the inflammatory cascades has attracted a lot of interest and attention in the drug discovery field since its discovery.

The story of IL-1R1 unfolds in the early 1980s, even before molecular cloning and characterization of IL-1α and IL-1β, as scientists had already started to identify the receptors for these two cytokines. In 1985, the first biochemical characterization of an IL-1 receptor was published, identifying an approximately 80 kDa transmembrane molecule with high affinity to IL-1, predominantly expressed by T-lymphocytes and fibroblasts (Dower et al., 1985). Three years later, Sims and colleagues reported the genetic sequence of *IL-1R1*, clearly demonstrating both IL-1α and IL-1β use the same receptor to deliver their information (Sims et al., 1988). In 1991, the existence of a second IL-1 receptor, the IL-1 receptor type 2 (IL-1R2), was recognized, a 66 kDa glycoprotein characterized by the lack of the intracellular domain (McMahan et al., 1991). In about a year, in 1992, it became clear that IL-1R1 stimulated the NF-κB signalling pathway - the same pathway activated by TNF-α - while IL-1R2 did not, this one serving as an endogenous inhibitor of IL-1 (Stylianou et al., 1992). Also, it was confirmed that both receptors existed as soluble ectodomain forms, functioning as receptor-like decoys and thus, limiting IL-1 activity (Symons et al., 1995).

While current treatments for most CNS pathologies, arguably, hold limited efficacy, IL-1R1 represents a worthwhile target in the search for neuroinflammation-associated CNS diseases therapeutics, due to its central role in neuroinflammation. Importantly, a growing body of evidence is showing that blocking the IL-1R1 signalling via pharmacologic or genetic means in different experimental models of said CNS diseases leads to reduced neuroinflammation and delayed disease progression (Wohleb et al., 2014; Newell et al., 2018; Yamanaka et al., 2021). Still, while there is substantial body of research on IL-1R1, there have been no small molecule modulators reported to date. As such, our interest in human IL-1R1 as a model target is linked not only to its involvement in disease, but also to the many peculiarities that render it a particularly challenging target.

1.1.4.1. The IL-1 family of ligands and receptors

There are 11 members in the IL-1 cytokine family, including seven agonists (IL-1α, IL-1β, IL-18, IL-33, IL-36α, IL-36β, and IL-36γ), three receptor antagonists (IL-1Ra, IL-36Ra, and IL-38), and one anti-inflammatory cytokine (IL-37). Importantly, these cytokines exert their effects through binding to a group of cell surface receptors, the interleukin-1 receptor (IL-1R) family members (Boraschi et al., 2018). The structural hallmark feature of this family consists in the

presence of immunoglobulin (Ig)-like domains in their extracellular ligand-binding region (Martin and Wesche, 2002; Ireland, 2008). Ig-like domains include 10 members of the IL-1R family: IL-1R1, IL-1R2, the regulatory receptors ST2 (IL-1RL1) and the single immunoglobulin IL-1R related molecule (SIGIRR) or IL-1R8, the IL-18 receptor (IL-18R)α, the IL-36 receptor (IL-1RL2), the co-receptors IL-1 receptor accessory protein (IL-1RAcP) and IL-18Rβ, the interleukin-1 receptor accessory protein-like 1 (IL-1RAPL1) and IL-1RAPL2 (Boraschi et al., 2018; Dinarello, 2018; Fields et al., 2019). All members of this superfamily share a Toll/IL-1R homologous region (TIR) in the intracellular signalling domain, except IL-1R2 which only contains a short cytoplasmic tail, unable to induce intracellular response. This TIR domain is responsible for some shared downstream signalling mechanisms and cell activation, being heavily involved in the regulation of adaptive immune responses and maintaining homeostasis (Narayanan and Park, 2015; Toshchakov and Neuwald, 2020).

Within the complex regulatory networks of IL-1 pathways, the soluble cytokines IL-1α and IL-1β, despite only sharing 27% amino acid sequence homology, adopt similar 3D structures and interact with the same receptor, the IL-1R1. Instead of the typical ligand-induced receptor activation, IL-1R1 engages a heterotrimeric complex to initiate downstream signalling. Fundamentally, binding of the agonists IL-1α or IL-1β to the extracellular domain of IL-1R1 (IL-1R1-ECD) triggers the recruitment of an accessory receptor, IL-1RAcP, resulting in a functional receptor complex that initiates IL-1R1 signalling cascades (**Figure I.5**) (Thomas et al., 2012; Günther et al., 2017).

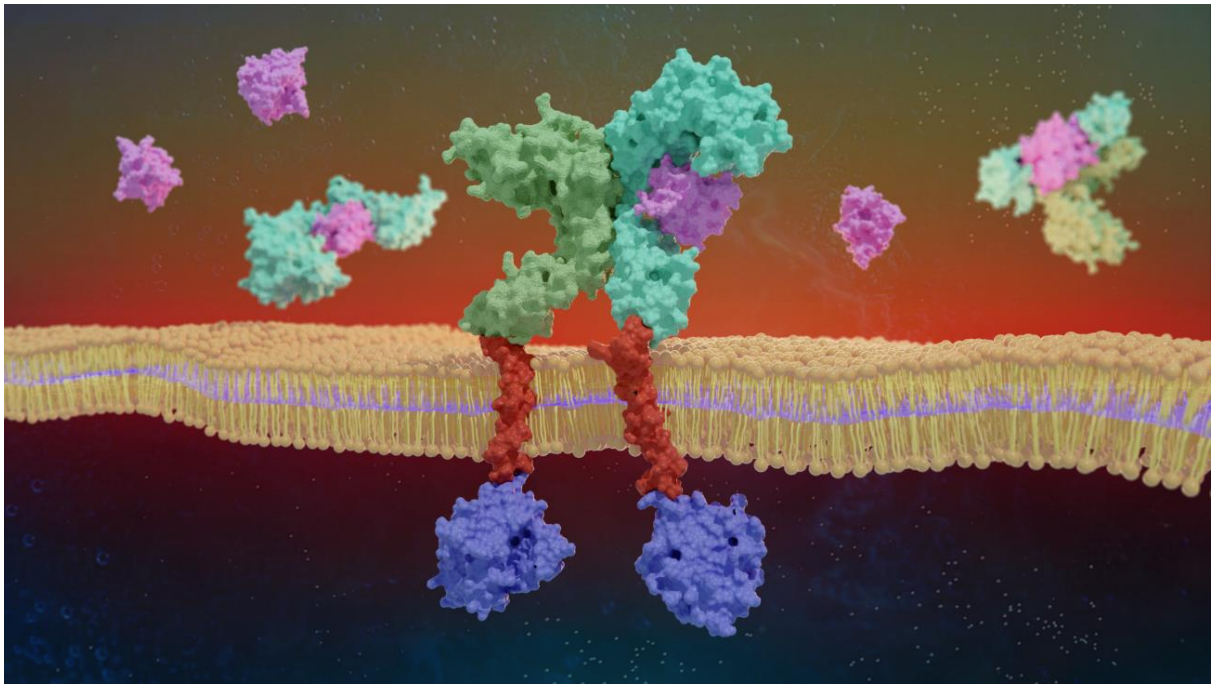

Figure I. 5 - An illustration of the IL-1β/IL-1R1/IL-1RAcP ternary complex. Binding of the IL-1 cytokine (coloured in pink) to the membrane-bound IL-1R1-ECD (coloured in green) recruits transmembrane IL-1RAcP (coloured in lime), initiating intracellular signalling via the TIR domains (coloured in blue). Both IL-1R1 and IL-1RAcP can

participate in the negative regulation of IL-1 signalling when cleaved to their soluble ECD forms. The lipid bilayer (cell membrane) is represented in yellow and transmembrane domains are coloured in red. The image was generated using imported VMD visualization states (Humphrey et al., 1996) uploaded in the Blender software (Kent, 2015). *Figure abbreviations: IL-1, interleukin-1; IL-1R1, interleukin-1 receptor type 1; IL-1R1-ECD, extracellular domain of IL-1R1; IL-1RAcp, interleukin-1 receptor accessory protein; TIR domain, the toll-interleukin-1 receptor homology domain.*

The IL-1/IL-1R1/IL-1RAcP complex lead to the dimerization of the TIR domains of IL-1R1 and IL-1RAcP proteins, providing an anchor point for the recruitment of the myeloid differentiation primary response protein 88 (Myd88) (see **Figure I.6**). This protein-protein interaction sparks the recruitment of other signalling molecules such as the IL-1R-associated kinases (IRAKs) and TNF receptor-associated factor 6 (TRAF6) to the protein complex. Subsequently, multiple intracellular phosphorylation and ubiquitination processes culminate in the activation of the p38 mitogen-activated protein kinase (MAPK) pathway, the c-Jun N-terminal kinase (JNK) and NF-κB. These changes result in the upregulation of mRNA transcription for inflammation-associated genes encoding IL-6, IL-8, iNOS, MCP-1, COX-2, IκBα, IL-1α and IL-1β (Sims and Smith, 2010; Cohen, 2014). Besides agonists IL-1α and IL-1β, IL-1R1 also binds an endogenous antagonist, IL-1Ra, which is not able to trigger IL-1R1 association with IL-1RAcP, therefore competitively blocking IL-1 signalling through IL-1R1 binding. IL-1R1 binds the three ligands, IL-1α, IL-1β, and IL-1Ra, with comparable affinities (0.1 to 1 nM K_d) (Dripps et al., 1991; Arend et al., 1998; Fields et al., 2019).

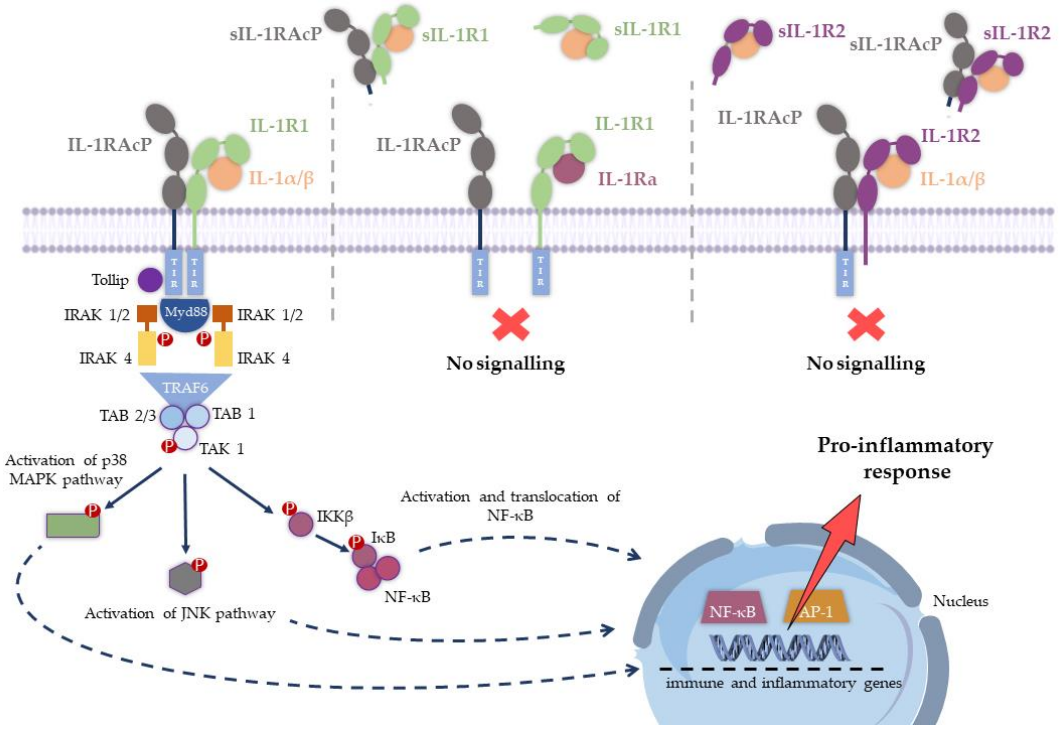

Figure I. 6 - Schematic representation of interleukin-1 signalling. Upon binding of IL-1α/β to the extracellular domain of membrane-bound receptor IL-1R1, IL-1RAcP is recruited, and signalling is initiated by the interaction of the intracellular TIR domains of the two polypeptide chains. When IL-1Ra binds IL-1R1, the IL-1RAcP is not

recruited, thereby blocking signalling. Similarly, when IL-1β binds IL-1R2, no signalling occurs as IL-1R2 lacks a cytoplasmic TIR domain. IL-1 signalling may also be inhibited by soluble forms of the receptor, sIL-1R1 and sIL-1R2, lacking the transmembrane and intracellular regions of the native form, binding both IL-1α, IL-1β and sIL-1RAcP. Adapted from Martin et al., 2021. *Figure abbreviations: IL-1, interleukin-1; IL-1R1, interleukin-1 receptor type 1; IL-1Ra, interleukin 1 receptor antagonist; IL-1RAcP, interleukin-1 receptor accessory protein; IL-1R2, interleukin-1 receptor type 2; TIR domain, the toll-interleukin-1 receptor homology domain; IRAK, interleukin-1 receptor-associated kinases; TRAF6, tumour necrosis factor receptor associated factor 6; TAK1, transforming growth factor-β-activated kinase 1; TAB, TAK1-binding proteins; p38 MAPK, p38 mitogen-activated protein kinases; JNK., c-Jun N-terminal kinase; IKKβ, I kappa B kinase β; NF-κB, nuclear factor-kappa B; AP-1, activator protein 1.*

The biological activities of IL-1 are also modulated through soluble IL-1 receptors (sIL-1R) (Symons et al., 1991; Garlanda et al., 2013). Post-translational shedding of the extracellular Ig domains is the major mechanism responsible for the release of soluble IL-1 receptors (sIL-1R1, sIL-R2 and sIL-1RAcP) from cell membranes (Elzinga et al., 2009; Hayashida et al., 2010). In the extracellular environment, the soluble extracellular IL-1R1 domain (sIL-1R1) may capture IL-1 molecules in solution, acting as a decoy, preventing signal transduction. Furthermore, sIL-1R1 binds IL-1Ra, limiting the effects of this IL-1 receptor antagonist on the membrane-bound receptor. Similarly, sIL-1R2 binds IL-1β with high affinity and recruits sIL-1RAcP, but does not initiate intracellular signalling, also acting as a decoy receptor. In contrast to sIL-1R1, IL-1Ra binds with weak affinity to this soluble decoy and both IL-1Ra and sIL-1R2 cooperate in the negative regulation of IL-1 (Smith et al., 2003; Schlüter et al., 2018).

The amplifying power of this signalling pathway is remarkable. The interaction of IL-1 with transmembrane IL-1R1 catalyse the activity of numerous intracellular molecules with fundamental mechanisms of immunoregulation. The domino-like cascade of IL-1 activity and signal amplification continues to intensify at every step of the pathway. Importantly, positive modulators (receptor agonists) and negative modulators (receptor antagonists, decoy receptors) cooperate to regulate the inflammatory response. However, an uncontrolled and sustained activation of immune cells by abnormal protein aggregates, such as Aβ plaques and α-synuclein aggregates, may drive IL-1R1 signalling dysregulation, generating a strong pro-inflammatory microenvironment, thus resulting in pathological outcomes. IL-1 signalling has been implicated in several inflammatory diseases, prompting the need to find druggable therapeutic targets within the components of the IL-1 inflammatory pathway (Garlanda et al., 2013; Mantovani et al., 2019).

1.1.4.2. Gene structure and expression

Human IL-1R1 is encoded by the *IL-1R1* gene, which is located on the long arm of chromosome 2 at band 2q12. The gene spans approximately 74 kilobase pairs comprising 14 exons and three distinct promoters lacking both TATA and CAAT boxes. These three promoters (referred to as exons 1A, 1B and 1C) generate transcripts with different 5′-untranslated regions (Sims et al.,

1995; Ye et al., 1996). While little is known about the regulatory mechanisms involving these promoters, their presence suggests that different cells may employ different IL-1R1 promoters to activate IL-1R1 transcription, allowing cell type-specific regulation of this receptor (Chen et al., 2009). Investigations on the genomic structures of the IL-1 receptor family suggest that IL-1R1, IL-1R2, IL-1RAcP, IL-1RL1 (ST2), IL-18Rα, IL-1RL2 and IL-18Rβ derived from ancestral gene duplications of a common proto-IL-1R (Copeland et al., 1991; Rivers-Auty et al., 2018). Murine and human IL-1R1 proteins show 69% identity at the amino acid level. In both, the *IL-1R1* and *IL-1R2* genes are adjacent, encoding similar transmembrane regions but only having a 28% homology in their extracellular domains (Dale and Nicklin, 1999).

The expression of IL-1R1 can be influenced by genetic polymorphisms. In humans, single nucleotide polymorphisms (SNPs) have been identified in *IL-1R1* and associated with severe hand osteoarthritis (Näkki et al., 2010), knee osteoarthritis (Smith et al., 2004), aggressive periodontitis (Kamei et al., 2014), inflammatory bowel disease (Latiano et al., 2013), type 1 diabetes (Bergholdt et al., 2000) and asthma (Mahdaviani et al., 2009). Moreover, Vasilyev et al. demonstrated that *IL-1R1* SNPs could be one of the factors influencing the expression of membrane-bound IL-1R1 on immunocompetent cells (Vasilyev et al., 2015). Some groups postulate that individuals carrying *IL-1R1* polymorphisms may be more susceptible to the action of IL-1 due to their increased expression of cell surface IL-1R1 proteins. Still, despite a clear association in these reports revealing a strong link between the distribution of polymorphisms along *IL-1R1* sequence and predisposition to human diseases, the exact mechanisms by which these SNPs affect IL-1R1 physiological levels and consequently, IL-1 signalling, remains uncertain.

The regulation of *IL-1R1* expression is likely to play a major role in controlling the effects of IL-1 since very few receptors are required for IL-1 signal transduction. Indeed, Sims et al. reported that in human THP-1 monocyte-like cells and murine 70Z/3 pre-B lymphoma cells, fewer than 20 receptors per cell were sufficient to mediate IL-1 signalling (Sims et al., 1993). Gene expression signatures of IL-1R1 have been reported in T helper 17 (Th17) cells (Chung et al., 2009), circulating T-cells (Klarnet et al., 1989; Jain et al., 2018), insulin-producing β cells (Benner et al., 2014), fibroblasts and endothelial cells (Song et al., 2018), and immature nature killer (iNK) cells (Hughes et al., 2010). IL-1R1 gene levels has also been found in innate immune cell types including neutrophils, macrophages, eosinophils, basophils and mast cells (Garlanda et al., 2013a). IL-1R1 expression can be regulated, both positively and negatively, by inflammation-related factors and other stress signals. The involvement of IL-1R1 in the brain has been linked to the pyramidal cell layer of the hippocampus, dentate gyrus, cerebellum, pituitary gland, and hypothalamus (Cunningham et al., 1992; French et al., 1999). In a recent study, Liu et al. employed genetic knock-in reporter mice to investigate the IL-1R1 cytoarchitecture and cell-type-specific roles in the CNS (Liu et al., 2019). They demonstrated

that ventricular IL-1R1 regulates monocyte recruitment, endothelial and ventricular IL-1R1 regulates IL-1-induced microglial activation and endothelial IL-1R1 mediates sickness behaviour, leukocyte recruitment, and neurogenesis (Liu et al., 2019). Small amounts of mRNA have been found in glial cells under basal conditions (Pinteaux et al., 2002), contradicting other studies which showed that IL-1R1-mediated signalling drives the activation of astrocytes (Lin et al., 2006). Under physiological conditions, expression of IL-1 and its receptors is low in the CNS compartment. However, levels of this cytokine increase dramatically after injury, and IL-1 elevation is associated with many neurodegenerative diseases. As such, under pathological conditions, IL-1R1 may be induced by IL-1β itself, elevating the mRNA levels of this receptor on glial cells. The significant expression of IL-1R1 in microglia will be further discussed in Part VI.

1.1.4.3. Molecular structure

IL-1R1 is a transmembrane signalling receptor composed of a 319-amino acid ectodomain sitting on top of a question-mark-shaped structure supported by a transmembrane domain (TM) and an intracellular 217-amino acid TIR domain. Vigers et al. have laid the groundwork for the structural elucidation of the IL-1R1 ectodomain (IL-1R1-ECD), describing the 3D crystal structure of this region determined at 2.5 Å resolution (**Figure I.7A**) (Vigers et al., 1997). The ectodomain folds into three Ig-like domains (D1, D2 and D3). Each domain is characterized by an extensive β-structure composed of seven to nine strands, arranged in a two-layer sandwich, and are stabilized by disulfide bonds involving pairs of highly conserved cysteine residues in the IL-1 receptor family (**Figure I.7B**). The two Ig-like domains, D1 and D2, are linked by a disulfide bond, separated from D3 via a 6-amino acid flexible linker lacking secondary structure. Thus far, there are five crystal structures of the IL-1R1-ECD published in the PDB (Berman et al., 2000). The exact structure of the TIR domain is unknown to date.

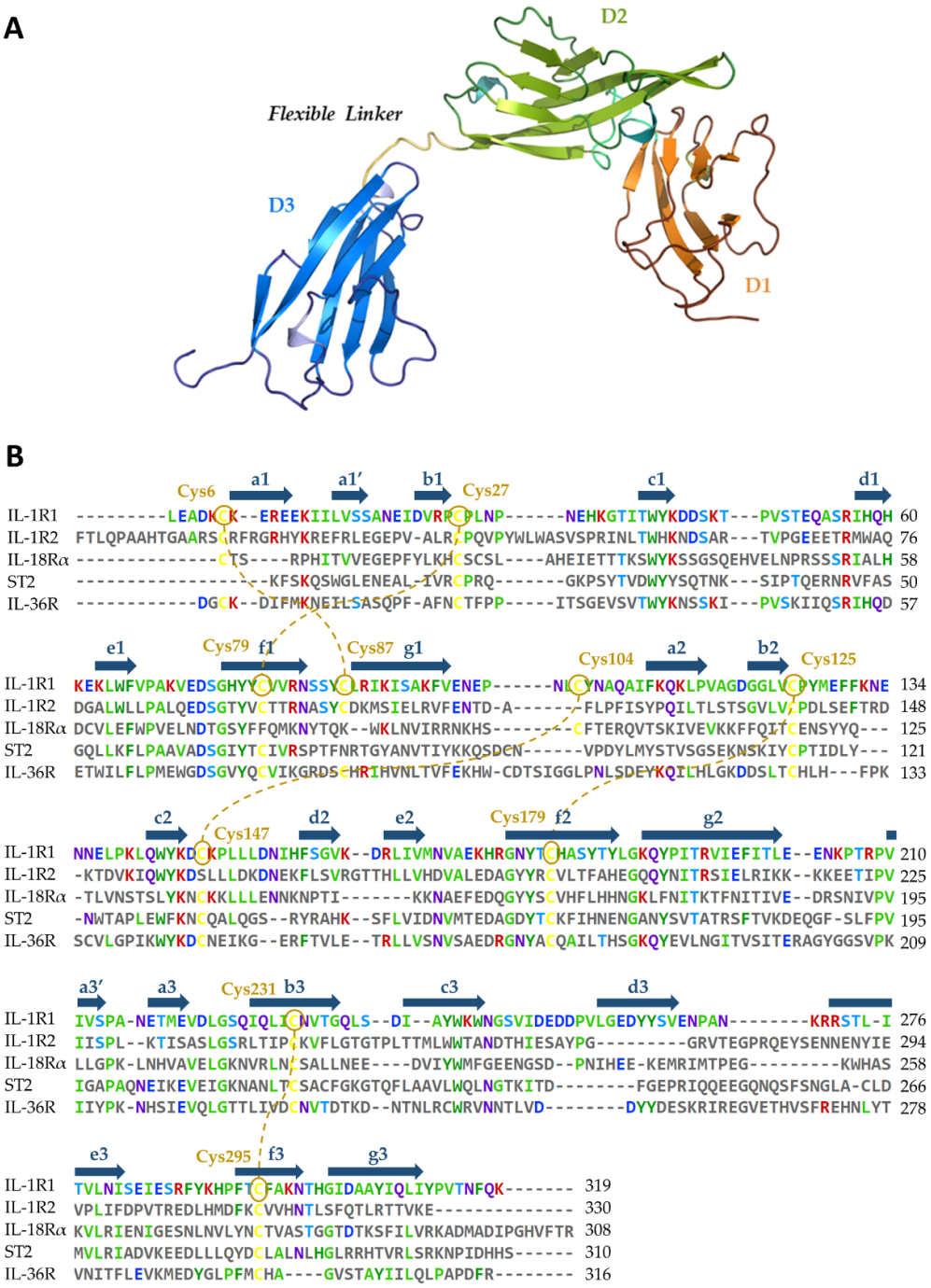

Figure I. 7 - (A) Molecular structure the IL-1R1 ectodomain. The coordinates were retrieved from the PDB (PDB entry 4GAF). Ig-like domains are labelled as D1 (orange), D2 (green) and D3 (blue), and the 6-amino acid flexible linker located between D2 and D3 represented in yellow. **(B) Alignment of IL-1R1, IL-1R2, IL-18Rα, ST2 and IL-36R ectodomains.** The β-strands were assigned using the DSSP algorithm (Kabsch and Sander, 1983), and are shown for the IL-1R1 sequence (a1-g1 located in D1, a2-g2 located in D2 and a3-g3 located in D3, represented as blue arrows). Brown circles show the conserved cysteine residues, and the connectivity between the disulfide bonds in the IL-1R1 structure is represented by brown dashed lines. IL-1R1 shares 25,5%, 18,4%, 19,6% and 29,3% sequence identity with IL-1R2, IL-18Rα, ST2 and IL-36R, respectively. The alignments were generated using the Clustal Omega Server (Sievers and Higgins, 2018). Adapted from (Tsutsumi et al., 2014). *Figure abbreviations: IL-1R1,*

interleukin-1 receptor type 1; IL-1R2, interleukin-1 receptor type 2; IL-18Rα, interleukin-18 receptor-α; ST2, defined as interleukin-33 receptor; IL-36R, interleukin-36 receptor.

Protein-protein interactions between IL-1β and IL-1R1 take place at two sets of interfaces located between D1-D2 and at D3, plus a hydrogen bond formed between IL-1β and the flexible linker. Upon complex formation, the IL-1R1 structure essentially does not change, maintaining the core β-structure and domain fold. In total, the cytokine IL-1β display a buried surface area within the interface of IL-1R1 of 1932 Å^2 over 47 residues. The binary complex IL-1β/IL-1R1 sparks a conformational change in the D3 domain of IL-1R1, helping to develop an interaction with the accessory protein IL-1RAcP (**Figure I.8**). On the heterotrimeric complex formation, the overall architecture between IL-1β/IL-1R1 does not change, presenting a root mean square deviation (RMSD) of 1.4 Å. Interestingly, the inhibitory complex of IL-1β with the decoy receptor IL-1R2 and IL-1RAcP share high structural similarity with the IL-1β/IL-1R1/IL-1RAcP complex, characterized by a RMSD of 1.8 Å between their C*α*-atoms.

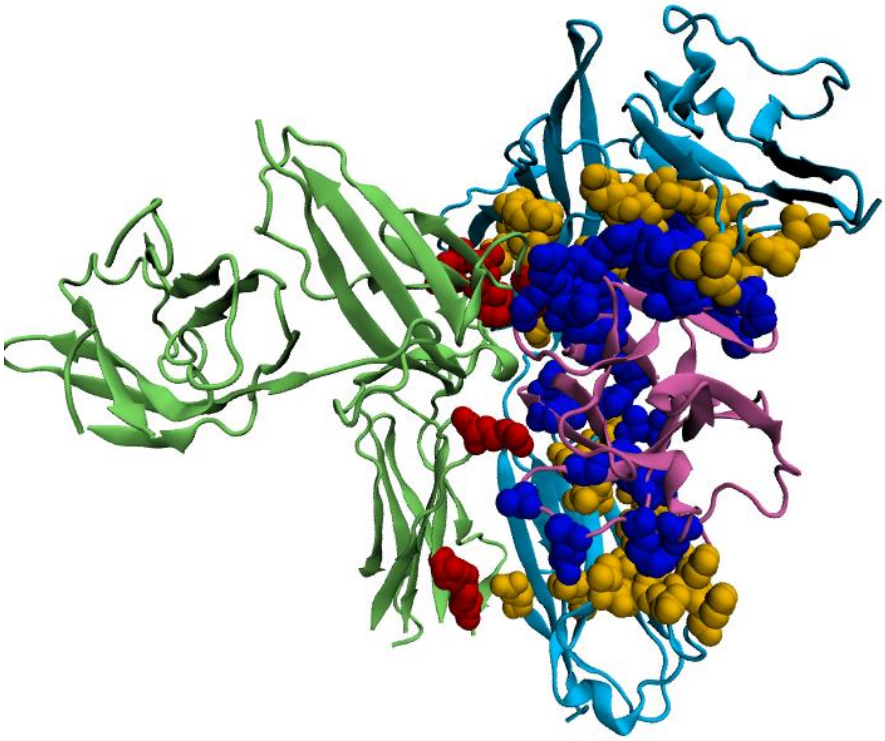

Figure I. 8 - The structure of interleukin-1β (IL-1β), interleukin-1 receptor type 1 (IL-1R1) and interleukin-1 receptor accessory protein (IL-1RAP) heterotrimeric complex. The coordinates were retrieved from the PDB (PDB entry 4DEP). IL-1β cytokine is coloured in pink, the extracellular domain of IL-1 receptor type 1 (IL-1R1-ECD) is coloured in cyan and the extracellular domain of IL-1 receptor accessory protein (IL-RAcP-ECD) is coloured in lime. Crucial residues involved in the protein-protein interfaces are shown as balls.

The characteristics of IL-1R1 interactions and the protein-protein interfaces crucial for ligand binding will be further discussed in Part II of this thesis.

1.1.4.4. Pipeline of IL-1 therapeutic modulators

The excessive stimulation of the IL-1/IL-1R1 molecular networks is associated with the pathogenesis of several disorders, extending from autoinflammatory diseases such as Familial Mediterranean fever (FMF) and Deficiency in IL-1 receptor antagonist (DIRA), to rheumatoid arthritis, type 2 diabetes, cancer and neuroinflammation-associated neurodegenerative diseases. Consequently, IL-1 has drawn considerable attention as a potential therapeutic target. Numerous avenues for blocking interleukin-1 in this broad spectrum of diseases have been exploited by the pharmaceutical industry or academia in the last decades (**Table I.3**).

Table 3. Summary of therapeutic agents available or in development for the modulation of IL-1 activity.

Therapeutic agent	Type	Target	Phase of development	Company	Therapeutic indication
Anakinra	Recombinant form of human IL-1Ra	IL-1R1	Approved	Amgen (now Swedish Orphan Biovitrum)	Rheumatoid arthritis (Furst, 2004) Gout (So et al., 2007) CAPS (Koné-Paut and Galeotti, 2014) Type 2 Diabetes (Larsen et al., 2007) Cardiovascular disease (Abbate et al., 2013; Kron et al., 2021)
Rilonacept	Fusion protein of IL-1RAcP, IL-1RI, and IgG-Fc	IL-1β IL-1α IL-1Ra	Approved	Regeneron	Recurrent Pericarditis (Klein et al., 2021) CAPS (Hoffman, 2009) Gout (Terkeltaub et al., 2009)
Canakinumab	Human IgG1 monoclonal antibody	IL-1β	Approved	Novartis	CAPS (Lachmann et al., 2009) TRAPS (Gattorno et al., 2017) HIDS/MKD (Sánchez-Manubens et al., 2019) Type 2 Diabetes (Rissanen et al., 2012) Still's disease (Sfriso et al., 2020)

Gevokizumab	Human IgG2 monoclonal antibody	IL-1β	Halted	Xoma	Behcet's Uveitis (Tugal-Tutkun et al., 2018)
LY2189102	Human IgG1 monoclonal antibody	IL-1β	Phase II	Lilly	Type 2 diabetes (Sloan-Lancaster et al., 2013)
Bermekimab (MABp1)	Human IgG1 monoclonal antibody	IL-1α	Phase II	XBiotech	Atopic Dermatitis (Bieber, 2021)
MEDI-8968 (AMG108)	Human IgG2 monoclonal antibody	IL-1R1	Phase II	MedImmune	COPD (Calverley et al., 2017)
Isunakinra (EBI-005)	Human IL-1β and IL-1Ra chimeric protein	IL-1R1	Halted	Eleven Biotherapeutics	Dry eye disease (Goldstein et al., 2017)
AF10847	peptide	IL-1R1	Preclinical	Array BioPharma	--
rytvela	peptide	IL-1R1	Preclinical	Elim Biopharmaceuticals	--
Inzomelid	Small molecule	NLRP3 inflammasome	Phase I	Roche (previously Inflazome)	CAPS (Chauhan et al., 2020)
Belnacasan (VX-765)	Small molecule	Caspase-1	Halted	Vertex Pharmaceuticals	Rheumatoid arthritis (Wannamaker et al., 2007) Epilepsy (Maroso et al., 2011)

Table abbreviations: interleukin-1 receptor type 1 (IL-1R1); interleukin-1α (IL-1α), interleukin-1β (IL-1β); interleukin-1 receptor antagonist (IL-1Ra); NLR family pyrin domain containing 3 (NLRP3); Cryopyrin-associated periodic syndrome (CAPS); TNF receptor-associated periodic syndrome (TRAPS); Hyperimmunoglobulin D Syndrome/Mevalonate Kinase Deficiency (HIDS/MKD; Chronic obstructive pulmonary disease (COPD).

Several reviews can be found in the literature describing in great detail potential pharmacotherapies developed to modulate IL-1 pathways (Dinarello et al., 2012; Fields et al., 2019). For the sake of concision, the next paragraphs focus only on therapeutics directly targeting IL-1R1.

Efforts to specifically target IL-1R1 have been focusing on antibodies or chimeric cytokine biologics (**Figure I.9**):

- Anakinra (Kineret®, Amgen), a recombinant non-glycosylated form of the natural human IL-1Ra, distinguishable by the addition of an N-terminal methionine residue, reached the US and Europe drug markets in 2001 and 2002, respectively, to treat rheumatoid arthritis. Fundamentally, this molecule targets the IL-1R1-ECD, competitively inhibiting IL-1α and IL-1β binding and thus, blocking intracellular signal transduction. Anakinra is rapidly removed from the body by renal filtration due to its small size (17,3 kD). However, it requires daily self-administration via subcutaneous injection, which may result in adverse side effects such as injection-site reactions, missed doses and, ultimately, decreased patient treatment compliance (Furst, 2004; Kaiser et al., 2012). Interestingly, a recent study reported that anakinra crosses a human *in vitro* model of the BBB derived from human umbilical cord blood stem cells, at a 4-7-fold higher rate than the monoclonal antibodies bermekimab (IL-1α antagonist) and canakinumab (IL-1β antagonist) (Sjöström et al., 2021).
- EBI-005 (isunakinra), a human IL-1β and IL-1Ra chimeric protein, developed in 2013 by Eleven Biotherapeutics, has been shown to bind IL-1R1 at a higher affinity than IL-1β (KD = 0.014 nM for EBI-005; KD = 2.0 nM for IL-1β). This biologic was optimized for topical ocular administration in patients with dry eye disease and allergic conjunctivitis (Hou et al., 2013). However, Phase III clinical trials were halted after EBI-005 failed to achieve primary endpoints.
- The monoclonal antibody (mAb) AMG108 (licensed to AstraZeneca and MedImmune and now termed MEDI-78998) binds IL-1R1-ECD, blocking IL-1β-mediated signalling pathways. In preclinical studies, this human mAb has shown efficacy in models of osteoarthritis, though, no significant clinical benefits were observed in Phase II trials (Cohen et al., 2011).

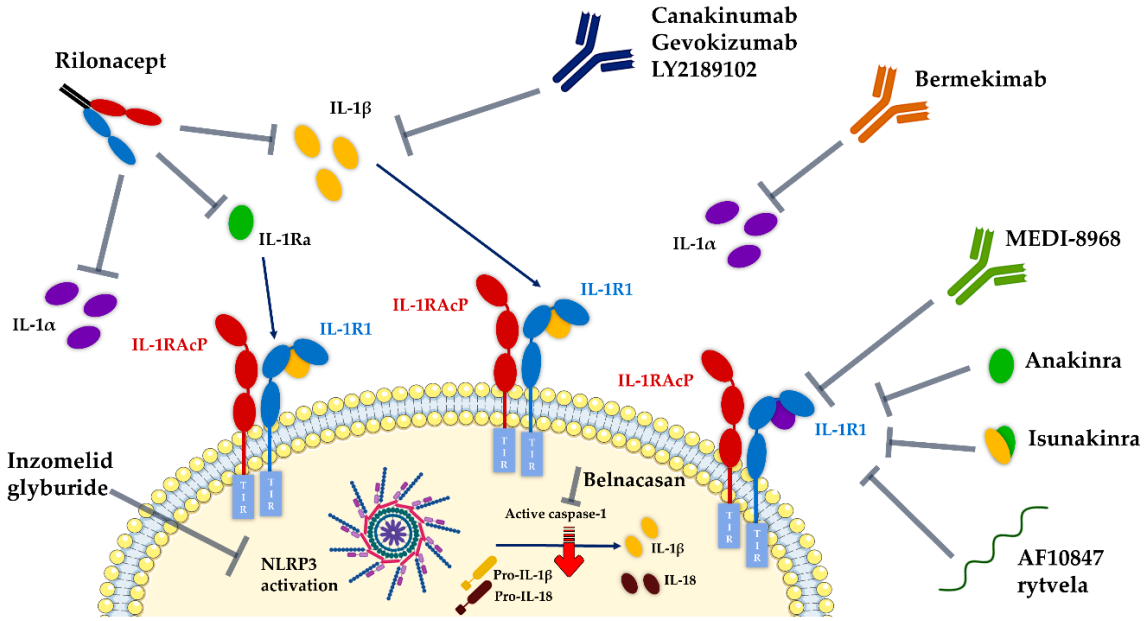

Figure I. 9 - Main strategies targeting interlukin-1 signalling. Therapeutic approaches targeting IL-1R1 include a recombinant form of IL-1Ra (anakinra), a chimeric IL-1Ra-IL-1β protein (Isunakinra), a fully human monoclonal antibody (MEDI-896), and peptides AF10847 and *rytvela*. Rilonacept stands as an engineered dimeric fusion protein consisting of the ECDs of the human IL-1R1 and IL-1RAcP linked to the Fc portion of human immunoglobulin G1 (IgG1), acting as decoy receptor, binding IL-1α, IL-1β and IL-1Ra. Monoclonal antibodies (mAb) antagonizing IL-1β are canakinumab, gevokizumab and LYS2189102, whilst bermekimab works by blocking IL-1α. The small molecules inzomelid and glyburide directly inhibit NLRP3 inflammasome activation, while belnacasan specifically inhibits caspase-1 and consequently the maturation of pro-IL-1β into the respective active form. The figure was prepared using BioRender. Adapted from (Kopf et al., 2010). *Figure abbreviations: IL-1, interleukin-1; IL-1R1, interleukin-1 receptor type 1; IL-1Ra, interleukin 1 receptor antagonist; IL-1RAcp, interleukin-1 receptor accessory protein; ECD, extracellular domain; TIR domain, the toll-interleukin-1 receptor homology domain; NLRP3, NLR family pyrin domain containing 3.*

While biologics targeting IL-1R1-ECD work relatively well at modulating IL-1 activity, an early goal of the field was to discover agonist or antagonist peptides with potential pharmaceutical application. In fact, it was back in 1996 that Yanofsky et al., by screening peptide phage display libraries, identified numerous small peptides binding to human IL-1R1-ECD, inhibiting IL-1-mediated cellular responses. By comparing their activity with IL-1α and IL-1β, they identified three different peptides exhibiting an IC_{50} below 3 nM (Yanofsky et al., 1996). One such peptide, AF10847 (21 amino acids), was later crystalized with IL-1R1 by Vigers et al., revealing an unexpected induced conformational change in the receptor. Indeed, the peptide interact with the D1-D2 interface of the IL-1R1-ECD, and at the same time D3 undergoes a 170° rotation when compared to that of IL-1R1:IL-1β crystal structure (Vigers et al., 2000). Importantly, these data demonstrated the possibility of different orientations between structural domains (D1, D2, D3) of the extracellular domain of IL-1R1 and shed light on the ability of IL-1R1 to adopt multiple conformations that can be exploited by small

molecule modulators. Almost a decade later, a selective D-peptide antagonist of IL-1R1, termed *rytvela*, was developed based on the flexible portions of the IL-1RAcP, showing efficacy and potency in a broad variety of *in vitro* IL-1β-dependent assays (Quiniou et al., 2008) and more recently, in reducing inflammation in models of neuro-retinal degeneration (Dabouz et al., 2020). Approximately at the same time, a short peptide (ilantide) derived from the IL-1Ra, capable of binding to the IL-1R1-ECD, was shown to be able to reduce the inflammation state in the CNS and pancreatic islets (Klementiev et al., 2014).

Although most IL-1R1-ECD targeting therapeutics are antibodies and peptides, they share the shortcomings of presenting generally large molecular weight, difficult dosing frequency, no simple production and inconsistent or unfavourable pharmacokinetic (ADME) profiles. Small molecule therapeutics may represent a more versatile option, combining adequate pharmacological properties (lower molecular weight, small polar surface area and lower hydrophilicity) and even potential allosteric modulation, which may in turn open avenues for the development of alternative solutions for targeting IL-1R1.

1.1.4.5. Why target IL-1R1 for immunomodulation in the CNS?

IL-1, IL-1R1 and its downstream mediators play pivotal roles in the modulation of inflammatory responses against immune challenges. IL-1 has been shown to be involved in a wide range of human pathologic conditions which have a high prevalence and pose a striking socioeconomic burden. This double-edge sword behaviour raises one important question: Is IL-1 a harmful driver of disease, a protective response, or something in between? We speculate it may be all the above, subject to dependency on cell subtypes, signalling proteins involved and stage of disease progression.

Once IL-1 is synthetized in the brain, it is plausible to deem a function for it in the biology of the CNS. Indeed, IL-1 has been associated with the regulation of fever (Nakashima et al., 1989), sleep (Krueger et al., 1998), neurogenesis (Koo and Duman, 2008) and modulation of long-term potentiation (del Rey et al., 2013). Interestingly, low levels of IL-1 have been hypothesized to help consolidate memory, whereas higher levels of IL-1 impair sensory function and memory (Depino et al., 2004; Gui et al., 2016). In a neuroinflammatory setting, IL-1, in particular IL-1β, is intimately involved in the CNS's innate immune response to injury, infections, or exposure to misfolded proteins. Once activated in response to injury, microglia and astrocytes represent the main source of IL-1β, and when secreted, it may further stimulate its own production in an autocrine/paracrine fashion and the release of other pro-inflammatory mediators, by binding to IL-1R1. Importantly, this dynamic signalling network of IL-1β production in activated glia ensures that injury signals are further propagated in the cellular milieu, driving potent neuroinflammatory changes in the brain (**Figure I.10**).

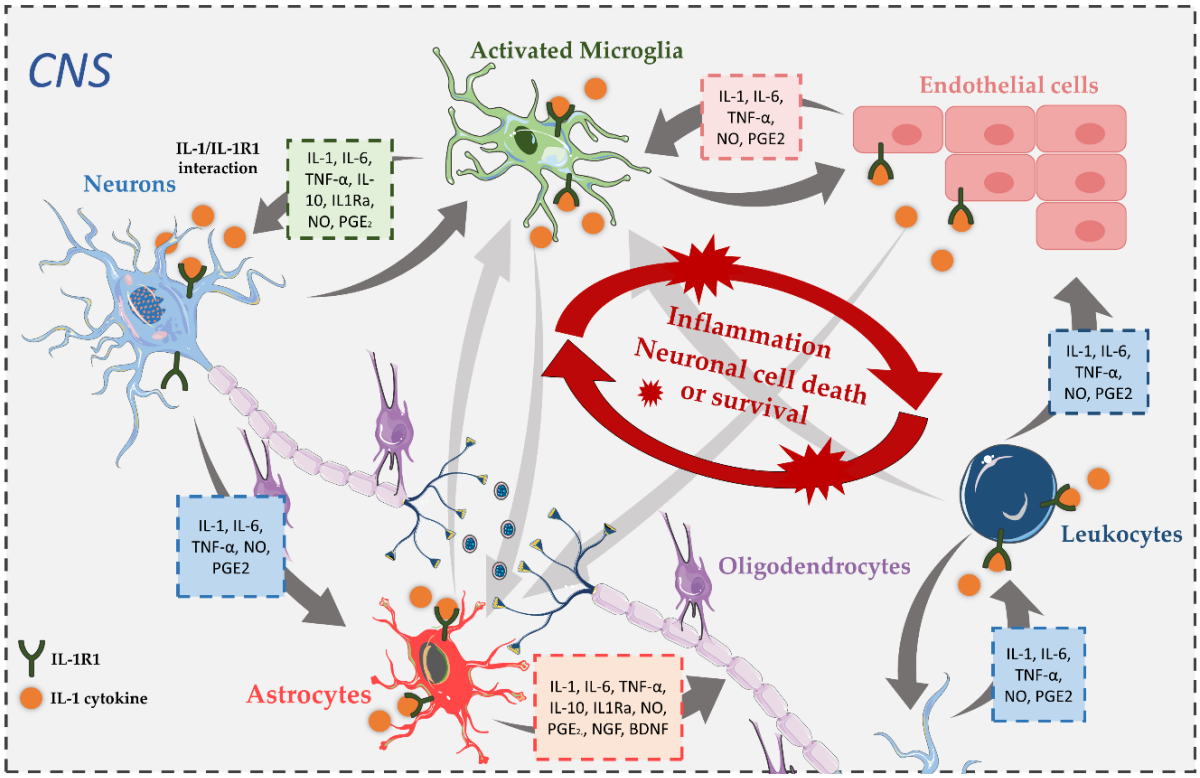

Figure I. 10 - CNS cellular communication of interleukin-1 signalling in neuronal injury. In the normal brain, expression of IL-1 is low, but acute CNS injury causes a sharp increase in IL-1 production. Different CNS cell types express IL-1R1, thereby enabling them to respond to IL-1β in an autocrine manner, as well as a paracrine manner, after neuronal injury. Upon IL-1/IL-1R1 interaction, these different cells can produce a wide range of pro-inflammatory and immune-regulatory mediators that contribute to neuronal death or survival through different signal transduction pathways. The figure was prepared using Servier Medical Art. *Figure abbreviations: CNS, central nervous system; IL-1, interleukin-1; IL-6, interleukin-6; IL-10, interleukin-10; IL-1Ra, interleukin-1 receptor antagonist; IL-1R1, interleukin-1 receptor type 1; TNF-α, tumour necrosis factor-α; NO, nitric oxide; PGE_2, prostaglandin E2; NGF, nerve growth factor; BDNF, brain-derived neurotrophic factor.*

Excessive IL-1R1 activation underlies a wide range of different CNS pathological conditions characterized by a strong neuroinflammatory component such as AD (Griffin et al., 1989; Holmes et al., 2003; Italiani et al., 2018), PD (Mogi et al., 1996; Tanaka et al., 2013), ALS (Meissner et al., 2010; van der Meer and Simon, 2010), multiple sclerosis (Hauser et al., 1990; McGuinness et al., 1997; Seppi et al., 2014), traumatic brain injury (Wang et al., 2006; Chung et al., 2019), Creutzfeldt-Jakob disease (Bertani et al., 2017), HIV-1 encephalitis (Zhao et al., 2001) and age-related macular degeneration (Hu et al., 2015). The biochemical basis by which IL-1 exerts neurodegeneration effects is still elusive. However, some clues to possible mechanism(s) are emerging (Liu and Quan, 2018). There is evidence that sustain NLRP3 inflammasome activation and IL-1 production in microglial cells playing a key role in neuroinflammation associated with AD. In a recent study, Ising and colleagues observed that mice lacking the NLRP3 inflammasome fail to induce the calcium/calmodulin-dependent protein kinase type II subunit alpha (CaMKIIα), which plays a critical role in tau

hyperphosphorylation and aggregation in AD. By contrast, microglia-derived IL-1β via NLRP3 activation increases the levels of CaMKIIα and promotes tau aggregation in neurons. Noteworthy, blocking the IL-1β signalling pathway through the administration of IL-1Ra, the natural antagonist which directly targets IL-1R1, hampered the effects of CaMKIIα and, consequently, tau phosphorylation (Ising et al., 2019). These data elucidates the role of microglial IL-1β in tau pathology, and is consistent with results from other studies (Bhaskar et al., 2010; Mancuso et al., 2019).

The role of IL-1β in neurodegeneration following ischemic brain injury has been the subject of a significant number of studies. This cytokine levels increase at an early stage (from 0 to 3 h post-ischemia), with the main source of IL-1β postulated to be microglia, and is sustained on later stages due to a delayed expression by astrocytes, neurons, endothelial cells and other immune cells (Minami et al., 1992; Pinteaux et al., 2009). On one hand, in animal models of cerebral ischemia, IL-1β has been shown to markedly increase cell damage and exacerbate injury (Stroemer and Rothwell, 1998; McColl et al., 2007). On the other hand, a wealth of preclinical studies reported that blocking IL-1 signalling through the administration of IL-1Ra provided neuroprotective effects, with decreased tissue loss and attenuated cognitive deficits, in ischemic stroke (Loddick and Rothwell, 1996; Clausen et al., 2016; Pradillo et al., 2017). Likewise, reduced neuronal damage has been observed after IL-1Ra exposure or treatment with anakinra in TBI experimental models (Toulmond and Rothwell, 1995; Newell et al., 2018; Evans et al., 2020). Further experimental studies by Basu and colleagues using IL-1R1 knockout mice revealed that the absence of IL-1 signalling after brain injury have a direct correlation with a substantial reduction in microgliosis and astrogliosis as well as with IL-6 and COX-2 production, highlighting the importance of this receptor in microglial activation (Basu et al., 2002; Lin et al., 2006). Together, these and similar observations prompted both IL-1Ra and anakinra to clinical trials for ischaemic and haemorrhagic stroke, yielding significant reductions in the levels of inflammation and improving cognitive function when given to patients in the early stages after a stroke (Emsley et al., 2005; Galea et al., 2018; Smith et al., 2018).

Amongst other relevant reports, a recent study showed that lack of the interleukin 1 receptor 8 (IL-1R8) or excessive IL-1β signalling impacts neuron synapse morphology, plasticity and function, through the over activation of IL-1R1. Both strategies led to the upregulation of the mechanistic target of rapamycin (mTOR) pathway and increased levels of the epigenetic regulator methyl-CpG-binding protein 2 (MeCP2), which is critically involved in neurological diseases characterized by defective plasticity, impaired cognition and intellectual disability. Interestingly, pharmacological treatment with anakinra restored MeCP2 expression and cognitive deficit in IL-1R8-deficient mice, highlighting that the inhibition of IL-1 signalling

may be efficacious for treating neurological diseases through immune system modulation (Tomasoni et al., 2017; Mantovani et al., 2019).

Despite promising *in vitro* and *in vivo* results in models of CNS diseases, the complexity of translating findings from animal studies to humans through feasible clinical trials, along with some contradicting data retrieved in human studies, seem to have faded the interest of pharmaceutical companies in IL-1R1 drug discovery. Nevertheless, the studies reviewed here make a strong case for IL-1R1 as a key player in CNS pathological conditions. Under pathological conditions, IL-1R1 is robustly activated by IL-1 secreted by surrounding glial cells, and the resulting inflammatory signals may be too strong for the CNS to override. Increasing impetus for exploring IL-1R1 as a therapeutic target is being derived from mounting non-clinical and clinical evidence on the use of IL-1R1-antagonizing biologics (e.g., anakinra) showing encouraging correlation with the substantial reduction of disease-linked microgliosis and astrogliosis, as well as of production of pro-inflammatory players like IL-6 and COX-2.

Altogether, given its direct role in modulating IL-1 overexpression and a myriad of other pro-inflammatory mediators involved in the neuroinflammatory landscape, as well as in sustaining inflammation in chronic neurodegeneration, targeting of IL-1R1 in specific tissues or organs, particularly the CNS, may still reveal itself a valuable therapeutic strategy against neurodegenerative diseases.

1.2. Medicinal Chemistry of Neuroinflammation

Despite the unprecedented investments in drug R&D, alongside major advances in the understanding of the molecular mechanisms of neurodegeneration, the number of approved disease-modifying therapeutics is almost null and only palliative treatments are available. For almost two decades, billions of dollars of research money were funnelled for example to the amyloid cascade hypothesis, disfavouring competing molecules, such as therapeutics directly targeting neuroinflammation (Sheridan, 2009; Makin, 2018). Fortunately, a paradigm shift in scientific thinking is well underway. Recognition of the necessity of neuroinflammation research for the successful development of game-changing therapeutics for neurodegenerative diseases is now a key goal of scientific community.

The ability to modulate neuroinflammatory responses via medicinal chemistry endeavours can open up exciting new avenues for translating this approach to clinical trials to intervene in human neurodegenerative disorders – from early target identification, hit and lead discovery, through recognition of synthetically accessible and *medchem-friendly* chemistry, all the way to the optimization of lead compounds - moving towards more innovative approaches, aiming to discover new targets or new chemical entities. The far-reaching scope

of neuroinflammation in neurodegenerative processes poses fundamental questions that must be addressed when structuring drug discovery efforts: *What are the most promising targets or molecular networks? Should we target upstream or downstream regulators of neuroinflammation? Do our lead molecules fulfil the molecular determinants to cross the blood-brain barrier? What is the best screening strategy? Target-based or phenotypic screening?* Such questions are key to a successful lead discovery campaign.

The pharmaceutical industry is increasingly integrating computer-assisted drug design (CADD) methods in the identification of a few small molecules that can serve as basis to further optimization and development of a new drug. Among CADD techniques, virtual screening (VS) has already proved to make hit identification more goal-oriented, enabling the cost-effective evaluation of large virtual chemical libraries to identify sets of chemical structures with higher likelihood of binding to and interfering with a selected pharmacological target of interest, which must then be tested in an adequate *in vitro* assay. We could argue that neuroinflammation is not a standard area which could be approached following classical strategies in drug design. Indeed, the sheer complexity of the CNS together with the presence of the BBB, across which most therapeutic agents need to permeate, adding a further pharmacokinetic hurdle, and a lack of validated biomarkers ends in low success rates in CNS drug development. From this perspective, CADD methodologies coupled with suitable experimental assays can be exploited to streamline and accelerate the quest for potential lead molecules, by objectively assessing the tractability of potential targets and guide the design of tailored bioactive CNS small molecule modulators.

The following sections will focus on the relevance of phenotypic screening versus target-based approaches (section 2.1.) and the application of CADD techniques (section 2.2) for the identification of potential neuroinflammatory small molecule modulators.

1.2.1. Phenotypic vs. Target-based screening

The process of lead discovery typically begins with either phenotypic or target-based screening approaches. The concept of phenotypic screening implies running an unbiased experimental screen to quantify measurable effects in cells (or the whole organism) and discover compounds that produce desired phenotypic changes. This approach is performed in a predictive cellular setting, without making assumptions about a specific target or a mechanism of action. Typically, this mechanism is only deconvoluted in later stages. In contrast, target-based screens establish early a particular target of interest, with target-specific readouts used to identify promising compounds which only later, often during the lead optimization stage, see their potential modulatory activity in a proper biological assay

confirmed (Haasen et al., 2017). It is hard to argue about one approach over the other, and they are often regarded complementary of each other.

Over the last two decades, advances in high-throughput screening (HTS) technologies and chemogenomics sparked the development of rational tailored target-based approaches to identify selective and specific high-affinity compounds for a particular target. Nonetheless, the efficacy in discovering disease-modifying therapeutic agents seems no different from the phenotypic-centric approach that has dominated the drug discovery scene in the 20th century, particularly when considering first-in-class compounds (Wagner, 2016). Currently, phenotypic assays are increasingly being integrated in the early stages of compound screening (Warchal et al., 2016). This is supported by the more and more complex cellular assay systems, including immortalized cell lines to primary cells, co-cultures, patient-derived cells, tri-dimensional (3D) cultures and organoid constructs - able to mimic disease-driving phenotypes alongside more robust assay readouts (Fang and Eglen, 2017).

Targeting neuroinflammatory-associated neurodegeneration processes is admittedly a daunting and challenging task. Put simply, a detailed understanding of the inflammatory processes involved in neurodegeneration is still unclear, there is an absence of validated therapeutic targets, reliable biomarkers and limited predictive validity of preclinical pharmacological models. So, phenotypic screening has a lot of appeal for finding completely new entry points or targets for CNS drug discovery, particularly grounded on two key considerations: (i) historically, much of the successful CNS drug development has been an empirical and in many cases serendipitous process, with some examples of recently approved CNS first-in-class drugs discovered using phenotypic screens being memantine (dementia treatment), levetiracetam (epilepsy treatment), rufinamide (epilepsy treatment) and ziconotide (severe chronic pain treatment) (Zhang et al., 2014; Swinney and Lee, 2020); (ii) the state of the CNS field, where there are high attrition rates for small molecules or the low-hanging fruit for target identification and validation is almost exhausted, is simultaneously a warning signal and an invitation - "if you can't drug it, turn it into a phenotypic screen" – to increase the chances of actually finding promising molecular entities (Brown and Wobst, 2020).

The target-agnostic nature of phenotypic screening entails the possibility of (i) identifying compounds that have a thus far unrecognized target or novel mechanism of action; (ii) discovering treatments for diseases for which even the root cause is unknown; (iii), a more direct *in vivo* and clinical translation than target-based approaches since the biological systems used are more robust and complex and different from isolated targets; (iv) potential to find desirable polypharmacology and (v) possibility to identify multiple disease relevant effects, not just one effect via one target. Nevertheless, phenotypic screens are often more time-consuming and expensive, and are associated with a more challenging hit validation due to

potential risk of false positives through non-selective/specific mechanisms and risk of unwanted mechanisms. Moreover, compound optimization via SAR is more complex than a target-based program due to cellular permeability, cell transport mechanisms, membrane interactions and off-target activities (Warchal et al., 2016).

Ultimately, a main advantage in performing phenotypic approaches is that discoveries may hold a greater chance of success in more advanced stages of drug development. Phenotypic screens expose candidate compounds to proteins in more biologically relevant contexts than screens involving purified proteins. Still, the major barrier to these approaches has been understanding the mechanisms of action following initial discovery. Notwithstanding, current advances in robust target deconvolution strategies should improve the identification of such mechanisms (Sydow et al., 2019; Brown and Wobst, 2020).

1.2.2. The role of computer-aided drug design: exploring the potential in neuroinflammation

Today, the influence of CADD in health sciences plays a major role in the R&D paradigm, helping scientists understand disease mechanisms and which treatments work best to modulate them, exploring ideas where solutions cannot be found analytically, and experimental testing are not feasible or takes too much time. CADD has always been able to react and follow the changes in the drug discovery environment and has been increasingly incorporated in the current medicinal chemistry toolbox, with its usefulness and impact tending to increase in the coming decades. The fast growth of freely-available bioactivity resources, e.g., PubChem (Kim et al., 2016) or ChEMBL (Gaulton et al., 2012) has sparked a new generation of powerful data-driven computational methods for numerous applications such as VS, and enhanced the involvement of academia in drug discovery campaigns. (Sliwoski et al., 2014; Dar et al., 2019).

The drug discovery process typically starts by the discovery and characterization of a molecular target and/or biochemical mechanism implicated in a disease of interest (e.g. disease-related genetics, genomics, proteomics, interactomics, etc.). While the process of target validation is complex and runs in parallel with (and transcends) the entire drug discovery and development process all the way to post-marketing and drug surveillance, the identification of a protein target is often the starting point of lead discovery and optimization endeavours. At this stage, CADD tools allow a more extensive coverage of chemical space, rendering the overall discovery process more exhaustive and efficient (Sliwoski et al., 2014). In practical terms, CADD can dramatically reduce the number of compounds for experimental testing.

When compared to experimental HTS and combinatorial chemistry, CADD can increase the number of novel hits due to its targeted search, by deconstructing molecular interactions that

create therapeutic activity whilst predicting analogues with improved activity. In the drug discovery paradigm, CADD usually comprises three main goals:

1. De novo design of compounds: by consecutively adding functional groups or by merging together different fragments into new chemotypes – based on existing knowledge of active compounds and/or a target molecular structure;
2. the VS of large compound libraries: to prioritise sets of predicted active molecules (virtual hits) to be experimentally tested;
3. the optimization of lead compounds: towards improved target affinity and/or activity (primary pharmacodynamics), target selectivity (secondary pharmacodynamics), bioavailability on target compartments or organs (pharmacokinetics, a.k.a. ADME), metabolism and toxicity profiles.

Nowadays, it is becoming difficult to compartmentalise or categorise CADD techniques. Nevertheless, they have been historically segregated into two main classes depending on the existing structural information – either on the pharmacological target at hand or known bioactive compounds:

1. Receptor-based approaches rely on the knowledge of the 3D structure of the target, most often a protein, and focus on predicting its interactions with a specific ligand. These methods typically make use of available information on protein-ligand complex structures and include, by order of increasing complexity and computational cost: receptor-based pharmacophore modelling and searches, molecular docking, and molecular dynamics simulations.
2. Ligand-based techniques are relevant where no experimentally determined 3D structures of the molecular target are available, but some reference substrates or inhibitors are known. Here, approaches like ligand-based pharmacophore modelling and searches, molecular similarity-based methods including fingerprint-based and 3D-based searches, and quantitative structure-activity relationships (QSAR) can be explored.

In the next subsections, a basic introduction to some of the CADD methodologies exploited in this project is provided. For further information, I point the readers to references (Sliwoski et al., 2014; Genheden et al., 2017). Also, we highlight and discuss some of the latest efforts encompassing ligand-based approaches (QSAR, 3D-shape similarity, pharmacophore modelling), structure-based drug design (SBDD) approaches (homology modelling, docking, pharmacophore modelling, molecular dynamics simulations), and combined approaches (virtual screening) covering different inflammatory target classes.

1.2.3. Virtual Screening

In lead discovery projects, HTS is a commonly used standard technique to identify pharmacologically active compounds. However, these screens require expensive equipment and labour, and the costs associated are high and hit rates low. VS represents an *in silico* method that allows the screening of vast compound libraries, typically with thousands to millions of molecular structures, more quickly and cost-efficiently, filtering ("like a funnel") promising candidates for further synthesis and experimental testing. Importantly, by making predictions as to which molecules are most likely to bind the target, VS narrows the search to a few, high-potential candidates (Lavecchia and Giovanni, 2013; Walters and Wang, 2020). Coverage and diversity of the chemical space is a key consideration when selecting a representative subset of compounds to be tested either by target-based or phenotypic screening approaches.

Structure-based and ligand-based are the two main approaches of VS (**Figure I.11**). Ligand-based VS strategies uses information about known active compounds to identify candidate compounds for experimental evaluation. This approach assumes that structurally similar compounds have identical biological effects, and can be performed via 3D-QSAR modelling, similarity or substructure searching and pharmacophore or 3D shape matching. Structure-based VS is employed when the 3D structure of the target is known, typically using molecular docking or structure-based pharmacophores to select compounds predicted to establish optimal interactions with the binding site of the protein. Regularly, pharmacophore-based screenings are preferred over docking as an initial filter to remove molecules which do not hold essential pharmacophoric and physicochemical features for binding. On the other hand, docking can be used in later stages for a more detailed evaluation or post-filtering of virtual hit compounds (Shoichet, 2004; Gimeno et al., 2019).

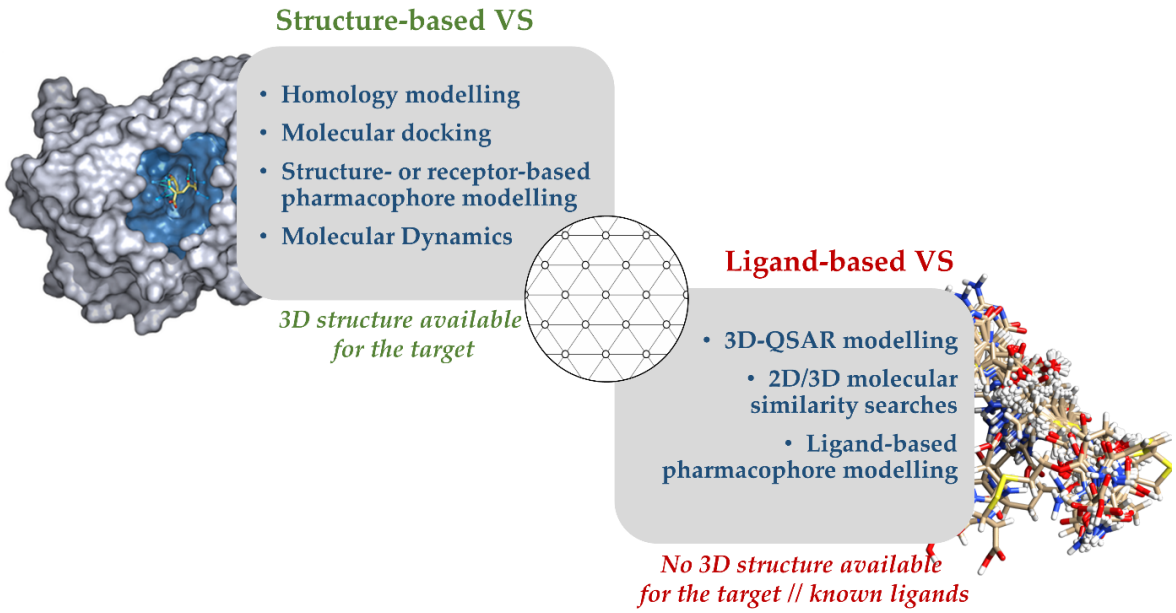

Figure I. 11 - Structure- and ligand based-methods for virtual screening. Depending on the availability of structure information, a structure-based approach or a ligand-based approach is used. The former relies on using information from the three-dimensional (3D) structure of the protein and ligand-based strategies use information on the biological and physicochemical properties of bound ligands. *Figure abbreviations: VS, virtual screening; 3D-QSAR, three-dimensional quantitative structure-activity relationships.*

The Protein Data Bank (PDB) is an important repository of atomic coordinates describing proteins and other important biological macromolecules (Berman et al., 2000). Established in 1971 at the Brookhaven National Laboratory, this database currently houses more than 174,000 3D structures, most of which have been determined using X-ray crystallography and a smaller set determined using nuclear magnetic resonance (NMR) spectroscopy and cryo-electron microscopy (cryo-EM). Importantly, this increasing wave of structural knowledge, together with advances in protein structure determination techniques, is boosting VS and SBDD approaches, providing much more precise and accurate data and in greater amounts, as well as the elucidation of the molecular mechanisms of protein-ligand binding and functional selectivity.

In recent years, the number and dimension of screening and bioactivity data repositories has expanded significantly. Chemical structure repositories such as ChEMBL (Gaulton et al., 2012), PubChem (Kim et al., 2016), ZINC (Irwin and Shoichet, 2005), DrugBank (Wishart et al., 2018), ChemSpider (Pence and Williams, 2010), among others, provide access to tens of millions of compounds for applications such as VS. Recently, Wang et al. assembled the open-access chemical library AICD (Anti-inflammatory Compounds Database) that explores the chemical space of anti-inflammatory compounds, by gathering over 79,781 small molecules with therapeutic potential for a total of 232 inflammation-related targets (Wang et al., 2019). In the field of immunology and inflammation, this dataset enriched in anti-inflammatory

compounds may be of relevance during *in silico* procedures, including pharmacophore modelling, molecular similarity searches and QSAR, leading to the identification of promising chemical entities for use in medicinal chemistry.

1.2.3.1. Ligand-based Virtual Screening

Ligand-centric approaches are based in the so-called *Similar Property Principle*, which states that molecules that are structurally similar are likely to have similar properties (Johnson and Maggiora, 1990). The fundamental applications of these methods spawn from (i) using a set of reference structures collected from known active compounds as query templates to find other compounds with similar physicochemical properties; to (ii) constructing Structure-Activity Relationships (SAR) models that predict biologic activity from chemical structures, suggesting chemical modifications with higher likelihood of yielding better molecules than random modifications. All these strategies are applied for *in silico* screening for compounds holding the biologic activity of interest, hit-to-lead, and lead-to-drug optimization, and also for the optimization of chemical absorption, distribution, metabolism and excretion, and pharmacokinetics (ADMET) properties (Acharya et al., 2011; Sliwoski et al., 2014).

1.2.3.1.1. Molecular Similarity Searching: encoding and decoding chemical structures

The application of computational algorithms for unbiased chemical similarity comparisons and database searching is fundamental in a lead discovery program. Molecular fingerprints are bit string representations of molecular structure and/or properties, wherein the absence ("0") or presence ("1") of a pre-defined substructure or fragment is recorded for each molecule. Two-dimensional fingerprints of a set of active molecules for a specific target allows for an easy comparison with compound databases by identifying and quantifying the overlapping elements between them. Such fingerprints are popular largely due to their speed and simplicity, being commonly applied for ligand-based VS, similarity searching and clustering (Sliwoski et al., 2014). However, they are usually not suited for scaffold hopping for example in a VS campaign, where generally novel molecules with similar scaffold profile are selected.

3D overlay tools such as shape-matching algorithms, molecular interaction fields (MIFs) descriptors or pharmacophores take in account the 3D (descriptor) conformations of a molecule while performing 3D similarity searches. Indeed, they usually rely on conformer ensembles to sample the conformational space, enabling an increased probability of finding different core structures but with similar shape, pharmacophoric and physicochemical properties. One of the most widely used methods is the Rapid Overlay of Chemical Structures (ROCS) software, developed by OpenEye, which uses ligand superposition and shape-based similarity scoring to rank molecules by their 3D similarity (Rush et al., 2005). This method will be described in greater detail in Part IV.

Different strategies integrating molecular similarity searches in VS workflows have been reported for the identification of small molecule modulators for key protein targets involved in the inflammatory pathways. For example, Xu et al. reported the identification of a novel chemotype as a nuclear factor erythroid 2 p45-related factor 2 (Nrf2) pathway activator after a combination of 2D fingerprint-based and 3D shape-based similarity searching (Xu et al., 2015). The potential activation of the Nrf2 transcription factor, located in the cytoplasm of cells, may protect against oxidative stress and inflammation associated with neurodegenerative conditions (Nakano-Kobayashi et al., 2020). Starting from an initial activator presenting a 1,2,4-oxadiazole group, a 2D fingerprint-based similarity analysis was computed against a ChemDIV collection of 699,674 compounds, yielding 37,104 similar virtual hits. Then, the authors conducted 3D-shape comparisons to filter the number of molecules to be tested experimentally, resulting in 12 promising virtual hits. Following *in vitro* experimental validations, the most potent compound was subjected to SAR studies, producing an active Nrf2 inducer shown to be active both *in vitro* and *in vivo*. Noteworthy, in LPS-treated mice, this compound was shown to reduce the levels of pro-inflammatory TNF-α, IFN-γ, IL-6, IL-12, and IL-17, presenting low toxicity (Xu et al., 2015).

Noha et al. devised a VS strategy targeting the I kappa B kinase β (IKK-β), a serine-threonine protein kinase critically involved in the activation of NF-κB. In this study, 3D similarity-based alignments performed with ROCS were used to trim down and prioritize virtual hits identified via ligand-based pharmacophores. Indeed, a set of compounds presenting high activity (IC_{50} < 100 nM) and selectivity for IKK-β was used to develop a 3D pharmacophore model, which was employed to screen the National Cancer Institute (NCI) compound database. ROCS software was then used to compare the retrieved compounds with two highly active and structurally diverse IKK-β inhibitors. The resulting virtual hits holding the highest shape and feature overlap were selected for biological testing, where one compound showed inhibitory activity in the low micromolar range on IKK-β enzymatic activity *in vitro* and on NF-κB transactivation (Noha et al., 2011).

In another study, Ha et al. combined ligand-based pharmacophore modelling and 3D shape-based similarity to identify small molecule antagonists of the CXC chemokine receptor 2 (CXCR2), a chemokine receptor expressed on various immune cells and known to play prominent roles in inflammatory pathologies. For this purpose, they virtually screened a database consisting of 5 million commercially available compounds with a validated ligand-based pharmacophore hypothesis derived from known CXCR2 antagonists. Thirteen selected hit molecules bearing sulphonamide moieties were further prioritized by an initial cell-based screen, leading to a potent compound inhibiting CXCR2 activation with an IC_{50} of 360 nM. ROCS was employed to carry out 3D-shape similarity searches based on the docked pose of this promising compound. Subsequently, 102 additional sulphonamide compounds were

identified and evaluated *in vitro*, resulting in a selective CXCR2 signalling modulator (Ha et al., 2015).

1.2.3.2. Structure-based Virtual Screening

SBDD uses both the knowledge of the 3D structure of a protein and *in silico* techniques to identify putative small molecules with biological activity against a desired target. The last two decades have been marked by a rapid growth in experimentally solved protein 3D structures, providing an unprecedented level of insight into the structural determinants of protein-ligand interactions. Accordingly, *in silico* methods, as homology modelling, molecular docking, structure-based pharmacophore modelling and molecular dynamics are nowadays routinely applied in drug discovery for (i) exploiting the structure and target function, (ii) analysing and predicting ligand-target interactions, and (iii) performing VS and rational design of chemical modulators targeting a protein of interest (Anderson, 2003; Śledź and Caflisch, 2018).

1.2.3.2.1. Proteins as pharmacological targets: identification and characterization

In general lines, the first step in a lead discovery program consists of target identification and characterization, entailing the selection of a macromolecule implicated in a disease of interest. Receptors, enzymes, ion channels and transporters represent a wide group of pharmaceutically appealing targets for which many chemical modulators have been discovered, either by serendipity or design. These molecules exert their action by binding to the target protein and preventing it from catalysing a reaction, opening a channel pore, or activating signalling cascades. Novel targets are increasingly selected for drug discovery programs based on genomic and proteomic data (Schenone et al., 2013). Triaging which of these are the most viable for intervention by small molecules is, however, essential at the start of a medicinal chemistry project if resources are not to be wasted on non-productive screening efforts.

This step includes the choice of protein target(s) which need to be efficacious, safe, meet clinical and commercial needs, and be *druggable*. Choosing the right targets for pharmacological interventions is especially complicated in complex diseases such as the ones of the CNS, due to their multifactorial nature, complex transcriptional activity, and lack of validated biomarkers. To shed light into novel and non-obvious "players", cheminformatics tools can play a critical role at this stage, through text mining methods and resources like OpenTargets (Koscielny et al., 2017) or STRING (Mering, 2003), which allow the integration of relevant biomedical data from scientific literature, patents, genomics, proteomics, metabolomics, phenotyping and compound profiling to identify potential pathways and targets. In parallel, ligand similarity to known active compounds or protein binding site similarity assessments to available structural targets via 2D (molecular fingerprints), 3D

(shape and electrostatics) similarity searches or MIFs comparisons, can be used to predict potential biological targets. The identification and characterization of protein binding sites for ligand interactions are of paramount importance to guide targeted therapies and optimization of the molecule(s). Importantly, the detailed characterization of binding site features, such as volume and shape, as well as the distribution of surrounding residues, will direct drug discovery efforts to follow strategies commonly employed to target protein-ligand interaction pockets or protein-protein interaction sites (Katsila et al., 2016; Agamah et al., 2020).

1.2.3.2.2. Molecular surface and protein binding sites

The 3D architecture of a protein is highly complex, display conformational heterogeneity, translating in a topological surface quite irregular, containing smaller and larger clefts, as well as internal cavities. The way in which ligands interact with macromolecular targets include complementarities in shape and electrostatics between binding sites and the ligand. Typically, these binding regions represent an enzymatic active site, but may also be protein-protein interfaces, natural ligand binding pockets, regions that induce allosteric regulation of protein function or from an *in silico* perspective, computationally determined *hot-spots* favourable for ligand binding. **Figure I. 12** exemplifies the irregular surface of a key protein involved in the neuroinflammation networks, the serine/threonine p38α mitogen-activated protein kinase (p38αMAPK) bound to small molecule inhibitor (PDB entry 4ZTH) (Roy et al., 2019). Different type of cavities can be perceived, including small pockets and larger cavities appropriate for ligand binding.

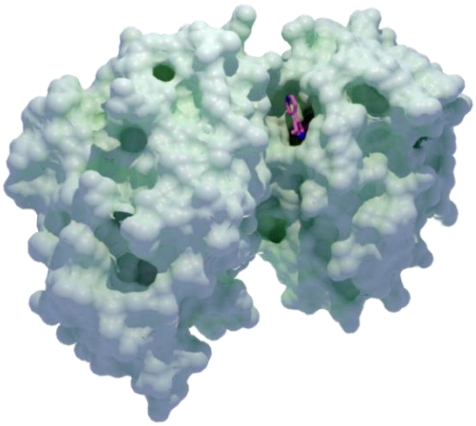

Figure I. 12 - Surface representation of the serine/threonine p38α mitogen-activated protein kinase (p38αMAPK) bound to a selective and central nervous system (CNS)-penetrant inhibitor (PDB entry 4ZTH).

Importantly, *a priori* characterization of binding pockets with topological and physicochemical parameters is required to assess the suitability of such regions to bind a molecule. Small molecule binding sites usually consist of deep concave pockets that can maximize favourable protein-ligand contacts. Typically, a binding site is lined with hydrophobic residues that are

critical for binding small molecules in aqueous environments. In addition, individual functional groups (including alcohols, thiols, thioethers, carboxylic acids, carboxamides, and a variety of basic groups) at defined locations on a protein's surface can have huge effects when located at the core of a binding interaction (Sheehan, 2011; Guo et al., 2015).

Nowadays, numerous computational approaches are employed to predict druggable protein binding sites, representing powerful tools to gain such structural knowledge, offering the unique ability to predict, model and dissect, at the atomic level, key protein-ligand interactions. Three different criteria are critical for the assessment of target druggability: (i) the presence or absence of a protein cavity with an appropriate volume and depth to accommodate a small molecule; (ii) the extent of structural, physicochemical and pharmacophoric properties of a drug-like molecule complementary to the protein binding site; and (iii) the shape and existence of sub-pockets or narrow clefts that can provide strong interacting *hot-spots* (Schmidtke and Barril, 2010; Fauman et al., 2011; Agoni et al., 2020). Still, it is worth empathizing that there is an entire universe of potential drug targets that don't really involves small molecule binding pockets at all. Protein-protein interactions represent one of the next major classes of therapeutic targets. For further information, I point the reader to references (Kuenemann et al., 2016; Scott et al., 2016)

In many cases, 3D protein structures may contain a bound ligand, in which case it should be relatively straightforward to define the binding site. However, if no ligand is present (*apo* protein) or there are unoccupied allosteric sites it may be possible to use computational tools to identify potential binding regions. Prediction of protein binding sites (or *hot-spots*) can guide the design of molecules able to modulate the target´s biological function at a molecular level. During the last two decades, several algorithms have been proposed to address automated prediction and identification of protein binding sites and it is still a very active field (Xie and Hwang, 2015). In Part II, pocket identification computational strategies and the methods used in this project will be approached in greater detail.

1.2.3.3. Homology modelling

In the absence of experimentally determined protein structures, computational methods are used to predict 3D protein models, providing insight into the structure and function of these proteins. Specifically, if known 3D structures that are evolutionarily related (homologous) to the target sequence are available, such structural data is used to model the actual target and are also useful to complete or refine flexible parts of the protein, such as loop regions. The most detailed and accurate structural prediction method is homology modelling (Fiser, 2010). This technique is a specific type of comparative modelling to predict protein structures based on the premise that similar proteins sequences give rise to similar tertiary structures.

Fundamentally, the basic principles of homology modelling rely on the assumption that the structural conformation of a naturally folded protein is more conserved throughout evolution than its amino acid sequence. Hence, proteins with similar sequence, at least 30% homology, tend to adopt the same fold (Rost, 1999; Koonin et al., 2002).

Typically, all homology modelling methods encompass the following steps: (1) identification of related proteins to serve as 3D template structures for the target sequence (2) sequence alignment of the target and template proteins, (3) copying coordinates for aligned regions and constructing missing atom coordinates of target structure, (4) model generation, including backbone generation, loop and side-chain modelling, and (5) model optimization and validation (Sliwoski et al., 2014; Lam et al., 2017). Three of the most prominent and commonly employed computational resources for structure prediction through homology modelling are MODELLER (Šali and Blundell, 1993), Phyre2 (Kelley et al., 2015) and SWISS-MODEL (Schwede, 2003).

Homology modelling main shortcoming is that it relies on the availability and identification of suitable template structures. Nonetheless, the importance and applicability of homology modelling is increasing with the increasing number of protein 3D structures in structural databases. Homology models contain critical information about the spatial arrangement of important residues in the protein, enabling the use of SBDD strategies.

Over the last decades, the applicability of homology modelling to predict structural determinants of proteins involved in the inflammatory landscape have been explored: from key players involved in cytokine signalling such as interleukin-2 receptor (IL-2R), interleukin-4 receptor (IL-4R) (Bamborough et al., 1994), interleukin-7 receptor (IL-7R) (Kroemer and Richards, 1996), interleukin-27 (IL-27) (Müller et al., 2019) and IFNs (Murgolo et al., 1993; Seto et al., 2008), through pattern recognition receptors like NOD1 (Majumdar et al., 2017), TLRs (Wei et al., 2009; Kubarenko et al., 2010), NLRP3 (Mekni et al., 2019; Samson et al., 2020), to other fundamental immune system players like P2X7 receptor (Bidula et al., 2019) or cathepsins (Fengler and Brandt, 2000).

1.2.3.4. Molecular docking

Molecular docking is a SBDD approach that attempts to predict non-covalent binding of a ligand to a target protein, in the 3D space (Brooijmans and Kuntz, 2003). In essence, ligands are fitted into a binding pocket of a protein, and typically ranked according to their predicted binding affinity or complementarity to the binding site. This technique can be applied for two different purposes, in hit identification (virtual screening) and in lead optimization. Docking programs allow the screening of massive virtual libraries of candidate molecules against targets of interest, in a feasible amount of time if reasonable computational resources are

available. Similarly, in lead optimization, analogues of a particular lead compound are docked and evaluated. These data are used to properly guide new synthetic chemistry efforts, prioritizing compounds for synthesis and experimental evaluation (Kitchen et al., 2004; Pantsar and Poso, 2018).

Currently, there are several docking algorithms and software available. Based on the different ways to address flexibility in the representation of the protein-ligand system, docking methods can be classified as: (i) rigid-body, simplistic model where both molecules are rigid, considering only static geometric or physiochemical complementarities; (ii) semi-flexible, where one, usually the ligand is considered flexible; and (iii) flexible, which consider both receptor and ligand flexibility simultaneously during docking (Sliwoski et al., 2014; Huang, 2018). In a methodological sense, all methods comprise two interrelated steps: ligand sampling and scoring. The first refers to the methods which are used to create different ligand conformations and aligning them within the binding site of the protein. The latter, the scoring, is required in the docking process for a quantitative estimation of the pose quality (Pantsar and Poso, 2018).

The first challenge a docking program faces is the ligand and protein conformational freedom. To tackle the issue of conformational flexibility, docking programs often have built-in conformational generators for ligand structures and, in some cases, also for the receptor structures. Though less common, some programs perform rigid docking but accept multiple ligand (and sometimes receptor) conformations as input. Conformational sampling algorithms used in docking programs fall in three major types: systematic search, random or stochastic algorithms and simulation methods. Systematic search algorithms sample all possible ligand binding conformations by exploring all degrees of freedom of the ligand, in a combinatorial way (Kitchen et al., 2004). In stochastic algorithms random conformational changes to the ligand are made. Such alterations are evaluated by using specific energy functions to determine if the position and torsion angles of each subsequently generated conformation is higher or lower in energy when compared to the previous one. In the end, the random changes may be accepted or rejected based on probabilistic criterion. AutoDock 4.0 (Morris et al., 1998) is an example of a docking program implementing this algorithm. Simulation methods perform deterministic searches to adequately sample the system's conformational space. These types of algorithms use energy minimization methods and molecular dynamics (MD) simulations, generating conformations by simulating the time-dependent movement of the molecules. (Kitchen et al., 2004; Salmaso and Moro, 2018).

Docking programs also face the challenge of predicting binding affinities for the ligands in the pool of all possible sampled conformations and interactions established within a binding site, and this is accomplished using what are called scoring functions. The existing scoring

functions for protein-ligand interactions can be categorized into four main groups based on the underlying principles of their work: empirical, force-field based, knowledge-based and machine-learning-based scoring functions (Li et al., 2019). Empirical scoring functions compute the fitness of protein−ligand binding by summing up the parametrized contributions of several individual terms, such as van der Waals, electrostatic interactions, hydrogen bonds, hydrophobic effects and the binding entropy, each representing an important energetic factor in protein−ligand binding (Guedes et al., 2018). Force-field based scoring functions assess the binding energy by calculating electrostatic and Van der walls interactions between the atoms of the ligand and the protein, using Coulombic formulations and Lennard-Jones potentials, respectively (Kuntz et al., 1982; Morris et al., 1998; Li et al., 2019). Knowledge-based scoring functions are derived from the ever-increasing structural data available for protein-ligand complexes, by computing sum pairwise statistical potentials between protein and ligand derived from the inverse Boltzmann statistical distributions, i.e., the geometric features between atoms of the protein-ligand complexes (Kitchen et al., 2004; Kadukova and Grudinin, 2017). Finally, machine-learning-based scoring functions extrapolate previously determined QSAR data into protein-ligand interaction evaluation (Deng et al., 2004), originating statistical models that compute protein-ligand binding scores when their properties as well as their interaction patterns are coded (Liu and Wang, 2015; Li et al., 2019).

In the last decades, many researchers have made use of experimentally determined 3D structures or homology models of inflammatory targets to perform docking calculations toward the prediction of binding affinities of new ligands and evaluation of potential interactions with key residues. For instance, Zusso et al. applied docking simulations to five largely prescribed fluoroquinolones – ciprofloxacin, levofloxacin, moxifloxacin, ofloxacin, and delafloxacin – to interpret their binding modes to the interface between TLR4 and the co-receptor myeloid differentiation protein-2 (MD-2). Binding of LPS to this complex triggers the activation of NF- κB, which increases the production of pro-inflammatory mediators such as TNF-α, IL-1β, IL-6 and ROS. From the docking analysis, compounds showed a dual mechanism of binding: (i) interacting with LPS recognition site in the MD-2 structure; or (ii) binding at the interface between MD-2 and TLR4 complex. Co-immunoprecipitation assays were used to confirm the inhibitory effect of ciprofloxacin and levofloxacin on TLR4–MD-2 dimerization as well as LPS binding to the TLR4–MD-2 complex, validating molecular docking observations. Both compounds were able to reduce the LPS-stimulated inflammatory response, via modulation of the TLR4–MD-2/NF-κB pathway (Zusso et al., 2019).

Accumulating studies have been trying to identify inflammation chemical modulators based on VS campaigns, using molecular docking as crucial component on hit identification and lead optimization. For example, Zhong et al. followed a structure-based VS strategy to identify TLR1-TLR2 protein-protein interface inhibitors. The authors docked a chemical library of

natural products and natural product-like compounds from ZINC database (>90,000 compounds), using a crystal structure of the human TLR2-TLR1 heterodimer co-crystallized with the agonist triacylated lipopeptide Pam3CSK4 (PDB entry 2Z7X). The 17 best-scoring compounds at the interaction domain of the TLR1-TLR2 interface were selected for biological testing. Of these, one compound reduced the release of pro-inflammatory cytokines TNF-α and IL-6 induced by Pam3CSK4 in RAW264.7 macrophages. Moreover, this molecule was able to decrease IκBα and IKKα/β phosphorylation, together with a reduction in the expression levels of IκBα, which are essential for NF-κB activation (Zhong et al., 2015).

In a recent study, De Leo et al. reported the discovery of 5,5'-methylenedi-2,3-cresotic acid as inhibitor of the HMGB1·CXCL12 heterocomplex, which act synergistically to activate the G-protein coupled receptor CXCR4 and promote cell migration and inflammation. The authors performed structure-based VS using three different docking programs - Glide (Friesner et al., 2004), AutoDock Vina (Trott and Olson, 2009), and AutoDock 4.2.6 (Morris et al., 2009) - and a ZINC subset containing 101,746 biogenic drug-like compounds selected according to Lipinski's rule of five. This compound dataset was docked against the functional domains, BoxA and BoxB, of HMGB1 (PDB entry 2YRQ). Virtual hits were selected based on energy ranking, distance filtering, visual inspection and ADME analysis. In total, the VS protocol yielded three sets of compounds for BoxA and three for BoxB for a total of 581 promising candidates. These molecules were post-filtered using a ligand-based pharmacophore query derived from known active HMGB1 inhibitors and clustered based on chemical diversity, using binary 2D linear fingerprints. From this procedure, 8 compounds representative of the clusters were tested for HMGB1 binding via NMR measurements, revealing 5,5'-methylenedi-2,3-cresotic acid as a ligand of HMGB1. Subsequent NMR and docking studies established the dual activity of this compound on both HMGB1 and CXCL12 and the dissociation of the HMGB1·CXCL12 heterocomplex (De Leo et al., 2020).

1.2.3.5. 3D pharmacophore modelling

As defined by the International Union of Pure and Applied Chemistry (IUPAC), a pharmacophore is "the ensemble of steric and electronic features that is necessary to ensure the optimal supramolecular interactions with a specific biological target structure and to trigger (or to block) its biological response". In other words, a pharmacophore describes: (i) the crucial, steric and electronic functions of molecules relevant for an optimal interaction with a protein target, and (ii) an abstract (simplified) representation accounting for common pharmacophoric properties of compounds regarding a target structure, and not a real molecule or association of functional groups (Langer and Hoffmann, 2006).

Within the context of Computer-Aided Drug Design (CADD), the concept of "pharmacophore" holds application in:

1. Construction of pharmacophores models for ligand optimization, e.g. through bioisosteric replacements;
2. Scaffold hopping, i.e. screening of robust virtual compound libraries comprising similar functional structures, for designing new active analogues bearing distinct scaffolds;
3. Pharmacophore merging, meaning a single molecule bearing pharmacophoric features arising from two different partners, aiming at the design of new active compounds.

In pharmacophore modelling, the interaction patterns of bioactive molecules with their targets are represented via a three-dimensional (3D) arrangement of abstract features, that encode typically six pharmacophore features: hydrogen bond acceptor (HBA), hydrogen bond donor (HBA), hydrophobic group (H), negatively charged group (N), positively charged group (P), aromatic ring (Ar). "Conventional" 3D pharmacophore features computed by the software LigandScout (Wolber and Langer, 2005) are illustrated in **Figure I.13**.

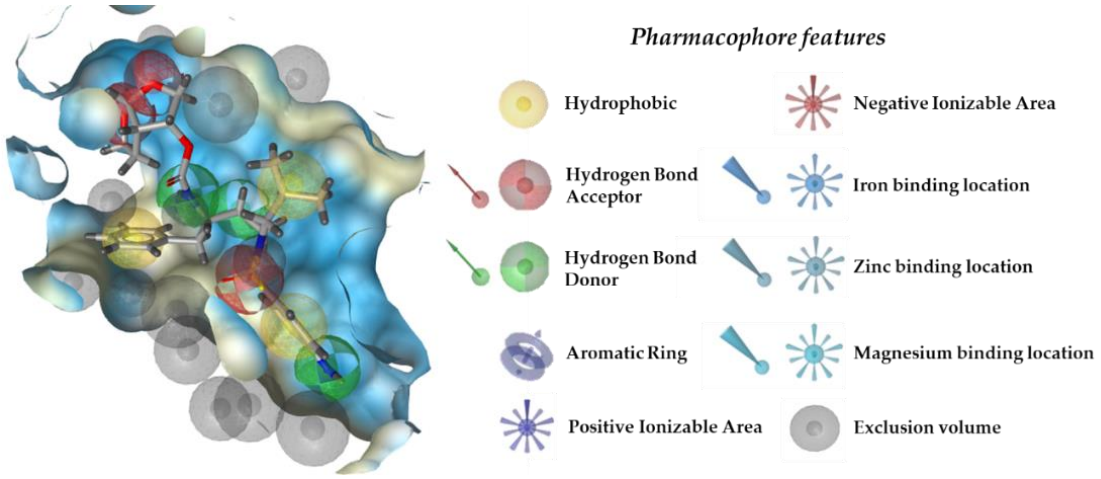

Figure I. 13 - Schematic representation of pharmacophore features. Example of a three-dimensional (3D) pharmacophore model from a protein–ligand complex generated with the LigandScout software (Wolber and Langer, 2005). LigandScout provides three geometric types of features: vector (hydrogen bond acceptors and donors, metal binding location for iron, magnesium and zinc atoms), point (hydrophobic interactions, negative ionizable areas, positive ionizable areas, exclusion volume) and plane features (aromatic rings).

There are several pharmacophore modelling tools that, based on the input employed for model generation, can achieve different types of pharmacophores:

1. Ligand-based pharmacophores: when a set of active ligands is available, it is possible to compute their shared pharmacophore using different algorithms. Several conformations of each active ligand are generated, matched and the best possible alignment is then used to derive the pharmacophore model.

2. Structure-based pharmacophores: protein-ligand interaction patterns are extracted from experimentally determined complexes, e.g. NMR spectroscopy and X-ray crystallography, deposited in PDB.
3. Receptor-based pharmacophores: based exclusively on the topology of the binding site and in the absence of a ligand. Potential cavities are calculated on the protein surface and once the binding site is selected, the program automatically calculates pharmacophore features based on the residues lining that site. This automatically-generated pharmacophore hypothesis can be manually refined to derive the final model (Langer and Hoffmann, 2006; Schaller et al., 2020).
4. Molecular Dynamics-based pharmacophores: this type represents an extension of receptor-based pharmacophores, wherein a set of MD snapshots are used to generate "dynamic" pharmacophore models. The frequency with which specific features occur during the MD simulation in relation with stability of the PDB features can be used to refine the receptor-based pharmacophore models by adding or removing features and weighting their importance (Wieder et al., 2016).

To date, several studies have reported the development or use of pharmacophore-based approaches towards VS protocols aiming to identify small molecule modulators of inflammatory responses. An overview of relevant reports concerning the application of 3D pharmacophore modelling within the inflammatory landscape is presented in **Table I.4**.

During the last two decades, successful examples of the application of ligand-based 3D pharmacophores in VS campaigns targeting inflammatory mediators have been reported. In 2008, Kim et al. applied ligand-based virtual screening to discover new chemical scaffolds for GSK-3β inhibition, starting from pharmacophore hypothesis generated with the HipHop module of the Catalyst program (Barnum et al., 1996), using a set highly active GSK-3β inhibitors. The best pharmacophore query comprised three HBA, one HBA and one H feature. This model was used for virtual screening against a library of 600,970 compounds, which was pre-filtered according to specific criteria (chemical diversity, drug-likeness via Lipinski's rule of 5, ADME properties) yielding 26,970 compounds. 56 virtual hits were selected based on docking poses, structural diversity, and synthetic accessibility. From these, three compounds exhibited inhibitory activity in the low micromolar range in an enzyme assay for human GSK-3β protein (Kim et al., 2008).

In a study by Waltenberger et al, ligand-based 3D pharmacophore hypotheses were developed for the microsomal prostaglandin E2 synthase-1 (mPGES-1), a key enzyme involved in prostaglandin E2 (PG)E2 synthesis. The pharmacophore models were used to screen two compound databases, NCI (247,041 compounds) and SPECS (200,015 compounds), yielding 29 chemically diverse compounds for biological testing. From these, nine compounds were

identified as novel bioactive substances (Waltenberger et al., 2011). In a third example, Temml et al. rationalized a pharmacophore-based virtual screening campaign towards the discovery of dual 5-lipoxygenase-activating protein (FLAP) and soluble epoxide hydrolase (sHE) inhibitors., two pro-inflammatory targets playing an important role in the arachidonic acid pathways. Using a set of 11 known FLAP inhibitors, the authors generated two different ligand-based pharmacophore models using LigandScout, which were subjected to VS of a SPECS virtual library (202,920 compounds). Twenty virtual hits were prioritized for experimental testing by previously reported structure-based sHE models, resulting in one novel and potent dual inhibitor for sEH and FLAP with activities in the nanomolar range (Temml et al., 2017).

Table I. 4 - Examples of pharmacophore modelling studies demonstrating the potential and wide variety of applications of pharmacophores for different targets involved in the inflammatory signalling pathways.

Target	Method	Result	Reference
Complement C3	Structure-based	One compound able to bind C3	(Mohan et al., 2018)
COX-2	Ligand-based	One potent and selective COX-2 inhibitor	(Palomer et al., 2002)
CXCR2	Ligand-based	One selective CXCR2 signalling modulator	(Ha et al., 2015)
FLAP+sEH	Ligand-based	One novel and potent dual FLA protein/sHE inhibitor	(Temml et al., 2017)
GSK-3β	Ligand-based	Three compounds with GSK-3β inhibitory activity	(Kim et al., 2008)
IKK-β	Ligand-based	Three compounds with IKK-β inhibitory activity	(Noha et al., 2011)
IL-15	Receptor-based	One compound with IL-15 inhibitory activity	(Quéméner et al., 2017)
IRAK-4	Structure-based	Six potent and structurally diverse IRAK-4 inhibitors	(Khanfar and Alqtaishat, 2019)
mPGES-1	Ligand-based	Nine novel chemical scaffolds inhibiting mPGES-1	(Waltenberger et al., 2011)
PPARγ	Structure-based	Five molecules as novel PPARγ ligands	(Markt et al., 2008)
p38α MAPK	Structure-based	Seven compounds with promising p38αMAPK inhibitory activity	(Gangwal et al., 2014)
ROCK-I+NOX2	Structure-based	Seven selective dual ROCK-I/NOX2 inhibitors	(Alokam et al., 2015)
TLR2	Receptor-based	Eight structurally diverse antagonists of TLR2	(Murgueitio et al., 2014)
TLR8	Structure-based	Three potent and selective TLR8 signalling inhibitors	(Šribar et al., 2019)
TRPV1	Ligand-based	Two compounds with TRPV1 inhibitory activity	(Feng et al., 2015)

Table abbreviations: complement component 3 (C3); cyclooxygenase-2 (COX-2); CXC chemokine receptor 2 (CXCR2); 5-lipoxygenase-activating protein (FLAP); soluble epoxide hydrolase (sEH); glycogen synthase kinase-3β (GSK-3β); interleukin-15 (IL-15); interleukin-1 receptor-associated kinase 4 (IRAK-4); microsomal prostaglandin E synthase-1 (mPGES-1); peroxisome proliferator activated receptor-gamma (PPARγ); mitogen-activated protein kinase p38α (p38α MAPK); rho kinase (ROCK-I); NADPH oxidase (NOX2); toll like receptor 2 (TLR2); toll like receptor 8 (TLR8); transient receptor potential vanilloid type 1 channel (TRPV1).

In the next subsection, receptor-based pharmacophore modelling will be covered in more detail, as in Part IV receptor-based approaches are exploited in attempt to devise a set of specific and selective pharmacophore hypothesis for a target of pharmaceutical interest.

1.2.3.5.1. Receptor-based pharmacophore modelling

When only the structural information of protein targets is available (there is no or enough known ligands to use as training set), putative receptor-based 3D pharmacophores models can be generated through analyses of the topology and physicochemical properties of the target binding site. Essentially, the computed model represents a mirror image of idealized ligand pharmacophore features, i.e., potential protein-ligand interactions in the binding site. Nowadays, several programs can directly convert the 3D atomic structure of the protein binding site into a pharmacophore model - Phase (Dixon et al., 2006), Catalyst (Greene et al., 1994), AutoPH4 (Jiang et al., 2020) and LigandScout (Wolber and Langer, 2005).

Because *a priori* knowledge of active ligands is not required, receptor-based pharmacophore models are not biased by the chemical space of previously identified actives (potential for scaffold hopping). In addition, these models allow the integration of excluded volume spheres to the pharmacophore, providing a more selective model to reduce false positives. In general, these excluded volumes attempt to penalize molecules occupying steric regions of the target protein that compounds cannot map. Importantly, in receptor-based pharmacophore modelling, an intensive examination of the binding site and its surrounding amino acids is critical for the estimation of the most relevant and potential interactions playing key roles in ligand binding. The main challenge faced in this approach is the numerous features generated (depending on the size and shape of the binding site), which make the corresponding pharmacophore very complex. These must be reduced to a reasonable number for screening purposes – an adequate balance between enough features to allow for specificity, but not too many of them, as this would be too restrictive and could lead to false negatives. At this stage, for instance, MD simulations can be applied to generate an ensemble of protein conformations, computing for each MD snapshot a pharmacophore model. Then, clustering of the aligned pharmacophores of the different snapshots can be performed to select the most representative features of that binding site (Wieder et al., 2017; Schaller et al., 2020).

Once receptor-based pharmacophore hypotheses are formulated, 3D pharmacophores models can be screened against virtual libraries of molecules to find the ones that fit the models and, hence, possess the most appropriate spatial arrangement of chemical features to bind the target. The consideration of ligand flexibility in these virtual libraries is performed by either generating all possible conformations and creating conformer libraries prior to the screening

step, or alternatively by the exploration of the conformational space as each molecule is screened. Some software packages, such as LigandScout or Pharmit (Sunseri and Koes, 2016) perform virtual screening on a pre-computed dataset of conformers for each library molecule, while others, such as Phase, allow conformer generation during the screening step sacrificing virtual screening speed (Schaller et al., 2020).

A successful application of receptor-based pharmacophore modelling in identifying lead compounds for inflammatory targets was demonstrated by Quéméner et al. by targeting the pleiotropic cytokine interleukin-15 (IL-15). The group generated a receptor-based 3D pharmacophore based on three residues, Asp8, Asn65 and Leu69, essential for the protein-protein interaction with interleukin-2 receptorβ (IL-2Rβ). The model consisted of three pharmacophore features: (i) one HBA and one HBD centred on Asp8; (ii) one H feature located between Ile68 and Leu69; and (iii) ten exclusion volumes defined by the binding region. The 3D pharmacophore was used for a VS campaign of 160,828 compounds derived from commercial and academic chemical libraries. A total of 24,115 molecules fulfilled the pharmacophoric requirements and were subjected to molecular docking studies where 240 compounds were selected for biological testing. From these, 36 compounds were found to bind IL-15, to inhibit the binding of IL-15 to the IL-2Rβ chain or the proliferation of IL-15-dependent cells or both. One ligand showing inhibitory activity in the 10μM range was optimized via synthesis and SAR analyses, leading to a collection of derivatives with IC_{50} values close to 50 nM in cell-based experiments (Quéméner et al., 2017).

1.2.3.6. Molecular Dynamics simulations

Molecular dynamics (MD) simulations are the archetypal computational technique to study in detail conformational changes in biomolecular systems at the atomic scale, gaining insight into time- and environment-dependent events, such as protein folding and unfolding processes or the impact of protein motions in ligand binding. The idea of MD is a simple one: calculate the forces acting on the atoms in a molecular assembly and analyse structural, dynamic and thermodynamic properties. This relationship is achieved by integrating Newton's law of motion:

$$\boldsymbol{F_i = m_i a_i = m_i \frac{\delta v_i}{\delta t} = m \frac{\delta^2 r_i}{\delta t^2}}$$

Equation 1.1

where the net force (*F*) for an atom (*i*) at a given time (*t*) is directly related to its mass (m) and acceleration (a). For each time step, the current positions (*ri*) and velocities (*vi*) can be used to calculate the change in the position of the particle in the system, resulting in a MD trajectory with positions as function of time. Numerical integration algorithms such as Verlet (Verlet,

1967) or leap-frog integrator (Cuendet and van Gunsteren, 2007) are employed to solve these equations and propagate the motion of the particles in a simulation. When adequate information on the movements of the individual atoms has been computed, it is possible to condense such data using methods of statistical mechanics to deduce microscopic system properties, i.e., velocities and positions, and equilibrium macroscopic system properties such as volume, pressure, temperature and number of particles (Rapaport, 2004).

MD simulation algorithms have been implemented in a number of software packages, including, but not limited to GROningen Machine for Chemical Simulations (GROMACS) (Berendsen et al., 1995; Abraham et al., 2015), Chemistry at HARvard Macromolecular Mechanics (CHARMM) (Brooks et al., 2009), NAMD (Phillips et al., 2005), Assisted Model Building with Energy Refinement (AMBER) (Case et al., 2005) and Desmond (Bowers et al., 2006). Constant improvements to the architecture and computing power extended the use of these algorithms to much larger systems including large macromolecular complexes, explicit solvent and/or membrane environment, greater conformational changes, and longer time scales. In recent years, MD engines have leveraged the acceleration of graphics processing units (GPUs), allowing now MD simulations to sample the protein conformational space more efficiently than ever before, thus providing more reliable data on the conformational flexibility and molecular motions of a protein.

Importantly, it is important to acknowledge that MD also has some limitations and pitfalls: (i) the *force field* define fixed charges with the atoms, preventing charge polarizability over time - polarizable force fields have been developed, however they require an extensive computational cost; (ii) chemical bonds cannot be broken or formed during a MD simulation and tautomer and ionization states are defined prior to the simulation, and thus chemical reactivity is not effectively described; and (iii) the selected time scales (nanoseconds to microseconds) may not be sufficient to describe certain dynamical properties, such as protein folding, ligand binding and unbinding processes, occurring at larger time scales (Ganesan et al., 2017).

1.2.3.6.1. The motions of a protein

Proteins are highly dynamic molecules that undergo conformational changes on temporal and spatial scales. A central aspect of all-atom MD is related to the wide range of timescales over which specific molecular processes in proteins occur (**Figure I.14**). The nature of protein internal motions can be categorized in: (i) local motions, including bond vibrations on the femtosecond timescale, side-chain rotamers on the pico- to the microsecond timescale and loop motions on the nano- to the microsecond timescale; (ii) rigid-body motions, such as helix, domain (hinge bending) and subunit motions on the nanosecond to second timescale; and (iii)

large-scale motions of secondary and tertiary structural elements, leading to larger domain motions and even both folding and unfolding events, typically taking milliseconds, seconds or more to occur (Henzler-Wildman and Kern, 2007). Failure to run a simulation long enough in order to gather sufficient amount of data or improper setup or insufficient equilibration of the initial structure(s) are common drawbacks in MD.

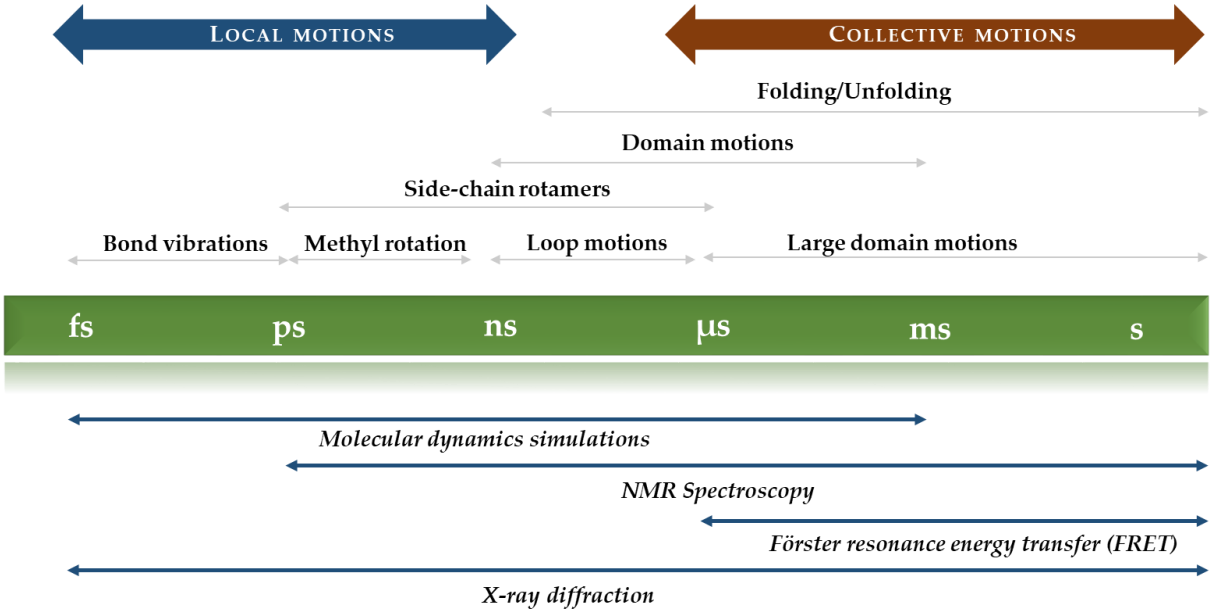

Figure I. 14 - Timescale of protein dynamic events. The local motions occur on the timescale of femtoseconds (fs) to nanoseconds (ns), whereas collective motions (including rigid-body and large domain motions) occur on the timescale of microseconds (µs) to seconds (s). MD simulations cover the fs to millisecond (ms) timescale.

From the sampling viewpoint, to properly assess these protein motions, not only does one need to have a long enough simulation, but also replicates of the simulation. Indeed, multiple simulations yield better sampling of protein conformational space than a single simulation - with a total sampling time equalling the aggregate sampling time of multiple simulations – allowing for more reproducible and reliable MD results (Knapp et al., 2018). Usually there is enough sampling for the faster local motions, however, sampling slow collective motions is challenging, often separated by high free-energy barriers. Notably, to overcome such problems, many enhanced sampling techniques have been developed and successfully employed, including steered molecular dynamics (Do et al., 2018), umbrella sampling (Kästner, 2011) and metadynamics (Barducci et al., 2011).

The first MD protein simulation was of BPTI (bovine pancreatic trypsin inhibitor), a 58-residue globular protein which was simulated, along with four water molecules, for 9.2 picoseconds, in 1977 (McCammon et al., 1977). Three decades later, the longest published MD simulation was reported, a one millisecond-long MD simulation of BPTI fully-solvated with explicit hydrogen atoms, 100,000 times longer than the first one (Shaw et al., 2010).

1.2.3.6.2. The Empirical Energy Function (or *force field*)

MD simulations are usually based on empirical molecular mechanics' calculations, which are commonly referred to as *force fields*. The fundamental interacting unit, in molecular mechanics, is the atom, not individual electrons and their motions. The potential energy profile of a collection of atoms is calculated by adding up the energy terms that describe interactions between bonded atoms (bonds, angles and torsions) and terms that describe the non-bonded interactions, such as van der Waals and electrostatic interactions, which together constitute the empirical *force field* (Guvench and MacKerell, 2008). The most common mathematical expression representing the classical total potential energy of any molecule is:

$$\boldsymbol{V}(\boldsymbol{r^N}) = \sum_{all\ bonds} k_l\,(l - l_0)^2 + \sum_{all\ angles} k_\theta\,(\theta - \theta_0)^2 + \sum_{all\ torsions} \frac{1}{2} V_n[1 + \cos(n\omega - \gamma)] + \sum_{\substack{non-bonded \\ atom\ pairs\ i,j}} \left(\varepsilon_{ij} \left[\left(\frac{r_{0ij}}{r_{ij}} \right)^{12} - 2 \left(\frac{r_{0ij}}{r_{ij}} \right)^{6} \right] + \frac{q_i q_j}{4\pi\varepsilon_0 r_{ij}} \right)$$

Equation 1.2

where the bonded terms represent the stretching of bonds (l), bond angle bending (θ), with the respective force constants kl and $k\theta$, and the rotation of torsional angles (ω) representing a periodic rotation of a dihedral angle with periodicity n and phase γ, with Vn determining the energetic barrier height. Non-bonded interactions are parametrized in terms of partial charges qi for Coulombic (electrostatic) interactions, and the parameters εij and rij, defining the depth and width of the Lennard-Jones potential (van der Waals), respectively (Genheden et al., 2017). These two potentials describe the short-range non-bonded interactions. The evaluations of the long-range electrostatic interactions are often performed using the Ewald summation (Procacci and Marchi, 1996) and particle mesh Ewald (PME) methods (Essmann et al., 1995).

The most prominent and commonly employed *force fields* are AMBER (Case et al., 2005), CHARMM (MacKerell et al., 1998), GROMOS (Schuler et al., 2001) and OPLS (Jorgensen et al., 1996), designed for biological macromolecules. The MMFF (Halgren, 1996) and GAFF (Wang et al., 2004) have been developed for the description of small, drug-like molecules, whereas GLYCAM (Kirschner et al., 2008) was specifically developed for carbohydrates. Besides the choice of *force field*, the representation of water molecules is of paramount importance since most biological processes occur in aqueous environments. When explicitly treating the solvent, the most widely used models for parameterization of water molecules have been SPC/E (simple point charge) (Berendsen et al., 1987) and TIP3P (transferable intermolecular potential with 3 points) (Jorgensen et al., 1983).

1.2.3.6.3. Statistical ensembles in MD simulations

The concept of ensemble is key in statistical mechanics, as averages corresponding to experimental observables are defined in terms of ensemble averages. MD simulations require that certain macroscopic parameters must be held constant to study the collection of all microstates of a system, i.e., all MD frames share the same macroscopic/thermodynamic state but may differ in the microscopic ones. Statistical ensembles are usually characterized by fixed values of macroscopic variables such as energy E, temperature T, pressure P, volume V, particle number N or chemical potential μ. **Table I.5** denotes the different types of statistical ensembles employed in the MD simulations.

Table I. 5 - Different ensembles in MD simulations.

Ensemble	Fixed Parameters
micro-canonical ensemble (*NVE*)	number of particles N, volume V and energy E
canonical ensemble (*NVT*)	number of particles N, volume V and temperature T
isothermal–isobaric ensemble (*NPT*)	number of particles N, pressure P and temperature T
grand canonical ensemble (μVT)	chemical potential μ, volume V and temperature T

The canonical ensemble (NVT) (Richardson and Brinkley, 1960) and the isothermal-isobaric ensemble (NPT) (Corti and Soto-Campos, 1998) are commonly used in MD, with the latter being the most widely used as it more accurately reflects laboratory conditions, where pressure and temperature are usually known. Examples of thermostats used to maintain constant temperature are the Berendsen weak coupling method (Berendsen et al., 1984) and Nosé-Hoover (Braga and Travis, 2005), while common choices for barostats include the Langevin method (Feller et al., 1995), Berendsen (Berendsen et al., 1984) and the Rahman-Parrinello method (Parrinello and Rahman, 1981).

1.2.3.6.4. Setting up a MD simulation: key considerations

A typical MD protocol consists of five main steps:

1. Preparation of the initial structure(s): starting coordinates for each atom are retrieved from experimental data, such as X-ray crystallography, NMR, cryo-EM or structural modelling. Missing residues and missing atoms such as hydrogens are added, and atomic clashes eliminated. Furthermore, protonation states of ionisable groups are computed to ensure a proper system configuration for MD simulations.
2. Energy minimization: prior to any simulation, the system undergoes a thorough energy minimization process, in a stepwise manner, to resolve any initial poor contacts and high-energy overlaps between atoms, without creating large distortions in the

overall structure. At each minimization iteration, the energy of the system is measured until a stable point or a minimum on the potential energy surface is reached. The resulting minimized structure is the underlying configuration about which fluctuations occur during the simulation. Two examples of widely used minimization algorithms are the Steepest Descent (Petrova and Solov'ev, 1997) and Conjugate Gradient (Fletcher, 1964).

3. Equilibration: initial velocities (at 0 K) are randomly assigned to the atoms through a Maxwell-Boltzmann distribution and, subsequently, the system is simulated in gradual steps toward thermal equilibrium at the target temperature. Indeed, the purpose of the equilibration stage is to ensure that the kinetic energy in the system is distributed appropriately among all degrees of freedom. Properties such as potential energy, kinetic energy, temperature, volume, pressure, and RMSD are monitored to ensure the stable behaviour of the system.
4. Production: once the system is in equilibrium the current velocities are used for production runs, in a simulated physiological environment. They are performed for the desired time scales, and the results of this stage are stored in a simulation trajectory, from which structural and energetics properties can be calculated and subsequently analysed (Braun et al., 2019).
5. Analysis: an essential step, which converts the enormous raw data accumulated in the production run to meaningful information. RMSD and root mean square fluctuation (RMSF) plots serve as first-line investigational tools to identify and quantify structural deviations from the starting structure. In addition, RMSD profiles can be used to cluster multiple structures based on structural similarity. Alternatively, reduced dimensionality of data can be exploited to manage reasonable numbers of conformations. Principal component analysis (PCA) converts a set of correlated observations (movements of selected atoms in a system) to a set of principal components (PCs) which are linearly independent (or uncorrelated), thereby reducing the dimensions of the simulation data. Part III will focus on some practical aspects of molecular dynamics simulations and trajectory data analysis.

Boundary conditions are an important requirement in any MD simulation. Given the limited number of solvent molecules in a MD simulation, this method allows the elimination of undesirable surface effects in finite size system, by treating it as infinite with the help of a unit cell. Periodic boundary conditions (PBC) are usually applied using a box with various geometries, a cubic box, a rhombic dodecahedron, or a truncated octahedron. This box which harbours the system of interest is replicated in different directions. In a methodological sense, when a molecule leaves the system on one face the periodic box, the equivalent periodic image

replaces it from the neighbouring box on the opposite side, leading to conservation of mass and number of particles (Genheden et al., 2017; Braun et al., 2019).

Choosing an appropriate time step is also a critical aspect in MD, defining how frequently the integration of the equations of motion is performed, and thus determining the accuracy of the trajectory. Generally, smaller time steps provide a better approximation of the expected dynamics of the system, still, it takes a very long calculation time and increases computational costs. In order to reach a compromise between computational costs and accuracy, dynamics of the covalent bonds involving hydrogen atoms are usually constrained using integration algorithms, such as SHAKE (Ryckaert et al., 1977) and LINCS (Hess et al., 1997). For all-atom simulations with these constraints is possible to achieve time step values in the range of 1.5 to 2 fs.

1.2.3.6.5. Combining MD simulations with Virtual Screening: enhancing performance

The integration of data on molecular flexibility during a VS campaign can substantially improve VS performances, namely when dealing with highly flexible targets and overcomes potential shortcomings associated with the choice of a single representative conformation for VS. MD simulations, despite their computational cost, are playing an ever-increasing role in structure-based VS strategies, allowing *in silico* approaches to expedite the modern drug discovery process. Drug design applications of MD extends from predicting target flexibility (Cozzini et al., 2008), unveiling transient pockets on protein interfaces (Eyrisch and Helms, 2007), generating ensembles of protein conformations for docking (Śledź and Caflisch, 2018), the validation and refinement of docking poses, and free energy calculations to understand protein-ligand binding (Miyata et al., 2010), to developing dynamic receptor-based pharmacophore models (Wieder et al., 2016) and optimizing protein structural models (Heo and Feig, 2018). Without much doubt, a key point for a successful VS campaign relies on the sampling accuracy and the ability to select the most representative conformations. For a broader view on the applications of MD in drug discovery, I recommend references (De Vivo et al., 2016; Salo-Ahen et al., 2020).

The combination of structure-based VS protocols with MD simulations have been successfully applied in the field of inflammation. In a first example, Dileep et al. conducted an *in silico* approach towards the development multi-target-directed ligands against phospholipase A2 (PLA2), lipoxygenase-5 (LOX-5) and COX-2 enzymes involved in the neuroinflammatory pathways. In this study, 67 hybrid molecules were designed by combining indole derivatives with selected NSAIDs, and 13 compounds, selected based on ADME and CNS-penetrant drug-like properties, were docked to the active site of the enzymes. Based on calculated binding energies, the hybrids were clustered into three groups and MD simulations totalling 5 ns were

employed to evaluate the binding stability of the three clusters. From this analysis, it was concluded that one cluster had a significant larger departure from the initial position with RMSD values higher than 4 Å and thus, was not considered for further studies. The authors finally selected one cluster harbouring three hybrid compounds, based on established protein-ligand interactions and better energy values compared to standard reference drugs, as promising neuroinflammatory modulators (Dileep et al., 2013).

The transient receptor potential vanilloid type 1 channel (TRPV1) has recently demonstrated to play an important role in in the neuro-immune axis, being expressed in microglia and astrocytes. Importantly, this channel is attracting a lot of attention for the modulation of neuroinflammatory responses (Kong et al., 2017). Feng et al. constructed 3D homology tetramer models for the TRPV1, using solved cryo-EM structures of rat TRPV1 as templates. MD simulation studies of 10 ns were performed on the three best homology models to retrieve the top 3 conformations of each model with the lowest energy. To select and validate the best model, a pre-screening was performed using a training set consisting of 10 TRPV1 active compounds and 990 compounds randomly selected from the National Cancer Institute (NCI) database. The best validated TRPV1 model was used for docking analyses to explore the binding modes of known agonists and antagonists. Tyr511, Thr550, Arg557, Glu570, and Leu670 were identified as key residues for the interaction. At this stage, 50 ns MD simulations were conducted to assess the conformational changes of TRPV1 upon antagonist/agonist binding, revealing an asymmetric interface between hTRPV1 monomers. Finally, a ligand-pharmacophore model was generated based on known antagonists and used to screen a library of 210,000 compounds from NCI, resulting in 15,672 compounds. From these, 38 compounds were selected for experimental testing based on docking score and pharmacophore fitness levels, yielding two promising hits with activity as TRPV1 antagonists (Feng et al., 2015).

1.3. Objectives of the Project

In recent years, harmful neuroinflammation has been increasingly recognized as a major factor involved in the onset and progression of several neurodegenerative and CNS disorders. The modulation of neuroinflammatory processes holds potential prospects for halting, or at least slowing down, the exacerbation of such disorders. The wide intent behind this project was the discovery of new compounds targeting molecules and pathways associated to the neurotoxic effects of uncontrolled pro-inflammatory microglial subtypes that prevail during harmful neuroinflammation, through the combination of state-of-the-art *in silico* and experimental testing methodologies. By modulating acute/chronic neuroinflammatory responses, considerable progress – in the sense of new alternative therapies – may be achieved for neurodegenerative disorders without effective treatment options.

As a means to discover novel neuroinflammatory modulators, the key objectives of this project were: 1) the characterization of putative neuroinflammatory targets with integration of structural dynamics (via MD) to extract insights on their druggability; 2) the discovery of new chemical entities able to modulate neuroinflammatory processes employing a multi-layered CNS-tailored virtual ligand screening approach; and 3) experimental validation of the predicted targets elucidated in (1), using *in vitro*/cell methods and experimental assays testing potential modulators discovered in (2).

From the viewpoint of the design of organic molecules to modulate neuroinflammation, IL-1R1 is both an appealing target and a challenging one. The wide range of intracellular events linked to IL-1R1 highlights this protein as a possible upstream regulator of neuroinflammatory networks and justifies consideration of IL-1R1 as a plausible therapeutic target for the modulation of neuroinflammation. Notably, while there is substantial body of research on IL-1R1, only sparse information is available in regard to small molecule ligands interacting with this protein. The availability of crystallographic structures of the IL-1R1 extracellular domain encouraged us to explore structure-based VS methods directed to the identification of compounds establishing optimal interactions within possible druggable cavities of IL-1R1. Coupled with an adequate *in vitro* model of human CHME3 microglia - together with the know-how extracted from several studies performed by Brites's lab on CHME3 microglial responses to inflammatory stimuli - the goals of this project were to evaluate the ability of the VS compounds in modulating the IL-1R1 signalling pathway in microglial cells stimulated with the pro-inflammatory cytokine IFN-γ. From the Medicinal Chemistry point of view, we aimed to identify promising candidate compounds to be used as modulators of pro-inflammatory microglial polarization and exuberant neuroinflammatory responses in pathological conditions.

PART II

In silico druggability analysis on IL-1R1: Predicting "hot" and "warm" spots for small molecule binding

"Codes are a puzzle. A game, just like any other game."

Alan Turing, in *The Imitation Game*

2.1. Introduction

The interleukin-receptor type 1 (IL-1R1) belongs to a superfamily of receptors with pivotal roles in the immune system. Excessive stimulation of IL-1R1 is associated with the pathogenesis of several disorders, such as Familial Mediterranean fever (FMF), rheumatoid arthritis, type 2 diabetes, cancer and neuroinflammation-associated CNS diseases (Dinarello et al., 2012). Structurally, protein-protein interactions in crystallographic structures of the extracellular domain of IL-1R1 (henceforth referred to as IL-1R1-ECD) have been evaluated in numerous studies and provided insight into the molecular mechanisms behind the interactions of IL-1R1 with their natural ligands (Krumm et al., 2014; Fields et al., 2019). Thus far, IL-1R1-ECD targeting therapeutics rely on monoclonal antibodies and peptides. Both have major limitations including, generally large molecular weight, difficult dosing frequency, no simple production and inconsistent or unfavourable pharmacokinetic (ADME) profiles. Within the neuroinflammatory context, these properties are even more relevant and thus, small molecule therapeutics represent a more versatile option, combining adequate drug-like properties (lower molecular weight, small polar surface area and lower hydrophilicity) with a potential BBB permeation.

In this chapter, one X-ray structure of the IL-1R1-ECD was selected upon structural quality evaluation and subjected to binding site prediction tools to detect potential pockets, or more broadly, any favourable regions (*hot-spots*) on the IL-1R1-ECD surface for interaction with small organic molecules. Yang provided the first hints on potential druggable binding sites in the IL-1R1-ECD surface (Yang, 2015), using the Schrödinger SiteMap algorithm (Halgren, 2009). Three different regions on the receptor surface were predicted to bind small molecules: (i) the interface between domains 1 (D1) and 2 (D2); (ii) the flexible linker between the Ig-like domains D2 and domain 3 (D3) and (iii) the interface region between the D1 and D3 when IL-1R1-ECD adopts a closed conformation. To add to the binding site analysis performed by Yang, we here pursuit the idea of combining multiple binding site prediction tools to obtain consensus but also different predictions, by combining their strengths and diluting their weaknesses. The motivation underlying such strategy was to infer from the crystallographic IL-1R1-ECD structure a comprehensive map of consistent predicted regions to bind small molecules toward the modulation of its biological function.

The results presented in this chapter are also the foundation of the work presented in Parts IV, V and VI of this thesis, where an integrated receptor-based virtual screening protocol targeting a putative IL-1R1 druggable binding site and respective *in vitro* experimental validation is performed - towards the discovery of small molecule modulators of IL-1R1 and related molecular networks.

2.1.1. Structural data on IL-1R1

Understanding the structural intricacies of IL-1R1 is pivotal not only to dissect general mechanisms of signal activation and inhibition via the IL-1 cytokines, but also to rationalize and predict feasible binding regions for the development of modulators. As of December 2021, a total of 5 crystal structures of protein complexes containing the IL-1R1-ECD could be found in the PDB (**Figure II.1**). Of these, four receptor-bound structures adopt an open conformation - PDB entries 1IRA (Schreuder et al., 1997), 1ITB (Vigers et al., 1997), 4DEP (Thomas et al., 2012) and 4GAF (Hou et al., 2013). The remaining structure corresponds to a closed conformation of IL-1R1 - PDB entry 1G0Y (Vigers et al., 2000).

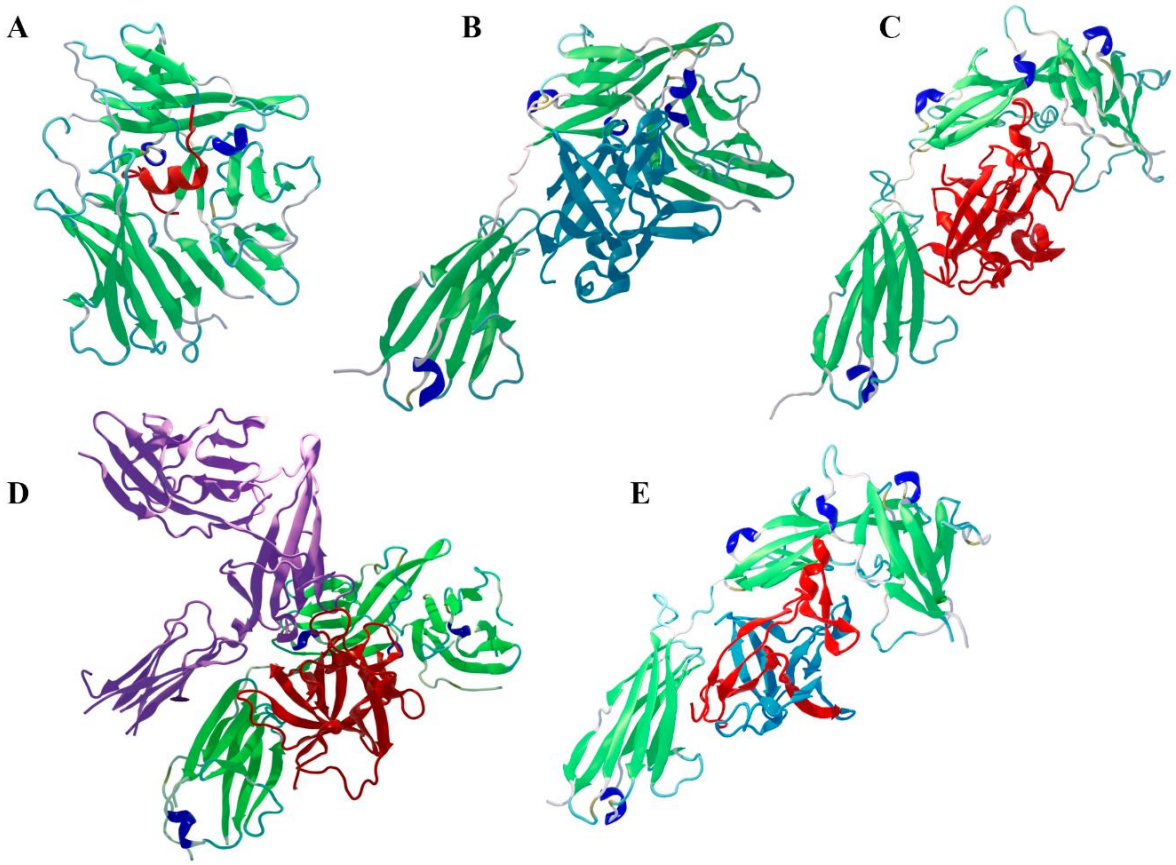

Figure II. 1 - Three-dimensional (3D) representations of the extracellular domain of interleukin-1 receptor type 1 (IL-1R1-ECD)-ligand bound complexes available in the PDB. X-ray structure of IL-1R1-ECD bound **(A)** to a small antagonist peptide AF10847 (coloured in red), adopting a closed conformation (PDB entry 1G0Y); **(B)** to interleukin-1 receptor antagonist (IL-1Ra, coloured in blue) (PDB entry 1IRA); **(C)** to interleukin-1β (IL-1β, coloured in red) (PDB entry 1ITB); **(D)** to IL-1β (coloured in red) and the receptor accessory protein (IL-1RAcP, coloured in purple) (PDB entry 4DEP); and **(E)** to EBI-005, a chimera of human IL-1β and IL-1Ra (coloured in blue and red) (PDB entry 4GAF).

Structurally, full-length IL-1R1 features an extracellular domain (ECD) containing three Ig-like domains (D1, D2 and D3), responsible for ligand recognition, a transmembrane (TM) α-helix

domain, and a cytoplasmic TIR domain responsible for initiating intracellular signalling. Vigers et al. reported the first crystallographic structure of the IL-1R1-ECD bound to IL-1β, solved at 2.5 Å resolution (PDB entry 1ITB) (Vigers et al., 1997). Importantly, these data provided a credible structural picture of the IL-1R1-ECD organization: i) D1 and D2 domains are tightly joint with a disulfide bridge that confers stability and structural rigidity to these domains, and ii) D3 domain is connected with a long and flexible linker to D2, which is able to move freely with respect to D1 and D2. The flexibility of this linker is crucial for positioning D3 for cytokine binding, allowing the formation of a stable complex and then recruitment of IL-1RAcP (Thomas et al., 2012). Structural alignment of the IL-1R1-ECD X-ray structures reveals structural differences in the D3 region, emphasizing the potential higher re-orientation ability of this domain when compared to the D1-D2 module. (**Figure II.2-A**). Interestingly, a structural complex of the IL-1R1-ECD with a small antagonist peptide is available (PDB entry 1G0Y), showing a 170° rotation of D3 relative to a reference D3 in the IL-1R1:IL-1β complex (PDB entry 1ITB), and thus exposing an unexpected binding mode for the peptide (**Figure II.2-B**) (Vigers et al., 2000). Recently, structural analyses employing a combination of small-angle X-ray scattering (SAXS) measurements with Molecular Dynamics (MD) simulations of the IL-1R1-ECD revealed an ensemble of closed conformations where D3 was also rotated, highlighting the role of this linker's flexibility-dependent function on two structurally similar IL-1R1 ectodomains – IL-1RAcP-ECD and IL-18Rβ-ECD (Ge et al., 2019).

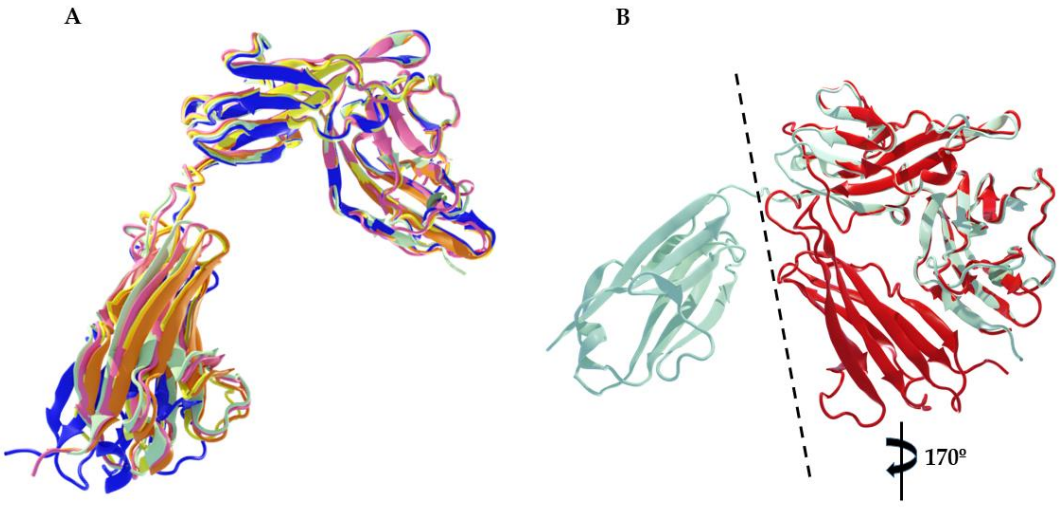

Figure II. 2 - (A) Structural alignment between the available open-bound conformations of the extracellular domain of interleukin-1 receptor type 1 (IL-1R1-ECD), revealing differences in the domain D3 (PDB entries: 1IRA, coloured in blue; 1ITB, coloured in pink; 4DEP chain B, coloured in orange; 4DEP chain E, coloured in yellow; 4GAF, coloured in grey); **(B) Rotation of the D3 in the closed-state** (PDB entry 1G0Y, coloured in red) **with respect to the IL-1R1-ECD open conformation** (PDB entry 4GAF, coloured in grey).

2.1.2. The IL-1R1 ectodomain surface: a look at key interactions

Fields et al. offered a remarkable analysis of the molecular mechanisms involving the IL-1 signalling complex formation (Fields et al., 2019). The IL-1R1-ECD adopts a question-mark-shaped architecture, forming two distinct binding regions, site A and B, which drive the interactions with IL-1 cytokines (**Figure II.3**). Site A of the receptor is located in the Ig-like D1 and D2 interface, while the D3 domain harbours site B. Site-directed mutagenesis of IL-1β revealed that three important residues, Arg11 (Gehrke et al., 1990), His30 (MacDonald et al., 1986) and Gln32 (Vigers et al., 1997), anchor the cytokine onto the receptor surface. The former two residues establish interactions with domain D2 of the IL-1R1-ECD - Phe111, Lys112, Gln113, Val124, Pro126 and Tyr127 – while the latter binds the D1-D2 interface – Ile14, Leu15, Val16, Gln108, Ala109, Ile110 and Phe111. Upon IL-1β binding, the contacts established at site B are essential to induce a conformational change in domain D3 of IL-1R1, further recruiting IL-1RAcP to initiate signal transduction (PDB entry 4DEP). In contrast, most of the interactions of antagonist IL-1Ra with IL-1R1 (PDB entry 1IRA) are established with domains D1 and D2, exhibiting only a few contacts with D3 (Schreuder et al., 1997). This binary complex is not able to recruit IL-1RAcP, pointing out that the D3 domain is fundamental for binding IL-1RAcP and consequently, required for signalling. Site-directed mutagenesis studies identified key residues at the IL-1Ra surface contributing to the strong binding interaction with IL-1R1-ECD - Trp-16, Gln-20, Tyr-34, Gln-36, and Tyr-147 (Evans et al., 1995). In a similar way to IL-1β, these residues establish contact mostly through a network of residues of the D1-D2 interface.

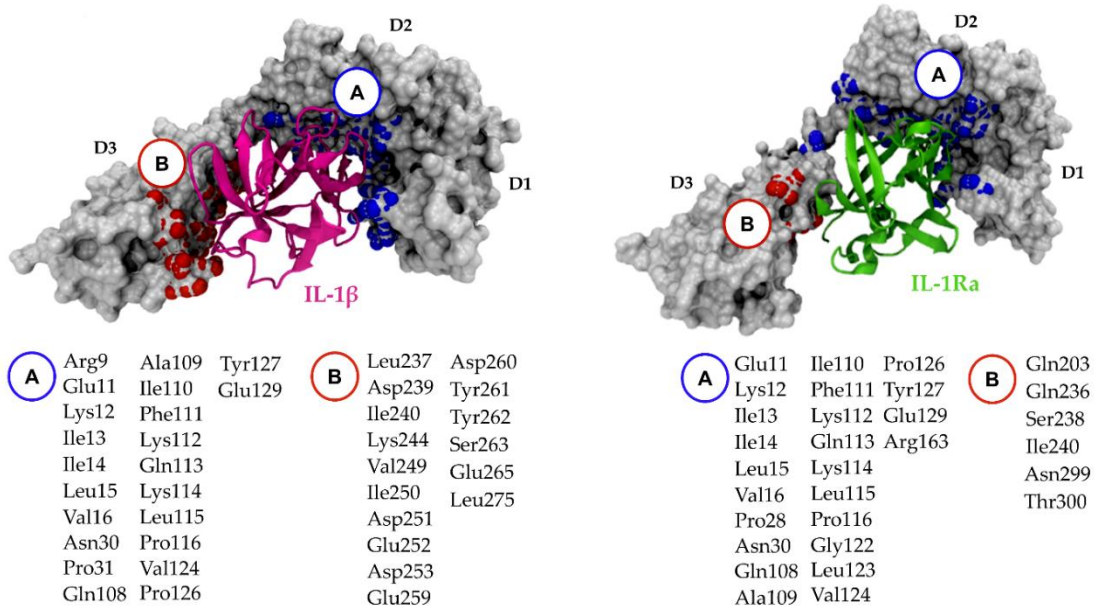

Figure II. 3 - Structures of the binary IL-1R1-ECD:IL-1β (PDB entry 1ITB) and IL-1R1-ECD:IL-1Ra (PDB entry 1IRA) complexes. In both panels, the IL-1R1-ECD is depicted in surface representation (gray), while IL-1β

(magenta) and IL-1Ra (lime) are shown in cartoon representations. The two binding regions are shown as spheres and coloured in blue (site A) and red (site B), respectively. Left panel: IL-1β interacts with the two sites on the receptor surface (IL-1R1-ECD residues involved are presented in blue and red). Right panel: IL-1Ra interacts mostly with site A (IL-1R1-ECD residues involved are presented in blue and red). *Figure abbreviations: IL-1β, interleukin-1β; IL-1R1-ECD, extracellular domain of IL-1R1; IL-1Ra, interleukin 1 receptor antagonist.*

The core residues of the IL-1R1 antagonist peptide (referred to as AF10847), complexed with the X-ray closed conformation of the IL-1R1-ECD (PDB entry 1G0Y), establish interactions at the D1-D2 interface, stabilizing the IL-1R1-ECD in a closed conformation. Within the core, Gln15 makes multiple hydrogen bonds with Val16 and Ala109, being essential for receptor binding (Vigers et al., 2000). Therefore, from a pharmacological point of view, the D1-D2 interface is a promising site for small molecule design because disrupting this interface could prevent cytokine binding (IL-1α and IL-1β) or stabilize the ectodomain in a closed conformation. Nonetheless, targeting the D3 domain may also represent a viable strategy, as small molecules can potentially impact on the relative orientation of this domain and further recruitment of IL-1RAcP. Pockets near both interfaces are thus good candidate sites for the development of small molecule therapeutics targeting IL-1R1.

2.1.3. Binding site prediction and analysis

A high-quality three-dimensional atomic structure of a target protein is a valuable resource to search for plausible binding sites for a putative ligand. The identification and characterization of potential binding sites represents the starting point for SBDD strategies. Typically, small molecule binding occurs inside pockets buried deep on the protein surface, allowing small molecules to establish strong physicochemical interactions. Usually, the identification of binding regions is relatively straightforward if small molecule binders have been discovered experimentally and/or the protein-ligand 3D complex structure is available. However, if only the apo structure of the target protein is on-hand, computational tools can be employed to predict surface pockets endowed with appropriate sizes, shapes and physicochemical properties to accommodate a complementary small molecule. These methods can be roughly divided into geometric, energy-based, sequence-based and structure-based similarity, machine learning and MD approaches (Simões et al., 2017; Zhao et al., 2020). **Table II.1** lists some of the most widely used computational methods for binding site prediction.

Table II. 1 - Representative examples of commonly employed binding site prediction methods.

Geometric methods			
Algorithm	**Type**	**Pocket descriptors**	**Reference**
DoGSiteScorer	Grid-based	Volume, shape, hydrophobicity (out of 40 descriptors)	(Volkamer et al., 2012b)
LIGSITE^{CSC}		Volume, surface area	(Huang and Schroeder, 2006)
DLID		Hydrophobicity, volume and buriedness	(Sheridan et al., 2010)
SiteMap	Grid and energy-based	Solvent accessible surface, exposure, hydrophobicity, volume and size	(Halgren, 2009)
SURFNET	Sphere-based	Shape	(Laskowski, 1995)
CASTp		Volume, surface area	(Liang et al., 1998; Tian et al., 2018)
Fpocket	Tessellation-based	Volume, solvent accessible surface, hydrophobicity, polarity	(Le Guilloux et al., 2009)
Energy-based methods			
Algorithm	**Type**	**Pocket descriptors**	**Reference**
GRID	Probe-based	Noncovalent contacts between probes and amino acids	(Goodford, 1985)
Q-SiteFinder			(Laurie and Jackson, 2005)
FTMap			(Ngan et al., 2012)
Sequence-based and structure-based similarity methods			
Algorithm	**Type**	**Pocket descriptors**	**Reference**
ConSurf	Evolutionary sequence conservation	Conserved amino acids in functional regions	(Glaser et al., 2003)
FINDSITE	3D template-based	Binding site similarity with proteins complexed with a ligand	(Brylinski and Skolnick, 2008)
Machine-learning methods			
Algorithm	**Type**	**Pocket descriptors**	**Reference**
DeepSite	Convolutional neural network	Physicochemical features of the protein atoms	(Jiménez et al., 2017)
P2Rank	Random Forests	Solvent accessible surface, physicochemical features	(Krivák and Hoksza, 2018)
MD-based methods			
Algorithm	**Type**	**Pocket descriptors**	**Reference**
MDPocket (extension of Fpocket)	Tessellation-based	Volume, solvent accessible surface, hydrophobicity, polarity	(Schmidtke et al., 2011)
trj_cavity	3D voxelized Grid-based	Volume	(Paramo et al., 2014)

The basic principles behind the geometric approaches rests on the assumption that binding regions for ligands are usually clefts or cavities in a protein. As such, these methods scan the 3D protein structure for the identification of pockets optimal in size and/or shape for small molecule binding. In general lines, geometric approaches fall into three main categories:

1. Grid-based algorithms: the main idea consists on embedding the protein within a 3D grid. A grid point is assigned either as part of the protein (if within particular geometric distance from an atom center), otherwise as solvent. These points are categorized as "pocket points" depending on geometric criteria such as *distance*, *solvent accessibility* and *depth.*
2. Sphere-based algorithms: this approach places sphere probes of radius *r* between the non-hydrogen protein atoms, reducing such radius if they intersect with any neighbouring atoms (pockets defined by the union of overlapping spheres).
3. Tessellation-based algorithms: based on the concept of α-shape proposed by Edelsbrunner and Mücke for computing the 3D structure of a given set of points in 3D space based on the Delaunay triangulation (Edelsbrunner and Mücke, 1994).

Energy-based methods detect pockets by computing non-bonded interaction energies between protein atoms and chemical probes. To do so, automated blind fragment-based docking is performed on the entire protein surface, where the contributions of electrostatic, van der Waals, hydrogen bonds, hydrophobic and solvent terms are evaluated. Basically, small molecule binding sites are determined to be at regions with the most favourable interaction energies between a molecular target structure and chemical probes. Consensus binding sites represent regions at which several probe molecules cluster (Henrich et al., 2009).

Sequence-based or evolutionary methods are based on the premise that proteins with distant phylogenetic relationships may have conserved sequence regions leading to similar *hot-spots* and/or binding of similar small molecules. On the other hand, when considering available 3D structural information on proteins, structure-based similarity methods may be used to draw binding site comparisons based on known binding regions. In recent years, the increasing amount of data concerning small molecule binding sites has led to the development of several machine learning algorithms. The strength of these methods rely on their ability of to "learn" patterns of (i) complex specific molecular interactions between ligands and molecular target, such as hydrogen bonds, hydrophobic contacts or pharmacophoric features; (ii) 3D structural features such as solvent accessible surface area or volume/depth; and (iii) the amino acid sequence (Fuller et al., 2009; Xie and Hwang, 2015; Zhao et al., 2020).

Molecular dynamics simulations are often employed to explore beyond the static experimental protein representations to identify prospective transient pockets that become apparent during conformational changes. In addition, MD can be used to study and characterize the dynamic

evolution of a binding pocket of interest during a simulation timescale (Feng and Barakat, 2018). Indeed, changes in pocket descriptors, such as shape, volume, hydrophobicity and other relevant physicochemical features, which may arise due to protein internal flexibility, can be assessed with these methods.

Importantly, all pocket detection methods have their own pros and cons with no individual method being the *magic bullet*. With this in mind, we used three open-access binding site prediction methods, i.e., DoGSiteScorer (Volkamer et al., 2012b), FTMap (Ngan et al., 2012) and Fpocket (Le Guilloux et al., 2009) to assess the IL-1R1-ECD structure for potential small molecule binding sites suitable for receptor-based drug-design strategies. The selection of these methods was based on two primary factors. First, the accessibility of the tools employed as open-source software, providing source code or a web-server for running the program, and where data is made available and can be visualized using other open-source software. Secondly, the utilisation of previous benchmark (or test) datasets to assess and compare the performance of the prediction methods, revealing overall good performances (Chen et al., 2011; Volkamer et al., 2012a; Wakefield et al., 2020).

2.2. Computational Methods

The following subsections detail the computational methods employed to evaluate the structural quality of the IL-1R1-ECD crystallographic structures available in the PDB and to predict potential binding pockets in the IL-1R1-ECD surface. The BlendMol plugin (Durrant, 2019) was used to produce high quality images of IL-1R1 structures from imported VMD visualization states (Humphrey et al., 1996) using the Blender software, an open-source 3D modelling and rendering program (Kent, 2015).

2.2.1. Structure quality evaluation

When selecting a 3D structure for SBDD programs, the experimental accuracy of the initial structural data is a critical factor that may impact the performance of these methodologies. The quality (accuracy) of a crystal structure is described by the resolution and the R-value. The first is a global number expressing the average uncertainty of all atoms in the structure, with high numbers corresponding to low resolution and vice-versa. The R-value expresses the level of agreement between the experimental observations and the structure factors predicted from the final structure. If the R-value is low (typically less than 20%) then the structure is most likely to be correct. Undoubtedly, any structural model, irrespective of it has been determined by experimental techniques or is purely computational, is prone to errors. These span from small atomic clashes, incorrect side-chain conformations, badly modelled flexible loops, wrongly placed water molecules to incomplete or totally inaccurate structural models (Joosten

et al., 2011; Read et al., 2011). In this work, we used the PROCHECK (Laskowski et al., 1993) software and ProSA-web server (Wiederstein and Sippl, 2007) to evaluate the structural quality of the IL-1R1-ECD X-ray structures deposited in the PDB (**Table II.2**), and select one structure to predict and characterize binding sites. PROCHECK provides a detailed residue-by-residue assessment of their geometries, comparing the overall quality of the structure to that of high-quality experimental structures with similar resolution. Reliable models are expected to have more than 90% of amino acid residues in most favoured and additional allowed regions. The G-factor, which is calculated by PROCHECK, is a measurement of how unusual the structure is - G-factor values below −0.5 are unusual. The results of PROCHECK analysis are represented on a graphical Ramachandran plot endowed with information about the backbone dihedral angles psi (Φ) against phi (Ψ) distribution of the amino acid residues. The ProSA algorithm measures structure quality and energy profiles in terms of a *Z*-score.

Table II. 2 - X-Ray crystallographic structures of IL-1R1 deposited at the Protein Data Bank (as of Dec. 2021).

PDB entry	Resolution (Å)	R-value (work)	Pub year	Description
1G0Y	3.00	0.223	2000	IL-1R1 complexed with antagonist peptide AF10847
1IRA	2.70	0.213	1997	IL-1R1 complexed with IL-1Ra
1ITB	2.50	0.229	1997	IL-1R1 complexed with IL-1β
4DEP 2 chains	3.10	0.210	2012	IL-1R1 complexed with IL-1β and IL-1RAcP
4GAF	2.15	0.215	2013	IL-1R1 complexed EBI-005, a chimera of human IL-1β and IL-1Ra

Table abbreviations: Interleukin receptor type-1 (IL-1R1); interleukin-1β (IL-1β); interleukin-1 receptor antagonist (IL-1Ra); interleukin-1 receptor accessory protein (IL-1RAcP).

The criteria applied to select a relevant IL-1R1-ECD crystal structure from the PDB was based on the following: (i) resolution ≤ 2.5 Å; (ii) an R-value ≤ 0.25; and (iii) good quality structure revealed by the Ramachandran plot and ProSA-web based *Z*-score analysis.

2.2.2. *Hot-spot* detection

Hot-spot analysis and druggability assessments were performed using a combination of three computational methods – DoGSiteScorer (Volkamer et al., 2012b), FTMap (Ngan et al., 2012) and Fpocket (Le Guilloux et al., 2009) - to comprehensively predict ligand binding pockets and their respective druggability scores on the IL-1R1-ECD surface.

DoGSiteScorer is an existing freely available implementation of a support-vector machine (SVM) which uses a Difference of Gaussian filter to learn from 3D protein structures and detect binding pockets and sub-pockets holding high likelihood of attracting and accommodating a drug-like ligand. This grid-based method calculates multiple geometrical properties, including pocket volume, size, shape and depth, as well as physicochemical features hydrogen bond acceptors and donors, amino acid composition and hydrophobicity ratio, for the predicted pockets. For druggability predictions, a subset of the above-referenced descriptors is incorporated into the SVM model, trained and tested on a non-redundant druggable dataset (Schmidtke and Barril, 2010). A simple druggability score (with values varying between 0 and 1) is output for each pocket and respective sub-pockets. The higher the score the higher the likelihood of the pocket being druggable. (Volkamer et al., 2012a).

FTMap performs rigid based docking of 16 probe-type molecules of varying size, shape, and polarity (ethanol, isopropanol, isobutanol, acetone, acetaldehyde, dimethyl ether, cyclohexane, ethane, acetonitrile, urea, methylamine, phenol, benzaldehyde, benzene, acetamide and N,N-dimethylformamide) using a Fast Fourier Transform (FFT) correlation approach, followed by energy minimization, rescoring and clustering. Probe clusters are ranked on the basis of their Boltzmann averaged energies and 6 clusters are retained per probe. Clusters of different probes are clustered using the distance between the centres of mass of the cluster centres to determine the so-called *hot spots*. The regions of the protein surface where the clusters of different probes overlap are more likely to be suitable binding sites, and the largest of overlapping areas are considered the main *hot-spots* (Kozakov et al., 2015).

Fpocket is an open-source geometric tool employing the concepts of Voronoi tessellation and α-spheres. Voronoi tessellation is a numerical algorithm to divide a 3D spatial domain into completely interlocking cells (Voronoi, 1908), where the α-sphere centers define the vertices of this tessellation. The α-spheres contact four atoms at an equal distance and do not contain any atoms. The spatial organization of the protein surface and their shape influence the radius of the α-spheres. This means that buried protein regions would be filled with numerous small spheres compared with large spheres at the outer surface, while clefts or cavities result in α-spheres of intermediate radius. These are then clustered to identify potential binding sites. At this stage, α-spheres are filtered by radius to remove the ones deemed too small to represent solvent accessible space (default parameters in Fpocket: minimum α-sphere radius - 3 Å; maximum α-sphere radius - 6 Å). The set of descriptors provided by this algorithm is related to: (i) α-spheres (number, density, polarity, radius); ii) physicochemical properties (solvent-accessible surface area, hydrophobicity, polarity, charge) and iii) geometric properties (volume and flexibility). Furthermore, Fpocket provides a druggability score between 0 and 1, where a lower score implies that small molecules are not likely to bind to the cavity and values higher than 0.5 indicate a potential druggable binding sites (Le Guilloux et al., 2009).

2.3. Results and Discussion

In this section, structural quality evaluations are presented for the available IL-1R1-ECD structures deposited in the PDB. Druggability analyses were performed to determine possible *hot-spots* on the receptor surface. Prior to applying the mapping procedures, the co-crystallized ligands and water molecules in the IL-1R1-ECD X-ray representations were removed. Druggability mapping was conducted with the DoGSiteScorer, FTMap and Fpocket algorithms.

2.3.1. Structural quality evaluation

All the IL-1R1-ECD X-ray structures retrieved from the PDB were subjected to structural quality evaluations with PROCHECK and ProSA-web server. The Ramachandran plot analysis obtained by PROCHECK and the *Z*-score determined by the ProSA-web server are depicted in **Table II.3** and the plots are provided in Figure **A-1** and **A-2** of the Appendix, respectively. Overall, the quality of the six IL-1R1-ECD structures is acceptable, where most of the backbone phi and chi angles are present ≥95% in most favoured and allowed regions. However, it is worth mentioning that PDB entry 1G0Y holds less than 80% in most favoured regions with 1.4% of residues holding phi/chi angles in the outlier region. In all Ramachandran plots, this disallowed region is populated by Lys161. This residue is located in a tight loop turn connecting two β-sheets, at the D2 surface. The overall G-factor values of the IL-1R1-ECD X-ray structures are lower than -0.5, highlighting the reliable stereochemical quality of the structures. The ProSA results showed *Z*-scores between -5.5 and -7.9, indicating no significant deviation from experimentally determined protein structures of similar lengths.

Table II. 3 - Ramachandran plot statistics and ProSA-web *Z*-score for the IL-1R1-ECD X-ray structures.

X-ray structure	Ramachandran plot[1]					ProSA-web Z-score
	Most favoured regions	Additional allowed regions	Generously allowed regions	Disallowed regions	G-factor	
1G0Y	213 (76.9%)	50 (18.1%)	10 (3.6%)	4 (1.4%)	0.1	-7.60
1IRA	249 (89.6%)	26 (9.4%)	1 (0.4%)	2 (0.7%)	-0.1	-7.89
1ITB	223 (80.5%)	46 (16.6%)	6 (2.2%)	2 (0.7%)	-0.1	-7.33
4DEP-chain B	232 (88.9%)	22 (8.4%)	5 (1.9%)	2 (0.8%)	-0.2	-5.56
4DEP-chain E	241 (88.3%)	28 (10.3%)	2 (0.7%)	2 (0.7%)	-0.1	-7.02
4GAF	240 (88.2%)	27 (9.9%)	4 (1.5%)	1 (0.4%)	-0.1	-6.84

[1] *distribution of non-glycine and non-proline residues in the Ramachandran plot; Total number of non-glycine and non-proline residues: 277 (1GOY); 278 (1IRA); 277 (1ITB); 261 (4DEP chain B); 273 (4DEP chain E); 272 (4GAF).*

Guided by these results, alongside the global indicators of X-ray data quality – resolution and R-factor - the selection of a suitable IL-1R1-ECD X-ray structure for further studies fell upon the IL-1R1-ECD structure in complex with chimeric antagonist EBI-005. This structure holds highest structural resolution (2.15 Å) than the other IL-1R1-ECD crystallographic structures, suitable R-values and reliable Ramachandran and *Z*-plots.

2.3.2. Putative IL-1R1 druggable binding sites

The binding site architecture is a critical facet in molecular recognition. The average volume of a putative cavity favourable to bind small molecules is estimated to be between 100 and 1000 $Å^3$ (Liang et al., 1998; Pérot et al., 2010). Besides the volume, the ability of binding sites to be complementary with small molecules rely on their shape, structural flexibility, and physicochemical properties, such as hydrogen bonding and hydrophobic effects, and thus not all proper-sized pockets are druggable. Accordingly, the utility of binding site prediction programs is mainly determined by their ability to recognize and prioritize such regions suitable for interactions with molecules that may be optimized into a therapeutic drug candidate.

Herein, binding site analyses were performed on the crystallographic open conformation of the IL-1R1-ECD at the best available resolution of 2.15 Å (PDB entry 4GAF). For the sake of comparison, additional druggability analyses were performed also on the available closed conformation of the IL-1R1-ECD (PDB entry 1G0Y), despite the high resolution of 3.00 Å. The druggability of the two crystallographic IL-1R1-ECD structures was first assessed using the DoGSiteScorer tool. **Table II.4** presents the druggability scores and calculated descriptors for the major cavities identified on the IL-1R1-ECD open conformation (**Figure II.4-A**). According to the analysis, there are 10 identified potential binding pockets within the open conformation of the IL-1R1-ECD (pockets referred as Po). Three pockets Po_0, Po_1 and Po_2 show druggability higher than 0.70, large pocket volume, high depth as well as adequate hydrophobicity ratio, suggesting that there is a high chance of binding small molecules in those regions. In particular, the two predicted pockets Po_0 and Po_1 overlap with residues that are critical for ligand binding (see sub-section 2.1.2.), whereas Po_1 is positioned near the D3 domain. The decomposition of the largest predicted pocket (Po_0) to its sub-pockets (**Figure II.4-B**), reveals three buried regions Po_0_0, Po_0_1, Po_0_6 close to each other, with druggability scores of 0.54, 0.52 and 0.68, respectively. The residues lining these sub-pockets are:

- Po_0_0: Leu15, Val16, Ser17, Ser18, Glu21, Asp23, Val24, Arg25, Pro26, Ala69, Cys104, Tyr105, Asn106, Ala109, Phe111, Pro126, Tyr127, Met128, Glu129, Phe130, Phe131, His180, Ile192, Thr193, Arg194 and Val195;

- Po_0_1: Glu11, Ile13, Ile14, Leu15, Arg25, Pro26, Pro28, Trp40, Ile92 and Tyr127;
- Po_0_6: Arg25, Trp40, Leu64, Phe66, Tyr77, Ile92, Ser93, Ala94 and Phe96.

These buried sub-pockets present volumes that seem appropriate for ligand binding and are surrounded by other smaller pockets, suggesting that the D1-D2 interface may be suitable for targeting by small molecule and even for fragment-based approaches. Additionally, the presence of Po_2, presenting the highest druggability score of 0.84, in the vicinity of Po_0 is a good indicator for the D1-D2 interface as an appealing binding site for small molecule therapeutics. Interestingly, a similar large binding pocket (volume of 1013.76 Å^3), as the one located at the D1-D2 interface (Po_0), is also identified in the IL-1R1-ECD closed conformation (pockets referred as Pc) (see **Figure A-3** and **Table A.1** of the Appendix). Essentially, similar pocket-lining residues and evidence of a suitable degree of hydrophobicity constitute this predicted site (Pc_1), highlighting that a potential hydrophobic small ligand candidate could bind to these pockets. Because the AF10847 peptide stabilizes IL-1R1-ECD in a closed conformation, the involvement of some of these residues in the binding of this peptide - Val16, Arg25, Ala109, Phe111, Tyr127, Glu129, Phe130 - suggests that small molecules bound in this region/sub-pockets may result in stabilization of the IL-1R1-ECD in a closed configuration.

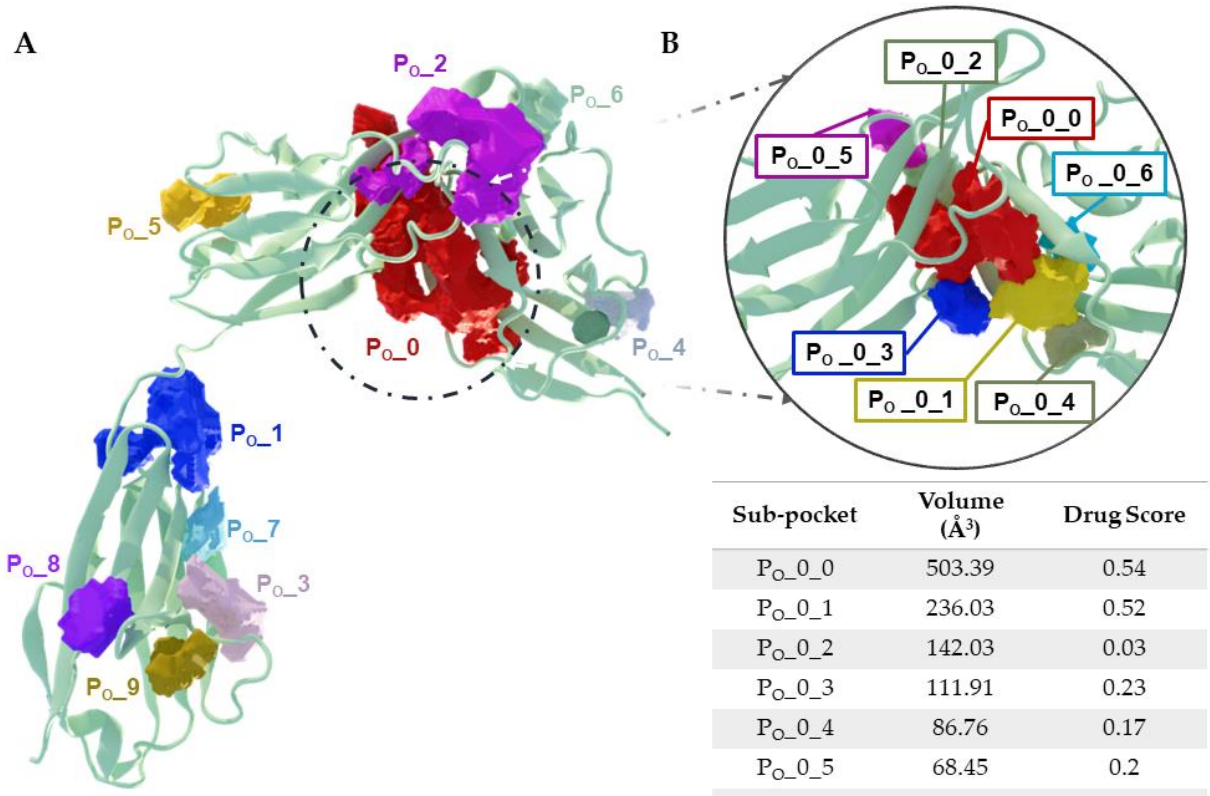

Sub-pocket	Volume (Å^3)	Drug Score
Po_0_0	503.39	0.54
Po_0_1	236.03	0.52
Po_0_2	142.03	0.03
Po_0_3	111.91	0.23
Po_0_4	86.76	0.17
Po_0_5	68.45	0.2
Po_0_6	61.22	0,68

Figure II. 4 - Binding pocket prediction on the extracellular domain of interleukin-1 receptor type 1 (PDB entry 4GAF), using the DoGSiteScorer tool. **(A)** Ten binding pockets are shown: Po_0 (red); Po_1 (blue); Po_2 (purple); Po_3 (mauve); Po_4 (dark grey); Po_5 (yellow); Po_6 (green); Po_7 (cyan); Po_8 (violet); Po_9 (brown). **(B)** The sub-

pockets composing Po_0 are illustrated in detail, with respective volume and druggability scores. Seven sub-pockets are shown: Po_0_0 (red); Po_0_1 (yellow); Po_0_2 (lime); Po_0_3 (blue); Po_0_4 (green); Po_0_5 (purple); Po_0_6 (cyan).

Table II. 4 - Predicted pockets by DoGSiteScorer on the IL-1R1-ECD surface (PDB entry 4GAF).

Pocket	Volume (Å^3)	Surface (Å^2)	Depth (Å)	Nº residues	Hydrophobicity ratio	HBA /HBD	Drug Score
Po_0	1209.78	1641.79	26.31	55	0.37	86/28	0.82
Po_1	575.29	1161.23	15.32	25	0.36	48/27	0.71
Po_2	490.77	605.27	22.21	27	0.38	29/16	0.84
Po_3	191.44	398.74	11.78	10	0.51	18/4	0.43
Po_4	179.47	464.04	9.93	9	0.42	20/11	0.29
Po_5	159.15	384.20	12.30	10	0.44	14/10	0.42
Po_6	144.36	446.18	8.91	11	0.58	16/6	0.27
Po_7	128.54	225.34	8.65	11	0.31	18/4	0.26
Po_8	122.51	218.92	8.29	10	0.44	6/8	0.24
Po_9	110.54	276.53	6.81	10	0.33	12/8	0.18

Table abbreviations: Hydrogen bond acceptors and hydrogen bond donors (HBA/HBD).

The second top-ranked binding site Po_1, with a volume of 575.29 Å^3, a surface area of 1161.23 Å^2 and a druggability score of 0.71, features residues of the flexible linker between D2 and D3, as well as D3 residues. Interestingly, substantial differences are found in the closed IL-1R1-ECD conformation. Indeed, the pocket volume, surface and depth are nearly doubled (1288.51 Å^3, 2094.76 Å^2 and 28.36 Å, respectively) when comparing the open and the closed conformation. Moreover, the druggability score increased to 0.81, indicating that this cavity should be able to harbour small molecule ligands. From the mechanistic standpoint, the conformational transition to a closed state may result in more stabilizing interactions, the domains pack close to one another, increasing the total hydrophobic surface, forming a more expanded binding pocket. Interestingly, the 170° rotational motion of the D3 in the closed conformation causes Po_8, which was predicted undruggable in the open conformation, to form an enclosed and druggable cleft (Pc_2) at the D1-D3 interface. Similarly, to the AF10847 peptide, small molecules binding at the interface between the D1 and D3 domains may stabilize the IL-1R1-ECD in a closed conformation. Of note, both Po_0 and Po_1 and Pc_2 binding sites are in line with the predictions performed by Yang (Yang, 2015).

The druggability of the IL-1R1-ECD was further assessed using FTMap. In this energy-based method, the number of clusters of multiple probe types in a potential binding site determines the druggability of that site. In fact, a particular region is considered druggable if it binds at least 16 probe clusters (consensus site, CS) and bears at least one additional *hot-spot* nearby. Druggability mapping predicted three key *hot-spots* (**Figure II.5 and Table II.5**). Of these, the largest consensus site (CS1o) binds 20 probe clusters, whereas CS2o and CS3o present 17 and 16 probe clusters, respectively. Visual analysis reveals that CS1o is located in the D3 region

(overlaps with P$_o$_8 identified by DogSiteScorer). CS2$_o$ and CS3$_o$ are key *hot-spots* found near each other, located at the D1-D2 interface, respectively, and are positioned close to a secondary *hot-spot* harbouring 14 probes (*hs*4$_o$) and two smaller binding 2 probes (*hs*7$_o$ and *hs*8$_o$). More importantly, both CS2$_o$ and CS3$_o$ overlap with the DogSiteScorer mapping analysis at this interface, highlighting this region of the IL-1R1-ECD as a potential druggable binding site for small molecules.

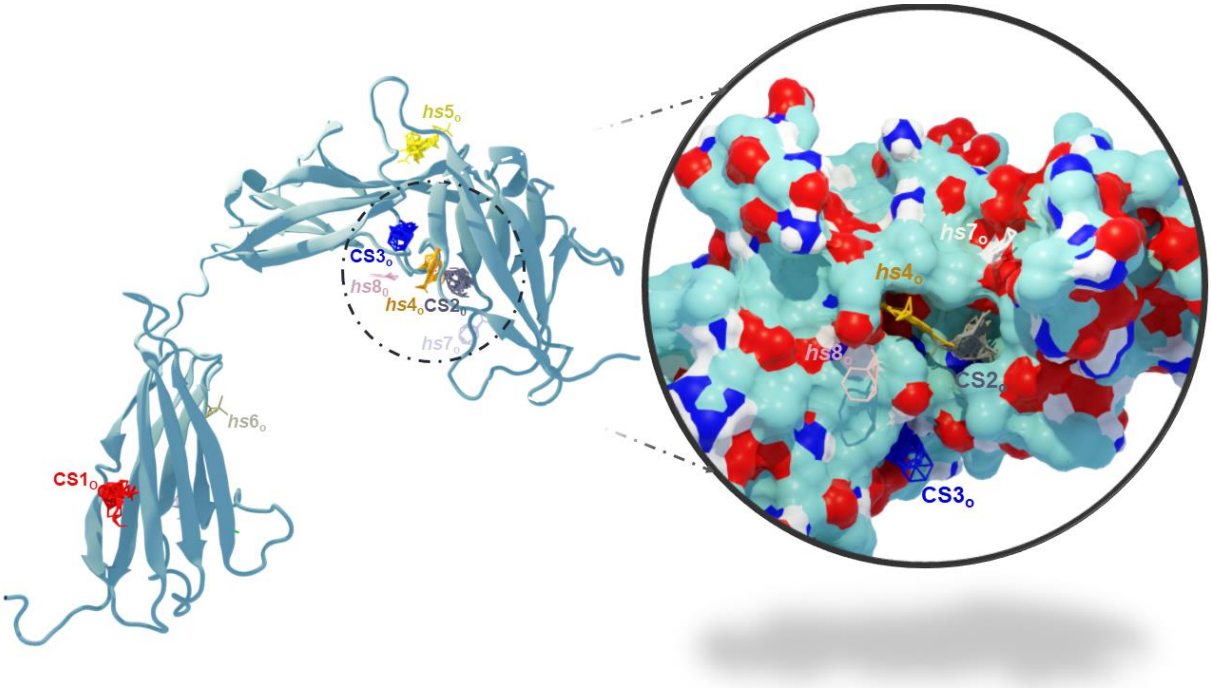

Figure II. 5 - Binding pocket prediction and druggability assessment on the extracellular domain of interleukin-1 receptor type 1 (PDB entry 4GAF), using the FTMap tool. The D1-D2 surface representation enclosed by the black line is illustrated in detail. Eight binding *hot-spots* are shown: CS1$_o$ (red); CS2$_o$ (dark grey); CS3$_o$ (blue); *hs*4$_o$ (orange); *hs*5$_o$ (yellow); *hs*6$_o$ (light grey); *hs*7$_o$ (silver) and *hs*8$_o$ (mauve). Consensus sites (CS) denote regions binding 16 or more probes. *Hot-spots* (*hs*) denote regions binding less than 15 probes.

Table II. 5 - Summary of FTMap druggability mapping results on the IL-1R1-ECD surface (PDB entry 4GAF).

Hot-spot	**Probe clusters**	**Probe composition**	**Key IL-1R1-ECD residues**
CS1$_o$	20	ACD, ACN, ACT, ADY, AMN, BDY, BEN, BUT, CHX, DFO, DME, ETH, EOL, PHN, THS, URE	Ser213, Pro214, Glu217, Leu229, Ile230, Trp243, Ile308
CS2$_o$	17	ACD, ACN, ACT, ADY, AMN, BDY, BEN, BUT, CHX, DFO, DME, ETH, EOL, PHN, THS, URE	Glu11, Ile13, Leu15, Arg25, Pro26, Pro28, Ile92, Tyr127
CS3$_o$	16	ACD, ACN, ACT, ADY, AMN, BDY, BEN, BUT, CHX, DFO, DME, ETH, EOL, PHN, THS, URE	Ile14, Val16, Ser18, Gln108, Ala109, Phe111, Lys112,
*hs*4$_o$	14	ACN, ACT, ADY, BDY, BEN, DFO, DME, ETH, EOL, PHN, THS, URE	Leu15, Asp23, Val24, Arg25, Tyr127, Glu129, Phe130
*hs*5$_o$	12	ACD, AMN, BUT, DFO, EOL, PHN, THS, URE	Ser18, Asn20, Glu21, Asn99, Pro191, Thr193
*hs*6$_o$	3	ACT, BEN, BUT	Val233 ,Tyr261, Leu275, Thr277

*hs*7o	2	BDY, CHX	Cy27, Leu29, Pro31, Glu62
*hs*8o	2	DME, PHN	Gln113, Val124, Pro126, Tyr127, Glu129

Table abbreviations: acetamide (ACD), acetonitrile (ACN), acetone (ACT), acetaldehyde (ADY), methylamine (AMN), benzaldehyde (BDY), benzene (BEN), isobutanol (BUT), cyclohexane (CHX), N,N-dimethylformamide (DFO), dimethyl ether (DME), ethane (ETH), ethanol (EOL), phenol (PHN), isopropanol (THS), urea (URE).

Figure II.6 depicts the distribution of non-bonded and hydrogen bonding interactions between probes and the IL-1R1-ECD residues. Key residues participating in non-bonded interactions are Ile13 (5,6%), Ile14 (5,6%), Leu15 (6,1%), Val16 (4,2%), Arg25 (7,3%), Pro26 (7,7%), Phe111 (4,9%), Tyr127 (5,2%), Leu229 (5,2%) and Ile230 (4,2%). Hydrogen bonding is mainly established with Ile14 (5,3%), Val16 (22,6%), Glu21 (4,1%), Arg25 (4,7%), Pro26 (8,2%), Glu129 (5,4%), Ser213 (5,3%) and Ile230 (15,6%). It is interesting to notice that most of these residues belong to the D1-D2 interface, emphasizing that this region is lined by key amino acids that may complement the molecular structure of small molecules to form aromatic, electrostatic, and hydrogen bonds.

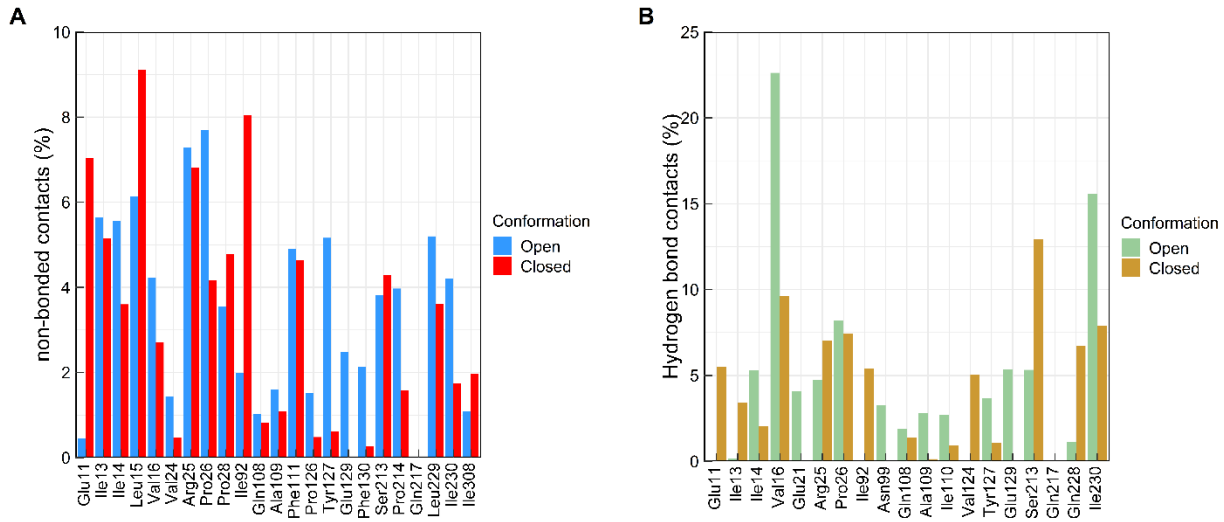

Figure II. 6 - Intermolecular (A) non-bonded and (B) hydrogen bond interactions between probes and residues for the open and closed conformations of the extracellular domain of interleukin-1 receptor type 1.

When similarly examined for the number of bound probes, the IL-1R1-ECD closed conformation (PDB entry 1G0Y) present a similar consensus site (CS1c) to that of CS2o at the D1-D2 interface of the open conformation, while the region (*hs*5c) equivalent to CS3o is populated by 11 probe clusters (see **Figure A-4** and **Table A.2** of the Appendix). Likewise, these binding sites are surrounded by smaller secondary *hot-spots* that are important for ligand binding. A similar observation to that of Po_8 of DogSiteScorer can be made for the largest *hot-spot*, CS1o, predicted in the open conformation. Upon open-to-closed conformational transition and respective D3 structural rearrangements, the establishment of D1-D3 interactions reshapes this consensus site into two highly populated *hot-spots* binding 14 probe

clusters each (*hs*3C and *hs*4C in the closed-state). Residues Arg9, Glu11, Pro28, Leu29, Asn30, Ile90, Ser213, Pro214, Ala215, Glu217, Met219, Val221, Ile227, Gln228, Leu229, Ile230 and Ile308 form this binding region at the D1-D3 interface. The conformational transition may also explain the new consensus site formed in the D2 region, potentially favouring the exposure of this binding site.

Finally, for comparing the results obtained with the other two binding site prediction algorithms, Fpocket was also employed to scan the entire IL-1R1-ECD surface for potential small molecule binding sites. **Figure II.7** illustrates the predicted pockets and **Table II.6** presents the calculated descriptors obtained using the Fpocket software package. For the IL-1R1-ECD open conformation, 13 pockets were identified, revealing one particular pocket (P1O) located in the D3 with a druggability score 0.717. This pocket is located in a region where both DogSiteScorer (pocket PO_7) and FTMap (*hot-spot hs*6O) also assigned a potential binding site, but, in this case, characterized by low druggability profiles. In the closed conformation (see **Figure A-5** and **Table A-3** of the Appendix), this binding region is predicted undruggable (P10C). It is worth noticing, that the D1-D3 interface is populated with a considerable pocket (P9C) with a volume of 481.16Å^3, but yet, not predicted druggable.

Surprisingly, all the predicted small molecule binding sites at the D1 and D2 regions (P2O, P3O, P5O, P6O, P7O, P10O, P11O, P12O and P13O) exhibit low druggability scores. Some of these pockets (P2O, P6O and P13O) overlap with the predictions made by both DogSiteScorer and FTMap at the D1-D2 interface. Notwithstanding, in the closed conformation Fpocket mapping yields a considerable larger pocket in the D1-D2 interface, presenting a druggability score of 0.997 (P1C). This pocket comprises the residues Glu11, Ile13, Leu15, Val16, Ser17, Ser18, Asp23, Val24, Arg25, Pro26, Pro28, Ile92, Tyr105, Asn106, Ala109, Phe111, Tyr127, Glu129, Phe130, Phe131, Thr193, Arg194 and Val195, which form the pockets P2O, P6O and P13O in the open conformation. We argue that while in the closed structure this interface is more shielded from the solvent, and consequently more hydrophobic than that of the open conformation of the IL-1R1-ECD, which results in increased predicted druggability. In contrast, in the open conformation these cavities are more exposed to the solvent, which may explain the lower druggability computed by Fpocket.

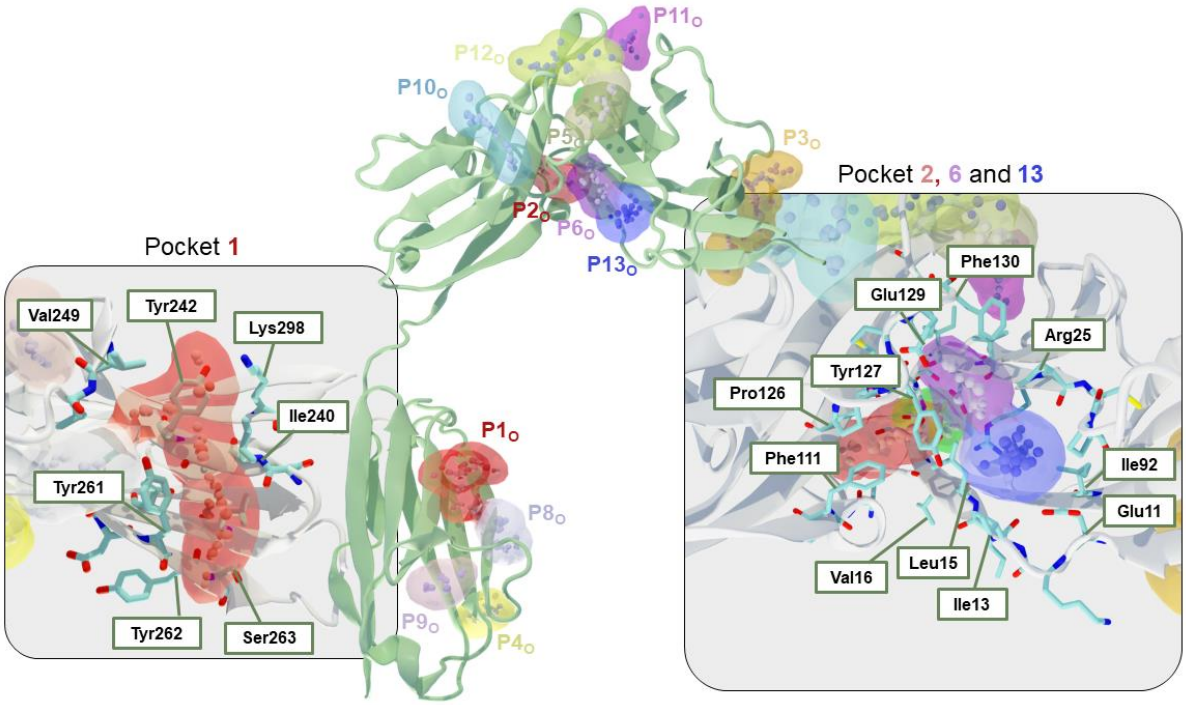

Figure II. 7 - Structural pockets identified by Fpocket, on the extracellular domain of interleukin-1 receptor type 1 (PDB entry 4GAF). Twelve binding pockets are shown: P1o (red); P2o (salmon); P3o (orange); P4o (yellow); P5o (lime); P6o (violet); P8o (grey); P9o (mauve); P10o (cyan); P11o (purple); P12o (green); and P13o (blue). Expanded views are provided for P1o, P2o, P6o and P13o.

Table II. 6 - Summary of Fpocket druggability mapping results on the IL-1R1-ECD surface (PDB entry 4GAF).

Pocket	Volume (Å³)	Total SASA (nm²)	Mean local hydrophobic density	Druggability score	Key residues IL-1R1-ECD
P1o	613.27	148.04	21.56	0.717	Asp239, Ile240, Ala241, Tyr242, Val249, Ile250, Glu259, Tyr261, Tyr262, Ser263, Leu275, Thr277, Lys298
P2o	188.22	65.72	12.80	0.137	Leu15, Val16, Ser17, Ser18, Tyr105, Asn106, Ala109, Phe111, Tyr127, Thr193, Arg194, Val195
P3o	723.42	205.32	17.35	0.098	Glu8, Arg9, Glu10, Tyr41, Asp44, Ser45, Lys46, Tyr78, Val80, Arg89, Lys91
P4o	225.89	57.68	8.00	0.002	Gln226, Ile227, Gln228, Asn280, Ile281, Ser282
P5o	249.63	63.35	3.00	0.000	His60, Lys61, Lys63, Trp65, Phe130, Lys132, Tyr183
P6o	185.39	77.66	17.00	0.136	Leu15, Val24, Arg25, Pro26, Tyr127, Glu129, Phe130
P7o	212.86	66.92	3.00	0.000	Ala19, Asn20, Ala69, Lys70, Val71, Glu72, Glu98
P8o	203.79	64.36	3.00	0.000	Ile250, Asp251, Glu252, Gly258, Glu259, Tyr261

P9o	219.24	77.50	4.00	0.000	Trp245, Asn246, Ser248, Val249, Ile250, As251
P10o	521.10	156.85	14.13	0.044	Lys132, Asn136, Glu137, Lys138, Pro139, Lys140, Lys161, Asp162
P11o	142.40	69.94	1.00	0.000	Gln53, Ala54, Ser55, Val67, Tyr185, Leu186, Lys188
P12o	437.56	128.83	2.00	0.000	Gln53, His60, Asn133, Glu134, Pro139, Tyr183, Thr184, Tyr185, Leu186
P13o	240.85	91.67	13.00	0.021	Glu11, Ile13, Leu15, Arg25, Pro26, Pro28, Ile92, Tyr127

Table abbreviations: solvent-accessible surface area (SASA); extracellular domain of interleukin-1 receptor type 1 (IL-1R1-ECD).

Summing up, there are many similarities in the occurrence of binding sites in the IL-1R1-ECD open and closed conformations, i.e., amino acids at equivalent positions in these protein structures are identified as potential binding *hot-spots* by DoGSiteScorer, FTMap and Fpocket. Based on the location of the *hot* and *warm spots* revealed by the three strategies, these potential binding regions have been grouped in two distinct areas of the protein, that are proposed as two promising druggable binding sites to develop IL-1R1 small molecule modulators:

1. The D1-D2 interface: All three strategies revealed a higher concentration of *hot-spots* at this interface in both open and closed conformations. In the open conformation, DogSiteScorer identified a large pocket Po_0 (volume of 1209.78 Å^3), encompassing residues important for cytokine binding. Equally, FTMap provided two closely spaced consensus sites binding 16 or more chemical probes with different sizes, shapes, polarity and hydrophobicity, reflecting the putative capacity of this region to bind small molecules. Intriguingly, Fpocket predicted pockets with low druggability scores at the D1-D2 interface (P2o, P6o and P13o). However, their moderate sizes (volumes of 188.82, 185.39 and 240.85 Å^3) and relative hydrophobic nature may be significant for structure-guided strategies. Of note, predictions on the closed conformation revealed a similar large binding site in this interface using the three algorithms. All these observations point out that the D1-D2 interface may own a topology favourable to small molecule targeting regardless of the conformation adopted.
2. The D3 domain: The predicted binding pockets and druggability scores at this domain are more variable than that of the D1-D2 interface. All three methods were able to predict druggable *hot-spots*, however, they differ in their location. DogSiteScorer identified a large pocket in the D3 domain near the flexible linker with a volume of 575.29 Å^3. In the closed conformation, the druggable site extends far beyond the linker, into the D2 domain, presenting large volume, depth and adequate hydrophobicity. Fpocket computed a large pocket with 613.27 Å^3 and endowed with substantial hydrophobic density, however, this

pocket presents a low druggability score in the closed IL-1R1-ECD state. Among the *hot-spots* produced by FTMap, a consensus site composed of 20 probes was predicted druggable, with no secondary cavities present nearby. Still, in the closed conformation this region contacts with the D1 domain, resulting in a larger surface and hydrophobicity. In addition, both DogSiteScorer and FTMap predicted pockets at the D1-D3 interface. Hence, we believe that the consensus site predicted by FTMap and the large pocket predicted by DogSiteScorer represent also valuable binding sites for SBDD experiments.

Small molecule therapeutics targeting these two regions should be capable of interfering with cytokine biding or disrupting the more relevant and persistent protein-protein contacts, blocking the formation of the fully active heterotrimeric IL-1 signalling complex (IL-1β:IL-1R1:IL-1RAcP).

2.3.3. Ligand-binding site differences across IL-1R1 orthologs

The information on whether a putative binding pocket on the target protein is structurally conserved may be relevant for the selection of an appropriate binding region for devising structure-based and virtual screening strategies. Differences in receptor structure and ligand-binding properties between ortholog species should also be considered when performing pharmacological testing experiments, both from efficacy and safety viewpoints. The availability of the gene sequences and molecular structures from different organisms represents an opportunity to analyse differences in the composition and conformation of ligand-binding sites between orthologs. For comparison with the sequence and structure of human IL-1R1 (*Homo Sapiens*, UniProt code P14778), herein we used the IL-1R1 sequences of the mouse (*Mus Musculus*, Uniprot code P13504) and the rat (*Rattus Norvegicus*, UniProt code Q02955), since both are the most common animals used in preclinical drug testing, and obtained their predicted molecular structures from the AlphaFold Protein Structure Database (Varadi et al., 2021) (**Figure II.8-A**).

A comparison of the sequence and structure of the two large anchoring sites of IL-1β to the human IL-1R1 (hIL-1R1) and the rat IL-1R1 (rIL-1R1) reveals 8 conserved residues out of 19 sequence-matched residues lining the receptor site A, and 9 conserved residues out of 16 sequence-matched residues lining the receptor site B. These residues are 17 out of 35 residues that are also conserved in mouse IL-1R1 (mIL-1R1), overall revealing a sequence identity of 42% and 47% for site A, respectively in the rat and the mouse, and of 56% and 50% for site B. We have also compared three putative binding sites predicted in the crystallographic structure of the IL-1R1-ECD (PDB entry 4GAF), by the algorithm DoGSiteScorer (Volkamer et al., 2012b). As anticipated, each of these regions, individually, are more conserved than the overall IL-1β binding sites A and B (**Figure II.8-B and Figure A-5** of the Appendix).

A

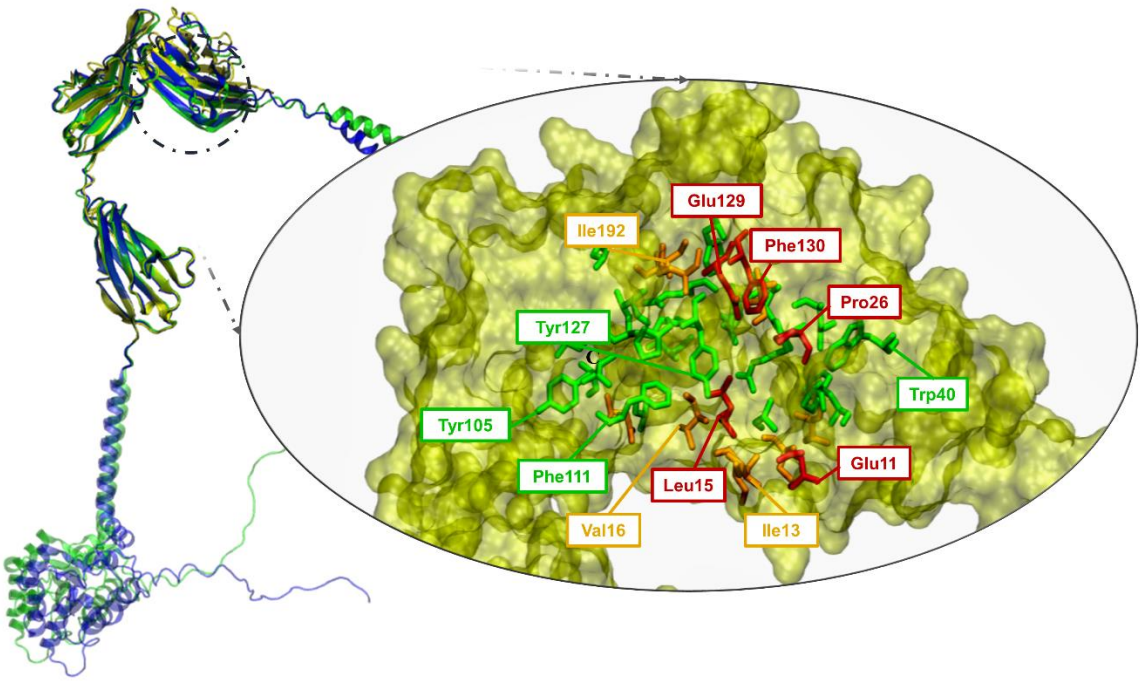

B

Res #	Human IL-1R1	Human Res	Rat Res	Mouse Res
		pocket P_O_0_0		
15	Leu	L	S	L
16	Val	V	F	F
17	Ser	S	S	L
18	Ser	S	S	S
21	Glu	E	E	E
23	Asp	D	D	D
24	Val	V	I	I
25	Arg	R	R	R
26	Pro	P	S	K
69	Ala	A	A	A
104	Cys	C	C	C
105	Tyr	Y	Y	Y
106	Asn	N	N	S
109	Ala	A	A	A
111	Phe	F	F	F
126	Pro	P	P	P
127	Tyr	Y	Y	Y
128	Met	M	L	V
129	Glu	E	D	S
130	Phe	F	F	Y
131	Phe	F	F	F
180	His	H	R	R
192	Ile	I	V	V
193	Thr	T	T	T
194	Arg	R	R	R
195	Val	V	V	V
		26	19	17
		%id -->	73	65

C

Res #	Human IL-1R1	Human Res	Rat Res	Mouse Res
		pocket P_O_0_1		
11	Glu	E	N	N
13	Ile	I	V	I
14	Ile	I	I	V
15	Leu	L	S	L
25	Arg	R	R	R
26	Pro	P	S	K
28	Pro	P	P	P
40	Trp	W	W	W
92	Ile	I	I	V
127	Tyr	Y	Y	Y
		10	6	6
		%id -->	60	60

D

Res #	Human IL-1R1	Human Res	Rat Res	Mouse Res
		pocket P_O_0_6		
25	Arg	R	R	R
40	Trp	W	W	W
64	Leu	L	L	L
66	Phe	F	F	F
77	Tyr	Y	Y	Y
92	Ile	I	I	V
96	Phe	F	V	V
		7	6	5
		%id -->	85	71

Figure II. 8 - Comparison of human, rat and mouse interleukin-1 receptor type 1 protein sequences and structure. Upper panel: **(A)** Structural alignment of rat (rIL-1R1, coloured in green) and mouse (mIL-1R1, coloured in blue) predicted structures (full-length) retrieved from the AlphaFold Protein Structure Database (Varadi et al., 2021) with the crystallographic structure of the extracellular domain of human IL-1R1 (hIL-1R1, coloured in yellow) (PDB entry 4GAF). The protein structures were superimposed using the MatchMaker tool of the UCSF Chimera 1.15 software program (Pettersen et al., 2004). The D1-D2 surface representation enclosed by the black circle is zoomed in, as well as conserved and non-conserved residues for the largest pocket (Po_0) predicted by DogSiteScorer. Lower panel: protein sequence alignment for residues (one-letter code) comprising three "druggable" binding

pockets – Po_0_0 **(B)**, Po_0_1 **(C)** and Po_0_6 **(D) –** predicted in the crystal structure of hIL-1R1 by DoGSiteScorer (Volkamer et al., 2012b). The sequence alignment was produced using the Clustal Omega Server (Sievers and Higgins, 2018). Conservation across orthologs is colour coded as green, for full conservation across the three orthologs (a whole green table line represents 100% conservation); yellow, for amino acid differences with similar side-chain properties; red, for amino acid differences with distinct side-chain properties.

Three smaller pockets are detected within the largest pocket (Po_0) and receive high *druggability* scores (). The overall sequence identity between hIL-1R1 and rIL-1R1 and mIL-1R1 is greater than 60%: (i) pocket Po_0_0 presents 7 and 9 non-conserved residues out of 27, with a sequence identity of 73 and 65% against rIL-1R1 and mIL-1R1, respectively; (ii) pocket Po_0_1 presents 4 non-conserved residues out of 10 residues compared to both rIL-1R1 and mIL-1R1 (sequence identity of 60%); and (iii) the smallest of these three pockets, Po_0_6, shows 1 and 2 out of 7 non-conserved residues (sequence identity of 85 and 71% for rIL-1R1 and mIL-1R1, respectively). Out of the three orthologs, mIL-1R1 is the only one that does not present a negatively charged side-chain, i.e. either aspartate (D) or glutamate (E), at position 129, which is known to be involved in the interaction with IL-1β or IL-1Rα. In addition, neither mIL-1R1 nor rIL-1R1 present a negatively charged residue at position 11 as in hIL-1R1, instead showing a glutamine (N). Within the core of the pocket, residue 26 is different across the three orthologs, with hIL-1R1 presenting a proline (P) and rIL-1R1 and mIL-1R1 showing a serine (S) and a positively charged lysine (K), respectively.

Focusing on the predicted binding pocket Po_1, which is located in the D3 domain, this site presents a sequence identity of 60 and 68% to the hIL-1R1, respectively compared to the rat and the mouse. Significant differences between ortholgs pertain two residues of the 6-amino acid linker, human P206 and T207, which are mutated to arginine (R) and aspartic acid (D), respectively, in rIL-1R1 and mIL-1R1, and the presence of N301 in mIL-1R1 instead of H301 observed in hIL-1R1 and rIL-1R1. Human IL-1R1 shares 55% and 48% amino acid identity with their rat and mouse orthologs at binding site Po_2, evidencing a lower degree of conservation between species in this region. Overall, the two top-ranked binding sites, Po_0 and Po_1, exhibit relatively high sequence and structural conservation, which is consistent with their performing an important structural or biological role, as some of the residues lining these sites are crucial for IL-1 cytokine interaction.

2.4. Concluding Remarks

In this chapter, structural quality evaluations have been conducted for all the IL-1R1-ECD X-ray structures deposited in the PDB to identify the structure holding highest overall structural quality for SBDD approaches. The selected structure was then used as reference for the identification of discernible druggable binding sites on the IL-1R1-ECD surface. Our idea was to provide useful hints for the SBDD of small molecules able to bind IL-1R1 and modulate the

neuroinflammatory networks. To reach this goal, three different computational applications for binding pocket prediction were employed. The detailed assessment and correlation of data from the different algorithms allows for the rationalization of targeting strategies. Importantly, the druggability landscape outlined in this chapter provided: (i) a potential druggable binding region located at the D1-D2 binding interface comprising of a collection of smaller pockets, which was predicted in consensus by the three applied methods; (ii) potential druggable *hot-spots* populating the D3 domain, particularly in the region close to the flexible linker and the interface region between the D1 and D3 domains when IL-1R1-ECD adopts a closed conformation, albeit predictions and virtual druggability scores varied significantly between the three strategies. Overall, based on analyses disclosed here, together with the binding site analyses performed by others (Yang, 2015), it seems plausible that the highest scoring predicted pockets represent promising focus points for targeting IL-1R1.

Despite the careful analysis carried out in this chapter, crystal structures being static snapshots of dynamic systems raise the possibility that different structures of the same binding site would be associated with contradicting druggability predictions. Hence, this implies the necessity to consider protein internal motions in predicting and characterizing binding sites and in designing new chemical binders. With this in mind, in Part III a careful analysis of the IL-1R1-ECD conformational space is conducted, with particular focus on the stability and conformational flexibility of the most relevant predicted putative binding sites.

The application of our pocket detection protocol was able to suggest and prioritize plausible binding sites regardless *a priori* knowledge of small molecule binders. Still, an even better starting point could be provided by an IL-1R1-ECD complex with a small molecule, so that there will be more valid binding positions. Nevertheless, the initial clues for the rational design of IL-1R1 modulators have been presented here to some extent.

PART III

Molecular Dynamics simulations of Soluble and Membrane-bound forms of IL-1R1: decoding the conformational landscape

"All things are made of atoms, and everything that living things do can be understood in terms of the jigglings and wigglings of atoms."

Richard Feynman, in *Six Easy Pieces*

3.1. Introduction

The interleukin-receptor type 1 (IL-1R1) is synthetized as an 80 kDa transmembrane protein featuring an extracellular domain (ECD) containing three Ig-like domains (D1, D2 and D3), a transmembrane (TM) α-helix domain, and a cytoplasmic TIR domain. This membrane-bound protein may also be cleaved by matrix metalloproteases to a soluble circulating form. Both the membrane-bound and the soluble forms of IL-1R1 are biologically active, regulating the inflammatory response through agonistic and antagonistic modulation of cytokine activity. The ECD is a molecular trait or common signature found in both IL-1R1 forms, vital for ligand recognition and binding (Dinarello, 1998; Fields et al., 2019; Mantovani et al., 2019). The "puzzling nature" of soluble and membrane-bound IL-1R1-ECDs make us raise questions and incite us to investigate the spectrum of conformations explored by the soluble IL-1R1-ECD in comparison with the membrane-bound IL-1R1-ECD: i) are conformational dynamics of the IL-1R1 majorly affected by membrane environment? ii) do IL-1R1 structural and conformational preferences translate into substantial differences in ligand recognition?

While extensive structural works on the soluble ECD portions of IL-1R1 have provided critical insights about the specificities of ligand binding to this protein, lack of a full-length receptor structure has hindered a comprehensive overview of the overall architecture and IL-1R1 domain arrangements. In this regard, in this chapter we attempt to predict the structural organization of full-length IL-1R1. Starting off from a high-quality crystal structure of the apo form of IL-1R1-ECD, we compare the conformational ensembles sampled by molecular dynamics (MD) simulations on the full-length (IL-1R1 ECD-TM-TIR) membrane model and in the soluble protein (IL-1R1-ECD). To the best of our knowledge, the presented work is the first study of this receptor dynamics, in the soluble and membrane-bound forms, via ten individual 600 ns MD runs, totalling 6 μs.

Guided by the results of Part II, as part of our initial effort toward the prediction and characterization of potential binding sites in the IL-1R1-ECD surface, we argued if the dynamic conformational behaviours observed for the two IL-1R1 forms could reflect in different physicochemical and topological properties of potential binding sites. Herein, to approach this issue, we study the evolution of a predicted binding site located at the D1-D2 interface, throughout the MD trajectories. Pocket conformations were grouped based on relevant physicochemical properties, by applying a clustering algorithm (K-medoids) for partitioning conformations with different features in this binding site, aiming at identifying groups of snapshots with similar pocket properties. Subsequently, representative MD conformations were identified and extracted for each cluster, toward the implementation of the virtual screening (VS) protocol presented in the next chapter.

Altogether, our simulations expand the current understanding of the dynamic features of the soluble and membrane-bound forms of IL-1R1, corroborating and mounting on the observations of other authors (Yang, 2015, 2020; Ge et al., 2019). The incorporation of dynamic features such as the ones highlighted in the present work provide a better understanding of the differences between soluble and membrane-bound IL-1R1-ECD conformational landscape and thus, may help consolidate the rationale of IL-1R1 drug-discovery programs.

3.2. Computational Methods

This section describes the material and methods employed in (1) the preparation and refinement of the soluble IL-1R1-ECD structural model; (2) the prediction and refinement of a 3D-model for the full-length IL-1R1; (3) the attachment of the resultant full-length IL-1R1 model to a POPC (1-palmitoyl-2-oleoyl-sn-glycero-3-phosphocholine) membrane; (4) the setup of all-atom MD simulations; and (5) the analyses of the MD trajectories including Principal Component Analysis (PCA) and clustering based on the backbone dihedral angles. The sequence of human IL-1R1 (*Homo Sapiens*, UniProt code P14778) was used to create the full-length IL-1R1 protein, by means of structural modelling methodologies. The quality of the structural models was evaluated using PROCHECK v.3.5.4 (Laskowski et al., 1993). MD simulations were run on a dual Intel® Xeon® CPU E5-2680 @2.70GHz, using message passing interface (MPI) parallelization, managed by Minho Advanced Computing Centre (MACC). MD simulation data were visualized using VMD v.1.9.3. (Humphrey et al., 1996) and analysed with RStudio 1.2.5033 (RStudio Team, 2020). The BlendMol plugin (Durrant, 2019) was used to produce high quality images of IL-1R1 structures from imported VMD visualization states using the Blender software (Kent, 2015).

3.2.1. Protein structure of soluble IL-1R1 (ECD)

As of December 2021, the PDB (Berman et al., 2000) holds 5 crystal structures of protein complexes containing the IL-1R1-ECD, with 100% coverage of the UniProt sequence encoding for the human IL-1R1-ECD. PDB entry 4GAF (chain B - IL-1R1-ECD) was selected because of its higher structural resolution (2.15 Å) (Hou et al., 2013). Then, the co-crystallized ligands and water molecules were removed, missing residues were modelled via structural modelling using MODELLER v9.19 (Šali and Blundell, 1993), and the best model selected on the basis of the lowest value of the DOPE score (Shen and Sali, 2006). The final model for soluble IL-1R1 comprises 319 residues.

3.2.2. Structural assembly and refinement of a full-length IL-1R1

A structural model for the full-length multi-domain IL-1R1 has been assembled by combining molecular modelling and MD simulations. The crystal structure of the IL-1R1-bound ECD was obtained from the PDB (chain B from PDB entry 4GAF), determined at 2.15 Å resolution, and prepared as described in sub-section 3.2.1. Next, the 20-residue TM peptide was modelled as a single α-helix via use of a MODELLER script (Sali, 2008), and PDB entry 1T3G for TIR domain (Khan et al., 2004) was chosen as template structure for homology modelling by using PDB's BLAST utility (Altschul et al., 1990). This crystal structure of the TIR domain of IL-1RAPL1 (Interleukin 1 Receptor Accessory Protein Like 1) holds 34% sequence identity (E-value of 1e-13) with the TIR amino acid sequence of IL-1R1, and has been solved at 2.3 Å resolution (Khan et al., 2004). Despite the low sequence similarity, the two proteins belong to the same family of structurally similar receptors, the IL-1 Receptor Family (Boraschi et al., 2018), thus both protein domains adopt a similar global fold, despite some differences in the positioning of TIR domain secondary structural elements (Toshchakov and Neuwald, 2020). For each model, a 1000-step steepest descent energy minimization was carried out to remove initial steric clashes using GROMACS software version 2019.3 (Abraham et al., 2015, 2019). All three individual models were aligned on the same axis using GROMACS tool *gmx editconf* and patched between the C- and N-terminal residues of adjacent domains using UCSF Chimera version 1.12 (Pettersen et al., 2004). Finally, the resulting full-length model was again energy minimized with an additional loop refinement step, using the MODELLER software in Chimera (Pettersen et al., 2004), to correct irregularities on the constructed peptide bonds. The final full-length IL-1R1 model presents 527 residues (IL-1R1-ECD - 319 residues; TM - 20 residues; TIR – 184 residues).

3.2.3 Construction of the full-length IL-1R1 membrane system

The full-length IL-1R1 model was embedded in a pre-equilibrated POPC bilayer containing 332 lipids by aligning the center of mass of the IL-1R1 TM domain with that of the membrane, using the *gmx mdrun membed* tool in GROMACS 2019.3 (Wolf et al., 2010). The overlapping lipids with the protein were removed, resulting in a total of 324 membrane lipids. Periodic boundary conditions were applied in all directions of a cubic simulation box, the system solvated using the TIP3P water model (Jorgensen et al., 1983) and neutralized with the addition of sodium and chloride ions at a 100 mM concentration. The resulting total number of atoms was 212.017.

3.2.4 MD simulations of full-length IL-1R1 membrane system

All-atom simulations were performed with GROMACS 2019.3, using the Amber99sb-ILDN force field (Lindorff-Larsen et al., 2010) for the protein and Berger parameters (Berger et al., 1997) for the POPC lipids. Energy minimization was carried out using the steepest descent algorithm for 50000 steps to remove close contacts between the IL-1R1 atoms and solvent or lipid bilayer. Equilibration of the protein-membrane system started with a 100 ps simulation under NVT conditions at 303 K. All bonds lengths were constrained with the LINCS algorithm (Hess et al., 1997), with a 2 fs time step. Electrostatic interactions were treated by using the particle-mesh Ewald (PME) method (Essmann et al., 1995), with a short-range cutoff of 12 Å. The cutoff distance of the van der Waals interaction was also of 12 Å. The temperature was coupled to the V-rescale thermostat (Bussi et al., 2007) with a time constant of 0.1 ps. Position restraints were applied first to all heavy atoms, and then backbone, and finally Cα-atoms, using a force constant of 1000 kJ/mol/nm^2. After NVT, a 10 ns NPT equilibration was performed, with pressure kept constant at 1 bar by using a semi-isotropic Parrinello-Rahman barostat (Parrinello and Rahman, 1981). The temperature was kept at 303 K using the Nose-Hoover thermostat (Braga and Travis, 2005), maintaining the position restraints from the NVT phase. After these equilibration steps, restraints were removed and five independent production runs, each for 600 ns, were performed starting from different initial velocities.

3.2.5. MD simulations of soluble IL-1R1 (ECD)

MD simulations in explicit solvent were performed for the isolated IL-1R1-ECD, using Amber99sb-ILDN force field (Lindorff-Larsen et al., 2010). The model was solvated with TIP3P water (Jorgensen et al., 1983) in a truncated octahedron box. The resulting total number of atoms was 164.708. After the entire system was neutralized with counter ions, 10000 steps of energy minimization were performed with the steepest descent algorithm. Temperature and pressure couplings were performed for 750 ps and 1 ns each, with V-rescale thermostat (Bussi et al., 2007) and Berendsen barostat (Berendsen et al., 1984), respectively. All other MD simulation settings were the same as described for the full-length IL-1R1 membrane system. Production simulations of 600 ns were performed in quintuplicate, starting from different initial velocities.

3.2.6. Principal Component Analysis

PCA was performed to extract the collective motions of the IL-1R1-ECD sampled in the MD simulations. The covariance matrix was constructed using the *gmx covar* function in GROMACS 2019.3 to define the backbone conformational space of the MD structures. Next, the MD trajectories were projected onto the first four eigenvectors, using 10000 frames per

trajectory (1 frame each 60 ps), with an initial RMS-fit to the starting MD snapshot Cα-atoms to remove the rotational and translational motions. To understand the global motions of the IL1R1-ECD, porcupine plots were generated and visualized via the modevector.py script from Pymol (Schrödinger LLC, 2020). Five crystal structures of IL-1R1-ECD bound to different ligands were used in the PCA as reference points in the conformational space sampled by the two IL-1R1-ECD forms - PDB entries 4DEP two ECD chains (Thomas et al., 2012), 4GAF (Hou et al., 2013), 1G0Y (Vigers et al., 2000), 1IRA (Schreuder et al., 1997) and 1ITB (Vigers et al., 1997).

3.2.7. Clustering based on the backbone dihedral angles of the linker

Conformational clustering based on the backbone dihedral angles, phi (φ) and psi (ψ), of the flexible linker residues was performed using the Partitioning Around Medoids (PAM) clustering method (Reynolds et al., 2006). Proline (Pro) 206 was not included due to limited number of ψ and φ possibilities owed to its 5-membered ring. The silhouette width value was used to select the best number of clusters obtained with the PAM algorithm. This value measures the quality of a clustering, where the optimal number of clusters *k* is the one that maximizes the average silhouette over a range of possible values for *k* (Kaufman and Rousseeuw, 1990). Representative structures of each cluster were chosen based on the medoids concept, i.e., structures closest to the absolute average of each cluster. Clustering was performed using 10000 frames of the linker region per MD trajectory (1 frame each 60 ps), after alignment of the Cα-atoms in each frame to the starting MD snapshot.

3.2.8. Pocket characterization on MD trajectories

The changes in the volume and shape of the binding site, located at the D1-D2 interface, estimated using Fpocket (Le Guilloux et al., 2009) were calculated throughout the MD trajectories with MDPocket (Schmidtke et al., 2011). This software is an extension of Fpocket, allowing the analysis of several physicochemical and geometric descriptors (for example, pocket volume, polar and apolar surface areas, hydrophobicity and polarity measures, pocket density and average radius, local hydrophobic density, etc.) for the pocket of interest. Before using MDPocket, 10000 MD snapshots of the soluble and membrane-bound IL-1R1-ECD proteins were superimposed onto each other, through least squares superposition of all Cα-atoms in each snapshot.

To visualize the space sampled by the pockets, PCA was performed based on physicochemical and geometric descriptors, to efficiently extract the most relevant pocket descriptors. Then, pocket conformations were grouped based on the selected descriptors, by applying the PAM clustering method. Similarly, to sub-section 3.2.7., the silhouette width value was used to select

the best number of clusters obtained with the PAM algorithm. For each cluster, representative conformations were extracted.

3.3. Results and Discussion

To characterize the conformational behaviour of membrane-bound IL-1R1-ECD, in this study a structural model was developed in which the full-length IL-1R1 is anchored to a POPC membrane. For both the soluble and membrane-bound IL-1R1-ECDs, five independent 600 ns long MD simulations, at 303 K, have been performed, totalling 3 μs for each system. In the following paragraphs, a detailed analysis of these simulations is presented.

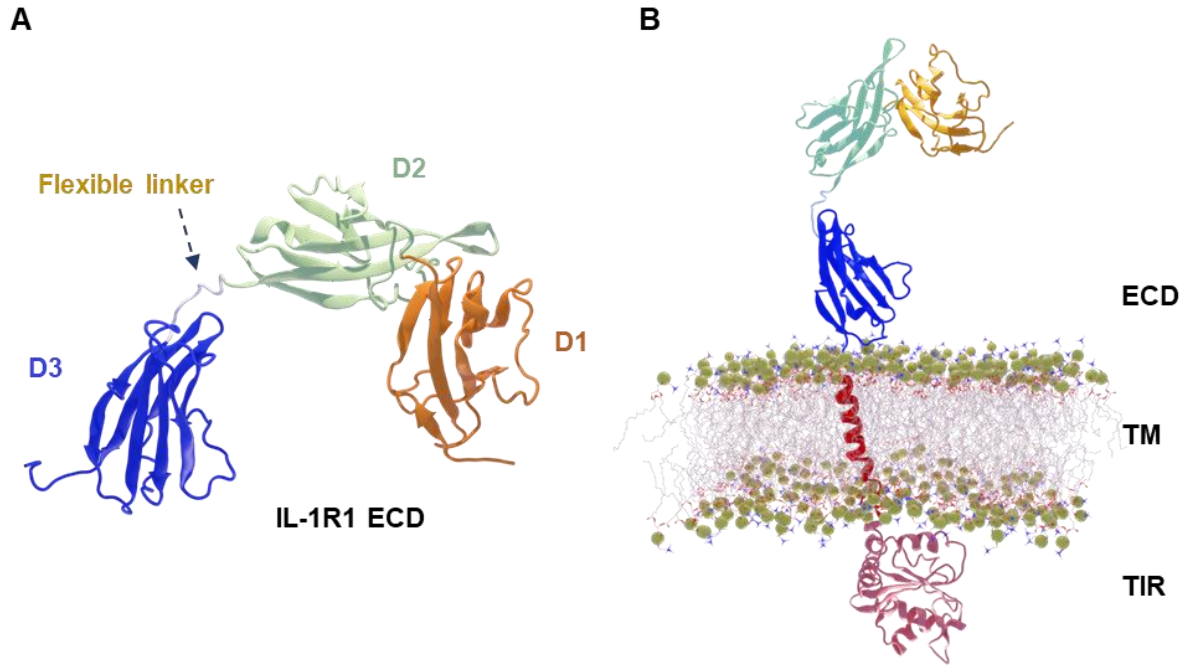

Figure III. 1 - Initial configurations of soluble and full-length membrane-bound interleukin-1 receptor type 1 (IL-1R1). (A) Structural organization of the soluble IL-1R1. Ig-like domains are labelled as D1, D2 and D3 and arrow indicates the 6 amino acid flexible linker (B) Overall architecture of the full-length IL-1R1 in a POPC membrane.

3.3.1. Structural quality and stability assessment of the full-length, membrane-bound IL-1R1

Figure III.1 depicts the overall structures of both the soluble, X-ray derived IL-1R1 and the modelled, membrane-bound, full-length IL-1R1. The quality of both structural models (prepared as described in the Methods section) was assessed and validated using PROCHECK (Laskowski et al., 1993). The models were also evaluated using the ProSA-web server (Wiederstein and Sippl, 2007), which measures structure quality and energy profiles in terms of a *Z*-score. The final snapshot (t = 600 ns) of each MD run was also assessed for quality using the same methods. The Ramachandran plot analysis obtained by PROCHECK and the *Z*-score

determined by the ProSA-web server are depicted in **Table III.1** and the plots are provided in the Appendix (**Figure B-1** and **B-2**). Analysis of the soluble and membrane-bound IL-1R1 structures show that the backbone phi and chi angles of >95% of the residues fall within favoured and allowed regions, highlighting the high quality of the models. The *Z*-scores for the soluble and the full-length IL-1R1 were -7.06 and -5.81, respectively, falling within the range of values of the known proteins determined by X-ray. Analysis of the final snapshot of each MD run revealed that the backbone angles remain within the favoured regions of the Ramachandran plot, and the respective *Z*-scores obtained do not disclose significant deviations from experimentally determined protein structures of similar size. Secondary structure assignments across the MD trajectories, obtained via the DSSP algorithm, reveal that the three Ig-like domains are mostly preserved across the 600 ns of simulation, with only subtle alterations. The changes in protein secondary structure along the soluble and membrane-bound IL-1R1 MD simulations are provided in Appendix (Figure **B-3** and **B-4**).

Table III. 1 - Ramachandran plot statistics and ProSA-web *Z*-score for initial structural models and the five MD runs of soluble and membrane-bound full-length interleukin-1 receptor type 1 (IL-1R1).

IL-1R1		**Ramachandran plot[1]**				***Z*-score**
		Most favoured regions	**Additional allowed regions**	**Generously allowed regions**	**Disallowed regions**	
Soluble	Pre-MD	250 (88.7%)	27 (9.6%)	3 (1.1%)	2 (0.7%)	-7.06
	S1[2]	243 (85.0%)	38 (13.3%)	4 (1.4%)	1 (0.3%)	-7.87
	S2[2]	253 (88.5%)	30 (10.5%)	0 (0%)	3 (1.0%)	-7.34
	S3[2]	239 (83.6%)	42 (14.7%)	3 (1.0%)	2 (0.7%)	-7.24
	S4[2]	238 (83.2%)	41 (14.3%)	5 (1.7%)	2 (0.7%)	-7.75
	S5[2]	237 (82.9%)	43 (15.0%)	5 (1.7%)	1 (0.3%)	-7.53
Full-length	Pre-MD	385 (82.4%)	65 (13.9%)	12 (2.6%)	5 (1.1%)	-5.81
	M1[2]	396 (84.8%)	60 (12.8%)	6 (1.3%)	5 (1.1%)	-7.25
	M2[2]	388 (83.1%)	72 (15.4%)	4 (0.9%)	3 (0.6%)	-7.16
	M3[2]	392 (83.9%)	69 (14.8%)	4 (0.9%)	2 (0.4%)	-6.99
	M4[2]	386 (82.7%)	73 (15.6%)	5 (1.1%)	3 (0.6%)	-6.73
	M5[2]	388 (83.1%)	72 (15.4%)	5 (1.1%)	2 (0.4%)	-7.19

[1] distribution of non-glycine and non-proline residues in the Ramachandran plot: [2] final snapshot from the simulation; Total number of non-glycine and non-proline residues: 286 (soluble IL-1R1); 467 (full-length IL-1R1).

The structural stability of the POPC membrane in the presence of full-length IL-1R1 protein was examined by computing the surface area occupied by each lipid (area per lipid), lipid order parameters and mass density profiles across the membrane, and equilibrium properties were compared with those from the literature. The area per lipid (ApL) is defined as the lateral membrane area (XY-dimension) of the simulation box divided by the number of lipids in one leaflet (Shahane et al., 2019). ApL values for the five membrane-bound IL-1R1 MD runs (M1-M5) are reported in **Figure III.2A**. The average ApL values calculated for the POPC system were 0.643 ± 0.007, 0.639 ± 0.007, 0.636 ± 0.007, 0.639 ± 0.007 and 0.637 ± 0.007 nm^2, respectively for M1, M2, M3, M4 and M5 – consistent with previous experimental and simulation ApL values of POPC membranes (Poger and Mark, 2010; Poger et al., 2016). The mass density profiles for multiple system components along the *z*-axis are plotted in **Figure III.2B**. Across the five membrane-bound IL-1R1 MD runs, the phospholipid bilayer density profiles are generally maintained: i) the water density in the hydrophobic membrane's core is null (0), implying that no water molecules reach the interior of the bilayer; ii) the headgroup densities are distributed between 36 and 37 Å, roughly corresponding to the thickness of the lipid membrane (Poger and Mark, 2010; Shahane et al., 2019); iii) the acyl chains are fully packed in the bilayer core (distances between 31 and 32 Å). Altogether, the calculated membrane environment density profiles point out to a correct organization of the bilayer hydrophilic and hydrophobic moieties holding the full-length IL-1R1. Deuterium order parameters ($-S_{CD}$) of the *sn1* and *sn2* acyl chains in phospholipids (**Figure III.2C** and **III.2D**) indicate that the membrane has not transitioned into a gel-like state and, overall, are in good agreement with order parameters for a pure POPC bilayer – as determined experimentally and from MD simulations (Ferreira et al., 2013; Piggot et al., 2017).

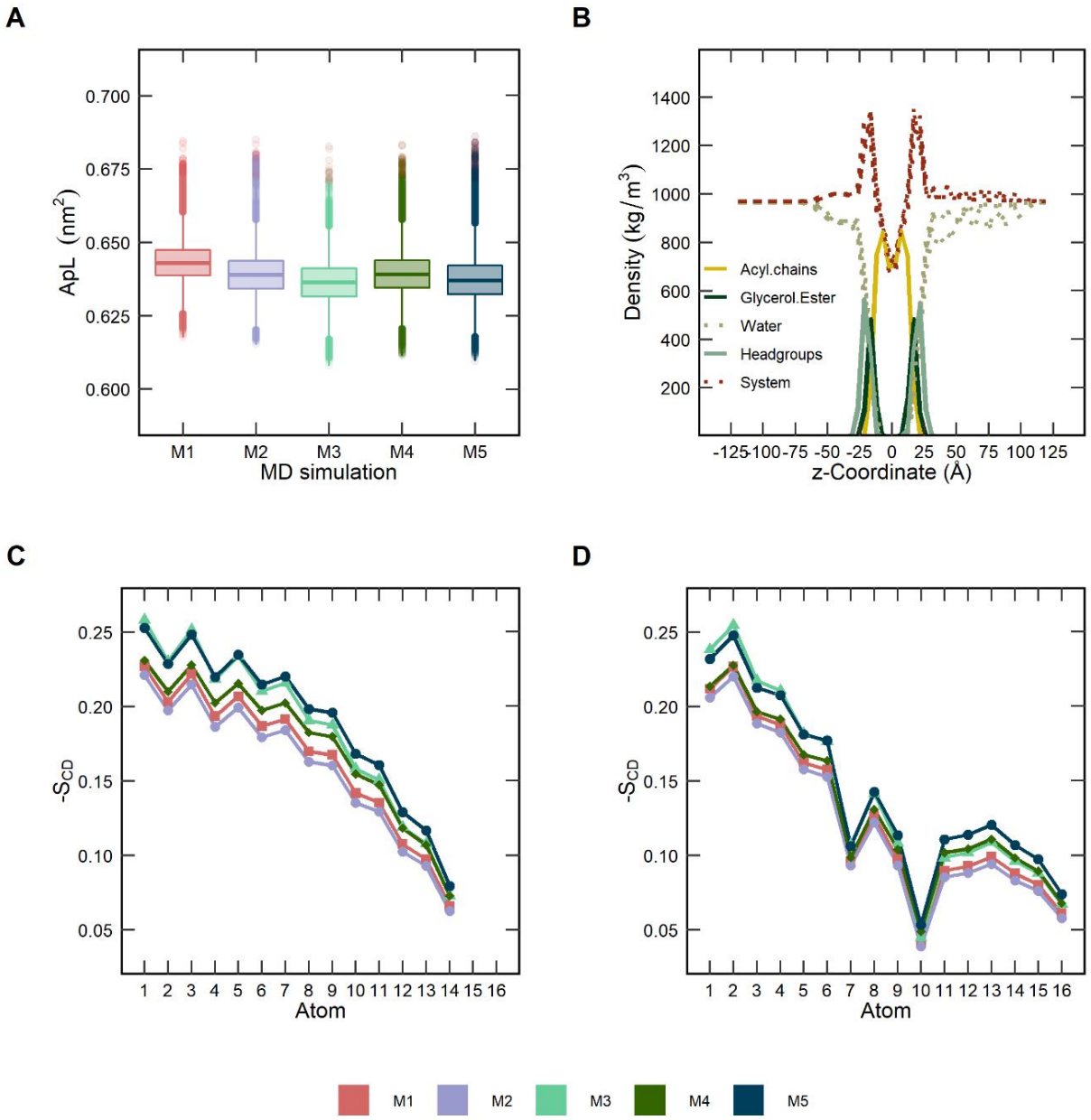

Figure III. 2 - Bilayer stability parameters throughout five MD runs (M1, M2, M3, M4 and M5) of the full-length interleukin-1 receptor type 1 in a POPC membrane. (A) Area per lipid (ApL) of the POPC bilayer; (B) Mass density profiles of the various components of the POPC bilayer; Deuterium order parameter S_{CD} profiles of the *sn1* (C) and *sn2* (D) lipid acyl chains.

3.3.2. Conformational dynamics of soluble and membrane-bound IL-1R1-ECDs

In this work, MD simulations have been used to study the conformational dynamics of soluble and membrane-bound IL-1R1, particularly focusing on the ECD region, with the key goal of obtaining structural insights of receptor dynamics and ECD transitions between the open and closed states. The root mean square deviation (RMSD) and the root mean square fluctuation (RMSF) were computed for the soluble and membrane-bound IL-1R1-ECDs after alignment of

the coordinates of Cα-atoms from all systems, using the starting MD snapshot as reference. Analysis of the RMSD profiles (**Figure III.3**) revealed significant conformational changes compared to the starting structure for the soluble IL-1R1. In the 2nd and 3rd replicas (S2 and S3), the ECD rapidly adopts a stable, closed conformation after ≈ 6 ns (average Cα-RMSD of 16.5 ± 0.02 Å and 16.9 ± 0.04 Å, respectively), mediated by D1/D3 beta-sheet interactions, preserving this rigid state along the rest of the trajectories. Two main conformational changes in IL-1R1-ECD are observed in the S5 replica throughout the simulation: (i) during the first 30 ns of simulation, it adopts an open, extended configuration, and (ii) it then undergoes an open-to-closed transition with significant structural rearrangements on D3 between 30 and 350 ns – with the respective RMSD values afterwards approaching those observed in the two replicas sampling the stable, closed state. These rearrangements can be ascribed to a twisting motion of D3 relative to D1-D2, dictated by the flexible linker. The remaining two runs, S1 and S4, show the ECD exhibiting wider variations in terms of RMSD profiles, mostly characterized by rapid increasing and fluctuating values until the end of the simulation. The mean Cα-RMSD of S1 and S4 is 18.8 ± 0.22 Å and 20.6 ± 0.24 Å, respectively, denoting a larger departure from the initial structure on average, compared with the other replicas. Interestingly, in S1 and S4 the D3 region undergoes a twist relative to the other two domains, allowed by the flexible linker connecting D2 and D3, with the ectodomain adopting a twisted, skewed conformation that looks considerably distinct from both the closed and the initially open conformations.

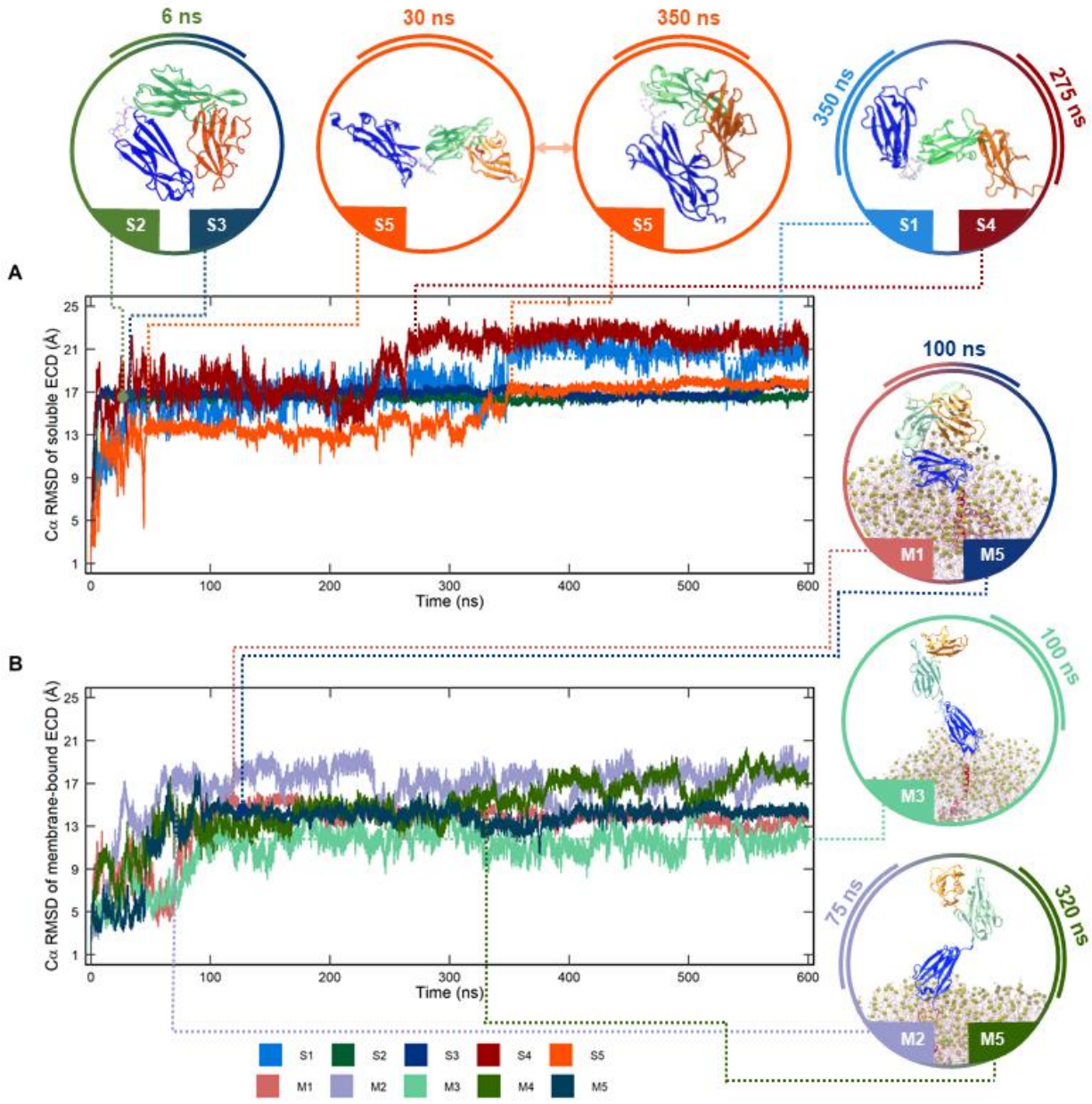

Figure III. 3 - Variation of the root mean square deviation (RMSD) of all Cα-atoms of the extracellular domain of interleukin-1 receptor type 1 (IL-1R1-ECD). (A) five 600-ns soluble IL-1R1-ECD MD simulations (S1, S2, S3, S4 and S5); (B) five 600-ns membrane-bound IL-1R1-ECD MD simulations (M1, M2, M3, M4 and M5).

The RMSD profiles of the membrane-bound IL-1R1-ECD follow essentially a similar trend to that of soluble ECD. Interestingly, during the first 100 ns of the M1 and M5 trajectories, IL-1R1-ECD explores an open configuration in a higher extent before transitioning into a more stable closed state. This is in contrast with what is observed in replicas of the soluble system transitioning into a similar closed state after around 6 ns of simulation (S2 and S3). The mean Cα-RMSD values in M1 and M5 are of 14.1 ± 0.07 Å and 14.1 ± 0.06 Å, respectively, suggesting that the membrane-bound IL-1R1-ECD shows lower deviations than those seen in the soluble form. Higher average RMSD values of 16.7 ± 0.3 Å and 14.8 ± 0.3 Å were computed for

trajectories M2 and M4, where IL-1R1-ECD adopts an extended and twisted open conformation in the later snapshots of the simulations – implying that the interdomain twist motion occurring between D3 and D1/D2 is a common feature shared by the two forms. However, in the M3 trajectory the ectodomain remains in a remarkably stable open conformation throughout the whole simulation length, without the occurrence of structural rearrangements around the flexible linker – resulting in a mean Cα-RMSD of 10.9 ± 0.2 Å.

The MD trajectories show that the conformational stability of the IL-1R1-ECD is higher when bound to a lipid bilayer, in comparison to the soluble form, even though, on average, the diversity of geometrical parameters is also less sampled in the membrane environment across the total 3 μs of simulation. Other structural properties such as the radius of gyration (Rg), intramolecular hydrogen bond networks (HB_{intra}) and the solvent-accessible surface area (SASA) of the soluble and the membrane-bound ECDs were evaluated. **Table III.2** shows that the ectodomains adopting a closed conformation in the soluble (S2 and S3) and in the membrane-bound IL-1R1 (M1 and M5) present similar Rg values, whereas a clear increment in Rg is observed for the systems exploring open conformations. Interestingly, in the S5 trajectory, the transition from the open to a somewhat distinct closed configuration is reflected in a slightly higher Rg when compared to the Rg calculated across those trajectories where the ECD largely adopted closed conformations. These differences seem to be ascribed to the interdomain rotational motion of the flexible linker. In S5, less intramolecular hydrogen bond formation is verified in comparison with those trajectories sampling closed ECD conformations, suggesting that the hydrogen bond framework of the IL-1R1-ECD may be altered due to the rotational motions of the flexible linker across the earlier 350 ns. The higher number of HB_{intra} observed for the soluble and the membrane-bound IL-1R1-ECD closed states points out that this conformation could be thermodynamically more stable. The closed conformations also expose a higher SASA across the soluble and the membrane-bound IL-1R1-ECDs (mean SASA between 180 and 182 nm^2), which is consistently below the SASA values in the open conformations (mean SASA between 184 and 197 nm^2). These structural properties extracted for the simulations are in good agreement with the ones computed for the closed (PDB entry 1G0Y) and open (PDB entry 4GAF) IL-1R1-ECD X-ray structures. Intriguingly, the number of HB_{intra} observed for the closed conformations was systematically lower than the HB_{intra} value of the IL-1R1-ECD closed crystal structure, indicating the transitional pathway to this structure as not been sampled during the simulation timescale.

Table III. 2 - Average values of multiple structural properties across five MD trajectories of soluble IL-1R1-ECD (S1, S2, S3, S4 and S5) and five MD trajectories of POPC-anchored IL-1R1-ECD (M1, M2, M3, M4 and M5). Reference values computed for the open (PDB entry 4GAF) and closed (PDB entry 1G0Y) crystal structures are presented.

System	Average RMSD (Å)	R_g (nm)	# HB_{intra}	SASA (nm^2)
4GAF [1]	--	3.0	229	179.4
1G0Y	16.8	2.2	249	174.4
S1	18.8 ± 0.22	2.9 ± 0.17	234 ± 7	178.7 ± 4.25
S2	16.5 ± 0.02	2.2 ± 0.06	240 ± 8	173.0 ± 2.74
S3	16.9 ± 0.04	2.2 ± 0.04	241 ± 7	172.7 ± 3.13
S4	20.6 ± 0.24	2.8 ± 0.20	233 ± 7	178.9 ± 3.77
S5	15.6 ± 0.20	2.4 ± 0.19	234 ± 8	176.4 ± 4.50
M1	14.1 ± 0.07	2.3 ± 0.18	239 ± 7	175.8 ± 4.28
M2	17.3 ± 0.13	3.1 ± 0.08	231 ± 7	184.7 ± 2.88
M3	11.7 ± 0.11	3.3 ± 0.15	232 ± 7	186.3 ± 2.60
M4	15.6 ±0.18	3.0 ± 0.15	233 ± 8	183.2 ± 3.13
M5	14.1 ±0.06	2.3 ± 0.18	238 ± 7	175.3 ± 4.35

[1] *reference structure used as starting point for MD simulations.*
Table abbreviations: root mean square deviation (RMSD); radius of gyration (Rg); intramolecular hydrogen bonds (HB_{intra}); solvent-accessible surface area (SASA).

Figure III.4 shows the RMSF of Cα-atoms compared with RMSF values derived from the crystallographic B-factors of IL-1R1 (PDB entry 4GAF). The latter were obtained using the relationship $RMSF = (3B/8\pi^2)^{1/2}$. The RMSF values correspond mainly to the N- and C terminal tails of the ECD and to loop regions. It is clear that both soluble and membrane-bound ECDs present significant mobility differences between replicas of the two systems. The MD trajectories where the soluble IL-1R1-ECD undergoes a conformational transition into a stable closed-state (S2 and S3) exhibited modest and nearly superimposable Cα-atom fluctuations, whereas larger Cα-atom fluctuations are detected in the MD trajectories where the membrane-bound IL-1R1-ECD majorly explore a closed configuration (M1 and M5). On the contrary, in those trajectories where IL-1R1-ECD adopts open twisted configurations, significantly larger fluctuations on the Cα-atoms of all residues are seen, with a somewhat expected sharp peak observed between residues 201 and 206. These residues comprise the flexible linker between D2 and D3. The higher RMSF values indicate that all three domains are prominently changing their spatial orientations throughout the simulations, due to the interdomain movements mediated by the flexible linker. Comparisons between the soluble and the bilayer-bound ECD

indicate that the former exhibits higher structural flexibility and more pronounced configurational transitions than the latter. This is likely due to the higher conformational freedom enjoyed by the soluble ECD, allowing it to explore a diversity of backbone conformations in higher extent compared to the membrane-bound ECD.

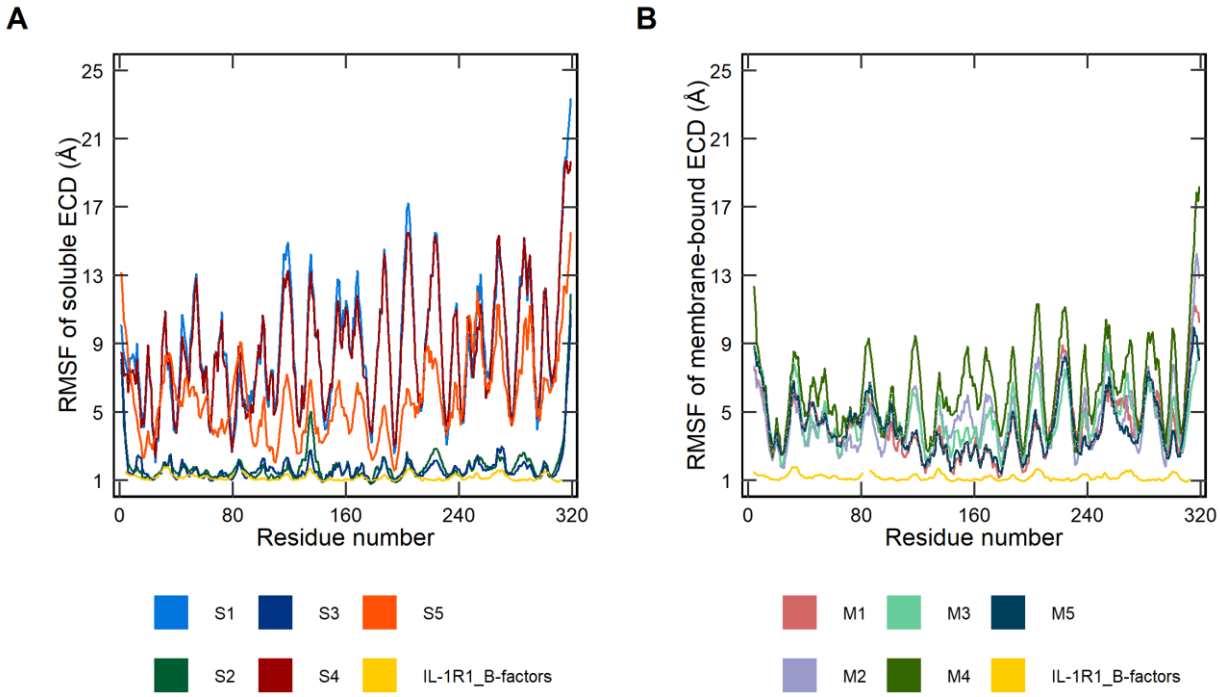

Figure III. 4 - Variation of the root mean square fluctuation (RMSF) of all Cα-atoms profiles as function of residue number for the extracellular domain of interleukin-1 receptor type 1 (IL-1R1-ECD). (A) five 600-ns soluble IL-1R1-ECD MD simulations (S1, S2, S3, S4 and S5); (B) five 600-ns membrane-bound IL-1R1-ECD MD simulations (M1, M2, M3, M4 and M5). The line coloured in yellow represents the fluctuations derived from the crystallographic B-factors of IL-1R1-ECD (PDB entry 4GAF).

To get further insight into the structural dynamics of both IL-1R1-ECD forms, the MD runs were analysed in terms of the interdomain hinge angles between D3/D1 and D3/D2. The flexible linker mediates conformational changes in solution, with hinge-bending and hinge-twisting motions moving the domains together (closed conformation) and apart (open conformation). The hinge angle was computed by measuring the relative displacement between the center of masses of the two domains in the XY-plane. **Figure III.5** illustrates the comparison of the interdomain hinge angles (ϕ) distributions for soluble and membrane-bound IL-1R1-ECDs within the timescale of the MD simulations. For both forms, two defined clusters of D3/D1 hinge angles are accessible, sampling both the closed and open conformations. In the soluble structure, most of the D3/D1 angles for closed conformations (prevalent in S2, S3 and S5) is concentrated within the 110° to 125° range, while the range on the open and twisted conformations (sampled by S1 and S4) is broadened, ranging between 150° to 180°. In line with the RMSD analysis, the S5 trajectory samples open extended conformations during the first 30 ns, reaching its largest angle of 171.5° at 23.4 ns, which

gradually closes up to ≈115°. Likewise, comparable patterns are observed for the membrane-bound ECDs, however two important differences stand out when comparing to the soluble state: (i) attachment to a membrane appears to limit the sampling of open-to-closed transitions, solely converging to a similar hinge angle (ϕ ≈120°) after ≈100 ns (M1 and M5), and (ii) a smaller hinge angle distribution (fluctuations between 150° and 172°) is observed in the open conformations (M2, M3 and M4) when compared to the corresponding structures of the soluble ECD (mostly sampled by S1 and S4). This last observation agrees with the hinge angles distributions of D3 relative to D2, where the soluble ECD exhibits larger interdomain movements in S1 and S4, whereas M2, M3 and M4 sample a narrow angle distribution within the conformational space. Importantly, these differences seem to sustain the view that the IL-1R1-ECD is more flexible in a soluble form predominantly due to the enhanced flexibility of the intrinsically flexible linker between D2 and D3.

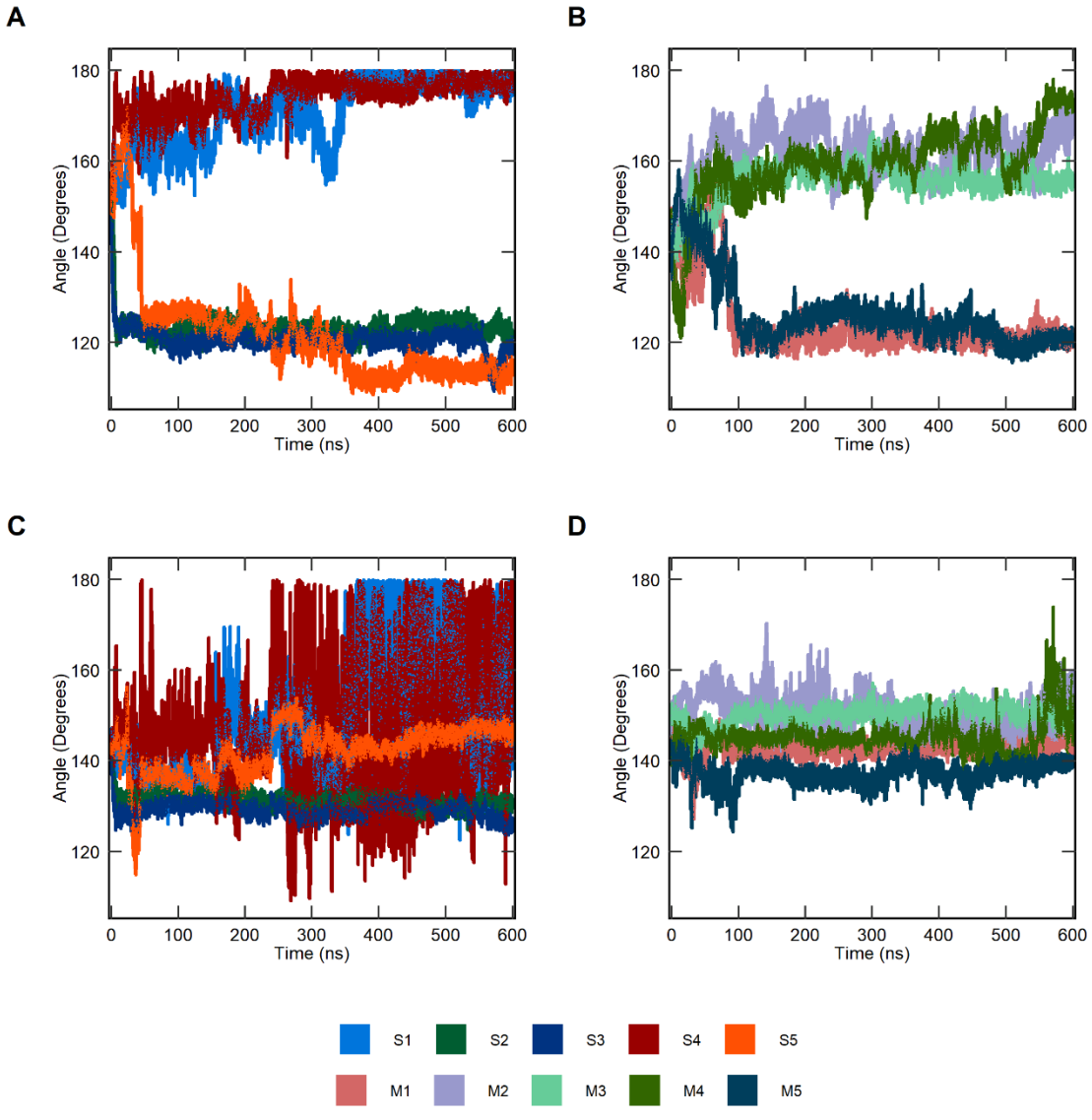

Figure III. 5 - Distributions of the interdomain hinge angles of the extracellular domain of imterleukin-1 receptor type 1 (IL-1R1-ECD) throughout the whole simulation length. (A and C) D1-D3 and D2-D3 hinge angles

for the soluble IL-1R1-ECD (S1, S2, S3, S4 and S5) and (B and D) D1-D3 and D2-D3 hinge angles for the membrane-bound (M1, M2, M3, M4 and M5) IL-1R1-ECD.

3.3.3 Principal Component Analysis of soluble and membrane-bound IL-1R1-ECDs MD trajectories

PCA was performed on protein backbone atoms to further study and help us focus on differences of conformational dynamics between the soluble and membrane-bound IL-1R1-ECDs. In essence, this technique converts a set of correlated observations, e.g. movements of selected atoms in a system, to a set of principal components (PCs) which are linearly independent, containing for example the dominant trends explaining rigid-body domain motions. The 2D plots of **Figure III.6** depict the distribution of conformations along the PC1/PC2 and PC3/PC4 for both the soluble and the membrane-bound IL-1R1-ECD structures extracted from the ten independent MD trajectories. The positions for the five available experimental structures of the IL-1R1-ECD were reported to map reference points onto the subspace spanned by the essential PCs. **Figure B-5** in the Appendix shows the resulting PCs analysis scree plot, indicating the proportion of variance accounted for by the principal components. The porcupine plots for the of the four most representative PCs are presented in **Figure B-6**. In both IL-1R1-ECD forms, the first two eigenvectors (PC1 and PC2) obtained from the PC analysis capture more than 85% of the total variance, suggesting that these vectors approximately describe the essential subspace of both systems. Movement along the first component (PC1) describes a collective motion from the closed to the open state, resulting in a change in the hinge angles, whereas the second (PC2) pertain the collective twisting motions of domains D1-D2 with respect to D3. PC3 and PC4 each account for only 2.2-7.7% and 1.9-3.0% of the observed variance in the soluble and membrane-bound ECD structures, respectively. This PCs represent motions of the D3 domain of IL-1R1 twisting about the flexible linker.

As seen from **Figure III.6**, the conformational landscape explored by the two IL-1R1-ECDs reveals relevant differences: (i) most of the soluble ECD conformations were mapped into two distinct regions of the conformational space, with a small number of intermediate conformations connecting them, i.e., adopting closed conformations in which the D1 and D3 domains contacted each other ($-25 < PC1 < 15$) and open extended, skewed states ($20 < PC1 < 50$); (ii) in the membrane-bound IL-1R1-ECD is observed a higher number of intermediate open states between the closed and open twisted conformations. Furthermore, the area spanned by PC1 and PC2 was much larger in the case of the soluble IL-1R1-ECD in comparison to the membrane-bound form, suggesting a higher degree of amplitude motion and, thus, flexibility of the soluble ECD structure. Interestingly, both IL-1R1-ECD forms sampled the entire conformational space covered by the X-ray structures deposited in the PDB, in the first

two PCs. However, non-overlapping areas of the conformational space between the MD simulations and the X-ray structures were observed in PC3 and PC4, despite their low contribution. This is clearer for the membrane-bound IL-1R1-ECD, which failed to capture essential structural dynamics in these two PCs of the five structures solved experimentally, whilst the soluble form was not able to sample the closing of the ECD with a 170º rotation of D3 relative to D1-D2, as verified in the closed antagonist-bound IL-1R1-ECD (PDB entry 1G0Y). These results point out to notable differences in the twisting motions of the two IL-1R1-ECD forms.

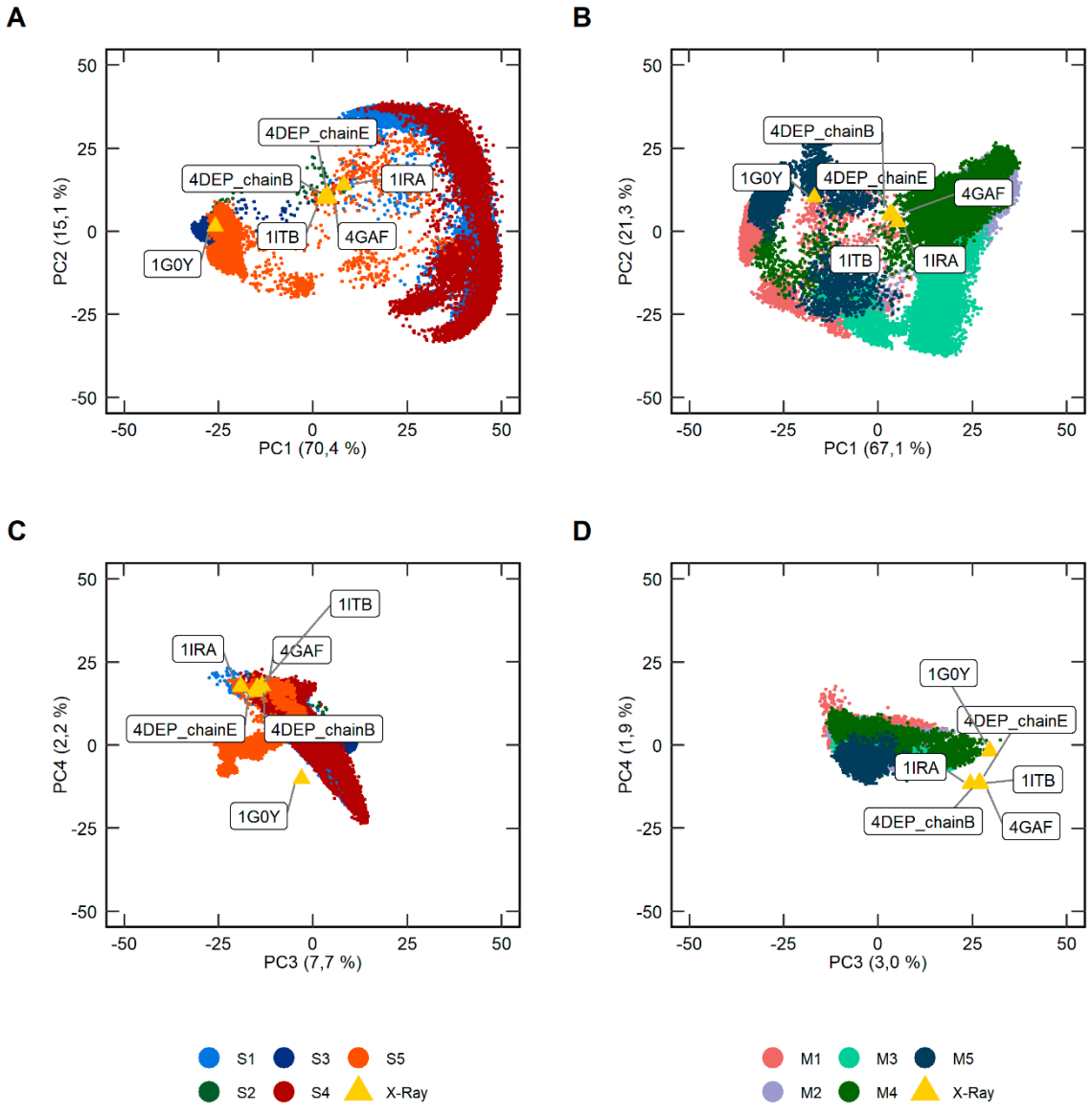

Figure III. 6 - Projections of the conformations adopted by the extracellular domain of interleukin-1 receptor type 1 (IL-1R1-ECD) onto the PC1-4 essential subspace. The experimental structures of IL-1R1-ECD (shown in yellow triangles) used as reference points are depicted with text labels. Sampled areas of (A and C) the five soluble (S1, S2, S3, S4 and S5) space; (B and D) five membrane-bound (M1, M2, M3, M4 and M5) IL-1R1-ECD MD simulations, in the two-dimensional PC1-PC2 and PC3-PC4 space.

A closer look at the plots of **Figure III.6** reveals interesting details on the conformational sampling of soluble versus membrane-bound IL-1R1-ECDs. While the ECD structures that explicitly adopt a closed configuration in the soluble system (prevalent in S2 and S3) exhibit transitions from open to closed states in a more confined subspace, the membrane-bound IL-1R1-ECDs visiting closed conformations (M1 and M5) sample wider intermediate structures on the transition pathway. We hypothesize that the open-to-closed conformational transition observed only later in the course of the MD trajectory for the membrane-bound IL-1R1-ECD is intimately linked with the limited ECD translational and rotational degrees of freedom owing to the presence of the lipid bilayer. Conversely, the higher conformational flexibility of the soluble ECD results in less intermediate states, suggesting this transition occurs on relatively short timescales. Hence, the different conformational profiles of soluble and membrane-bound IL-1R1-ECDs may explore alternative closed-state populations. As mentioned above, the RMSD and RMSF curves, as well as the hinge angle distribution for the membrane-bound IL-1R1-ECD simulations also seem to support this interpretation (**Figures III.3**, **III.4** and **III.5**). Indeed, the restricted flexibility of the membrane-bound IL-1R1-ECD is supported by the open configurations, where each replica (M2, M3 and M4) visits a more confined conformational space when compared to the soluble ECD (S1 and S4).

3.3.4. Clustering of soluble and membrane-bound IL-1R1-ECDs MD trajectories

The flexible linker connecting D2 and D3 domains is of primary importance for the conformational dynamics of IL-1R1. As such, we performed a clustering analysis based on the backbone dihedral angles (φ, ψ) of this linker to determine and compare the extent of accessible conformations of this region sampled by the soluble and membrane-bound IL-1R1-ECDs. Here, we build on the idea of using the torsion angles of this region to better examine and map out the conformational states and transitions of the two IL-1R1-ECD forms. The sin- and cos-transformed scaled dihedral angles were classified into clusters using PAM method. The average silhouette method was used to estimate the optimal number of clusters (k) for each IL-1R1-ECD form. The clusters were ranked by the number of structures. **Figure III.7** illustrates the silhouette analysis for the soluble and membrane-bound IL-1R1-ECDs. In the case of the soluble ECD, the best silhouette width value was obtained for 8 clusters, whereas k=4 provided the best score for the membrane-bound counterpart. Importantly, this standard metric provides evidence for a wide dispersal of linker orientations in the soluble system, and a need to choose a higher k to an optimal partitioning of the sampled dihedral angles given that the flexible loop shows the highest fluctuation in this IL-1R1-ECD form.

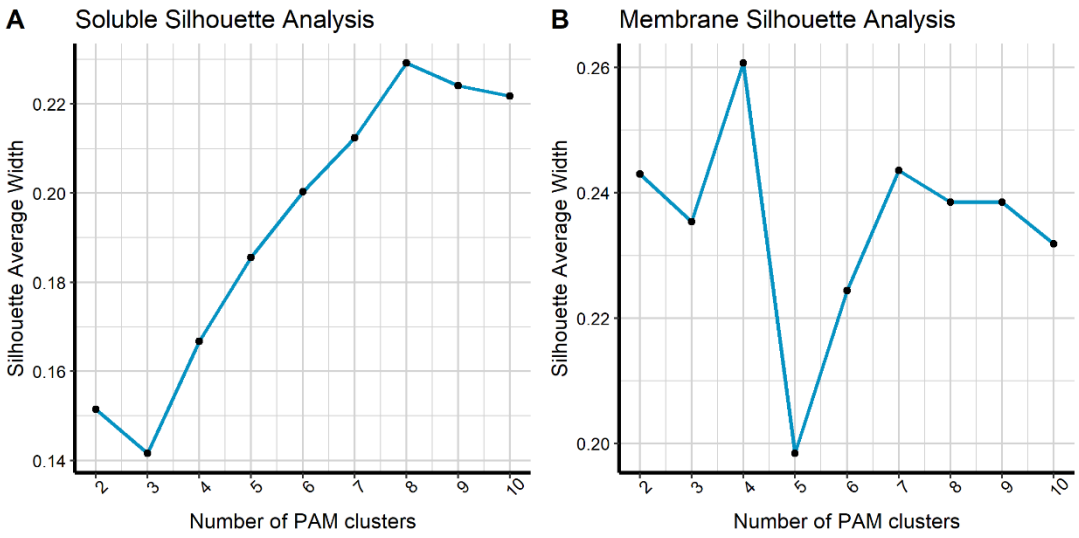

Figure III. 7 - Average silhouette width of different number of clusters (*k*) for the backbone dihedral angles (φ, ψ) of the flexible loop connecting D2 and D3 domains. Silhouette scores for (A) the soluble and (B) membrane-bound interleukin-1 receptor type 1.

Figures III.8 and **III.9** provide information on the cluster populations and backbone dihedral angles (φ, ψ) of residues Leu201, Glu202, Glu203, Asn204 and Lys205 for each cluster representative. For the sake of illustration, only clusters holding >5% of the total population are represented in **Figure III.8**. Furthermore, the representative IL-1R1-ECD conformations derived from their backbone torsion angles of the linker were aligned to the D3 domain of the crystal structure (PDB entry 4GAF) to better visualize and compare the conformational dynamics between the soluble and membrane-bound receptors. Among the 8 clusters extracted from the soluble ECD simulations (**Figure III.8A**), backbone dihedral angle populations contributing to closed IL-1R1-ECD conformations are found in five clusters – 1S (21.9%), 3S (18.2%) 5S (10.3%), 7S (4.3%) and 8S (2.6%). The most populated, third and eighth clusters comprise the closed states prevalent across S2 and S3 trajectories, whereas the fifth and seventh clusters contain the structurally distinct closed conformations adopted by the soluble IL-1R1-ECD throughout the S5 trajectory. The major difference between these two different groups of conformations resides in the orientation of the Phi (φ) angle of Asn204, which differs significantly (**Figure III.9A**). We hypothesize that during the transition from open to closed IL-1R1-ECD, deviations on Asn204φ causes the linker in 5S and 7S to twist, allowing D3 to rotate relative to domains D1 and D2, yielding twisted-closed conformations. Indeed, the backbone ϕ angle adopted by Asn204 in these 5S and 7S conformations characterized by 85° and 110° rotations, respectively, agrees well with the Asn204φ angle measured in the closed IL-1R1-ECD X-ray structure (PDB entry 1G0Y), where D3 is rotated almost 170° relative to the first two domains of the receptor. Most the linker orientations sampling IL-1R1-ECD closed conformations undergo a change Glu202ψ and/or Glu203ψ angles (**Figure III.9B**), suggesting that the open-to closed conformational transition is

dependent on changes in these dihedral angles. The remaining clusters are densely populated with open twisted conformations. Clusters 2S (21.7%), 4S (15.3%) and 6S (5.9%) contain linker configurations inducing open twisted, skewed IL1R1-ECD states. As evident from **Figure III.9D**, residues Glu203ψ and Asn204ψ angles have relatively large deviations in these conformations, when compared to the open IL-1R1-ECD X-ray structure (PDB entry 4GAF). Accordingly, variations in these dihedral angles may drive the conformational change to twisted open states.

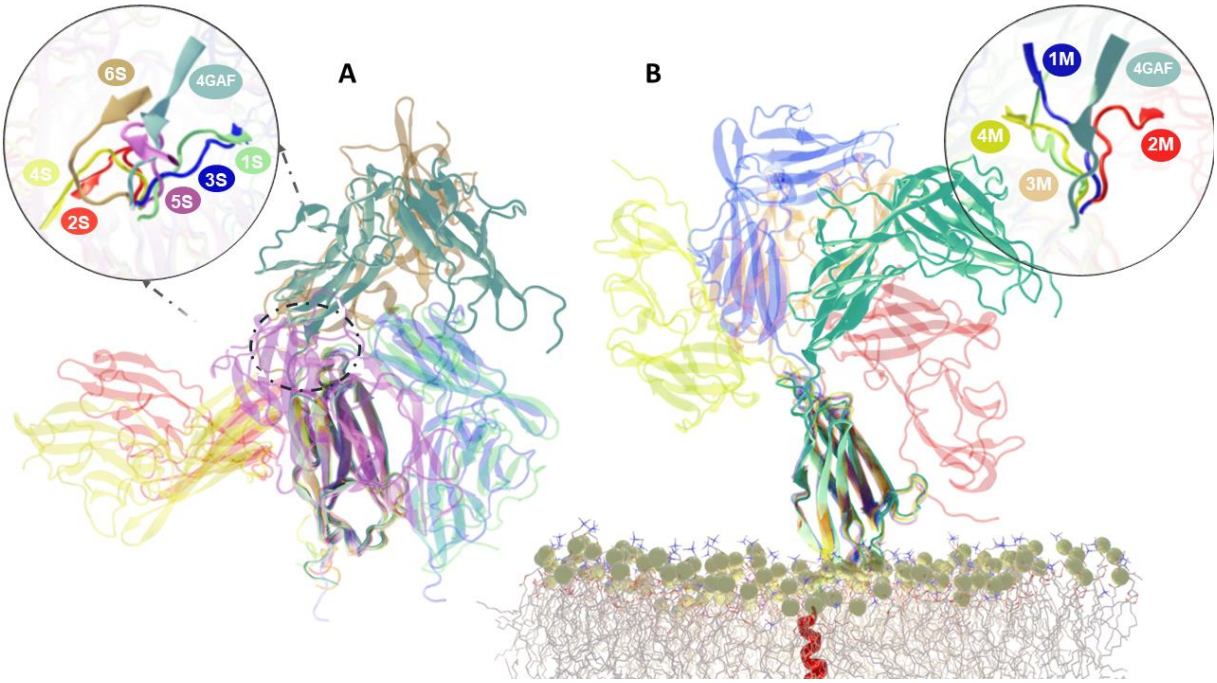

Figure III. 8 - Cluster representative structures of the extracellular domain of interleukin-1 receptor type 1 (IL-1R1-ECD) with a zoomed view of flexible linker orientations, derived from a clustering approach for linker conformations based on backbone dihedral angles (φ, ψ). Representative conformations for (A) the soluble and (B) membrane-bound IL-1R1-ECD MD simulations. All structures were aligned to the D3 domain of the X-ray structure of open IL-1R1-ECD configuration (PDB entry 4GAF), which is shown in dark green. Represented clusters of soluble ECD: Cluster 1 [1S] (green); Cluster 2 [2S] (red); Cluster 3 [3S] (blue); Cluster 4 [4S] (yellow); Cluster 5 [5S] (purple); Cluster 6 [6S] (brown). Represented clusters of membrane-bound ECD: Cluster 1 [1M] (blue); Cluster 2 [2M] (red); Cluster 3 [3M] (orange); Cluster 4 [4M] (yellow).

For the membrane-bound IL-1R1-ECD, the distribution of linker orientations in the clusters is different (**Figure III.8B**). The most populated cluster (1M) in the membrane-bound system comprises approximately 62,0% of backbone dihedral angles defining open conformations very similar to the open crystallographic structure. Indeed, backbone dihedral angles of 1M largely agree with the experimental data in this regard (**Figure III.9C** and **III.9D**). The population of dihedral angles representing closed ECD conformations is associated to cluster 2 (2M), containing 16,5% of the total ϕ and ψ angles. This cluster reproduces similar effects in phi and psi angles distributions as observed in clusters 1S, 3S and 8S (**Figure III.9A** and **III.9B**). Moreover, from this analysis it can be appreciated that the flexible linker of the soluble form

samples a wider range of closed conformations as compared to the membrane-bound IL-1R1-ECD system. The third (3M) and fourth (4M) clusters represent orientations of the backbone dihedral angles leading to open, twisted conformations, holding 11,8% and 10,2% of the total population, respectively. A comparable pattern of changes in Glu203ψ and Asn204ψ angles was found in these linker orientations, consistent with the observations made on the soluble system (**Figure III.9D**). Overall, comparison backbone dihedral angles (φ, ψ) extracted from the 5 residues composing the flexible linker of the soluble and membrane-bound IL-1R1-ECD demonstrates that the former samples a wide array, and far from its starting point, conformational populations, whereas the membrane-bound IL-1R1-ECD seems to undergo conformational changes with more limited structural deviations. Therefore, it can be concluded that the allowed backbone-dihedral angle conformational space is more restricted in the membrane-bound IL-1R1-ECD.

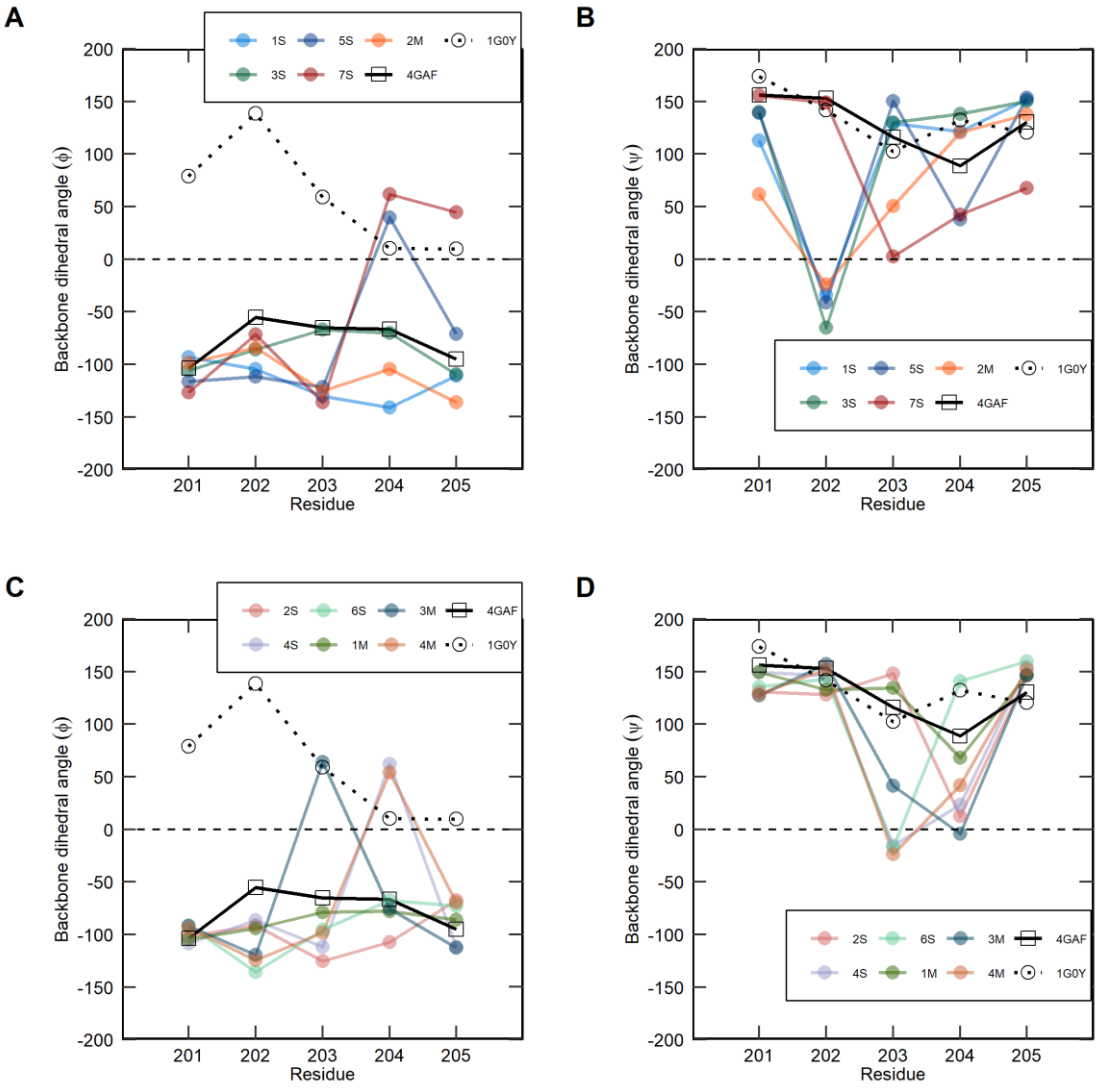

Figure III. 9 - Comparison of the calculated backbone dihedral angles, ϕ (A and C) and ψ (B and D), for the representative clusters of the extracellular domain of interleukin-1 receptor type 1 (IL-1R1-ECD) with those measured in the X-ray structures. The black solid line denotes the open IL-1R1-ECD (PDB entry 4GAF) and the

dashed line denotes the closed, twisted IL-1R1-ECD conformation (PDB entry 1G0Y). Represented clusters of soluble ECD: Cluster 1 [1S] (light blue); Cluster 2 [2S] (red); Cluster 3 [3S] (dark green); Cluster 4 [4S] (mauve); Cluster 5 [5S] (blue); Cluster 6 [6S] (light green). Represented clusters of membrane-bound ECD: Cluster 1 [1M] (green); Cluster 2 [2M] (orange); Cluster 3 [3M] (blue); Cluster 4 [4M] (brown).

3.3.5. Conformational dynamics of a putative binding site

The predicted binding site, located at the D1-D2 interface of the IL-1R1-ECD surface (**Figure III.10)**, was analysed with MDpocket (Schmidtke et al., 2011). To assess the stability of the pocket and its propensity to anchor small molecules, a characterization by means of two descriptors was performed: the pocket volume and the mean local hydrophobic density (**Figure III.11**). While the former reflects the size of the pocket, which is fundamental to the establishment of interactions with compounds, the second is a powerful predictor of the druggability of a binding site. The average volume of the pocket was ~ 411 $Å^3$ and 354 $Å^3$ for the soluble and membrane-bound IL-1R1-ECDs trajectories, demonstrating that both forms sample similar pocket volumes during the simulations. Likewise, the mean local hydrophobic density distributions are quite similar in the soluble and membrane-bound IL-1R1-ECDs, presenting average values of 53,7 and 49,9, respectively. These observed similar values are coherent with a higher stability of the D1 and D2 domains throughout the simulations, which can be related to a disulfide bond holding together these two domains, and highlights that irrespective of the IL-1R1-ECD form and conformational changes adopt, they minimally impact the geometrical and physicochemical environment of this potential binding region.

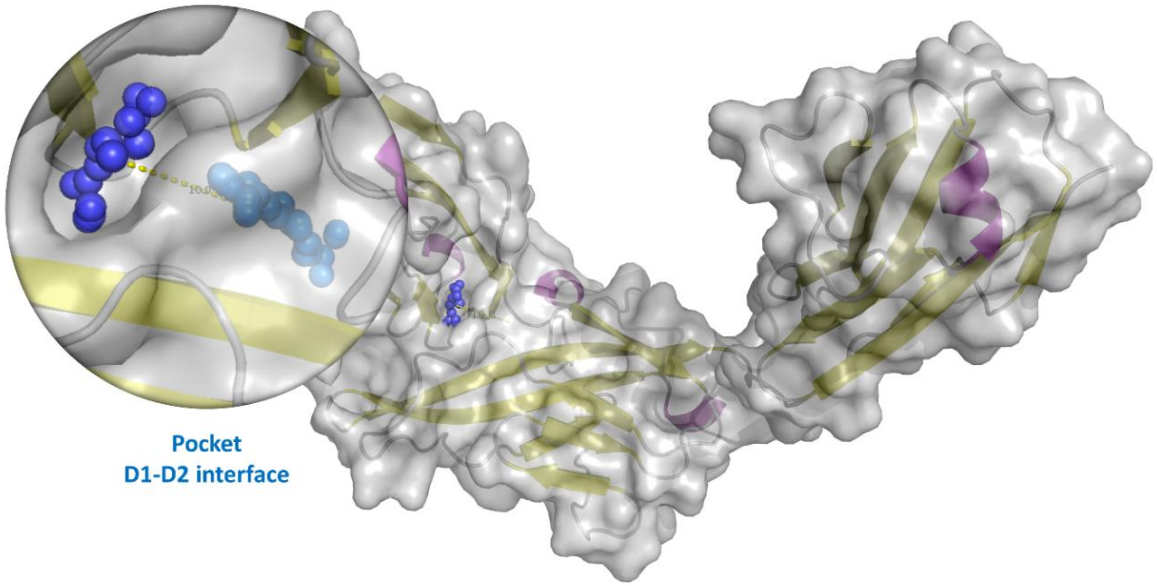

Figure III. 10 - Pocket located at the D1-D2 interface of the extracellular domain of interleukin-1 receptor type 1 (IL-1R1-ECD), detected with Fpocket. The pocket is formed by two adjacent sub-pockets (coloured in blue). The grid points lining the pocket were used as input for MDPocket.

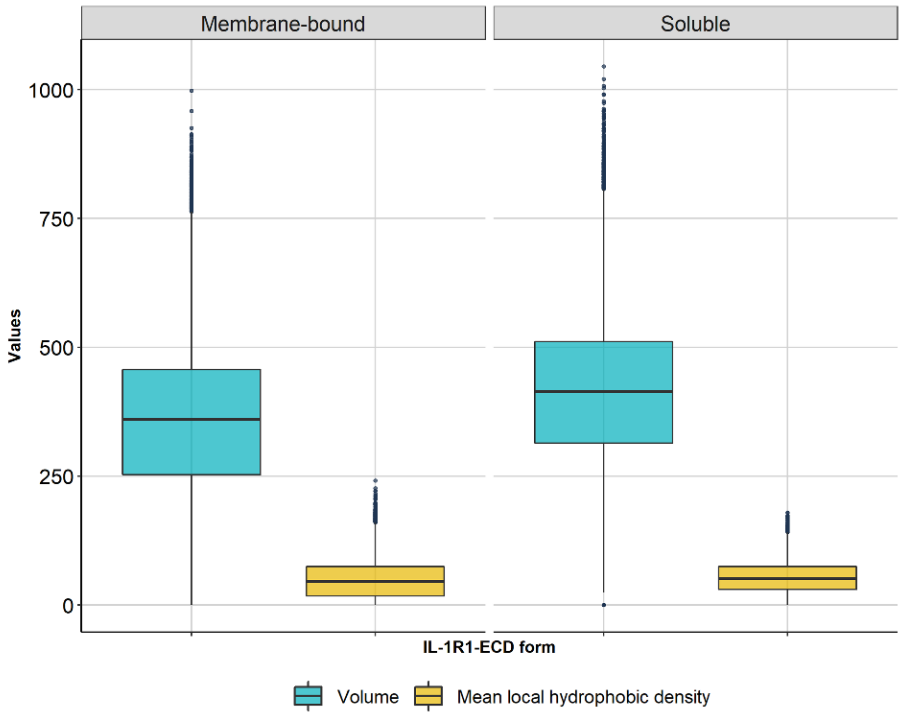

Figure III. 11 - Box-plot of the pocket volumes changes and mean local hydrophobic densities observed during the molecular dynamics simulations of the soluble and membrane-bound interleukin-1 receptor type 1. The volume is coloured in light blue and mean local hydrophobic density in yellow.

A PCA was performed to analyse and compare the contribution of the MDPocket's molecular descriptors to the physicochemical diversity explored by the putative IL-1R1 pocket during the MD simulations. The descriptors were projected onto the first two eigenvectors (PC1 and PC2), which capture ~60% of the pocket variability (**Figure B-7 and Table B-1** in the Appendix**)** for the two IL-1R1 forms. Overall, similar contributions were found on the soluble and membrane-bound IL-1R1 forms, with the pocket volume, solvent accessible surface area and apolar solvent accessible surface area presenting a higher influence in PC1, while the proportion of polar atoms and of apolar alpha spheres influences PC2 in a higher extent. These observations highlight parallel physicochemical properties between the pockets of soluble and membrane-bound IL-1R1-ECDs.

To extract representative pocket conformations for VS, the conformations of the pocket were clustered based on the molecular descriptors, using the PAM algorithm. In a similar manner to sub-section 3.3.4, the optimal number of clusters was estimated with the silhouette method, yielding *k*=3 as the best score for both forms (see **Figure B-8** in the Appendix). **Table III. 3** presents the main physicochemical features of the three extracted pocket conformations per IL-1R1-ECD form as well as the population of each cluster. Details on the application of these conformations in VS are presented in the Part IV.

Table III. 3 - Summary information about the representative pocket conformations extracted from the soluble and membrane-bound IL-1R1-ECD simulations. Four MDPocket descriptors computed for the cluster representative conformations are depicted, as well as the size of each cluster.

System	Cluster	Cluster size (%)	Volume (Å^3)	SASA (Å^2)	Proportion polar atoms	Mean local hydrophobic density
Pocket soluble	1	53.2	577.45	348.66	35.90	63.45
	2	23.8	398.50	239.64	27.94	52.51
	3	23.0	343.95	181.07	29.17	77.60
Pocket membrane	1	49.9	339.05	213.68	33.33	68.88
	2	28.0	528.22	325.70	39.13	66.54
	3	22.1	176.66	112.31	56.25	10.33

Table abbreviations: solvent-accessible surface area (SASA).

3.4. Concluding Remarks

In this chapter, we conducted all-atom MD simulations totalling 6 μs of IL-1R1 in a soluble form and inserted in a POPC lipid bilayer to compare the conformational landscape explored by the ectodomain (ECD) of both forms. Multiple MD runs allowed the exploration of the conformational space accessible to proteins through distinct structural pathways. Our MD simulations showed that the stability of the soluble and membrane-bound IL-1R1-ECD structures was maintained throughout the simulation timescales, without evidence of unfolding of secondary structure elements (i.e., α-helices and β-sheets). In addition, the full-length IL-1R1 protein remained stably bound to the POPC membrane, whose biophysical properties stayed consistent during the respective simulations. To the best of our knowledge, this is the first time that the full-length membrane-anchored IL-1R1 has been dynamically reproduced *in silico*.

The comparative conformational analysis of the two IL-1R1-ECDs forms suggests that the transition from open to closed states throughout the MD trajectories does not occur in a similar fashion – as imprinted in their Cα-RMSD profiles. PCA analysis reveals that the membrane-bound ECD visits more intermediate open conformations than the soluble ECD, before fully transitioning to the closed state, whereas the open-to-closed transition of the soluble IL-1R1-ECD is less populated by intermediate states. While both soluble and membrane-bound forms are able to sample a large population of open ECD conformations, our simulations demonstrate that the soluble receptor is able to explore to a higher extent the rotational

flexibility enabled by the linker connecting D2 and D3. By contrast, membrane-bound IL-1R1-ECD exhibits reduced conformational mobility. We thus contemplate that the distinct conformational path-ways observed are most likely induced by different degrees of D3 mobility via the flexible linker. In this sense, membrane anchoring and the close contact between the ECD of IL-1R1 and the lipid-bilayer surface seems to limit the conformational dynamics of the IL-1R1-ECD, when compared to the soluble form.

The flexibility of protein loops, i.e., the ability to adopt multiple conformations, is often critical to biological function and molecular recognition. These flexible, short regions allow significant hinge movements of structural domains, while maintaining the individual domains' 3D shape. To understand these movements in the IL-1R1-ECD, we measured the deviations in the hinge angles of the two ECD forms. We observed considerable differences in the overall distribution of hinge angles, revealing a wider mobile hinge-like motion of the soluble IL-1R1-ECD. Indeed, the hinge angles between D1-D3 ranged from 110° to 180°, compared to 120° to 172° angles occurring in the membrane-bound ECD. Hand-in-hand with the analysis of structural properties, these results suggest that the soluble and membrane-bound forms could favour the open, closed, and intermediate conformations of the ECD differently, which could reflect on different ligand recognition patterns and, hence, biological activity.

From our PCA results, the good overall agreement of our simulations with experimental data suggests that we have captured much of the essential structural dynamics of the two IL-1R1-ECD forms in the first two principal components (PCs), accounting for more than 85% of the total variation. Still, a notable difference between the soluble and membrane-bound IL-1R1-ECDs stand out when looking to PC3 and PC4, indicating different twisting motion patterns and low collinearity with the IL-1R1-ECD structures solved experimentally. These differences pointed to distinct arrangements of the flexible linker as the basis for the markedly different structure-dynamic relationships between the two IL-1R1 forms and the experimental data. With this in mind, the linker conformations sampled from the MD simulations were clustered based on the backbone dihedral angles (φ, ψ) of this region. For the soluble IL-1R1-ECD, a higher number of clusters was obtained, reflecting the extensive conformational diversity of the soluble system, suggesting a higher intrinsic interdomain flexibility of the linker in this IL-1R1 form. The dihedral angle changes on the closed and open-twisted conformations were similar in both forms: (i) the major contributions for closed conformations came from deviations on Glu202ψ and/or Glu203ψ angles; and (ii) changes in Glu203ψ and Asn204ψ torsion angles were mostly correlated with the adoption of open-twisted IL-1R1-ECD states. Interestingly, the soluble ECD features linker orientations leading to twisted-closed conformations characterized by 85° and 110° D3 rotations relative to D1-D2. Contributions to these conformations came in a great extent by changes of Asn204φ angle. Given the resemblance of these conformations with the twisted-closed IL-1R1-ECD crystallographic

structure, we expect that this structure should largely be sampled when the timescale of the simulations is extended in the future.

A single crystal structure only captures one conformation, providing limited information about a protein's dynamic behaviour, which can be an essential regulator of ligand recognition and binding. Therefore, it is important to consider the dynamic properties of proteins when predicting binding pockets. The geometrical and physicochemical evolution of a potential binding pocket located at the D1-D2 interface was assessed for the two IL-1R1 systems. Overall, the pockets behave similarly during the MD simulations, with a cumulative volume and mean local hydrophobic density comparable between forms. PCA was used to reduce cavity descriptor dimension to efficiently cluster and select representative pocket within a large set of conformations, yielding for each IL-1R1 form three cluster representative conformations.

The most relevant question of our work is arguably whether, and if so, how, the soluble form differs from the membrane-bound IL-1R1-ECD, in particular in relation to the structural and conformational preferences. It is concluded that major differences between the soluble and membrane-bound IL-1R1-ECDs appear to be mainly governed by the rearrangements of the linker connecting the D2 and D3 domains. We hypothesize that, in the soluble environment, in the absence of the structural restraints imposed by the lipid-bilayer, the φ/ψ torsional angles of the D2-D3 linker have a wider range of accessible values, whereas when anchored to a membrane the torsion angles of the linker are limited to a smaller set of possibilities, yielding limited and distinct IL-1R1-ECD conformations. Since both forms of IL-1R1 occur physiologically, our results contribute to the understanding of the distinct structure-dynamics behaviours of the soluble versus membrane-bound forms of IL-1R1, which may be of particular relevance in the context of therapeutic targeting of both ECD forms.

PART IV

An innovative, multi-layered, receptor-based virtual screening protocol targeting the extracellular domain of IL-1R1: a tale of hide and seek

"...the only simplicity to be trusted is the simplicity to be found on the far side of complexity."

Alfred North Whitehead

4.1. Introduction

The meteoric rise and ease of access to high powered computing cloud-based infrastructures and resources together with the rapidly increasing availability of protein 3D structures and public molecular databases have spurred the field of virtual screening (VS) forward at a rapid pace. In essence, the aim of VS consists on the prioritization of hit compounds for experimental validation among a large tailored virtual library, improving hit rates and the chemical diversity of the hits. The synergistic use of different and versatile cheminformatics tools (e.g., molecular docking, pharmacophore modelling and molecular similarity searches and analyses) at different steps of the VS workflow is critical to discover novel scaffolds and to an overall increase in chemical diversity of the hit list. Equally important, at an early stage of the VS workflow, screening libraries can be trimmed down using specific physicochemical properties according to the structural requirements of the biological target in question or the biodistribution to be attained, e.g., Lipinski's Rule-of-Five for *drug-likeness* or blood-brain barrier (BBB) permeation. Given their relevance within the context of the present chapter, a detailed explanation of the molecular filters used herein to tailor chemical libraries is provided in the next subsection.

In this chapter, a novel virtual screening pipeline with filtering layers was designed to discover IL-1R1 small molecule modulators. The key features of the designed framework include: a) receptor-based pharmacophore mapping using experimental and representative molecular dynamics (MD)-based IL-1R1 structures obtained in Part II and Part III of this work; b) pharmacophore-based virtual screening using a chemical library meeting the physicochemical criteria for BBB permeability; c) clustering of chemical structures by maximum common substructures (MCS); d) a hierarchical filtering approach based on a molecular docking stage and subsequent ranking via established protein-ligand interactions and pharmacophore fitness levels; e) compound prioritization within the top-ranked molecules via docking results and 3D-shape comparisons against a compound dataset holding relevant bioactivity profiles; and f) selection of promising compounds for biological evaluation based on chemical diversity and commercial availability.

Pharmacophore modelling and searches are computationally very efficient, enabling the VS of very large databases, either in a ligand-based or structure-based manner. The *pharmacophore* concept encodes a 3D map – with respect to a molecular structure – that represents a minimal set of features that adapt to the complementary casting mold of a target binding site. Importantly, a number of studies showed that the integration of information obtained from MD simulations can be useful to refine pharmacophore models by statistically characterizing the occurrence frequency and interaction patterns of pharmacophoric features (Sydow, 2015; Wieder et al., 2016). Here, we compared receptor-based pharmacophore models obtained from

a IL-1R1 X-ray structure with the pharmacophore models derived from representative MD conformations obtained in the previous chapter. The main goals of this effort were (i) to identify consensus features among MD conformations and compare with those incorporated in static pharmacophores models and (ii) to derive and characterize the most important pharmacophoric features on IL-1R1 binding site for VS endeavours.

One of the core elements of this VS framework has its roots in the basic dogma of Medicinal Chemistry, which asserts that structurally related small molecules often share similar properties and bind to the same target proteins. The modern understanding of molecular similarity analysis derived from the *Similar Property Principle* implies that close analogues may be either all active (albeit to a varying degree) or inactive, and thus screening too similar compounds may result in redundancy. With this in mind, in order to perceive shared scaffolds and thereby emphasize the extent and type of chemical (dis)similarities in the VS hit compounds, the MCS - the largest common part between two or more molecules excluding hydrogen atoms - was computed for each hit compound (Raymond and Willett, 2002).

To reduce the number of compounds to purchase, to undergo experimental testing and ultimately to synthesise, docking simulations were employed to predict and rank VS hits within each MCS cluster as putative binders to the IL-1R1 binding site. On the basis of chemical diversity, ranking of binding modes through intermolecular interactions with important amino acid residues in the binding site and fitness to the respective pharmacophore model, were integrated as a filtering criterion, allowing prioritization of compounds in each cluster. Subsequently, a 3D shape-based molecular similarity analysis was envisaged for compound prioritization based on known bioactivity values and thus, improve the hit rate and the identification of potential bioactive small molecules. The final selection of screening candidates (*cherry picking*) resulted from the combination of all conducted analysis, i.e., by manually inspecting docking poses, 3D-shape similarity scores, structural diversity and prioritized by factors such as commercial availability and intellectual property considerations.

4.1.1. The CNS physicochemical property space

From the pharmacological viewpoint, targeting the pro-inflammatory IL-1R1 may hold promise as a therapeutic strategy for central nervous system (CNS) diseases featuring neuroinflammation. Still, low CNS bioavailability of therapeutic agents have been constantly puzzling the scientific community due to the presence of the BBB. More than 98% of small molecules do not cross the BBB, whereas larger molecules essentially never succeed (Pardridge, 2007). Therefore, an important aspect to take into consideration during the screening/design of IL-1R1 small molecule modulators, within the setting of compartmentalized CNS inflammation, is their ability to cross the BBB.

The landmark study by Lipinski et al. famously derived a set of physicochemical properties for an adequate oral bioavailability profile of drugs, which became known as Lipinski's Rule of Five, given the fact that all numbers are multiple of five (Lipinski et al., 2001). These widely accepted and commonly applied rules for *drug-likeness* have spawned several studies attempting to fine-tune the physicochemical characteristics for optimal CNS exposure (Hitchcock and Pennington, 2006; Wager et al., 2010; Mikitsh and Chacko, 2014; Rankovic, 2015). Importantly, the main molecular parameters determining the ability of compounds to cross membranes include the molecular weight (MW), topological polar surface area (tPSA), lipophilicity, commonly expressed as octanol/water partition coefficient (clogP), the number of hydrogen-bond donors (HBD) and acceptors (HBA), ionization state (pKa) and rotatable bond (RB) count. Overall, numerous authors suggest a *window of opportunity* for designing CNS-penetrant compounds based on the following *medchem* rules:

- MW < 450 Da;
- LogP values between 2–5;
- PSA < 90 $Å^2$;
- HBA ≤ 7 and HBD ≤ 3;
- RB ≤ 8.

In this chapter, we approached the search for potential novel and chemically diverse IL-1R1 small molecule modulators by using a CNS-tailored virtual screening deck, assembled via the CNS-critical physicochemical parameters above referred. It is worth emphasizing, nevertheless, that the exact cut-off values for each of these parameters are still an *on-going* subject of continuous research and debate in the scientific community. These strict rules were used to trim down a library of more than 162 million compounds, yielding an *in silico* library endowed with molecules holding physicochemical properties matching those for BBB permeability.

4.2. Computational Methods

In this section, I detail the computational methods and parameters employed at different steps of the established VS framework against IL-1R1 (**Figure IV.1**). Since this protocol is a cascade of steps, the output of one step is the input for the following.

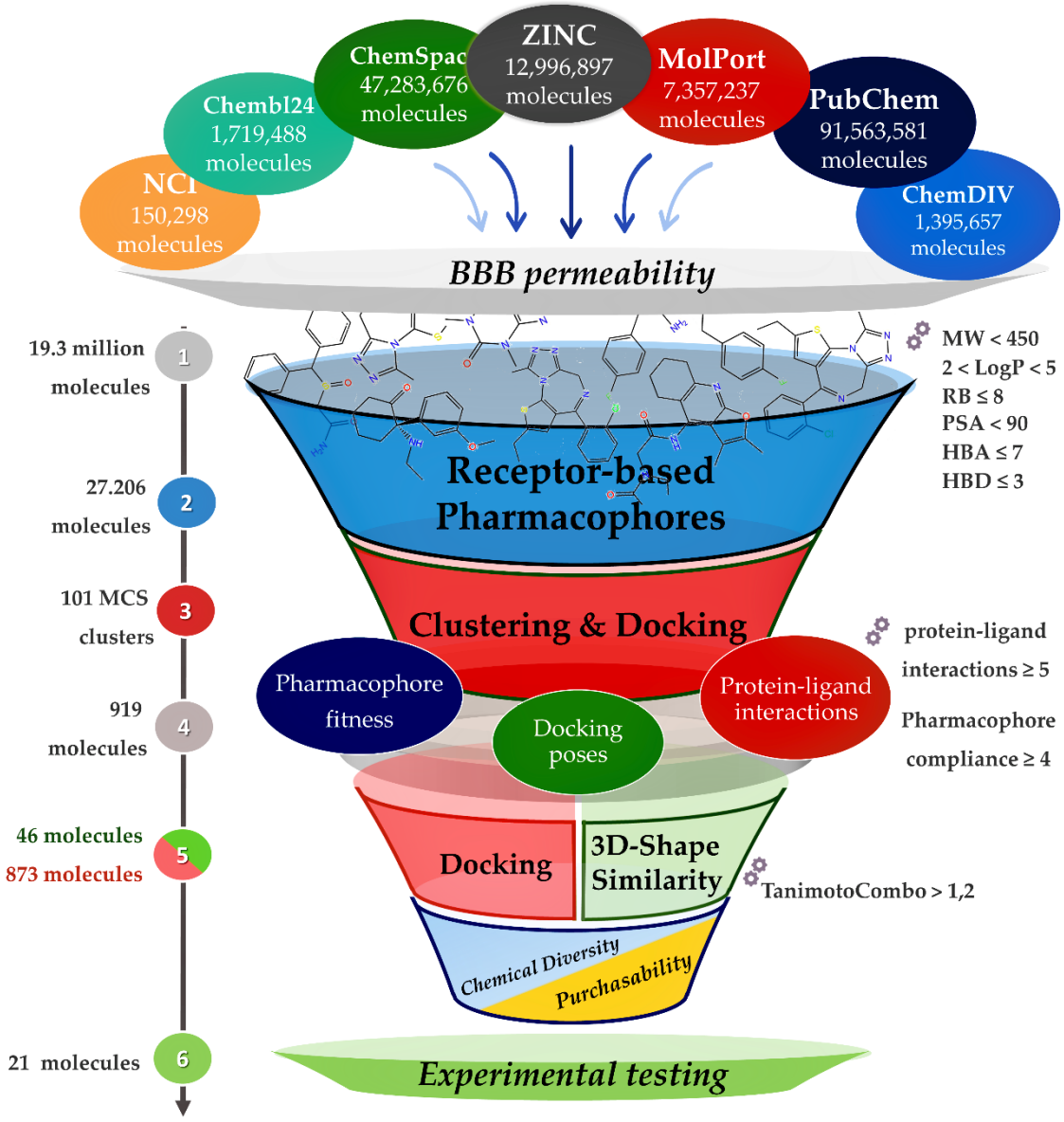

Figure IV. 1 - Schematic representation of the applied virtual screening cascade. This figure was inspired by a similar scheme in (Pérez-Regidor et al., 2016). *Figure abbreviations: BBB, blood-brain barrier; MW, molecular weight; logP, octanol-water partition coefficient; RB, rotatable bonds; PSA, polar surface area; HBA, hydrogen bond acceptors; HDB, hydrogen bond donors; MCS, maximum common substructure.*

4.2.1. Receptor-based pharmacophore modelling

LigandScout software v. 4.4.5, an industry-standard pharmacophore modelling package provided by Inte:Ligand (Wolber and Langer, 2005), was used to develop receptor-based pharmacophore models for IL-1R1. LigandScout allows for the generation of pharmacophore hypotheses based on the binding site topology, guided by the structural, physicochemical and pharmacophoric characteristics of that region. The computed 3D pharmacophore models contain idealized ligand pharmacophoric features - hydrophobic interactions (H), hydrogen

bond donors/acceptors (HBD/HBA), positive/negative ionisable areas (P/N) and aromatic rings (Ar) - together with a series of excluded volumes defining areas sterically hindered by the macromolecular environment and the shape of the binding site. The resultant 3D query pharmacophore models may then be screened against virtual libraries of compounds.

In Part III, we investigated the conformational flexibility of a binding pocket in the extracellular domain of IL-1R1 (IL-1R1-ECD), located at the D1-D2 interface. The idea was to study the differences between representative MD pocket conformations and an initial X-ray predicted binding site. Briefly, this site remained quite stable throughout the MD simulations, suggesting that this could be a viable region for small molecule binding. Due to the considerable size of the pocket and based on the different sub-pockets composing this cavity (see Part II), the pharmacophore models devised in this chapter were generated for two regions (**Figure IV.2**): i) a sub-pocket located at the core of the D1-D2 interface (henceforth referred to as sub-pocket 1); and (ii) a cavity formed primarily on three β-sheets located at the D1 region (henceforth referred to as sub-pocket 2).

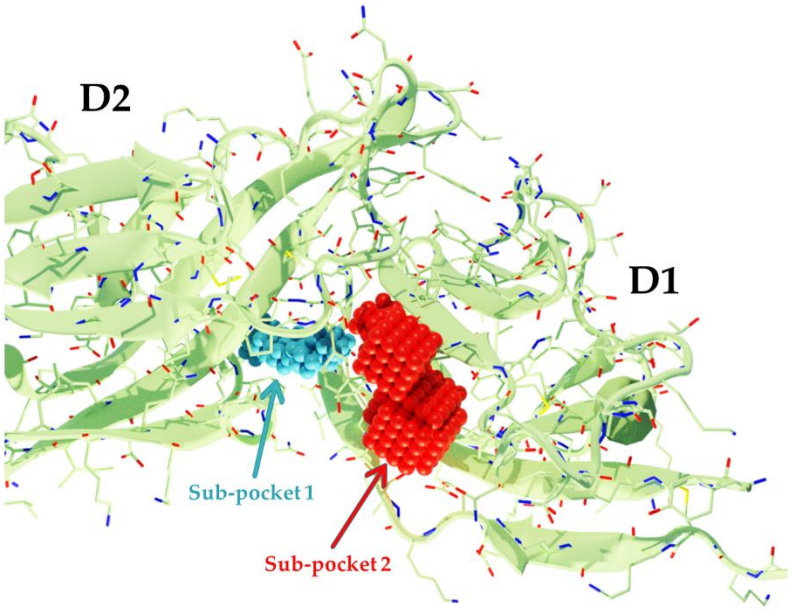

Figure IV. 2 - Predicted sub-pockets on the extracellular domain of interleukin-1 receptor type 1 used for pharmacophore modelling. Sub-pocket 1 (cyan) and sub-pocket 2 (red) are shown in a VDW (van der Waals) representation.

To carry out receptor-based pharmacophore perceptions in both sub-pockets, the following IL-1R1-ECD conformations were selected: (i) representative pocket conformations extracted from the MD clustering analysis (three cluster centroids for both soluble and membrane-bound IL-1R1-ECD – see Part III); (ii) six random selected MD conformations (three for each IL-1R1-ECD form); (iii) and the IL-1R1-ECD X-ray structure (PBD entry 4GAF). In total, 13

receptor conformations were used for 3D pharmacophore modelling. The pharmacophore models derived from the MD simulations and from the X-ray structure were then compared in a related manner as described by Wieder et al. (Wieder et al., 2016). A *merged* pharmacophore model was generated consisting of all features that are seen either in the experimental PDB structure or any of the MD-derived conformations, and their frequency was used to prioritize features in the model using the following considerations:

1. PDB pharmacophore features or MD-derived features present more than 80% of the time in the IL-1R1-ECD structures were considered *essential*;
2. PDB pharmacophore features or MD-derived features present more than 50% of the time in the IL-1R1-ECD structures were considered *important*;
3. PDB pharmacophore features or MD-derived features present less than 50% of the time in the IL-1R1-ECD structures were considered *not significant*.

The pharmacophore features were considered identical (and the frequency count was incremented) if the interacting environment residue(s) and the feature type were the same. On the basis of feature occurrence and their interaction patterns, three pharmacophore hypothesis combining predicted *essential* and *important* features were constructed for each sub-pocket.

4.2.2. Pharmacophore-based virtual screening

The resultant pharmacophore models were used as a 3D query to retrieve chemical compounds complementary to the pharmacophore features. Pharmacophore-based virtual screenings were performed using the online platform Pharmit (Sunseri and Koes, 2016), which enables the user the importation of pharmacophores from external programs such as LigandScout. For each defined combination of pharmacophore features, we selected and searched the pre-built compound databases available in Pharmit:

1) ZINC comprising 121,278,048 conformers for 12,996,897 molecules;
2) ChemBL24 comprising 22,744,939 conformers for 1,719,488 molecules;
3) ChemSpace comprising 235,890,796 conformers for 47,283,676 molecules;
4) MolPort comprising 106,341,521 conformers for 7,357,237 molecules;
5) ChemDiv comprising 20,709,131 conformers for 1,395,657 molecules;
6) NCI (National Cancer Institute) Open Chemical Repository comprising 1,589,632 conformers for 150,298 molecules;
7) PubChem comprising 443,659,442 conformers of 91,563,581 molecules.

The choice of filter definitions was a paramount aspect in this project, considering our goal of identifying small molecules that, besides being capable of targeting IL-1R1, could hold the ability to effectively crossing the BBB and thus, modulating neuroinflammation. Before

performing pharmacophore-based virtual screenings, filtering of the above-mentioned compound libraries was based on a combination of empirical *medchem* rules for BBB permeation: MW ≤ 450 Da; PSA ≤ 90 Å^2; 2 ≤ LogP ≤ 5; HBA ≤ 7; HBD ≤ 3; RB ≤ 8. In total, our final screening pool (number of molecules) for pharmacophore-based virtual screening consisted of:

1) ZINC comprising 5,257,020 molecules;
2) ChemBL24 comprising 565,226 molecules;
3) ChemSpace comprising 4,122,050 molecules;
4) MolPort comprising 3,309,363 molecules;
5) ChemDiv comprising 499,071 molecules;
6) NCI (National Cancer Institute) Open Chemical Repository comprising 19,147 molecules;
7) PubChem comprising 5,512,033 molecules.

During the search, a maximum number of 100 conformers were generated for each molecule and geometrical cut-off criteria was applied, using the receptor as exclusive shape, meaning that compounds clashing with the receptor structure were discarded (tolerance of 1 steric clash). Afterwards, redundant molecules between databases were eliminated based on their structural identity using their InChI (IUPAC International Chemical Identifier).

4.2.3. Clustering via Maximum Common Substructure

The *Konstanz Information Miner* (KNIME) is an open-source visualization software for data mining workflows, providing an excellent platform for cheminformatics and drug discovery (Berthold et al., 2008). The default implementation in KNIME integrates a wide range of nodes for cheminformatics purposes. In this project, to analyse (and visualize) the extent and type of chemical diversity in the VS compound datasets derived from each pharmacophore, scaffolds were grouped into hierarchical clusters by considering their MCS as a measure of similarity. This was accomplished via the Molecular Substructure miner (MoSS) (Borgelt et al., 2005) (**Figure IV.3**), a node in KNIME used for frequent molecular substructures and discriminative fragments in compound datasets.

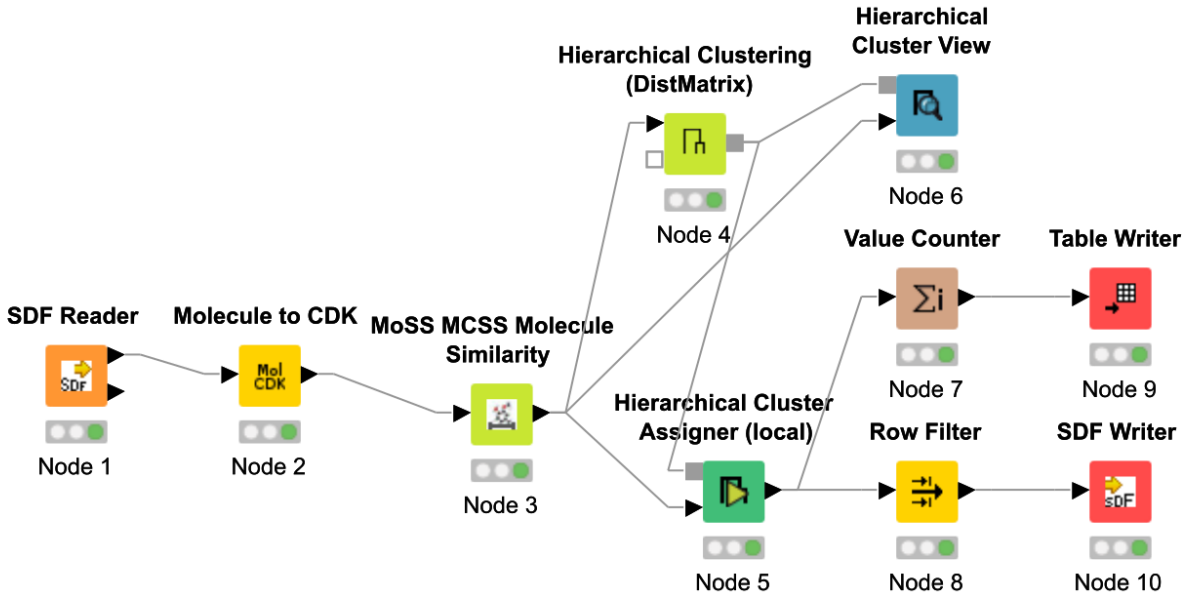

Figure IV. 3 - KNIME workflow employed to cluster molecular structures based on their Maximum Common Substructure (MCS). This workflow relies in three main steps: (1) calculating molecular distances using the maximum common substructure as a metric of similarity (*MoSS MCSS Molecule Similarity* node), (2) hierarchical clustering (*Hierarchical Clustering (DistMatrix)* node), and (3) assigning a threshold (distance threshold = 0.85) for cluster assignment (the *Hierarchical Cluster Assigner* node).

4.2.4. Molecular docking

Each MCS cluster was docked into its respective IL-1R1 sub-pocket using AutoDock v. 4.2.6. (Morris et al., 1998). The crystal structure of IL-1R1-ECD (PDB entry 4GAF) was used for this purpose. This receptor structure and all ligands were prepared using AutoDockTools v. 1.5.6 (Morris et al., 2009), by converting all files to PDBQT format, adding and merging non polar hydrogens, and computing Gasteiger charges. AutoGrid v. 4.2.6 was used to generate atom-specific affinity maps, electrostatic and desolvation potential maps for AutoDock, employing the default grid points and spacing of 60 and 0.375 Å, respectively, and a distance-dependent dielectric of -0.1465. The grid box for molecular docking was generated around the binding site residues of the protein. The Lamarckian genetic algorithm, as implemented in AutoDock, was used to generate orientations/conformations of the ligands. Ten docking runs were performed, with an initial population of 150 random individuals and a maximum number of 27,000 generations and 2,500,000 energy evaluations. Water molecules were excluded from the docking calculations. All other parameters were kept at their default values.

The scoring of the generated docking poses of the compounds within each MCS cluster was calculated using the AutoDock scoring function. Clearly, selection of only a few poses on the basis of the docking score might be unsuitable for IL-1R1, not only because of the well-known limitations of the scoring functions (Leach et al., 2006; Warren et al., 2006) but also lack a reference small molecule ligand bound to IL-1R1 to validate docking poses. Therefore, the

binding poses from the most populated/representative cluster for each docked molecule were considered for further analyses, despite the binding energy of the poses.

4.2.5. Quantitative analysis of protein-ligand interactions

The interactions between the docked poses of the compounds and the IL-1R1 residues lining the binding site were analysed in a programmatic way using an *in-house* script integrating the BINding ANAlyzer (BINANA) - a python-implemented algorithm for analysing ligand binding (Durrant and McCammon, 2011). The BINANA algorithm makes use of the AutoDock outputs to characterize key binding features: (i) close contacts receptor and ligands below or equal 2.5 Å and below or equal 4.0 Å; (ii) hydrogen bonds (distance cutoff = 4.0 Å and angle cutoff ≤ 40°); (iii) hydrophobic contacts; (iv) salt bridges; and (v) π-interactions, involving π-π stacking interactions between aromatic rings, T-stacking or edge-face interactions (perpendicular interactions of aromatic rings) and cation-π-interactions.

4.2.6. 3D Molecular similarity against the PubChem Bioassay database

Molecular shape complementary is known to correlate strongly with biological activity (Rush et al., 2005; Kortagere et al., 2009). It is therefore tempting to search for small molecules, with reported biological activity, holding shape complementarities to the VS hits, in order to filter and prioritize compounds from a large library to a number small enough for biological testing. The PubChem BioAssay database is an open-access repository providing bioactivity information of compounds tested in biological assay experiments, where each assay is referenced by a unique AID identifier (Wang et al., 2012). A single biological assay reports experimental activity results for a set of small molecules over a specific biological target, which in most cases is a protein. As of December 2021, 293 million bioactivity outcomes from more than one million assays were available in this database. The vast amount of available data allows for the development of 3D similarity searches against compound datasets exhibiting relevant biological activities on specific targets or molecular networks of interest.

In this project, with the aim of prioritizing compounds for experimental testing within the top-ranked VS compounds - not only by the docking poses achieved – we performed 3D shape similarity comparisons between the 919 top-ranked compounds and one dataset from the PubChem BioAssay database - *AID-743279*. This dataset contains 17,187 active compounds able to inhibit NLRP3 inflammasome signalling via cell-based phenotypic screening, using IL-1β downregulated levels as a read-out. This PubChem bioactivity dataset was selected based on the following criteria:

1. Small molecules with bioactivity signatures against IL-1R1-related proteins and molecular networks tested in adequate phenotypic assay;
2. Since the assay detects IL-1β reduction as the desired outcome, it is plausible that some of these compounds may target IL-1R1.

The comparison between compounds endowed with suitable pharmacophoric and physiochemical features to target IL-1R1 binding sites, and compounds with known biological data within the IL-1R1 signalling pathway may be useful to prioritize compounds for further experimental validation. Therefore, we leveraged these data as a reference to identify small molecules with similar 3D molecular architectures to a relevant active dataset, with the goal of identifying selective compounds that may be useful as tool or even lead compounds in a neuroinflammation experimental setting.

4.2.6.1. Conformer generation

Chemical structures, represented as SMILES, were obtained from the PubChem BioAssay *AID-743279*. Molecules were subjected to the following pre-processing workflow, based on OpenEye Scientific Software tools: (1) tautomer selection; (2) pKa normalization; (3) low-energy 3D conformer generation; (4) partial charges calculation; and (5) generation of 3D conformers (**see Figure IV.4**).

The first two steps of this workflow comprise tautomer generation and selection, and pKa prediction and selection, using *tautomers* and *fixpka* modules implemented in QUACPAC v.1.7.0.2 (OpenEye Scientific Software, 2013). By default, the tautomer generator program uses a *reasonable* function to obtain a representation regarding the physiologically preferred form, i.e. low-energy (the function works with a form of the molecule with formal charges removed), neutral pH (ionization states not enumerated) and aqueous-phase *tautomers*. Next, for pKa normalization, *fixpka* program was used to obtain molecules in their most energetically favourable ionization state at pH 7.4.

In the third task, single low-energy 3D conformers of compounds were calculated with the *oeomega* module (classic mode) implemented in OMEGA v.3.0.0.1 (Hawkins et al., 2010; OpenEye Scientific Software, 2019), followed by calculations of AM1BCC partial charges, using the module *molcharge* (method *am1bccsym*) implemented in QUACPAC v.1.7.0.2. (OpenEye Scientific Software, 2013).

The aim of the last task was to generate multiple conformers for all molecules in the PubChem dataset, calculated with the *oeomega* module (*rocs* mode) implemented in OMEGA v.3.0.0.1. The conformer ensembles were generated with a maximum of lowest-energy 50 conformers being retained.

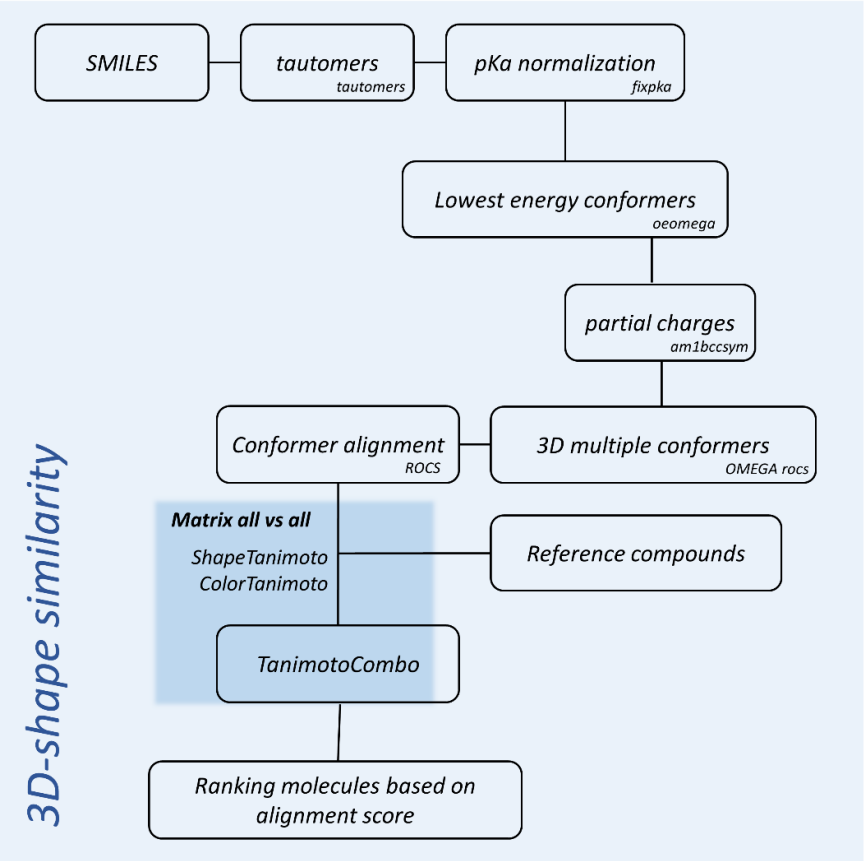

Figure IV. 4 - Flowchart for the 3D-shape similarity measurements. Molecule pre-processing and shape-based overlays used in this workflow were performed with OpenEye software package.

4.2.6.2. Shape and chemical similarity

3D-shape similarity comparisons were performed using ROCS v.3.2.2.2 (Rapid Overlay of Chemical Structures) (OpenEye Scientific Software, 2018). ROCS is a shape-based ligand-centric superposition method, which aligns molecules based on their volume represented by a set of atom-centred Gaussian functions. This representation of atoms allows a fast shape comparison of molecules due to the straightforward calculation of molecular overlaps providing sufficient speed for VS of large chemical databases. This method evaluates molecular similarity by measuring the shape and chemical (*colour*) definitions of two compounds (**Figure IV.5**), calculating Tanimoto coefficients from aligned overlap volumes:

$$\boldsymbol{Tanimoto_{a,b}} = \frac{\boldsymbol{O_{a,b}}}{\boldsymbol{O_a + O_b - O_{a,b}}} \boldsymbol{x\ 100}$$

Equation 1.1

where *Oa,b* is the aligned overlap volume between molecules *a* and *b*, *Oa* is the volume of molecule *a* and *Ob* is the volume of molecule *b*. The *colour* component included in ROCS take

the electrochemical feature types of overlapping groups - hydrogen bond donors/acceptors (HBD/HBA), positive/negative ionisable areas (P/N), hydrophobic interactions, and aromatic rings (Ar) - into consideration. The 3D overlays of chemical structures are ranked using a TanimotoCombo score, which consists of equally contributing components that assess the degree of volumetric (ShapeTanimoto) and chemical match (ColorTanimoto) similarity upon alignment. This score ranges between 0 (no overlap/similarity) and 2 (excellent shape and chemical-feature match).

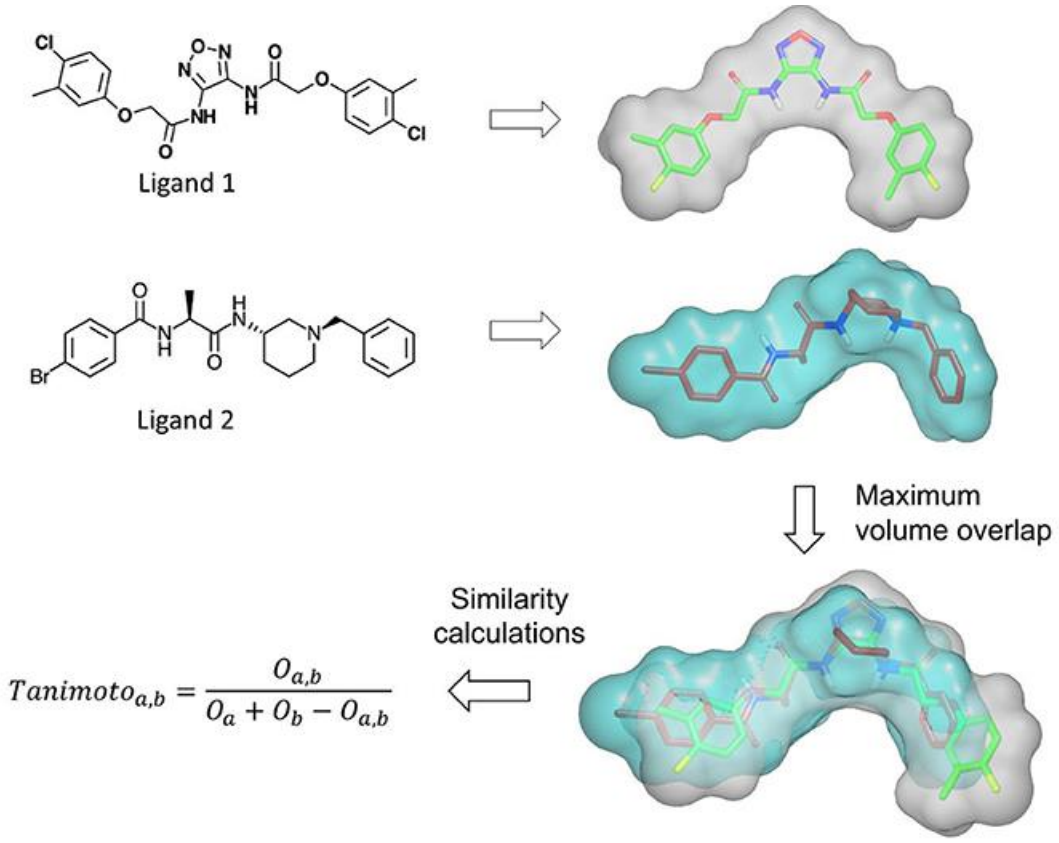

Figure IV. 5 - Schematic representation of the superposition of two molecules performed by the Rapid Overlay of Chemical Structures (ROCS) algorithm. The figure was adapted from (Kumar and Zhang, 2018).

Using OpenEye ROCS v.3.2.2.2, 919 low-energy conformers of the VS top-ranked compounds were overlaid with up the 17,187 active compounds retrieved from PubChem BioAssay database - *AID-743279*. Compounds holding a TanimotoCombo score higher than 1.2 were analysed in detail and considered for experimental testing.

4.3. Results and Discussion

In the following sub-sections, we report the results obtained for the VS procedure implemented to identify chemical scaffolds binding to the predicted sub-pockets on the IL-1R1-ECD surface. The results are presented for each stage of the VS protocol.

4.3.1. Receptor-based pharmacophore modelling

Two sub-pockets within the D1-D2 interface region of the IL-1R1-ECD, harbouring key residues involved in cytokine binding, were selected as the target for searching small molecule modulators of IL-1R1. 3D pharmacophore queries were devised for each sub-pocket by combining the feature frequency information derived from the X-ray structure of IL-1R1 and from MD representative conformations of the pocket of interest. As mentioned in the Methods section, the frequency count of pharmacophore features may be useful to validate or optimise static pharmacophore models, since additional information on dynamics can be reasonably used to prioritize important pharmacophore features. A detailed analysis of the occurrence percentages of pharmacophoric features using the PDB and MD conformations is provided in **Table IV.1**. By analysing the frequency profile of individual pharmacophore features, it can be recognized that the PDB features appear more stable than the MD-derived ones. In other words, all IL-1R1 conformations analysed display high frequencies for most PDB features and low frequencies for the MD-derived features. Still, a higher degree of stability differences is perceived on hydrogen bond features when compared to the other feature types. We argue that the definition of hydrogen bond interactions encoded in LigandScout might explain these differences. This software assign hydrogen bonds features by applying direction and distance constraints, i.e., the interaction partners must be within a specified angle range and nearer than a certain distance threshold limit. On the other hand, hydrophobic or charged features have a distance constraint only. As such, subtle changes in the geometry of the binding site environment may lead more easily to different acceptor-donor pairs classifications as hydrogen bonds.

Table IV. 1 - Statistic variations of the pharmacophoric features in the IL-1R1 conformations.

Sub-pocket 1							
	Merged features	**PDB features**			**MD-derived features**		
Feature type	**Total[1]**	**Total[1]**	**>80% [2]**	**>50% [3]**	**Total[1]**	**>80% [2]**	**>50% [3]**
Hydrophobic	12	8	4	6	4	0	1
N	1	1	1	1	0	0	0
P	4	3	2	3	1	0	0
Aromatic	5	3	2	3	2	0	1
HBA	6	2	1	1	4	1	2
HBD	9	5	1	3	4	0	2
Sub-pocket 2							
	Merged features	**PDB features**			**MD-derived features**		
Feature type	**Total[1]**	**Total[1]**	**>80% [2]**	**>50% [3]**	**Total[1]**	**>80% [2]**	**>50% [3]**
Hydrophobic	14	10	3	7	4	0	1
N	2	1	1	1	1	0	1
P	3	2	2	2	1	0	0
Aromatic	5	3	2	3	2	0	0
HBA	6	3	0	2	3	0	1
HBD	8	5	1	4	3	0	1

[1] total frequency count for a particular feature type; [2] number of instances of a particular feature type present >80%; [3] number of instances of a particular feature type present >50%.
Table abbreviations: negative ionizable (N): positive ionizable (P); hydrogen bond acceptors (HBA); hydrogen bond donors (HBD); Protein Data Bank (PDB); Molecular dynamics (MD).

Three distinctive pharmacophore arrangements were constructed for these two IL-1R1 potential binding regions by using specific combinations of the essential and important features (present >80% and >50%, respectively), discerned from the frequency analysis. **Figures IV.6** and **IV.7** display the occurrence frequency and interaction patterns for the most dominant pharmacophore features and the three final models developed for sub-pocket 1 and 2, respectively.

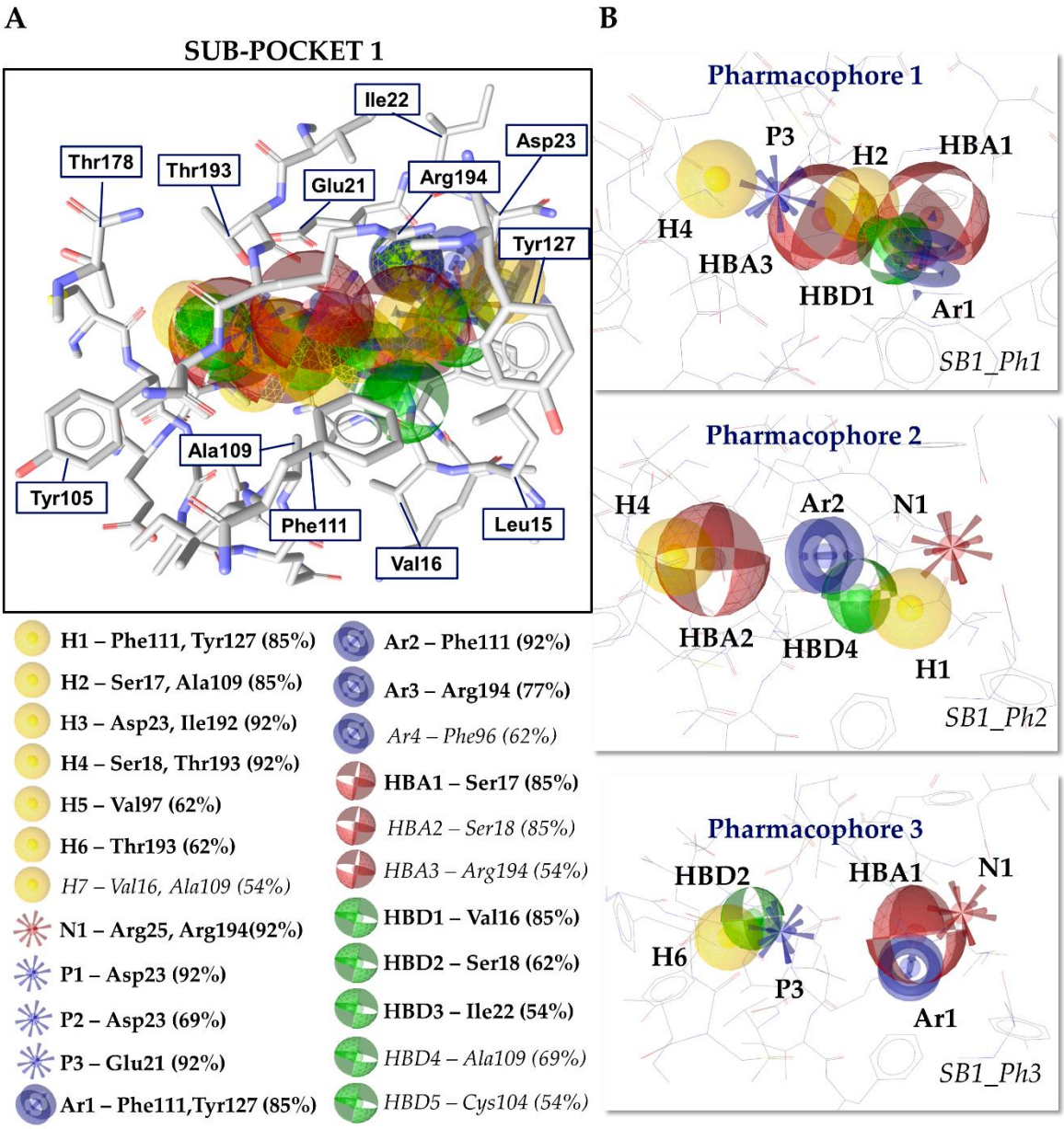

Figure IV. 6 - Receptor-based three-dimensional (3D) pharmacophore queries generated with LigandScout for the sub-pocket 1 of interleukin-1 receptor type 1 (IL-1R1). (A) Merged pharmacophore model consisting of all features that are present either in the experimental structure or in the molecular dynamics (MD) snapshots. The detailed pharmacophore analysis located below the merged model represents the frequency in percent with which individual features are present in the pharmacophore models from which the merged model was constructed. Bold features indicate features appearing in the crystal structure and MD-derived structures, whereas italic features appear only in the MD snapshots. (B) 3D models of pharmacophore hypothesis devised using different combinations of features based on the frequency information. Feature types are colour- and shaped-coded as follows: aromatic interactions (Ar, blue spheres), hydrogen bond donors (HBD, green spheres), hydrogen bond acceptors (HBA, red spheres), hydrophobic interactions (H, yellow spheres), positively ionizable groups (P, blue stars) and negatively ionizable groups (N, red stars). The radius of the sphere corresponds to the applied spatial tolerance. For the sake of clarity, exclusion volume spheres are not displayed.

For sub-pocket 1, the generated pharmacophore model 1 (SB1_Ph1) consists of: two hydrophobic centers located between Ser17 and Ala109 (H2), and Ser18 and Thr193 (H4); an aromatic feature directed towards the side-chains of Phe111 and Tyr127 (Ar1); a positive ionisable area near the carboxylate group of Glu21 (P3); a hydrogen bond donor feature pointing towards the carbonyl oxygen of Val16 (HBD1); and two hydrogen bond acceptor features, which pair with the side-chains of Ser17 (HBA1) and Arg194 (HBA3). Pharmacophore query 2 (SB1_Ph2) is characterized by: two hydrophobic regions involving contacts with Phe111 and Tyr127 (H1), and Ser18 and Thr193 (H4) side-chains; a negative ionisable feature (N1) interacting with guanidinium groups of Arg25 and Arg194; an aromatic ring pointing towards Phe111; a hydrogen bond acceptor feature directed to the hydroxyl group of Ser18; and a hydrogen bond donor feature pointing towards the carbonyl oxygen of Ala109. Pharmacophore hypothesis number 3 (SB1_Ph3) contains: a hydrophobic group located near Thr193 (H6); a positive (P3) and a negative ionic (N1) area spaced by 8 Å, establishing interactions with the nearby Glu21 and Arg194, respectively; one aromatic ring feature observed between the aromatic moieties of Phe111 and Tyr127 (Ar1); a hydrogen bond acceptor directed to the hydroxyl group of Ser17 (HBA1); and one hydrogen bond donor near Ser18 (HBD2).

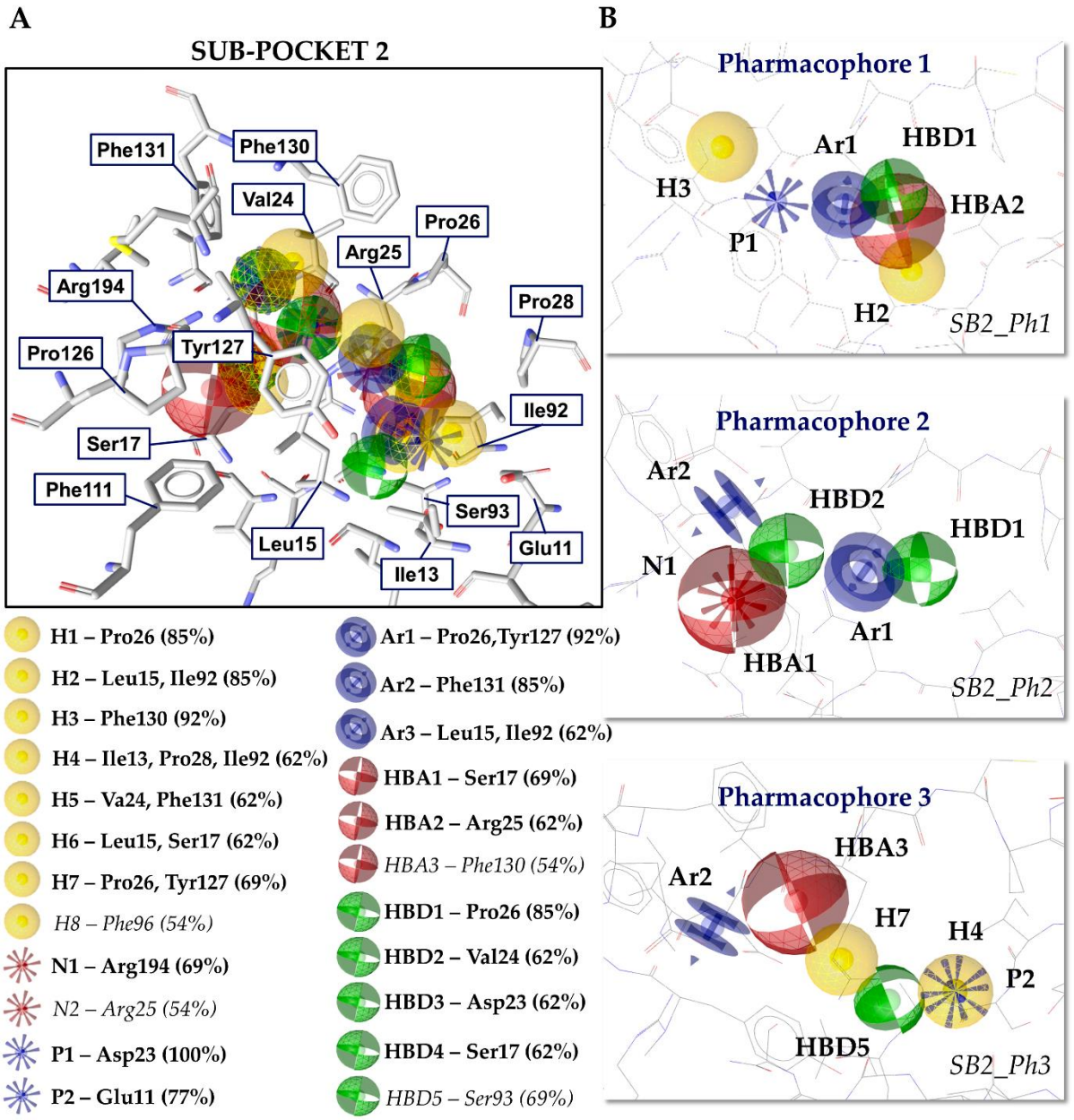

Figure IV. 7 - Receptor-based three-dimensional (3D) pharmacophore queries generated with LigandScout for the sub-pocket 2 of interkeukin-1 receptor type 1 (IL-1R1). (A) Merged pharmacophore model consisting of all features that are present either in the experimental structure or in the molecular dynamics (MD) snapshots. The detailed pharmacophore analysis located below the merged model represents the frequency in percent with which individual features are present in the pharmacophore models from which the merged model was constructed. Bold features indicate features appearing in the crystal structure and MD-derived structures, whereas italic features appear only in the MD snapshots. (B) 3D models of pharmacophore hypothesis devised using different combinations of features based on the frequency information. Feature types are colour- and shape-coded as follows: aromatic interactions (Ar, blue spheres), hydrogen bond donors (HBD, green spheres), hydrogen bond acceptors (HBA, red spheres), hydrophobic interactions (H, yellow spheres), positively ionizable groups (P, blue stars) and negatively ionizable groups (N, red stars). The radius of the sphere corresponds to the applied spatial tolerance. For the sake of clarity, exclusion volume spheres are not displayed.

As to sub-pocket 2, pharmacophore query 1 (SB2_Ph1) contains six features encompassing: one aromatic centroid located at the geometric center between the Pro26 ring and Tyr127 aromatic side-chain (Ar1); two hydrophobic features interacting with Leu15, Ile92 (H2) and Phe130 (H3) amino acids; a positive ionisable region near the carboxylic side-chain of Asp23 (P1); a hydrogen bond acceptor involving the guanidinium group of Arg25 (HBA2); and a hydrogen bond donor pointing towards the backbone carbonyl group of Pro26 (HBD1). In pharmacophore model 2 (SB2_Ph2), features Ar1 and HBD1, observed frequently in the generated pharmacophore models, were maintained. Differently, this model also includes an aromatic feature engaged with the benzene ring of Phe131 (Ar2), one negative ionisable region located near Arg194, a hydrogen bond acceptor feature pointing towards the side-chain $^{-}$OH group of Ser17, and a hydrogen bond donor feature directed to the backbone carbonyl of Val24. Finally, pharmacophore query 3 (SB2_Ph3) holds six features, including: Ar2, which is also observed in second pharmacophore model; two hydrophobic centers contacting the side-chains of Pro26, Tyr127 (H7), Ile13, Pro28 and Ile92 (H4); positive ionisable feature placed near the COO^{-} group of Glu11; a hydrogen bond acceptor involving the backbone nitrogen of Phe130 (HBA3); and a hydrogen bond donor with the hydroxyl group of Ser93 amino acid (HBD5).

4.3.2. IL-1R1 pharmacophore-based virtual screening results

The pharmacophore models SB1_Ph1, SB1_Ph2, SB1_Ph3, SB2_Ph1, SB2_Ph2 and SB2_Ph3 were then used to search pre-existing chemical databases to identify molecules that best match with the pattern of that pharmacophore 3D maps, using Pharmit. This software was employed because it allows the incorporation and access to pre-built libraries from both public and commercial sources such as NCI Chemical Repository, ChEMBL, MolPort, ZINC, ChemSpace, and PubChem, providing an interactive screening of millions of chemical compounds. Importantly, prior to pharmacophore-based virtual screening experiments, chemical libraries were filtered based on empirical physicochemical properties for BBB permeability (see Methods section). In this way, all pharmacophore models were subjected to screening using CNS-tailored libraries, i.e., containing molecules putatively endowed with physicochemical properties suitable for CNS penetration.

The amounts of retrieved compounds captured by each pharmacophore model are shown in **Table IV.2**. Noticeably, some pharmacophore models were found rather restrictive and retrieved a lower number of molecules, while others return a large number. For instance, the pharmacophore models SB1_Ph3 and SB2_Ph2 retrieved 1604 and 2341 molecules, respectively, probably owed to the two aromatic features or the two ionisable regions present in each pharmacophore. In contrast, SB1_Ph2, SB2_Ph1 and SB2_Ph3 identified more than 5000

molecules, demonstrating that different pharmacophore models may have quite different performance in screening a chemical database.

Table IV. 2 - Description of 6 pharmacophore hypothesis devised for the two IL-1R1 sub-pockets and the number of compounds captured by each pharmacophore model.

Sub-pocket 1				
Query	**# features**	**Hypothesis Description[1]**	**Constraints**	**# retrieved compounds**
SB1_Ph1	7	HBA1-HBD1-Ar1-H2-HBA3-P3-H4	Ar, H, N, P, HBD- radius 1.5 Å HBA - radius 2.25 Å Steric constraints - binding site surface atoms (tolerance of 1) [1]	3333
SB1_Ph2	6	H1-N1-HBD4-Ar2-HBA2-H4		7721
SB1_Ph3	6	HBA1-Ar1-N1-P3-HBD2-H6		1604
Sub-pocket 2				
Query	**# features**	**Hypothesis Description**	**Constraints**	**# retrieved compounds**
SB2_Ph1	6	H2-HBA2-HBD1-Ar1-P1-H3	Ar, H, N, P, HBD- radius 1.5 Å HBA - radius 2.25 Å Steric constraints - binding site surface atoms (tolerance of 1) [1]	7178
SB2_Ph2	6	HBD1-Ar1-HDB2-HBA1-N1-Ar2		2341
SB2_Ph3	6	P2-H4-HBD5-H7-HBA3-Ar2		5029

[1] *exclusive shape constraint, which filters compounds with steric clashes with the receptor (tolerance of 1 steric clash).*
Table abbreviations: negative ionizable (N): positive ionizable (P); hydrogen bond acceptors (HBA); hydrogen bond donors (HBD); hydrophobic interactions (H); aromatic rings (Ar).

4.3.3. Inspection and ranking of virtual screening hits

The high amount of VS retrieved molecules (27206) makes it unfeasible (in terms of human resources, time and trial cost) to perform an experimental validation of all the predicted molecules. Therefore, to narrow down the number of molecules to be tested experimentally, a combination of MCS clustering and molecular docking was used for filtering and ranking the screened compounds based on the docking poses achieved, protein-ligand interactions and pharmacophore fitness levels of subsets with maximal chemical diversity. Throughout the following sub-sections, we present the main results derived from the implementation of such strategy.

4.3.3.1. Docking

KNIME chemistry node MoSS was used to cluster the molecules retrieved by each pharmacophore model, based on MCS. All compounds in each MCS cluster were docked into the two sub-pockets of IL-1R1 using the program AutoDock4 and its built-in free energy scoring function. Given that the docking program assigns a binding energy to each predicted pose (**Figure IV.8**), it would be expected and relatively easy to rank the molecules by their binding energies. Still, the limited accuracy of scoring functions in discerning between actives and inactives, together with the absence of known reference small molecules bound to IL-1R1 to be used as starting points to validate docking poses, made us consider as other criteria for ranking (docked) compounds: quantification of protein-ligand interactions established and pharmacophore compliance. To our understanding, a higher number of poses concentrating on the same residues of a given binding site should correlate with a stronger preference for these residues, thereby indicating that compounds establishing interactions with these residues have a higher propensity to bind to the protein. Moreover, it provides an alternative to energy ranking for the identification of probable poses and can serve to reduce the number of unlikely poses.

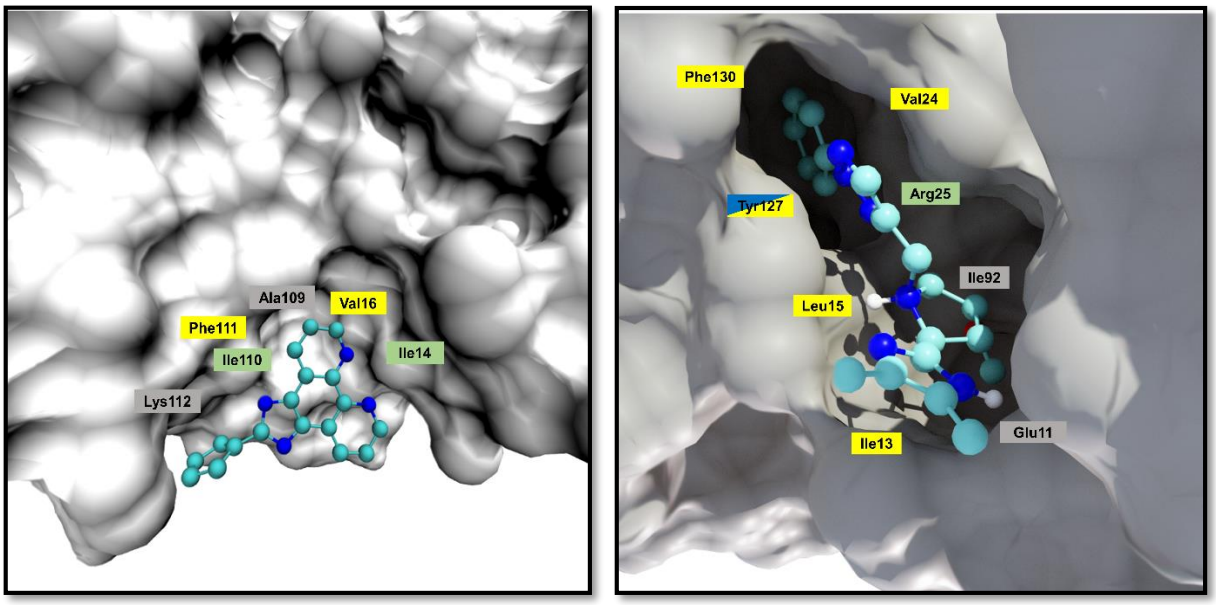

Figure IV. 8 - Comparison of top-scoring poses generated by Autodock for sub-pockets 1 and 2 of IL-1R1 extracellular domain. Left side: IL-1R1 sub-pocket 1 complexed with molecule establishing interactions with residues on one side of the sub-pocket: Ile14, Val16, Ala109, Ile110, Phe111, Lys112. Right side: IL-1R1 sub-pocket 1 complexed with molecule establishing interactions with residues on both sides of the sub-pocket: Glu11, Ile13, Leu15, Val24, Arg25, Ile92, Tyr127, Phe130. The binding region of sub-pocket 1 presents a shallow surface indentation, whereas sub-pocket 2 presents a deep binding region. The interaction type is color-coded: hydrogens bonds are coloured green, hydrophobic interactions are coloured yellow, aromatic interactions are coloured blue and close contacts are coloured gray.

4.3.3.2. Quantitative analysis of protein-ligand interactions

Protein-ligand interaction analyses for the docked ligands on IL-1R1 were computed with the program BINANA to trace the binding propensities of small molecules on the two sub-pockets. **Figure IV.9** provides a detailed mapping of the intermolecular pairwise interactions established between the compounds captured by each pharmacophore model and the respective sub-pocket amino acids, after the molecular docking stage. For sub-pocket 1, encompassing the docked compounds devised from pharmacophores SB1_Ph1, SB1_Ph2 and SB1_Ph3 (**Figure IV.9A**, **IV.9B** and **IV.9C**), 2.5 Å-contacts were significantly higher for Val16, Ser17, Ala109, Phe111, Tyr127 and Arg194. Also, these residues are by far the most implicated in intermolecular contacts at a 4.0 Å distance cutoff, with more than 80% of the docked poses presenting established contacts with them. Such observations are considerably correlated with the prevalence of hydrogen bonds and hydrophobic interactions, crucial weak intermolecular interactions for determining the specificity and stability of receptor-ligand binding. Indeed, hydrogen bonding were preferentially formed with Val16 (11%), Ser17 (9%), Ser18 (10%), Ala109 (10%), Phe111 (19%), Tyr127 (13%) and Arg194 (14%). Likewise, the established hydrophobic interaction network is higher amongst these residues. In terms of other important non-covalent interaction patterns, the presence of cation-π interactions seemed to be more relevant for Tyr127 and Arg194, whereas π-π and T-stacking interactions are particularly formed with Phe111 and Tyr127. A salt bridge with the side-chain of Glu21 is found on average in 14% of the ligands docked at sub-pocket 1. Several other interactions were prevalent, though less common: hydrogen-bond interaction with Glu21 (3%), hydrophobic contacts with Ser18 (56%) and Thr193 (47%). This suggests that most of the IL-1R1-ligand interactions are formed primarily by residues on one side of the sub-pocket 1 binding interface, whereas the complementary side is scarce on pairwise interactions.

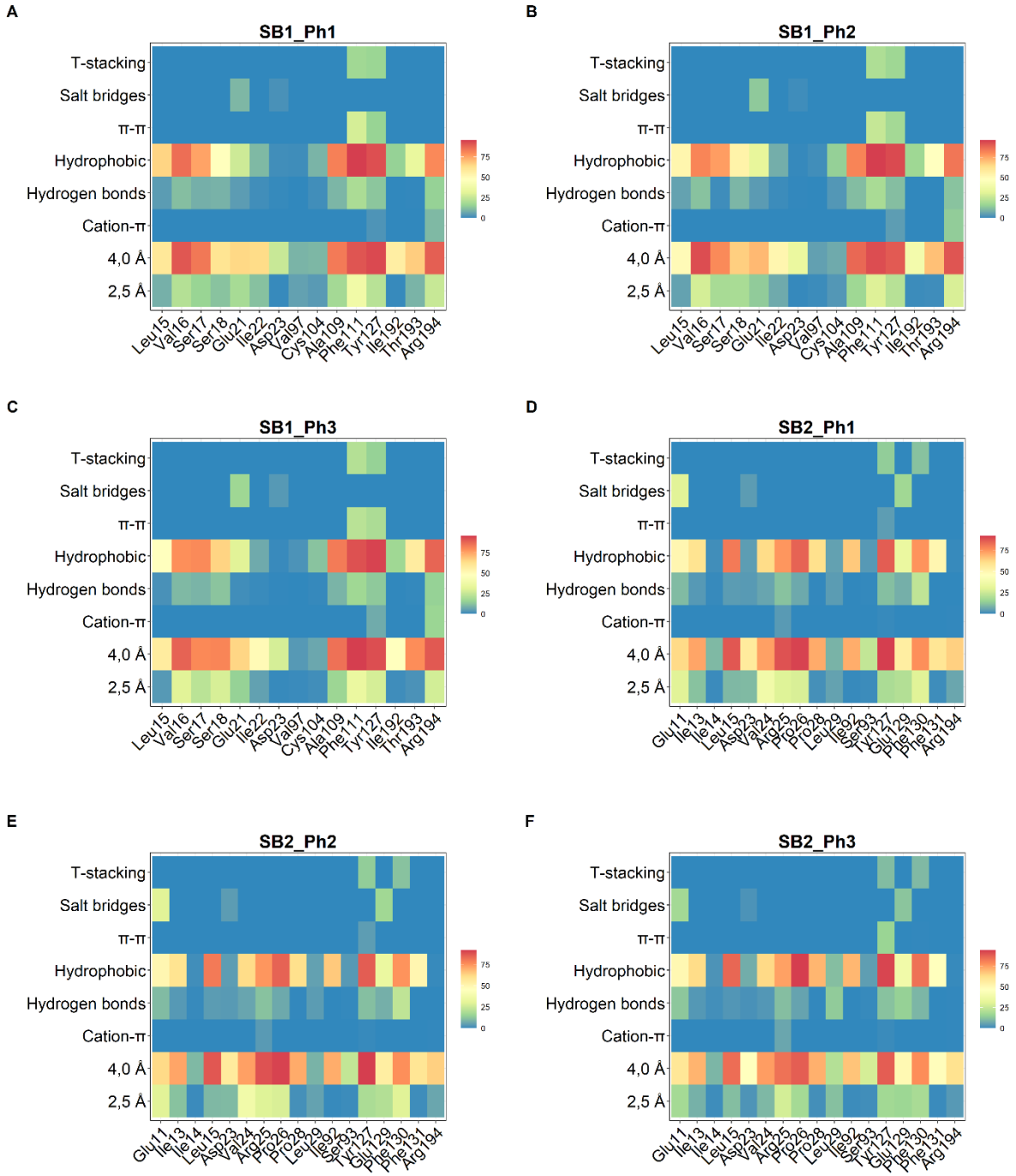

Figure IV. 9 - Heatmap of protein-ligand interaction patterns for the docked poses of each pharmacophore compound dataset at (A-C) sub-pocket 1 or (D-F) sub-pocket 2. Type of interactions analysed: close contacts within 2.5 and 4.0 Å radius, hydrophobic interactions, hydrogen bonds, salt bridges and π-interactions (π–π stacking, T-stacking and cation–π interactions). The percentage of contacts for each interaction type are color-coded: few interactions are coloured blue, while red colour indicates a larger contribution of the amino acid residue binding to the corresponding ligands.

Looking at the protein-ligand interaction profiles in sub-pocket 2 (Figure **IV.9D**, **IV.9E** and **IV.9F**), the compound datasets retrieved from the respective pharmacophores SB2_Ph1, SB2_Ph2 and SB2_Ph3 models exhibited similar pairwise interactions with the IL-1R1. They

differ with regard to: (i) the hydrogen bonds involving Leu29, which are more prevalent in SB2_Ph3 (14%), when compared to SB2_Ph1 (2%) and SB2_Ph2 (4%); (ii) a hydrogen bond interaction with Phe130, reaching values of 38% and 23% in SB2_Ph1 and SB2_Ph2, respectively, contrasting with the 10% verified for the compounds of pharmacophore SB2_Ph3; and (iii) the establishment of a salt bridge with Glu11, which is found in 30% and 18% of the ligands from SB2_Ph2 and SB2_Ph3, respectively, while only 3% of the docked structures of SB2_Ph1 present a salt bridge with Glu11. Interestingly, most of the ligands interact with residues from both sides of the sub-pocket 2 interface. Indeed, the 2.5 Å- and 4.0 Å-contacts span from Glu11 to Arg194, which are on opposite sides of the sub-pocket 2, presenting hydrophobic interactions with Leu15 (83%), Pro26 (91%), Tyr127 (91%) and Phe130 (83%). Overall, hydrogens bonds were primarily established with Glu11, Val24, Arg25, Leu29, Tyr127, Glu129 and Phe130, while salt bridges were preferentially formed with Glu11, Asp23 and Glu129. Another interesting feature characterizing a fraction of the docked ligands is their tendency to form perpendicular aromatic stacking arrangements with Tyr127 (average of 13%) and Phe130 (average of 13%), two aromatic residues lining sub-pocket 2. Cationic-π and π-π-interactions were evident for Arg25 and Tyr127, although with lower prevalence (5 and 7%, respectively).

4.3.3.3. Fitness of the virtual hits to the IL-1R1 pharmacophore models

The docked poses of the VS compounds were used as a post-screening tool to assess their compliance with the postulated pharmacophoric features for IL-1R1 binding. Detailed results are provided in **Table IV.3**. As expected, docking protocols employed in sub-pocket 2 were able to identify ligands that fit, in a higher extent, the pharmacophoric requirements of this region. The quantitative analysis of protein-ligand interactions also seems to support this interpretation. In contrast, ligands mapping to the pharmacophore models and fitting to the sub-pocket 1 of IL-1R1 yielded poor pharmacophore overlapping profiles.

Table IV. 3 - Compliance of the docked poses to the pharmacophore models devised for the two IL-1R1 sub-pockets.

Sub-pocket 1								
		Pharmacophore compliance (number of features)						
Query	**Total molecules**	**7**	**>6**	**>5**	**>4**	**>3**	**>2**	**>1**
SB1_Ph1	3333	0	32 (1,0%)	95 (2,9%)	201 (6,0%)	927 (27,8%)	2201 (66,0%)	3305 (99,2%)
SB1_Ph2	7721	*NA* [1]	65 (0,8%)	210 (2,7%)	813 (10,5%)	2521 (32,6%)	5002 (64,8%)	7467 (96,7%)
SB1_Ph3	1604	*NA* [1]	5 (0,3%)	12 (0,7%)	41 (2,6%)	621 (38,7%)	1273 (79,4%)	1600 (99,8%)
Sub-pocket 2								
		Pharmacophore compliance (number of features)						
Query	**Total molecules**	**6**	**>5**	**>4**	**>3**	**>2**	**>1**	
SB2_Ph1	7178	3183 (44,3%)	4002 (55,7%)	4781 (66,6%)	5991 (83,5%)	6903 (96,2%)	7171 (99,9%)	
SB2_Ph2	2341	305 (13,0%)	927 (39,6%)	1462 (62,5%)	1881 (80,4%)	2012 (85,9%)	2290 (97,8%)	
SB2_Ph3	5029	1702 (33,8%)	2698 (53,6%)	3525 (70,0%)	4001 (79,6%)	4761 (94,7%)	4978 (99,0%)	

[1] *NA, not applicable.*

From the filtering pipeline performed over the 27206 molecules retrieved via pharmacophore-based VS, compounds were ranked and prioritized based on 1) protein-ligand interactions ≥5 with amino acid residues that are involved in a pharmacophore and are known to be essential for cytokine binding; 2) compliance with at least 4 pharmacophore features; and 3) a maximum number of 4 compounds per MCS cluster. This yielded 919 top-ranking compounds from different MCS clusters and devised from the two sub-pockets. Most of these compounds derived from sub-pocket 2, since docked compounds at sub-pocket 1 mainly established interactions with residues on one side of the pocket, failing to identify molecular structures that matching the pattern of the pharmacophores generated for this region.

4.3.4. 3D-shape similarity analysis

To additionally increase the chance of finding a IL-1R1 small molecule modulator, 3D-shape similarity searches using ROCS and Tanimoto scoring (ShapeTanimoto and ColorTanimoto, for shape and chemical similarity, respectively) were performed. This methodology was employed as a screening model for the identification of molecular scaffolds within the 919 top-

ranking compounds possessing similar 3D structures with a bioactivity dataset of 17,187 compounds, originating from PubChem, which were shown to able to downregulate IL-1β production via a cell-based phenotypic screening.

Initial pre-processing calculations were performed on the VS and PubChem datasets, such as generation of tautomeric forms, pKa ionization, low-energy conformer calculation and partial charges assignment. The last step comprised multiconformer generation for each dataset (as described in the Methods section). To calculate the 3D molecular shape overlays, each compound in the VS dataset (multiconformer datasets) was aligned to a query, corresponding to the lowest-energy 3D-conformer of each active molecule from the PubChem dataset. Then, the 3D shape-based similarity of a given compound to the PubChem active compounds was ranked by a TanimotoCombo score, including both shape fit and colour (by combination of the shapeTanimoto plus ColorTanimoto), ranging between 0 and 2, with 2 representing maximal similarity (identity). Using this scoring scheme, 46 compounds among the 919 hits from the ROCS screening were found to have TanimotoCombo coefficients higher than 1.2 and were considered for selection.

4.3.5. Selection of virtual hits for experimental evaluation

Visual inspections of the 919 top-ranking compounds along with their docking and 3D-similarity scores were used to select an initial set of compounds for biological testing. The criteria used in the visual inspection for the assessment of the compounds included:

- Complementarity between ligands and IL-1R1 surface in terms of spatial occupancy of the sub-pocket;
- Direct inspection of their molecular properties, including MW, logP and PSA;
- Established interactions with important residues such as Leu15, Arg25, Pro26, Phe111, Tyr127 and Phe130 and compliance with pharmacophore features;
- Structural diversity, by selecting compounds showing sufficient physicochemical diversity among each other (different MCS clusters);
- Purchasability and commercial availability.

Out of all the top-ranking compounds, 21 compounds were selected for biological testing. Ten of the compounds were primarily selected according to their docking poses and established interactions, while eleven compounds were selected based on 3D-shape similarity measurements. All 21 compounds were available in shelve from different chemical suppliers and were purchased to be experimentally tested.

4.4. Concluding remarks

The main purpose of Part IV was to identify molecular scaffolds that explore the structural features of IL-1R1 for the development of small molecule modulators. The VS strategy presented here combined both receptor-based pharmacophore modelling and a filtering cascade grounded on molecular docking and 3D-shape similarity. Essentially, prioritization of compounds for experimental testing was performed according to the ranking generated vai docking poses, established protein-ligand interactions and pharmacophore compliance levels. In parallel, a side branch of prioritization employing ligand 3D-shape similarity was performed to enable the identification of molecules with similar shape and potentially interacting atoms to a dataset holding bioactive molecules that modulate the activity of the pro-inflammatory cytokine IL-1β.

First, the predicted sub-pockets for small molecule binding derived from the results of Part II and III were translated into six pharmacophore models by assigning receptor-based pharmacophore features based on the frequency of their appearance in the X-ray and MD structures. In other words, pharmacophore features present in the IL-1R1 structures with a high probability were likely to be more important than features exhibiting a low probability. Even though the frequency information alone may not be enough to rank pharmacophoric features, since receptor-based pharmacophore modelling is based only on the 3D-topology of the binding site, it generates many features and thus, statistical feature frequency can help make an informed decision about which features should be prioritized. Still, a significant drawback of such approach is that it leaves it up to the user to manually select which features to prioritize, which precludes their applicability in an unsupervised and automated manner.

The 3D pharmacophore models were translated into a flexible search query appropriate for the pharmacophore-based VS with Pharmit. The six pharmacophores were then used to screen pre-filtered CNS-tailored subsets of chemical databases available on Pharmit. From these, 27206 molecules fulfilling the pharmacophoric requirements were retrieved, clustered by MCS with the goal of identifying as many diverse compounds as possible, and docked to IL-1R1 sub-pockets. Interestingly, most of the poses of the docked compound in sub-pocket 2 showed hydrophobic interactions with Leu15, Pro26, Tyr127 and Phe130, while hydrogen bonding was formed mainly with Glu11, Val24, Arg25, Leu29, Tyr127, Glu129 and Phe130. Importantly, amino acids from both sides of sub-pocket 2 interface were involved in protein-ligand interactions. On the contrary, ligands accommodated primarily to one side of sub-pocket 1, showing interactions with crucial residues such as Val16, Ala109, Phe111, Tyr127 and Arg194. Due to the scope and limitations of docking scoring functions as well as the more or less subjective nature of binding site annotation, 919 top-ranking compounds were prioritized based by quantitative analysis of protein-ligand interactions and pharmacophore model

compliance. The inclusion of 3D-shape similarity analysis enabled the prioritization of more (and more diverse) molecules holding shape and chemical complementarity with bioactive molecules within the IL-1 signalling pathway. In the end, 21 compounds were selected for biological testing based on commercial availability and structural diversity. Of these, 10 originated from the docking poses and 11 from the 3D-shape similarity searches.

One of the limitations of the VS workflow implemented against IL-1R1 is that of the utilisation of a single docking and scoring function to evaluate docked poses. Different docking programs (consensus scoring) and different scoring functions may improve the identification of molecules consistently giving good scores, providing better assessments of protein-ligand interactions and more reliable pose rankings. I would like to emphasize on the fact that this limitation is known and an automated and systematic of incorporating several docking and scoring protocols in the VS framework is currently underway. Despite these limitations, we demonstrated efficient usage of pharmacophore modelling, molecular docking and application of structure-based filters in retrieving, retaining, and ranking small molecules to specifically target IL-1R1, allowing reliable assessments to be made.

PART V

Safety Evaluation and Physicochemical Characterization: the solubility and toxicity handshake

"Not all chemicals are bad. Without chemicals such as hydrogen and oxygen, for example, there would be no way to make water, a vital ingredient in beer."

Dave Barry

5.1. Introduction

The tortuous path to the successful development of disease-relevant chemical modulators is often plagued by undesirable features (low bioavailability, high toxicity, poor pharmacokinetics) and artefactual, false positive readouts - frequent hitters, pan-assay interference compounds (PAINS) and aggregators. Importantly, the assessment of *in vitro* ADME, toxicity properties and computational scrutiny of "nuisance promiscuous compounds", apart from *in vitro* potency and selectivity on target, is a critical step in the earlier phases of a *medchem* project. As such, at this stage, we are particularly interested in identifying potential modulators with adequate solubility profiles, low propensity to aggregate in solution, limited cytotoxicity and not holding red-alert structures. In this chapter, we made use of experimental approaches to assess the solubility and toxicity of the virtual screening (VS) hits. We further reveal the results of the application of a computational algorithm designed to identify compounds that are likely to show frequent hitter behaviour.

Fundamentally, every drug screening campaign focuses on the expectation/exploration of chemical compounds that bind to a given target and modulate its activity. Nevertheless, the result of a single experiment does not always assure that the compound displays biological activity on the target itself, as some of these screening hits produce positive experimental results without performing a specific, drug-like interaction with the protein. Indeed, these "bad actors" have subversive reactivity that mimics the drug-like interaction and yields false signals throughout a variety of assays. Many of these false hits are PAINS or colloidal aggregators, that should be approached with great caution in any sort of screen for activity (Baell and Walters, 2014; Reker et al., 2019). Herein, a set of structurally related compounds, sharing maximum common substructure (MCS) with the 21 promising compounds retrieved by the VS protocol, were evaluated in terms of potential assay-interference behaviour.

The solubility of a compound isn't the single most important factor in developing drug candidates, however, is a critical parameter on a compound's bioavailability profile and can represent a major obstacle during drug development. Indeed, poor solubility can impact the i*n vitro* data obtained, through the precipitation or aggregation of compounds, causing underestimated activity, unreliable data, and inaccurate structure-activity relationships (SAR) (Lipinski et al., 2001). Hence, it is essential to evaluate solubility at an early stage before experimental testing. The estimation of solubility in aqueous (buffered) solution of the selected VS compounds was conducted by a turbidimetric (kinetic) solubility assay. This method enables a rapid determination of the kinetic solubility of compounds using small amounts of their *stock* dimethyl sulfoxide (DMSO) solutions.

Late-stage safety and toxicity issues are also a major bottleneck that hamper the traditional drug design and discovery process. First hints and evaluations about potential compound cytotoxicity are generally experimentally assessed by *in vitro* cell viability and cytotoxicity assays with cultured cells. Essentially, the results from preliminary cytotoxicity screenings are fundamental to remove toxic compounds and guide the selection of testing concentrations for other assays (Gerets et al., 2009). With these considerations in mind, in this project we probe the toxicity potential of the 21 VS compounds in HepG2 human hepatocellular carcinoma cell lines and, since these compounds are intended to target neuroinflammation, in human microglial CHME3 cell lines. The next sections will briefly overview these cell lines as *in vitro* models for drug screening and toxicity studies.

5.1.1. Cell lines as *in vitro* models for drug screening and toxicity studies

Cell-based screens are located way up near the top of the screening cascade. These systems are typically used during the preclinical drug screening process to identify/validate druggable targets and to analyse the efficiency of putative therapeutic agents to modulate disease networks. Moreover, they afford the opportunity to evaluate the toxicity profiles in these cell culture systems, helping to decide which compounds should be moved forward. Cell lines can grow both as adherent cells and or in a suspension, depending on the origin of the cell type. Ideally, compounds should be characterized against a panel of cell lines which represent a disease state model holding pertinent molecular abnormalities, as well as alterations in cellular signalling pathways (Allen et al., 2005; O'Brien, 2014).

For *in vitro* studies, two different cell lines were used during the experimental work: (i) HepG2 cells, an immortalized cell line consisting of human liver carcinoma cells, to evaluate the effects of the compounds on cell proliferation and viability; (ii) human CHME3 microglial cell line, derived from human foetal microglia immortalized with simian virus 40 (SV-40) large T-antigen, implemented to study the cytotoxic and immunomodulatory effects of potential IL-1R1 modulators.

5.1.1.1. The human HepG2 (hepatocellular carcinoma) cell line

The HepG2 cell line is widely used in the pharmaceutical industry for the initial toxicity screening of new chemical entities. Interestingly, this cell line was established from a liver tumour biopsy obtained from a 15-year-old Caucasian male in the 1970s (Donato et al., 2015). With the proper culture conditions, these cells display robust morphological and functional differentiation, holding many of the genotypic features of normal liver cells (Sassa et al., 1987). In addition, HepG2 cells are characterized by their high availability, culture conditions

(simpler than primary hepatocytes) and easy standardization among laboratories. These features make the HepG2 cell line suitable for drug screening purposes (Miret et al., 2006).

5.1.1.2. The human CHME3 microglial cell line

The CHME3 (or HMC3) microglia, established in 1995, was the first microglial cell line of human origin (Janabi et al., 1995). Importantly, these cells recapitulate key features seen in freshly isolated primary microglia, including microglial surface markers, phagocytic ability, morphological properties and inflammatory responses to pro-inflammatory stimuli. There are numerous examples in the literature reporting changes in CHME3 microglia upon different conditions by assessing cell viability, morphological changes, phagocytic ability, and cytokine production (Lindberg et al., 2005; Hjorth et al., 2010; Fernandes et al., 2018). Under basal conditions, these cells have been shown to express high levels of the inflammatory cytokine IL-6, alongside with low levels of TNF-α, IL-1α, IL-1β, and caspase-1. Furthermore, the anti-inflammatory cytokines IL-10 and TGF-β and the neurotrophic growth factor BDNF were also detected at basal levels in the steady-state CHME3 microglia (Dello Russo et al., 2018).

Treatment of this cell line with the inflammatory stimuli LPS or IL-1β increase the cytokine secretion and ramp up the expression of neuroinflammatory genes, such as *IL-1β*, *IL-6*, and *TNF-α*. Furthermore, these cells have been found to respond to IFN-γ with consistent overexpression of the classical inflammatory-associated markers MHCII, CD68 and CD11b, and marked increases of pro-inflammatory cytokines when in combination with IL-1β and TNF-α (Dello Russo et al., 2018; Cappoli et al., 2019). Therefore, these cells faithfully reproduce microglial properties under immune stimulation with the acquisition of activated phenotypes, representing a useful tool to study neuroinflammation *in vitro* and to screen potential immunomodulatory molecules.

5.2. Materials and methods

In this section it is presented and described the computational method swiftly deployed to flag PAINS and potential aggregates in a compound dataset, and the experimental methods used for solubility and cytotoxicity measurements.

5.2.1. Prediction of frequent hitters

Hit Dexter v. 2.0 was employed to predict compounds likely to behave promiscuously, based on chemical structure (Stork et al., 2019). This computational algorithm consists of a machine learning approach designed to evaluate how likely a small organic molecule may trigger a positive response or false-positive readouts in biochemical assays. Hit Dexter includes models trained on data measured with primary screening assays (PSA) and confirmatory dose-

response assays (CDRA). Four machine learning models (classifiers) are used to predict promiscuity:

1. Compounds which are likely to show moderate or high hit rates in PSA and are regarded as potentially promiscuous compounds;
2. Compounds which are likely to show high hit rates in PSA and are regarded as potentially highly promiscuous compounds;
3. Compounds which are likely to show moderate or high hit rates in CDRA and are regarded as potentially promiscuous compounds;
4. Compounds which are likely to show high hit rates in CDRA and are regarded as potentially highly promiscuous compounds.

In addition, this software also provides a metric for the prediction of aggregators based on similarity-based approaches to a dataset of known aggregators and dark chemical matter. Due to intellectual property concerns, 21 molecules sharing similar MCS with the 21 VS hits, i.e., located in the same MCS clusters determined during the VS stage (see Part IV), were the ones interrogated for probability of non-specificity and aggregation behaviour.

5.2.2. Compounds and preparation of *stock* solutions

The 21 compounds identified from the VS workflow, were provided in powder form from their respective chemical vendors and dissolved in pure DMSO, at a concentration of 100 mM and stored at −20°C. We confirmed that the compounds were soluble in DMSO and did not show detectable aggregation.

5.2.3. Turbidimetric solubility assay

Turbidimetric solubility experiments were performed *in vitro* to determine the kinetic solubility of the selected compounds - small volumes of the *stock* solution were added incrementally to the aqueous (buffered) solution of interest until the solubility limit was reached. Solutions of each compound were prepared at multiple micromolar concentrations (5, 10, 20, 50, 100, 150, 200, 400 and 600 μM), in 96-well plates, by diluting the respective concentrated DMSO stock solution into HEPES buffer (10 mM, pH=7.4). The final DMSO concentration in each well was 2.0% (v/v). Turbidity measurements were taken at 630 nm using a Microplate Reader (Synergy HT™ from BioTek®), at 24 h time point (3 replicates per concentration). Immediately before the turbidity measurements, the solutions were gently shaken for 1 minute for homogenization. Estimated solubility range was determined with the onset of precipitation based on an increase in absorbance levels.

5.2.4. HepG2 cell viability assay

5.2.4.1. Cell culture and treatment

Adherent human HepG2 cells were routinely cultured in 75 cm^2 (T75) flasks at 37°C, 5% CO2, in Dulbecco's modified eagle medium (DMEM) supplemented with 10% heat-inactivated foetal bovine serum (FBS), 1 mM sodium pyruvate, 2.0 g/L sodium bicarbonate and 1% penicillin-streptomycin (pen-strep). Medium was changed every two or three days.

5.2.4.2. AlamarBlue Cell Viability Assay

HepG2 cells were seeded at a density of $27x10^3$ cells/well into 96-well plates at the volume of 100 µL per well, for 24 h to ensure adhesion to the wells. Then, the medium was removed and fresh medium, along with increasing compound concentrations (based on the turbidimetric solubility measurements for each compound) were added to the cells at a final DMSO concentration of 1% (v/v). Control cells were exposed to 1% (v/v) DMSO. Cell viability was determined by the AlamarBlue assay in three independent experiments performed 48 h-post compound treatment. This assay is based on the ability of viable active cells to metabolize resazurin (blue) by reducing it to the fluorescent molecule resorufin (bright red). After medium removal, resazurin dissolved in medium culture at 10% of the final solution was added to each well and the microplates were further incubated for 45 min. Fluorescence was measured quantitatively with a microplate spectrophotometer (Synergy HT™ from BioTek®) exciting at 530 nm and detecting the emission at 590 nm. The cell viability was obtained using the following expression:

$$Cell\ viability\ (\%) = \frac{Fl\ 590nm\ compound\ treated\ cells}{Fl\ 590nm\ control\ untreated\ cells}\ \text{x}\ 100$$

5.2.5. CHME3 cell viability assay

5.2.5.1. Cell culture and treatment

CHME3 microglia were cultured in T75 culture flasks in high-glucose DMEM, supplemented with 10% FBS, 2% AB/AM and 1% L-glutamine, at 37°C with 5% CO2, with medium change every 2 to 3 days. For each new experiment, microglial cells were plated (5×10^4 cell/well) on 24-well cell culture plates, as previously described by Brite's lab (Fernandes et al., 2018).

5.2.5.2. MTS Cell Viability Assay

For CHME3 microglia, increasing compound concentrations (based on the turbidimetric solubility measurements for each compound) were added to the cells at a final DMSO concentration of 0.1% (v/v). The control cells were incubated in medium containing 0.1% DMSO (v/v). Compound cytotoxicity was assessed quantitatively by the MTS [3-(4,5-dimethylthiazol-2-yl)-5-(3-carboxymethoxyphenyl)-2-(4-sulfophenyl)-2H-tetrazolium] assay. Viable cells in the presence of phenazine methosulfate (PMS) reduce the MTS solution to the water-soluble formazan that is released to the culture medium, with an absorbance maximum at 490 nm. Hence, the amount of formazan produced is proportional to the number of viable cells present in culture. After preparation of a combined PMS/MTS solution (1:20), the plates were incubated, at 37°C in a humidified atmosphere containing 5% CO2, diluted in fresh culture medium, without serum, at concentrations of 1/10 per well. After 1 h incubation, the absorbance was measured using a microplate reader (Bio-Rad Laboratories; Hercules, CA) at the wavelength of 490 nm. The cell viability was obtained using the following expression:

$$Cell\ viability\ (\%) = \frac{Abs\ 490nm\ compound\ treated\ cells}{Abs\ 490nm\ control\ untreated\ cells}\ x\ 100$$

5.2.6. Statistical analysis

The results of three different experiments are expressed as mean ± standard error of the mean (SEM). Analyses and graphical presentations were performed with the GraphPad Prism software version 8 (GraphPad Software Inc., San Diego, CA).

5.3. Results and Discussion

In this section we report the results of the application of a machine learning model for the prediction of potential promiscuous compounds and aggregators among structurally analogous compounds (similar MCS) to the VS hits. Furthermore, we describe the results obtained from turbidimetric solubility measurements and *in vitro* cytotoxicity and viability assays performed with the VS hits. The 21 compounds were renamed under the code "**NCM-V#**".

5.3.1. Analysis of assay interference compounds

Twenty-one (21) analogue compounds to the VS hits were subjected to a PAINS analysis via Hit Dexter 2.0 to flag potential liabilities and predict promiscuity profiles for these molecules. PAINS refer to a class of chemical compounds showing unspecific activity against many unrelated targets, leading to false-positive results in experimental assays. **Figure V.1** provides

the detailed promiscuity analysis for the set of 21 analogue compounds to the VS hits, using Hit Dexter 2.0. Overall, among the predictions performed by this algorithm, it was found a large proportion of compounds predicted to be non-promiscuous, by the PSA (primary screening assays) and the CDRA (confirmatory dose–response assays) classifiers, with a probability of **>0.90** at moderate confidence. However, the promiscuous probabilities increased substantially for compounds 17 and 19, at high confidence. Both were predicted to be promiscuous with a probability **>0.50** in the PSA, and compound 19 maintained this tendency in the CDRA classifier. As such, these two scaffolds were flagged as potential hitters during the realization of experimental assays. Still, most compounds showed low promiscuous probabilities even at high confidence and therefore, a higher likelihood of these core scaffolds to be specific rather than promiscuous.

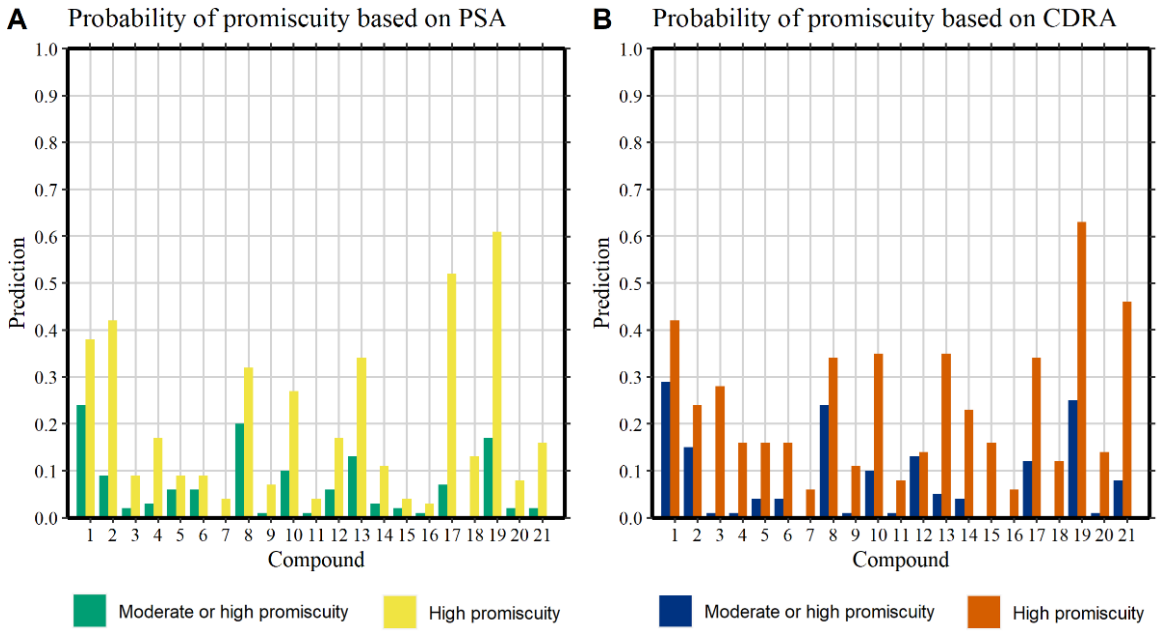

Figure V. 1 - Prediction of promiscuity on 21 analogue compounds to the virtual screening (VS) dataset, using Hit Dexter 2.0. (A) Probability of promiscuity based on primary screening assays (PSA) classifier at moderate (coloured green) and high (coloured yellow) confidence. (B) Probability of promiscuity based on confirmatory dose-response assays (CDRA) at moderate (coloured blue) and high (coloured orange) confidence.

5.3.2. Turbidimetric solubility measurements

More than two decades ago, Lipinski et al. measured and compared turbidimetric solubilities on 353 commercial drugs, indicating that 87% had solubility >65 μg/mL, while only 7% had a solubility <20 μg/mL (Lipinski et al., 2001). From then on, the amount of available information on *in vitro* solubility assays has increased significantly, enabling the implementation of three general categories for compound classification based on their solubility range: (i) compounds

below 10 μg/mL are classified as poorly soluble; (ii) between 10 and 60 μg/mL are moderately soluble and (iii) above 60 μg/mL are considered soluble (Kerns et al., 2008).

Table V.1 reports the turbidimetric solubility measurements determined for the VS hit compounds, by diluting a test compound solution prepared in DMSO into aqueous buffer. Of the 21 compounds experimentally tested, compounds **NCM-V02**, **NCM-V06**, **NCM-V08**, **NCM-V10**, **NCM-V11**, **NCM-V12**, **NCM-V13**, **NCM-V14** and **NCM-V16** showed no turbidity up to the highest compound concentration tested (600 μM). For compounds **NCM-V04** and **NCM-V17**, an increase in turbidity was observed throughout the course of the experiment, still, these molecules displayed aqueous solubility greater than 60 μg/mL. Seven compounds revealed moderate aqueous solubility, in the range of 10–60 μg/mL (**NCM-V01**, **NCM-V07**, **NCM-V15**, **NCM-V18**, **NCM-V19, NCM-V20** and **NCM-V21**), whereas compounds **NCM-V03, NCM-V05** and **NCM-V09** were poorly soluble (<10 μg/mL).

Table V. 1 - Turbidimetric solubility data for VS selected compounds

Compound (NCM)	Determined turbidimetric solubility (μM)	Determined turbidimetric solubility (μg/mL)
V01	60-100	20-33
V02	>600	>216
V03	20-30	6-10
V04	350-400	137-156
V05	25-37	8-12
V06	>600	>251
V07	80-120	25-38
V08	>600	>183
V09	10-20	4-7
V10	>600	>210
V11	>600	>205
V12	>600	>220
V13	>600	>171
V14	>600	>205
V15	60-80	19-25
V16	>600	>172
V17	160-190	62-74
V18	40-55	13-18
V19	80-120	25-38
V20	80-120	23-34
V21	80-120	24-36

5.3.3. Toxicity profiling in human HepG2 cell line

Cell viability of HepG2 cells was determined in the presence of increasing concentrations of the test compounds to obtain a preliminary assessment of the *in vitro* toxicity. **Figure V.2** shows the cell viability in the HepG2 cell line after 48 h of exposure to different concentrations of the 21 compounds, divided in three groups based on turbidimetric solubility measurements:

(1) **NCM-V02**, **NCM-V04, NCM-V06**, **NCM-V08**, **NCM-V10**, **NCM-V11**, **NCM-V12**, **NCM-V13**, **NCM-V14**, **NCM-V16** and **NCM-V17** – tested in the concentrations of 5, 10, 20, 50, 100, 150, 200, 250 and 300 μM; (2) **NCM-V01**, **NCM-V07**, **NCM-V15**, **NCM-V18**, **NCM-V19, NCM-V20** and **NCM-V21** – tested at 2.5, 5, 10, 15, 20, 40, 60, 80 and 100 μM and (3) **NCM-V03, NCM-V05** and **NCM-V09** – tested at 2.5, 5, 10, 15, 20, 50 μM, except compound NCM-V09 (tested up to 20 μM).

As shown in **Figure V.2A**, for most of the high-soluble compounds (group 1) there was a reduction in cell viability in a concentration-dependent manner. Nevertheless, compounds **NCM-V12** and **NCM-V14**, throughout the spectrum of concentrations tested, did not produce significant changes on cell viability when compared to the 1% DMSO control cells. The plot highlights the relatively low toxicity of compounds **NCM-V02** and **NCM-V11** in HepG2 cells, even at high concentrations, whereas compounds **NCM-V08** and **NCM-V16** presented a fairly significant decrease at 100 μM, reaching at 300 μM values of 59.5% and 41.4% of cell viability loss. Compared to the control cells, a substantial reduction in cell viability was observed for the remaining five compounds identified from the VS framework, with **NCM-V04** and **NCM-V13** exhibiting high cytotoxic effects at 100 μM and presenting cell viability of 0.6% and 24,3%, respectively. Strikingly, compound **NCM-V17** exhibited high cytotoxicity in all tested concentrations (for clarity of presentation, this compound was inserted in **Figure V.2C**). The cell viability profiles following *in vitro* exposure to the second group of compounds (**Figure V.2B**) revealed a similar shape for compounds **NCM-V15**, **NCM-V18** at different concentrations ranging from 2.5 to 100 μM (cell viability remained above 80%). Compounds **NCM-V19** and **NCM-V20** decreased cell viability roughly by 23-28% at 100 μM when compared to the control cells. In contrast, HepG2 cells were more sensitive to compounds **NCM-V01**, **NCM-V07** and **NCM-V21** treatment at concentrations higher than 50 μM. Concerning the third group of compounds **NCM-V03**, **NCM-V05**, the cell viability curves (**Figure V.2C**) showed substantial cellular toxicity at all tested concentrations. Compound **NCM-V09** precipitated in all tested concentrations and was withdrawn from further experiments.

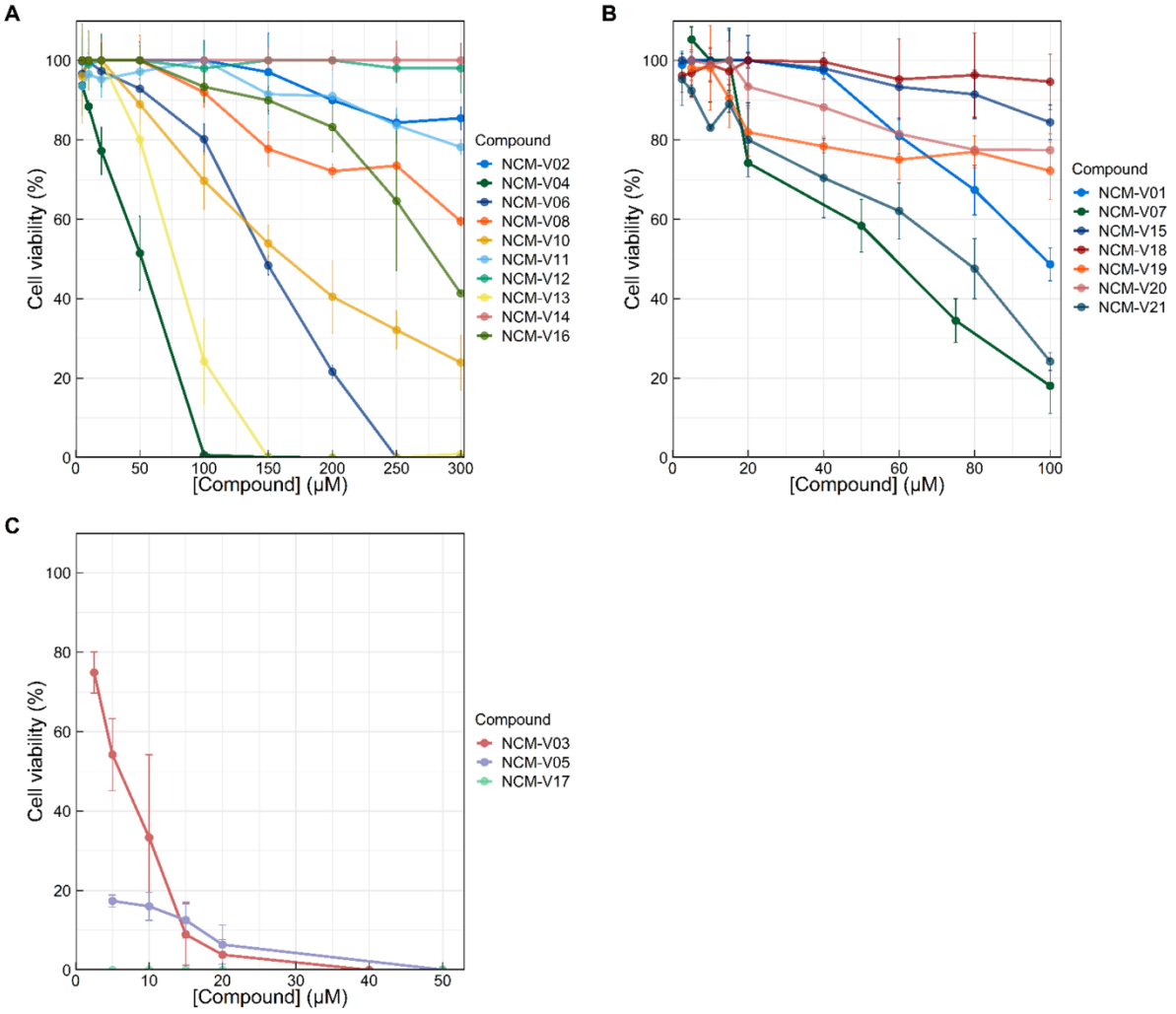

Figure V. 2 - Cell viability assay of HepG2 cells treated with increasing testing compound concentrations. Effect of the group 1 **(A)**, group 2 **(B)** and group 3 **(C)** on the cell viability of HepG2 cells, 48 h post-treatment using the Alamarblue assay. **(D)** Representative image of HepG2 cells. The cell viability of treated cells was calculated relative to control, 1% DMSO untreated cells (viability set as 100%). Data are representative of three independent experiments and are presented as mean ± SEM of n = 3 wells per group.

The effects of the VS hits on the cell viability of HepG2 cells are summarized in **Table D-1** in the Appendix (data are reported as mean ± SEM**).** Based on the results achieved, compounds from group 1 (except for **NCM-V17** – withdrawn due to high cytotoxic effects) and group 2 were used in subsequent assays, whereas the compounds from group 3 were discarded due to high cytotoxicity on HepG2 cells. In other words, compounds **NCM-V01, NCM-V02, NCM-V04, NCM-V06, NCM-V07, NCM-V08, NCM-V10, NCM-V11, NCM-V12, NCM-V13, NCM-V14, NCM-V15, NCM-V16, NCM-V18, NCM-V19, NCM-V20** and **NCM-V21**, were selected for further experimental testing, whereas compounds **NCM-V03, NCM-V05**, **NCM-V09** and **NCM-V17** were discarded.

5.3.4. Toxicity profiling in human CHME3 microglial cell line

Following initial toxicity characterization in HepG2 cells, the cytotoxic effects of the VS hit compounds were also assessed using the MTS cell viability assay on the CHME3 microglia cell line. Microglia were treated with the compounds prioritized from the above sub-section, each at 20, 50 and 100 µM, during 24 h. The maximum final DMSO concentration in each well was of 0.1% (v/v). Reducing the DMSO concentration resulted in the precipitation of compounds **NCM-V02**, **NCM-V12, NCM-V18** and **NCM-V20**. Hence, these compounds were excluded from further evaluations. **Figure V.3** discloses the effects of the compounds, divided in two groups (group 1 and 2) based on turbidimetric solubility measurements, on CHME3 cell viability after 24 h of exposure. As shown in **Figure V.3A**, no changes in cell viability were observed for compound **NCM-V14** at 20, 50 and 100 µM concentrations, suggesting that this compound did not significantly reduce cell viability. The cytotoxic profile of compounds **NCM-V08** and **NCM-V16** was less pronounced, with cell viability always above 75% when compared to the 0.1% DMSO control cells. Cell viability was greater than 90% for compounds **NCM-V10** and **NCM-V11** for concentrations up to 50 µM, decreasing to 69.4% and 58.2% respectively, at 100µM concentrations. Compounds **NCM-V04**, **NCM-V06** and **NCM-V13** posed higher cytotoxicity, which was particularly evident at 50 µM, inducing a significant decrease in microglia cells viability at the highest concentration (cell viability: **NCM-V04** – 18.9%, **NCM-V06** – 33.1%, **NCM-V13** – 0%).

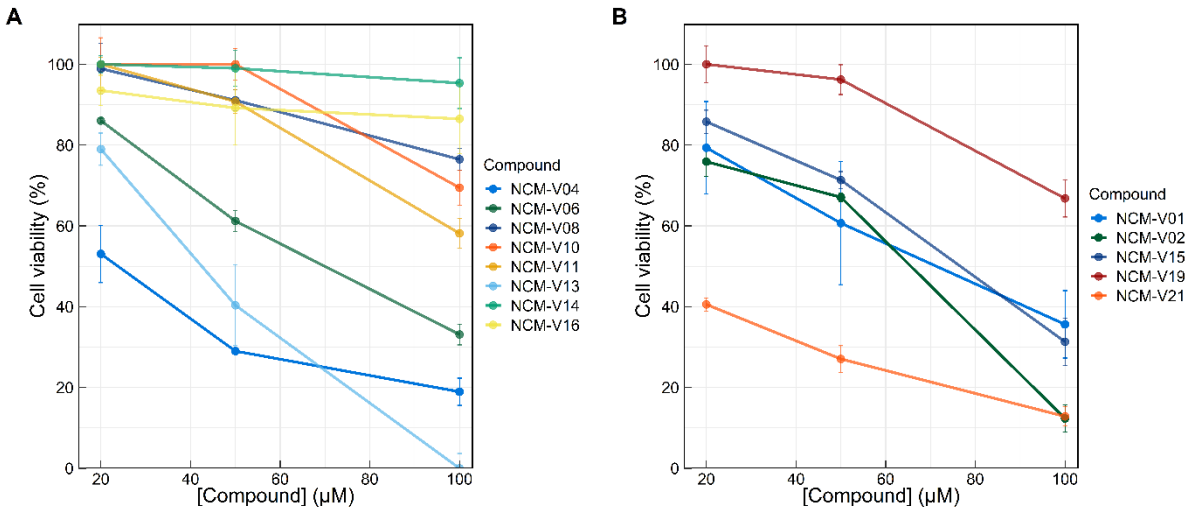

Figure V. 3 - Cell viability assay of CHME3 microglia cells treated with increasing testing compound concentrations. Effect of the most-soluble **(A)**, moderately soluble **(B)** groups on the cell viability of CHME3 cells, 24 h post-treatment using the MTS assay. The cell viability of treated cells was calculated relative to control, 0,1% DMSO untreated cells (viability set as 100%). Data are representative of two independent experiments and are presented as mean ± SEM of n = 3 wells per group.

Figure V.3B shows the concentration-dependent cytotoxicity for group 2: **NCM-V01**, **NCM-V07**, **NCM-V15**, **NCM-V19** and **NCM-V21**. Cell viability decreased approximately 35% for compound **NCM-V19** at 100 μM, while compounds **NCM-V01, NCM-V07** and **NCM-V15** presented an enhanced cytotoxicity at this concentration (cell viability: **NCM-V01** – 35.6%, **NCM-V07** – 12.3%, **NCM-V15** – 31,3%), when compared to the respective control cells. After 24 h exposure, compound **NCM-V21** showed a strong cytotoxic effect throughout the concentrations tested. The effects of the VS hits on the cell viability of CHME3 cells are summarized in **Table D-2** in the Appendix (data are reported as mean ± SEM).

5.3.5. Compound prioritization for phenotypic screening: *in-depth* analysis

The prioritization of compounds for phenotypic experiments was based on their cytotoxic profiles in HepG2 and CHME3 cell lines, and on the solubility measurements. These three distinct assay stages were closely accompanied by direct analysis of *in silico* predictive assessments of compound promiscuity. In this way, compound prioritization was set to: i) high aqueous solubility; ii) suitable toxicity profiles in HepG2 and CHME3 cell lines; and iii) prediction probabilities of no assay-interference behaviour.

The likelihood of the core scaffolds, composing the 21 compounds selected from the VS campaign, to be promiscuous was low, with probability values falling between 0-30%. Still, compounds 17 and 19 presented promiscuous probability values higher than 50% and were kept "under the radar" on *in vitro* assays. Turbidimetric solubility assay results indicated that 52% of the compounds fall into the high aqueous solubility range, whereas 33% showed moderate aqueous kinetic solubility. At the other extreme, in the poor aqueous solubility range, 15% of the VS hits were in this category. The primary cytotoxicity screen implicated all 21 compounds. The effects of these molecules on cell viability were assessed using HepG2 cells, a well characterized and frequently used cell line in toxicological and pharmacological studies. The primary screen resulted in three molecules withdrawn due to high toxicity in HepG2 cells and one discarded due to precipitation, with most compounds exhibiting an LD_{50} >100 μM in this cell line. Curiously, compound **NCM-V17** whose scaffold was predicted to be highly promiscuous with likelihood higher than 50%, showed a high degree of cytotoxicity in all tested concentrations. Compounds were counter-screened in CHME3 microglial cells using again cell viability as read-out. Overall, the CHME3 cell line was more sensitive to each compound treatment than the HepG2 cell line. Interestingly, of the 13 compounds experimentally tested (four molecules withdrawn due to precipitation), 5 compounds (**NCM-V08, NCM-V10**, **NCM-V11**, **NCM-V14** and **NCM-V16**) revealed to be relatively well tolerated and safe based on the toxicity profiles in HepG2 and CHME3 cell lines. In general, the

cytotoxicity profile of compound **NCM-V14** in CHME3 microglia roughly matches that of verified for the HepG2 cell line, highlighting the relatively low toxicity of this compound, even at high concentrations. The other top four compounds revealed suitable toxicity profiles in both cell lines, causing less than 40% reduction in cell viability at a concentration of 100 μM. From these, compounds **NCM-V08**, **NCM-V14** and **NCM-V16,** presenting high aqueous solubility and predicted to be non-promiscuous, were prioritized for microglial phenotypic assays to assess their potential immunomodulatory properties over microglial phenotypic polarization.

5.4. Concluding Remarks

Phenotypic experimental evaluation of many molecules is highly expensive and a time-consuming process. Herein, we developed a screening progression cascade for triaging compounds to significantly reduce the number of compounds to be profiled and confirmed for activity through the more complex cell-based assays. In this chapter, we have systematically studied important criteria for good small molecule modulators: assay-interference behaviour, solubility and toxicity. Using an *in silico* method for the prediction of problematic compounds together with *in vitro* turbidimetric solubility measurements and toxicity profiling in HepG2 and CHME3 cell lines, we categorized compounds based on those three physicochemical criteria, and prospectively prioritized compounds for further cell-based phenotypic assays.

According to our results, the 21 compounds purchased from the respective chemical suppliers appear to not possess molecular scaffolds that have been associated with various types of assay interference. Nevertheless, it is worth emphasizing that despite PAINS-related promiscuity are usually considered a poor starting point for medicinal chemistry endeavours, some of these compounds may interact with a protein of interest in a specific drug-like way, and thus could be further optimized through medicinal chemistry. Amongst the 21 compounds, 18 compounds showed moderate to high aqueous solubility, whereas three compounds displayed poor solubility. To assess the cytotoxicity of the VS hits, primary screens were first performed using HepG2 cells, followed by counter screens with a reduced set of screen compounds in a more relevant, neuroinflammation-like, cell-based system – CHME3 microglial cells – to further down select and prioritize compounds for studies in disease-relevant phenotypic models. The results demonstrated that **NCM-V08**, **NCM-V14** and **NCM-V16** displayed suitable cytotoxicity profiles against HepG2 and CHME3 cells, and thus, these compounds were selected for further experiments.

PART VI

Microglia-based phenotypic screening for the discovery of new neuroinflammatory modulators

"I listen to what you say, but I hear what you mean"

Hercule Poirot, in *Hercule Poirot Novels by Agatha Christie*

6.1. Introduction

One of the problems of conventional drug discovery methods is the focus on a single target without considering the entire genomics and proteomics networks that are linked to it. Putting into perspective some of the ideas presented in the introductory chapter on the importance of phenotypic screening in drug discovery, we have been compelled to explore a platform that could foster the search for modulators that alter the microglia phenotypes associated with harmful neuroinflammation and validate target hypotheses. As mentioned throughout the previous chapters of this thesis, chronic and sustained microglia pro-inflammatory/damaging phenotypes are linked to the overproduction of neurotoxic factors, like iNOS and ROS, and pro-inflammatory cytokines, e.g. TNF-α and IL-1β. In this context, small molecules modulating harmful pro-inflammatory responses of microglial cells may protect from microglia-mediated neurotoxicity and be beneficial to mitigate the progression of chronic neuroinflammatory-mediated diseases.

In this chapter, we employed microglia-based phenotypic screenings to search for small molecules, designed to target IL-1R1, to modulate the harmful effects of microglial pro-inflammatory activation. As proof-of-concept, we used an *in vitro* human microglial model based on the use of CHME3 microglial cell line stimulated with IFN-γ to recapitulate microglial phenotypes predominant in an inflammatory milieu, and consistent with the phenotypes occurring in neurodegenerative diseases characterized by uncontrolled inflammatory processes. IFN-γ is a pro-inflammatory T-lymphocyte cytokine that serves critical functions in both innate and adaptive immunity. Lately, it was demonstrated that IFN-γ plays a pivotal role in AD-associated neuroinflammation, as it is deeply involved in the pathophysiological mechanisms of this disease (Roy et al., 2020).

The stimulation with IFN-γ is known to increase the production of proinflammatory-associated genes, inducing proliferation and moderate activation of microglia, including up-regulation of iNOS, ROS and IL-6 (Rock et al., 2005; Spencer et al., 2016; Ta et al., 2019). Accordingly, it represents a robust and reliable *in vitro* model system, mimicking pro-inflammatory microglial phenotypes, to identify pharmacological tool compounds (activators or inhibitors) and to explore specific signalling pathways on neuroinflammatory responses.

The focus of the project behind this thesis is the use of IL-1R1 as a model target for the modulation of detrimental neuroinflammatory processes. IL-1 is a potent microglia stressor, activating downstream kinases and transcription factors resulting in NF-κB-mediated gene transcription and increased cytokine and chemokine secretion such as IL-6 and TNF-α, as well as itself by positive feedback loop (Mantovani et al., 2019). In this final chapter, we investigated the ability of compounds **NCM-V08**, **NCM-V14** and **NCM-V16** to modulate the production of

key pro-inflammatory factors in IFN-γ-induced CHME3 microglia-inflammatory responses. In the screenings, six main pro-inflammatory players produced by activated microglia, i.e., IL-1R1, IL-1β, IL-6, NF-κB, NLRP3 and iNOS, were set as phenotypic markers. Altered levels of these markers were used as indicators of the immunomodulatory ability of VS hits. Although these genes/proteins appear first as unrelated and distinct players, they all are actually linked together in intracellular signalling via at least the NF-κB transcriptional machinery (**Figure VI.1**).

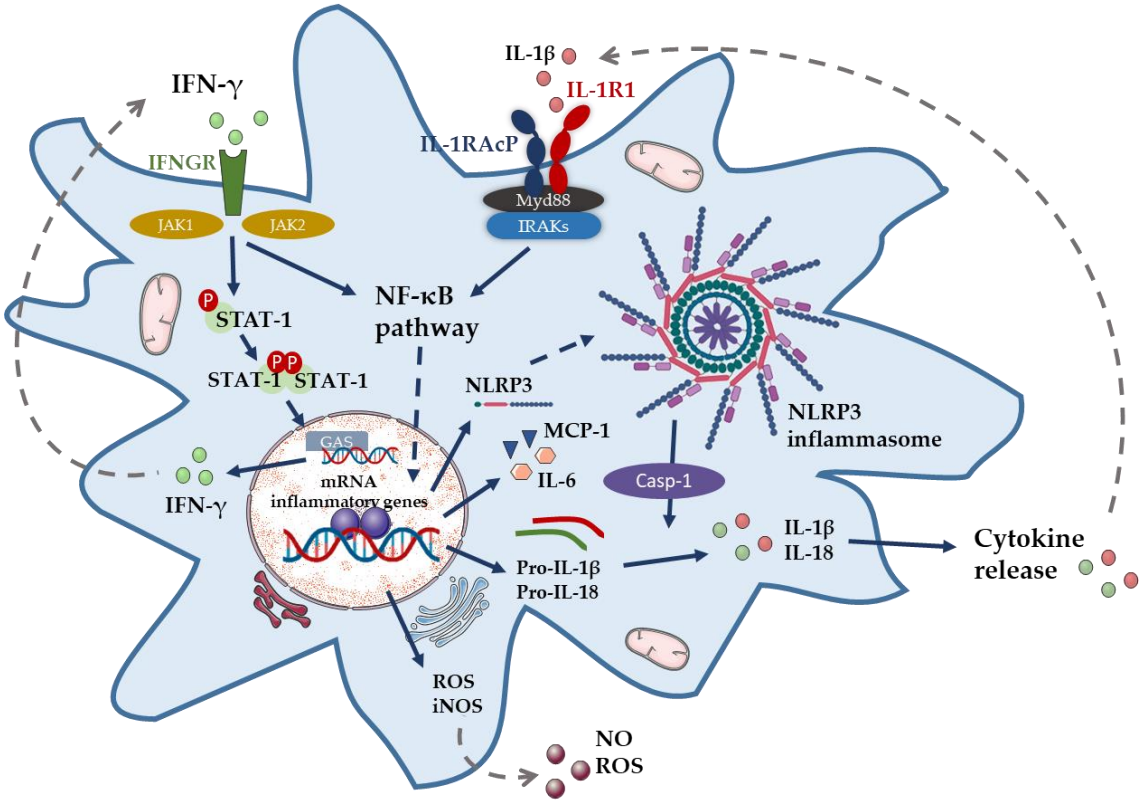

Figure VI. 1 - Inflammatory stimulated responses of microglial cells by interferon-γ (IFN-γ). Canonical IFN-γ signalling pathway requires binding to its receptor, IFN-γ receptor (IFNGR) leading to the activation of the Janus kinase/signal transducer and activator of transcription (JAK/STAT) pathway. Activated JAK proteins phosphorylate the STAT1 binding site, triggering the formation of phosphorylated STAT1 dimers and subsequent translocation to the nucleus where it binds to γ-activated site (GAS) elements and promotes gene transcription. In addition, IFN-γ signalling can activate a pro-inflammatory cascade involving the nuclear factor-kappa B (NF-κB) network, with increased production of IFN-γ, NLR family pyrin domain containing 3 (NLRP3), interleukin-6 (IL-6), monocyte chemoattractant protein-1 (MCP-1), pro-interleukin-1β (pro-IL-1β) and pro-interlukin-18 (pro-IL-18). Both of these pathways are able to individually induce inducible nitric oxide synthase (iNOS) expression but the synergy between these pathways greatly amplifies the response. Consequently, iNOS expression leads to nitric oxide (NO) production. Upregulation of NLRP3 via NF-κB activation primes the assembly of the inflammasome complex, which then activates caspase-1 (Casp-1). This enzyme then proteolytically cleaves the pro-forms of IL-1β and IL-18, enabling the release of these mature cytokines, enhancing the inflammatory response. Subsequently, IL-1β binding to membrane interleukin-1 receptor type 1 (IL-1R1) promotes the engagement of the co-receptor IL-1

receptor accessory protein (IL-1RAcP), resulting in the recruitment of myeloid differentiation primary response 88 (MyD88) and IRAKs (interleukin-1 receptor-associated kinases), which activate the NF-κB pathway. Autocrine/paracrine IL-1 activation of canonical NF-κB signalling exacerbate microglial pro-inflammatory phenotype, forming a vicious inflammatory cycle. Ultimately, microglial release of these pro-inflammatory mediators, when at elevated levels or chronically, may lead to neuronal dysfunction.

6.1.1. Expression of IL-1R1 in microglia: what we know

Produced mainly by cells of the immune system, IL-1R1 operates in various parts of the body as a key cytokine receptor in inflammation and immune responses. Within the CNS, functional IL-1R1 is highly expressed among vascular endothelial cells, with lower but detectable expression in microglia, astrocytes, and neurons. However, the presence of IL-1R1 in microglia is not entirely consensual. Indeed, the expression of this receptor was reported in some *in vitro* studies (Pinteaux et al., 2002; Sato et al., 2012) but was not confirmed in others (Krasnow et al., 2017; Liu et al., 2019). Nevertheless, microglial IL-1R1 expression has been reported to be increased in different *in vivo* models of neuroinflammation, providing evidence of IL-1R1 important role in the molecular pathogenesis of neuroinflammatory responses (Friedman, 2001; Wang et al., 2006; Bruttger et al., 2015; Zhang et al., 2018a; Guo et al., 2020). Importantly, Basu et al. demonstrated in IL-1R1 null mice that this receptor is fundamental for the activation of microglia and the induction of pro-inflammatory mediators such as IL-6, in response to brain injury (Basu et al., 2002). These observations indicate that microglial IL-1R1 production is more strongly associated with an activated status of human glial cells. Of particular relevance to this work, immunocytochemical analysis revealed immunoreactivity for IL-1R1 in the human CHME3 cell line (Hjorth et al., 2010). Here, immune stimulation with IFN-γ was performed to increase the inflammatory status of CHME3 microglia.

6.2. Materials and methods

This section contains information on the two molecular biological techniques, Real Time quantitative Polymerase Chain Reaction (RT-qPCR) and Immunocytochemistry (ICC), used to evaluate the response of microglia to IFN-γ exposure and the effects of the compounds of interest on microglial pro-inflammatory markers.

6.2.1. Cell culture and treatment

CHME3 microglia were cultured in T75 culture flasks in high-glucose DMEM (4.5 g/L), supplemented with 10% FBS, 2% AB/AM and 1% L-glutamine, at 37°C with 5% CO2, with medium change every 2 to 3 days, and grown to confluence. For each new experiment, microglial cells were seeded (5×10^4 cell/well) on 24- or 6-well cell culture plates, as previously described by Brites's lab (Fernandes et al., 2018) (**Figure VI.2**). Then, to polarize microglia cells

into a pro-inflammatory activated state, cells were incubated with IFN-γ (50 ng/mL) during 12 or 24 h. These two different time-points were chosen based on previous studies demonstrating IFN-γ induced microglial activation into pro-inflammatory phenotypes in such conditions (Nguyen and Benveniste, 2002; Spencer et al., 2016; Moritz et al., 2017). In addition, these two time periods allow the evaluation and comparison of compound testing outcomes on the induction of pro-inflammatory mRNA and protein expression levels. After 12/24 h incubation with IFN-γ, cells were then treated for additional 12h/24 h with the three selected VS hits (20 μM), in the presence of DMSO, at a final concentration of 0.1% (v/v). Non-treated cells (without either IFN-γ or compounds) were considered as controls.

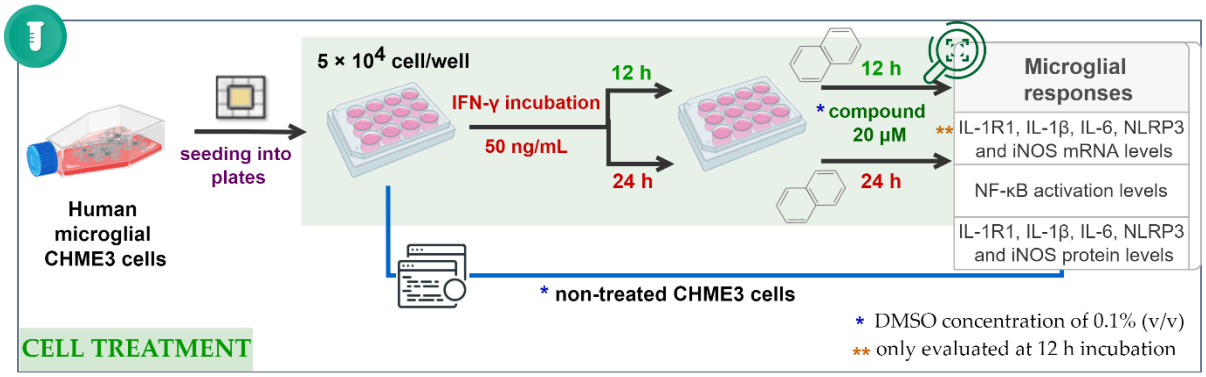

Figure VI. 2 - Schematic representation of the experimental cell treatment design of this study. Human microglial CHME3 cells were seeded into cell culture plates (5x10⁴ cell/well) and maintained for 24 h. CHEM3 cells were treated with interferon-γ (IFN-γ) for 12 h or 24 h. After incubation with IFN-γ, microglial cells were treated with the VS compounds at the concentration of 20 μM at a final dimethyl sulfoxide (DMSO) concentration of 0.1% (v/v), over a period of time similar to that of the stimulation with IFN-γ (12 h or 24 h). CHME3 microglial responses were evaluated in terms of (i) pro-inflammatory markers expression by Real-Time quantitative PCR; (ii) nuclear factor-kappa B (NF-κB) by immunocytochemical staining; and (iii) pro-inflammatory protein markers levels by immunocytochemical staining. The control non-treated CHME3 cells were maintained for the same periods of time, with cell culture medium containing 0.1% DMSO (v/v).

6.2.2. Immunocytochemistry

After incubation with the compounds, CHME3 microglia were washed with PBS, fixed with 4% (w/v) paraformaldehyde, permeabilized using 0.2% Triton X-100 for 20 min, and then blocked for 30 min at room temperature with PBS containing 3% bovine serum albumin (BSA). Cells were incubated overnight at 4°C with the mouse primary antibody anti-IL-1R1, mouse anti-NLRP3, mouse anti-iNOS, and rabbit anti-NF-κB. Microglial cells were then washed with PBS and incubated for 2 h at room temperature with secondary antibodies, i.e., goat anti-mouse Alexa Fluor 488 and goat anti-rabbit Alexa Fluor 488. Cells were stained for F-actin cytoskeleton using Alexa Fluor 594 Phalloidin antibody. After washing with PBS, cell nuclei were stained with Hoechst 33258 dye (1:1000, Sigma-Aldrich) and coverslips were mounted in microscopy slides using PBS:glycerol mounting media. Manufacturers and dilution factors

used for the antibodies are provided in **Table VI.1**. Fluorescence was visualized using an AxioCam HR camera (Zeiss) adapted to an AxioSkope® microscope. Merged images of UV and fluorescence of eight random microscopic fields were acquired per sample. Quantification of fluorescence intensity was performed with Image J software (Schneider et al., 2012) and normalized to the total number of cells (Pinto et al., 2017; Vaz et al., 2021).

Table VI. 1 - List of antibodies, sources, species and dilutions used in the immunocytochemistry protocol.

Primary antibody against	Source	Species	Dilution used
IL-1R1	Santa Cruz Biotechnology, sc-393998	Mouse	1:50
NLRP3	Adipogen, AG-20B-0014	Mouse	1:200
NF-κB	Santa Cruz Biotechnology, sc-372	Rabbit	1:500
iNOS	BD Transduction Laboratories, #610329	Mouse	1:100
Secondary antibody	**Source**		**Dilution used**
Anti-mouse AlexaFluor 594	Invitrogen Corporation, A-11005		1:1000
Anti-mouse AlexaFluor 488	Invitrogen Corporation, A-11001		1:1000
Anti-rabbit AlexaFluor 594	Invitrogen Corporation, A-11012		1:1000
Anti-rabbit AlexaFluor 488	Invitrogen Corporation, A-11008		1:1000
AlexaFluor 594 Phalloidin	Invitrogen Corporation, A12381		1:50

Table abbreviations: IL-1R1, interleukin-1 receptor type 1; NLRP3, NLR family pyrin domain containing 3; NF-κB, Nuclear factor-kappa B; iNOS, inducible Nitric Oxide Synthase.

6.2.3. Total RNA extraction, reverse transcription and RealTime-PCR

Total RNA was extracted from CHME3 microglia using TRIzol® reagent according to the manufacturer instructions. Extracted RNA was quantified using Nanodrop® ND-100 Spectrophotometer (NanoDrop Technologies) and reverse transcription was achieved with the Xpert cDNA Synthesis Mastermix Kit (GRiSP) (Cunha et al., 2016; Vaz et al., 2019). RT-qPCR was performed on a QuantStudio 7 Flex Real-Time PCR System (Applied Biosystems) using an Xpert Fast Sybr Blue (GRiSP). The samples were amplified using the following conditions: 50°C for 2 min followed by 95°C for 2 min and finally 50 cycles at 95°C for 5 s and 62°C for 30 s. The specificity of the amplification was ensured by melt-curve analysis, immediately after the amplification protocol. β-actin was used as internal control for the RT-qPCR assay. Relative mRNA concentrations were calculated using the $2^{-\Delta\Delta CT}$ method. All samples were assessed in duplicate. Results were normalized to β-actin and expressed as fold change *vs.* non-treated CHME3 microglia (control). Primer sequences are listed in **Table VI.2**.

Table VI. 2 - Sequences used as primers for detection of mRNA expression levels in CHME3 microglia

Gene	Forward primer (5′-3′)	Reverse primer (5′-3′)
IL-1R1	GTGCTTTGGTACAGGGATTCCTG	CACAGTCAGAGGTAGACCCTTC
NLRP3	TGCTCTTCACTGCTATCAAGCCCT	ACAAGCCTTTGCTCCAGACCCTAT
IL-1β	CAGGCTCCGAGATGAACAAC	GGTGGAGAGCTTTCAGCTCATA
IL-6	CCGGAGAGAGGAGACTTCACAG	GGAAATTGGGGTAGGAAGGA
iNOS	ACCCACATCTGGCAGAATGAG	AGCCATGACCTTTCGCATTAG
β-actin	GCTCCGGCATGTGCAA	AGGATCTTCATGAGGTAGT

Table abbreviations: IL-1R1, interleukin-1 receptor type 1; NLRP3, NLR family pyrin domain containing 3; IL-1β, interleukin-1β; IL-6, interleukin-6; iNOS, inducible Nitric Oxide Synthase.

6.2.4. Statistical analysis

All data are presented as mean ± SEM from at least five independent experiments. Comparison between different groups was made by one-way analysis of variance (ANOVA) followed by post hoc Bonferroni's test. Analyses and graphical presentation were performed with the GraphPad Prism software version 8 (GraphPad Software, Inc., San Diego, CA). The statistical significances were achieved when $p < 0.05$.

6.3. Results and Discussion

We evaluated the ability of VS hit compounds to rescue CHME3-microglia activation after treatment with IFN-γ, a pro-inflammatory molecule that has been shown to stimulate microglia into a pro-inflammatory phenotype (Rock et al., 2005; Ta et al., 2019). First, to validate the prevalent phenotype induced by 12 h of microglia incubation with IFN-γ, a panel of genes known to be overexpressed during neuroinflammation (*IL-1R1*, *IL-1β*, *IL-6*, *NLRP3* and *iNOS*) was assessed by RT-qPCR. To evaluate **NCM-V08**, **NCM-V14** and **NCM-V16** potential immunomodulatory activities, their influence on the mRNA and protein pro-inflammatory profiles after IFN-γ stimulation in microglia was assessed considering the following conditions: (i) RT-qPCR in CHME3 cells pre-exposed to IFN-γ for 12 h and treated with the compounds for additional 12 h; (ii) ICC at two defined time-points, i.e., CHME3 microglia exposed to 50 ng/mL IFN-γ for 12 h and 24 h, and then incubated with the compounds for additional periods of 12 h and 24 h. To assess the modulatory properties of the VS hits on IFN-γ stimulated microglia, we used a compound concentration of 20 μM.

6.3.1. IFN-γ-mediated stimulation of CHME3 microglial cells leads to the up-regulation of pro-inflammatory-associated genes

In this work, we investigated the transcriptional profile of pro-inflammatory markers in CHME3 microglial cells stimulated with IFN-γ. To characterize the effects of IFN-γ on microglial gene expression, CHME3 cells were either untreated (control) or treated with 50 ng/mL of IFN-γ during 12 h. As shown in **Figure VI.3,** CHME3 microglia stimulated with IFN-γ exhibited a significant up-regulation of pro-inflammatory genes *IL-1R1* (2.1-fold, $p < 0.01$), *IL-1β* (1.8-fold, $p < 0.05$), *IL-6* (1.8-fold, $p < 0.05$), *NLRP3* (1.8-fold, $p < 0.05$) and *iNOS* (2.0-fold, $p < 0.01$) at 12 h when compared to untreated microglia. These data point to a predominant switch of CHME3 microglia to a pro-inflammatory activated phenotype, upon treatment with IFN-γ. Importantly, IFN-γ revealed to induce a robust and reproducible expression of the pro-inflammatory IL-1R1 signalling axis in human CHME3 microglia *in vitro*, turning the model suitable for screening potential small molecule modulators of IL-1R1 and related signalling pathways.

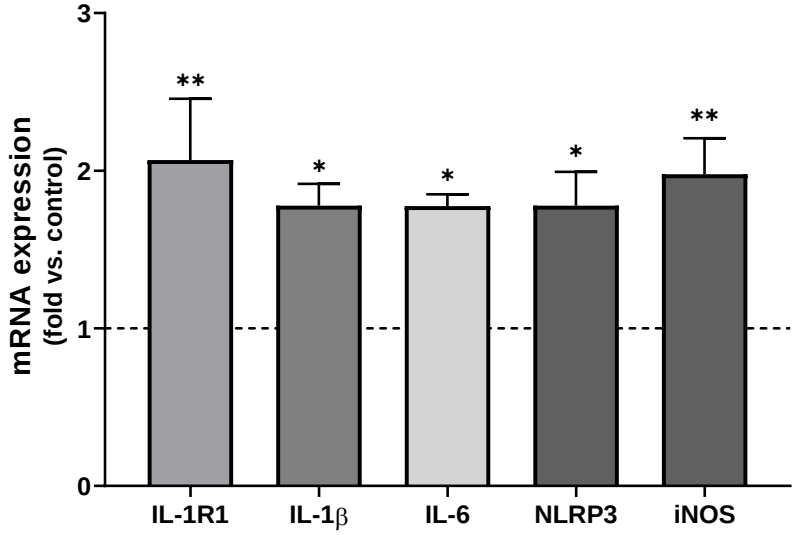

Figure VI.3 - CHME3 microglia treated with IFN-γ present transcriptional upregulation of inflammatory mediators. Microglial cells were treated for 12 h with 50 ng/mL IFN-γ. After incubation, CHME3 expression of *IL-1R1*, *IL-1β*, *IL-6*, *NLRP3* and *iNOS* was determined by RT-qPCR. Results are mean ± SEM fold change vs. respective controls (untreated cells) from at least 5 independent experiments performed in duplicate. *$p < 0.05$ and **$p < 0.01$ vs. respective controls. *Figure abbreviations: IFN-γ, interferon-γ; IL-1R1, interleukin-1 receptor type 1; IL-1β, interleukin-1β; IL-6, interleukin-6; NLRP3, NLR family pyrin domain containing 3; iNOS, inducible Nitric Oxide Synthase.*

6.3.2. VS compounds downregulate mRNA expression of pro-inflammatory-associated markers in IFN-γ-stimulated microglia

The IL-1/IL-1R1 signalling axis is known to activate several transduction pathways, including the NF-κB transcription factor associated to the induction of several inflammatory genes, such as *IL-1β*, *IL-6*, *NLRP3* and *iNOS* (**Figure VI.3**). Importantly, these pro-inflammatory markers play a central role in microglia-mediated neuroinflammation. The ability of the three selected VS hits, prioritized based on the results of Part V - **NCM-V08**, **NCM-V14** and **NCM-V16** - to modulate IFN-γ-driven microglia-inflammatory responses was assessed through the measurement of both gene/protein expression levels of the above-mentioned inflammatory mediators. The results of the RT-qPCR assay revealed that the increased levels of inflammatory-associated genes, *IL-1R1*, *IL-1β*, *IL-6*, *NLRP3* and *iNOS*, after IFN-γ stimulation for 12 h were markedly suppressed by 12 h treatment with **NCM-V14** (**Figure VI.4**). Similarly, incubation with **NCM-V16** reduced *IL-1R1* and *IL-1β* ($p < 0.05$), but no significant differences were observed in IFN-γ upregulation of *IL-6*, *NLRP3* and *iNOS* gene expression levels. Likewise, there were no significant changes following treatment with **NCM-V08** for 12 h. These results reveal **NCM-V14** as the most promising immunomodulator in terms of gene expression, though benefits were also achieved with NCM-V16, in relation to the pro-inflammatory IL-1R1-driven pathway in the IFN-γ-activated CHME3 microglial cells.

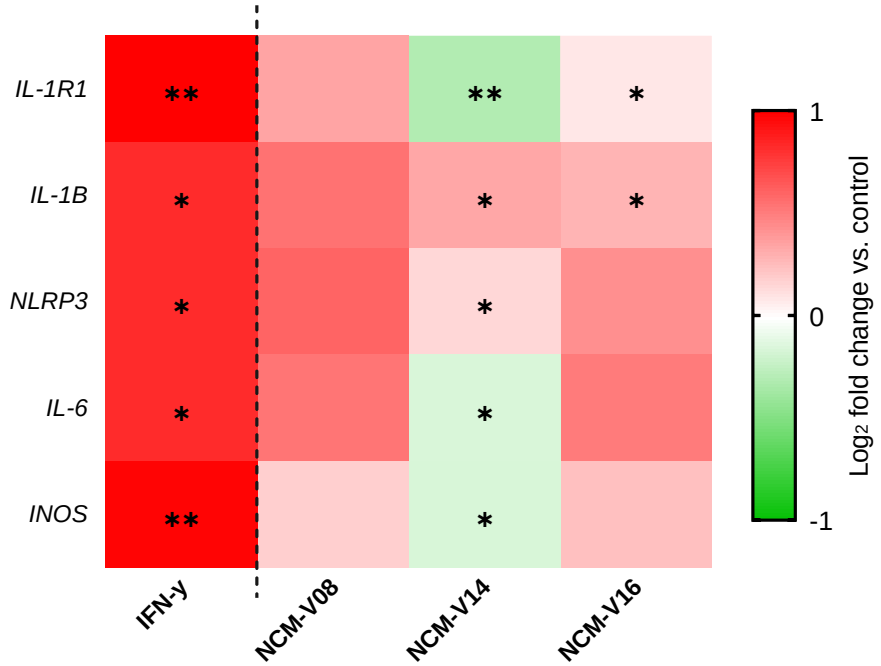

Figure VI. 4 - Heatmap of Log_2 fold change (relative to non-treated-control) for gene expression in CHME3 microglial cells following 12 h IFN-γ-stimulation and 12 h compound treatment. Log_2 fold change was calculated

based on the ΔCT values relative to control samples, with the colour red implying increased expression while green implies decreased expression. The IFN-γ-enhanced mRNA upregulation relative to untreated control (first column, red) is presented for comparative analysis. Each row shows the relative expression level for a single gene, and each column shows the expression level for a single compound. Data are representative of 5 independent experiments. Significant differences between IFN-γ-stimulated and compound-treated IFN-γ-stimulated microglia are indicated by * $p < 0.05$, ** $p < 0.01$. *Figure abbreviations: IFN-γ, interferon-γ; IL-1R1, interleukin-1 receptor type 1; IL-1β, interleukin-1β; IL-6, interleukin-6; NLRP3, NLR family pyrin domain containing 3; iNOS, inducible Nitric Oxide Synthase.*

6.3.3. VS compounds restore the levels of IL-1R1 protein in IFN-γ-stimulated microglia to values similar to the non-treated cells

Given the innovative *in silico* framework implemented and explored with the objective of discovering IL-1R1 small molecule modulators, we also assessed the impact of the compounds of interest on CHME3 microglial IL-1R1 protein levels after IFN-γ (50 ng/mL) stimulation. In line with the gene expression data, CHME3 microglia exposed during 24 h to IFN-γ showed a slight but significant increase in IL-1R1 protein levels (1.5-fold increase from control, $p < 0.05$; **Figure VI.5**). Interestingly, as depicted in **Figure VI.5B**, IFN-γ-enhanced protein levels of IL-1R1 were significantly downregulated after microglial treatment for 24 h with **NCM-V08** (60% decrease relatively to IFN-γ-induced microglia, $\boldsymbol{p} < 0.05$), **NCM-V14** (70% decrease relatively to IFN-γ-induced microglia, $\boldsymbol{p} < 0.01$) and **NCM-V16** (70% decrease relatively to IFN-γ-induced microglia, $p < 0.01$). In contrast, no significant differences were observed in IL-1R1 steady-state levels upon exposure of CHME3 cells to IFN-γ for 12 h and compound treatment for additional 12 h, when compared to control cells (**Figure E-1**, provided in the Appendix). Overall, the increased immunoreactivity for IL-1R1 evident at 24 h after IFN-γ incubation, but not at 12 h, suggest a possible temporal delayed induction of this protein. It is known that the transcriptome analysis can be used as a powerful tool to predict the corresponding proteins, since sometimes genes and proteins do not correlate due to regulation of translation and protein turnover (Edfors et al., 2016; Moritz et al., 2019).

As depicted in **Figure VI.5**, no significant cell morphological changes were observed after F-actin staining of CHME3 microglial cells incubated with **NCM-V08**, **NCM-V14** and **NCM-V16** at the concentration of 20 μM.

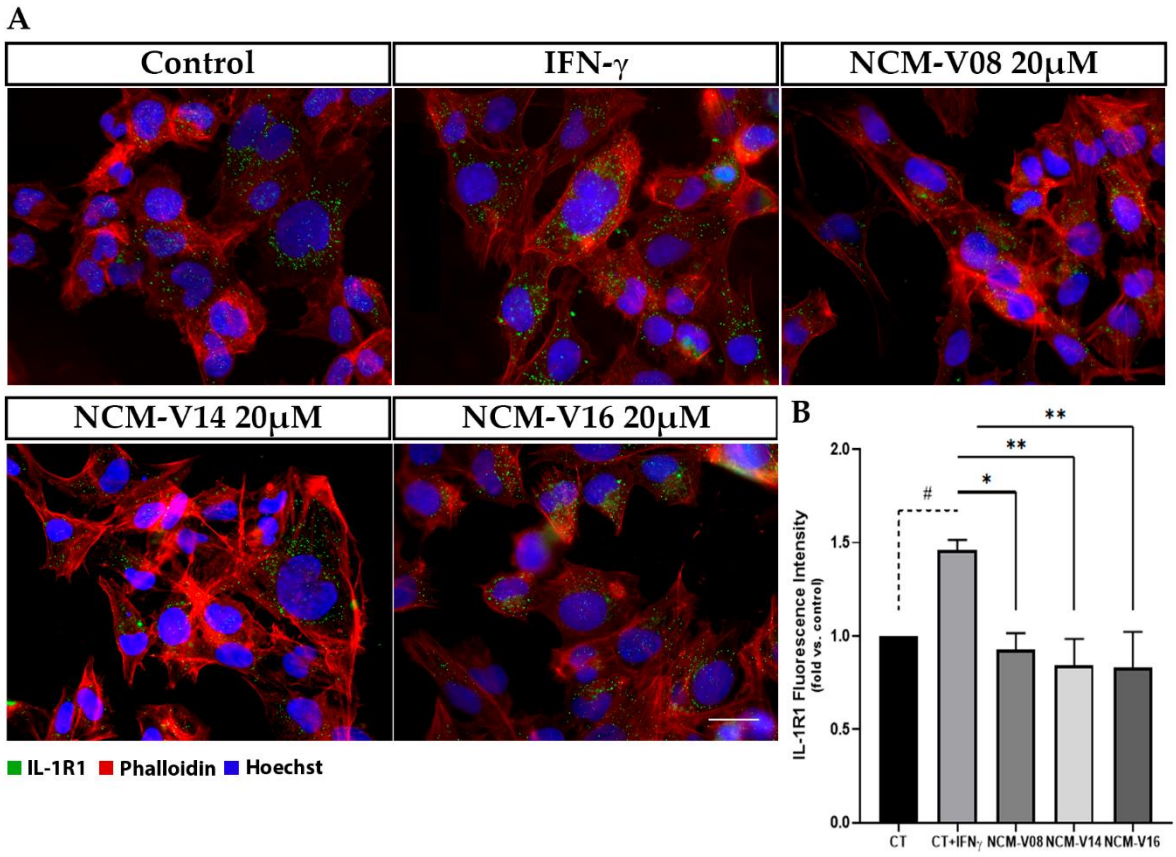

Figure VI. 5 - IFN-γ-induced microglial upregulation of IL-1R1 microglial protein levels is reduced by NCM-V08, NCM-V14 and NCM-V16. CHME3 cells were treated with 50 ng/mL IFN-γ for 24 h, and then with the compounds of interest (20 μM) for 24 h. After incubation, detection of IL-1R1 levels was performed by immunocytochemistry using anti-IL-1R1 antibody, as indicated in Materials and methods. **(A)** Representative images of immunofluorescence staining showing IL-1R1 (green) and F-actin (Phalloidin, red) in CHME3 cells. Cell nuclei were detected by Hoechst (blue). Scale bar=40 μm. **(B)** Quantification of IL-1R1 mean fluorescence intensity. Results are mean ± SEM fold change vs. respective controls (untreated cells) from 5 independent experiments. Significant differences from the control group are indicated by # $p < 0.05$; differences between IFN-γ-stimulated and compound-treated IFN-γ-stimulated microglia are indicated by * $p < 0.05$, ** $p < 0.01$. *Figure abbreviations: CT, control cells; IFN-γ, interferon-γ; IL-1R1, interleukin-1 receptor type 1.*

6.3.4. VS compounds inhibit IFN-γ-induced nuclear translocation and activation of NF-κB

NF-κB is a key transcription factor that regulates the inflammatory process, stimulated by pro-inflammatory cytokines, such as TNF-α and IL-1β. There is evidence that IFN-γ may play a role in the NF-κB pathway activation and subsequent pro-inflammatory gene transcription (Gough et al., 2008). Hence, we investigated whether NF-κB signalling was activated in the IFN-γ-stimulated CHME3 microglia, and if so, whether exposure to **NCM-V08**, **NCM-V14** and **NCM-V16** treatment was able to abrogate its activation. As such, we quantified nuclear translocation of NF-κB p65 subunit as an indicator of NF-κB activation, by

immunofluorescence after 12 h and 24 h incubation. As shown in **Figure VI.6**, CHME3 cells treated with IFN-γ for 12 h showed an increased transference of NF-κB p65 subunit into the nuclei (1.6-fold, $p < 0.01$), when compared with the non-treated cells. Importantly, NF-κB translocation levels were significantly decreased by **NCM-V14** (60% decrease relatively to IFN-γ-induced microglia, $p < 0.01$) and **NCM-V16** (50% decrease relatively to IFN-γ-induced microglia, $p < 0.01$). However, no significant differences were observed in NF-κB basal levels upon 24 h exposure of CHME3 microglia to IFN-γ (**Figure E-2**, provided in the Appendix), probably resultant from adaptive mechanisms of the cell (Lauro and Limatola, 2020). Still, IFN-γ induced a slight increase albeit not significant of NF-κB nuclear translocation that was reversed by **NCM-V14** and **NCM-V16**. Importantly, we hypothesize that these distinct NF-κB activation results (at 12 h and 24 h incubation) may derive from microglial activated feedback mechanisms to counteract the NF-κB signalling system. Indeed, the metabolic pathways involved in microglial activity adapt and may contribute to the phenotypic transition toward a more homeostatic state (Eggen et al., 2013; Lauro and Limatola, 2020).

Since NF-κB could highly induce pro-inflammatory factors by enhancing their transcription and based on the above-mentioned gene expression data pointing out that **NCM-V14** and **NCM-V16** modulate the mRNA levels of NF-κB-regulated pro-inflammatory genes, including *iNOS*, *IL-1β*, and *IL-6*, these observations strengthen and provide good indications on **NCM-V14** and **NCM-V16** potential at reducing inflammation-associated events in conditions of exacerbated microglial pro-inflammatory activation.

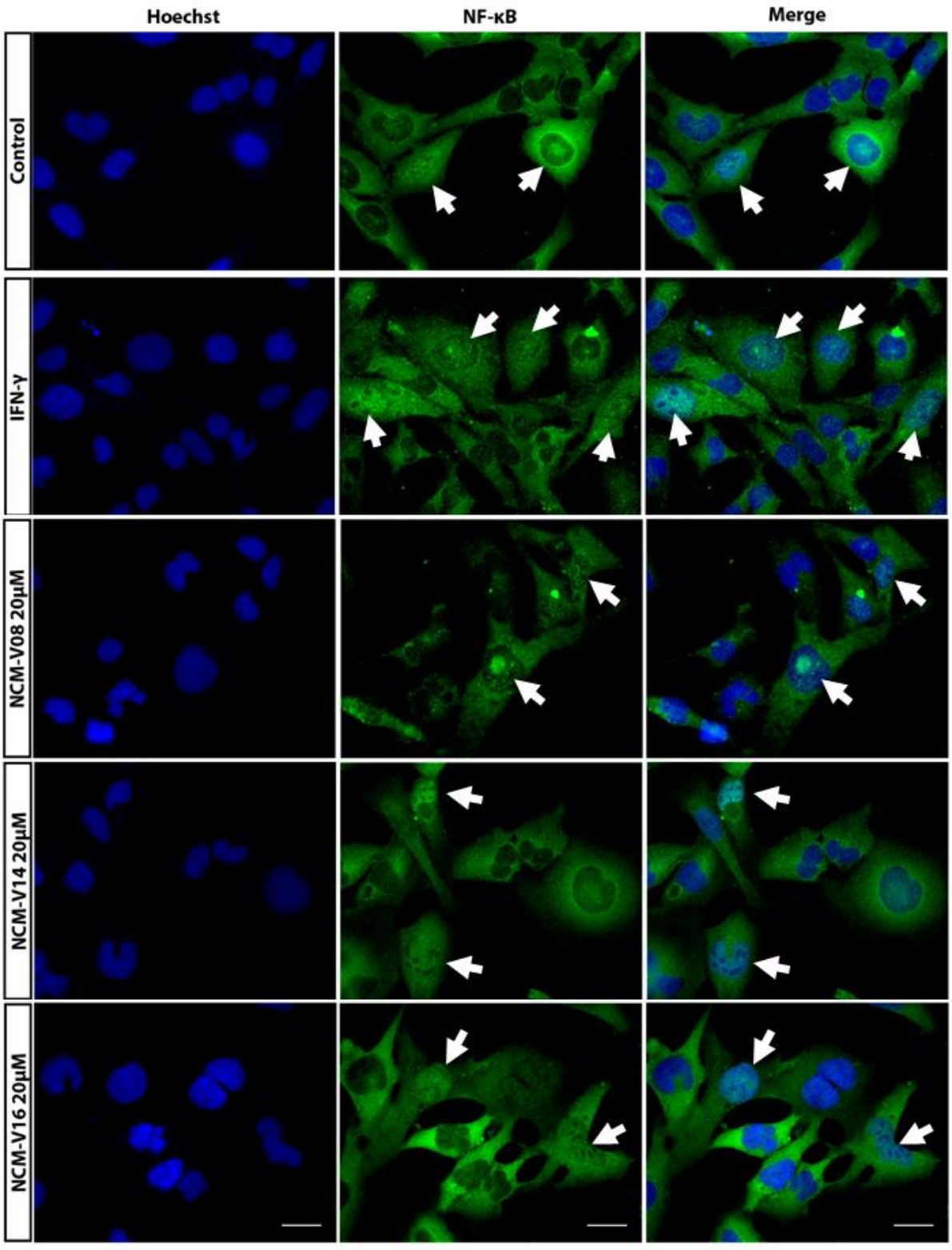
Hoechst
NF-κB
Merge
Control
IFN-γ
NCM-V08 20μM
NCM-V14 20μM
NCM-V16 20μM

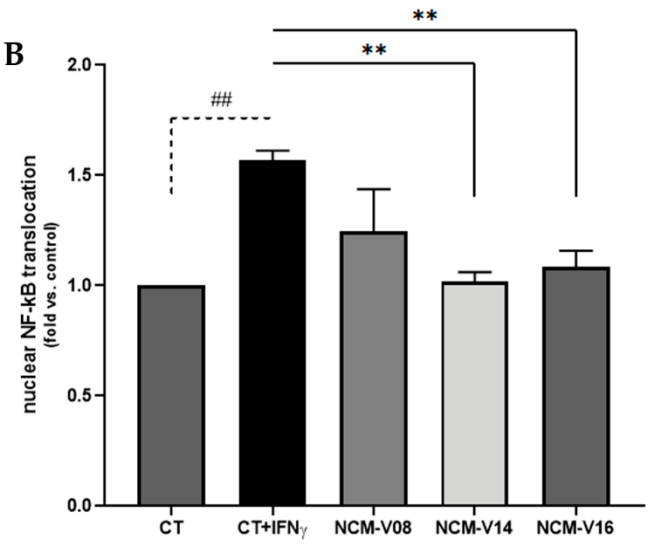

Figure VI. 6 - IFN-γ-induced microglial upregulation of NF-κB p65 nuclear translocation is reduced by NCM-V14 and NCM-V16. The nuclear translocation (white arrows) of the NF-κB p65 subunit was determined by an immunofluorescence assay. CHME3 cells were treated with 50 ng/mL IFN-γ for 12 h, and then with the compounds of interest (20 μM) for 12 h. **(A)** Representative images of immunofluorescence staining showing NF-κB p65 (green) translocation into the nucleus in CHME3 cells. Cell nuclei were detected by Hoechst (blue). Scale bar=40 μm. **(B)** Quantification of nuclear NF-κB p65 subunit translocation. Results are mean ± SEM fold change vs. respective controls (untreated cells) from 5 independent experiments. Significant differences from the control group are indicated by ## $p < 0.01$; differences between IFN-γ-stimulated microglia and compound-treated IFN-γ-stimulated microglia are indicated by ** $p < 0.01$. *Figure abbreviations: CT, control cells; IFN-γ, interferon-γ; NF-κB, Nuclear factor-kappa B.*

6.3.5. VS compounds restore the levels of NLRP3 protein in IFN-γ-stimulated microglia to values similar to the non-treated cells

Processing of the full-length precursor to the biologically active mature IL-1β is tightly regulated by the NLRP3 inflammasome. This multi-protein complex is highly expressed in microglia during neuroinflammation and may exacerbate injury at elevated levels (Scheiblich et al., 2017). A major upstream process involved in NLRP3 inflammasome formation is the NF-κB signalling network. Previous studies suggest a link between increased levels of NF-κB and the NLRP3 inflammasome (Bauernfeind et al., 2009). Recently, Zhao et al. suggested that the NLRP3-IL-1β-IL-1R1 axis is fundamental in the transition of acute to chronic neuroinflammation (Zhao et al., 2020). Therefore, we evaluated the impact of IFN-γ and the three VS hits on NLRP3 protein levels, at 12 h and 24 h. Interestingly, we observed that 12 h IFN-γ stimulation slightly increased NLRP3 protein levels (1.3-fold, $p < 0.05$). However, at 24 h only a net but not significant increase was observed in microglia (**Figure E-3**, provided in the Appendix). Importantly, as depicted in **Figure VI.7**, the IFN-γ-enhanced NLRP3 protein levels were significantly downregulated after 12 h incubation with **NCM-V14** (50% decrease

relatively to IFN-γ-induced microglia, $p < 0.001$) and **NCM-V16** (30% decrease relatively to IFN-γ-induced microglia, $p < 0.05$). No significant changes were observed with **NCM-V08** treatment after 12 h and 24 h incubation.

Overall, these results demonstrated that the timing of changes in NLRP3 mRNA and protein levels were similar in IFN-γ-stimulated microglia. Indeed, IFN-γ increased NLRP3 gene expression and protein at 12 h, but the NLRP3 transcript levels appeared to recover by 24 h after IFN-γ treatment. Nevertheless, despite a mild stimulation of NLRP3 protein levels by IFN-γ in CHME3 microglia, which was verified by others (Kopitar-Jerala, 2017), incubation with **NCM-V08** or **NCM-V16** for 12 h was able to restore NLRP3 protein levels to basal unstimulated conditions in the presence of IFN-γ.

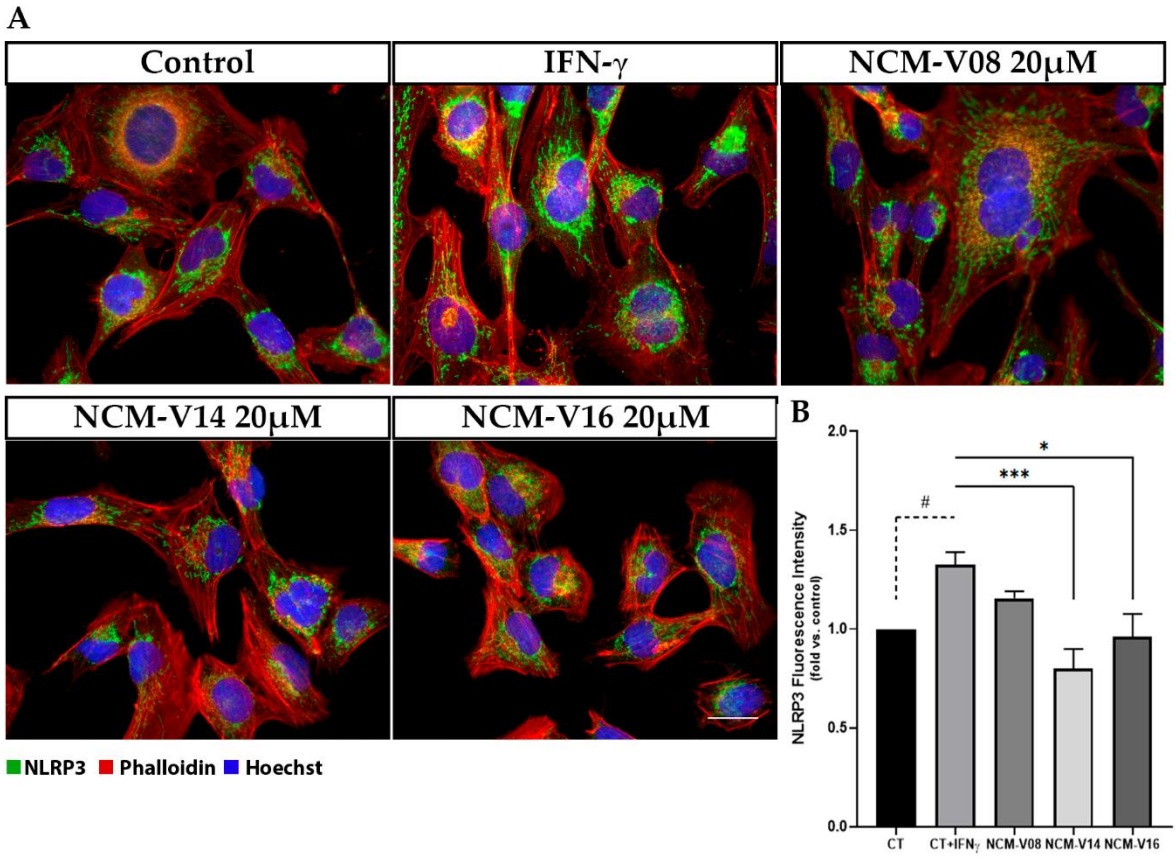

Figure VI. 7 - IFN-γ-induced microglial upregulation of NLRP3 protein levels are reduced by NCM-V14 and NCM-V16. CHME3 cells were treated with 50 ng/mL IFN-γ for 12 h, and then with the compounds of interest (20 µM) for 12 h. After incubation, detection of NLRP3 levels was performed by immunocytochemistry using anti-NLRP3 antibody, as indicated in Materials and methods. **(A)** Representative images of immunofluorescence staining showing NLRP3 (green) and F-actin (Phalloidin, red) in CHME3 cells. Cell nuclei were detected by Hoechst (blue). Scale bar=40 µm. **(B)** Quantification of NLRP3 mean fluorescence intensity. Results are mean ± SEM fold change vs. respective controls (untreated cells) from 5 independent experiments. Significant differences from the control group are indicated by # $p < 0.05$; differences between IFN-γ-stimulated microglia and compound-treated IFN-γ-stimulated microglia are indicated by * $p < 0.05$, *** $p < 0.001$. *Figure abbreviations: CT, control cells; IFN-γ, interferon-γ; NLRP3, NLR family pyrin domain containing 3.*

6.3.6. VS compounds restore the levels of iNOS protein in IFN-γ-stimulated microglia to values similar to the non-treated cells

The aberrant induction of iNOS and concomitant NO release in the CNS microenvironment are key important factors involved in neuronal dysfunction. Several signalling pathways determine the expression of iNOS in microglial cells, emphasizing this enzyme as a relatively straightforward marker of pro-inflammatory activated microglial phenotypes (Zhao et al., 2004; Saha and Pahan, 2006; Sonar and Lal, 2019). Exposure of microglial cells to IFN-γ was shown to induce the expression of iNOS and subsequent NO production (Ta et al., 2019). As such, we aimed to evaluate the effect of **NCM-V08**, **NCM-V14** and **NCM-V16** on iNOS production in IFN-γ-stimulated CHME3 microglia, at 12 h and 24 h. As shown in **Figure 8**, after 24 h microglia cells stimulated by IFN-γ showed enhanced iNOS protein levels (1.5-fold, $p < 0.05$). This increased iNOS activity in activated microglia was dampened in the presence of the three VS compounds, **NCM-V08** (60% decrease relatively to IFN-γ-stimulated microglia, $p < 0.05$), **NCM-V14** (70% decrease relatively to IFN-γ- stimulated microglia, $p < 0.01$) and **NCM-V16** (80% decrease relatively to IFN-γ- stimulated microglia, $p < 0.01$). In contrast, after 12 h incubation, the iNOS protein expression profiles were not significantly affected either by IFN-γ stimulation or compound treatment, when compared to control cells (**Figure E-4**, provided in the Appendix)

In general, consistent with the downregulation of IFN-γ-induced iNOS mRNA expression, **NCM-V14** treatment attenuated IFN-γ-induced iNOS protein level increase. In comparison, **NCM-V08** and **NCM-V16** reduced the levels of iNOS protein expression, though both compounds did not affect iNOS mRNA levels at 12 h incubation.

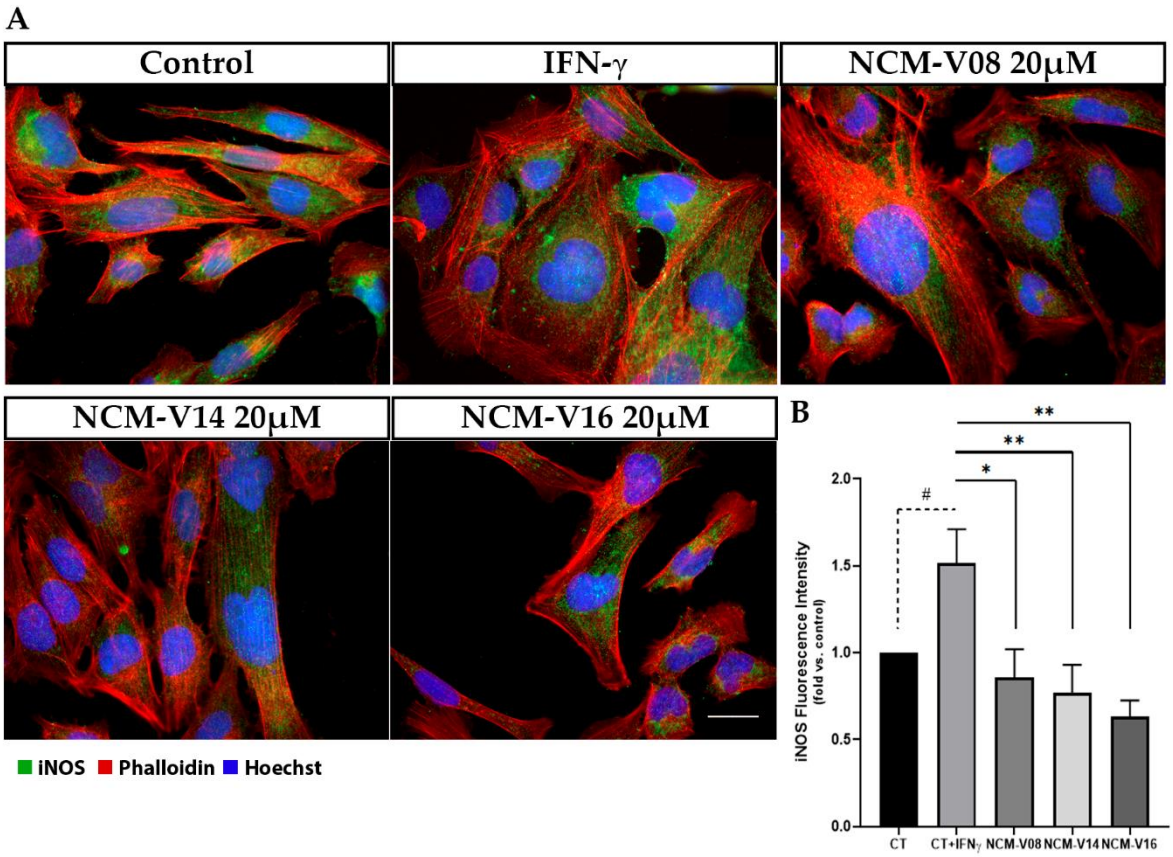

Figure VI. 8 - IFN-γ-induced microglial upregulation of iNOS protein levels are reduced by NCM-V08, NCM-V14 and NCM-V16. CHME3 cells were treated with 50 ng/mL IFN-γ for 24 h, and then with the compounds of interest (20 μM) for 24 h. After incubation, detection of iNOS levels was performed by immunocytochemistry using anti-iNOS antibody, as indicated in Materials and methods. **(A)** Representative images of immunofluorescence staining showing iNOS (green) and F-actin (Phalloidin, red) in CHME3 cells. Cell nuclei were detected by Hoechst (blue). Scale bar=40 μm. **(B)** Quantification of iNOS mean fluorescence intensity. Results are mean ± SEM fold change vs. respective controls (untreated cells) from 5 independent experiments. Significant differences from the control group are indicated by # $p < 0.05$; differences between IFN-γ-stimulated microglia and compound-treated IFN-γ-stimulated microglia are indicated by * $p < 0.05$, ** $p < 0.01$. *Figure abbreviations: CT, control cells; IFN-γ, interferon-γ; iNOS, inducible Nitric Oxide Synthase.*

6.4. Concluding Remarks

Despite the deteriorating role of dysregulated neuroinflammation in many CNS diseases, the number of existing immunomodulatory approved drugs targeting exacerbated and harmful neuroinflammation is quite limited because of insufficient efficacy or undesired side effects. Therefore, there is a growing need for small molecule therapeutics that modulate neuroinflammation. This need is amplified when one realizes that most of the current approved CNS immunomodulatory drugs are macromolecules. Indeed, using them as therapeutic approaches have several disadvantages for clinical use in chronic CNS disorders, such as high costs and inconvenient dosing regimens. Clearly, there is a demand for orally

active, brain-penetrant compounds to test as potential modulators for neuroinflammation-associated immune imbalance, mainly in uncontrolled pro-inflammatory conditions.

In this chapter, the human immortalized CHME3 microglial cell line, with a phenotype closely related to primary microglia, and stimulated with IFN-γ, was used as an *in vitro* model to screen for neuroinflammatory modulators. In selecting pro-inflammatory stimuli to activate microglia we chose to examine microglial responses to IFN-γ instead of LPS, which despite the larger utilization, is less effective to produce pro-inflammatory phenotypes in this microglial cell line. When compared to untreated cells, IFN-γ moderately increased microglial activation markers *IL-1R1*, *IL-1β*, *IL-6*, *NLRP3* and *iNOS* after 12 h. At the protein level, there was distinct temporal induction patterns of the pro-inflammatory components in the two time points analysed, respectively 12 h and 24 h. Indeed, IFN-γ stimulation elicited a higher nuclear NF-κB translocation and NLRP3 protein levels at 12 h, which was lost after 24 h incubation, whereas the induction of IL-1R1 and iNOS was more delayed, evidencing enhanced levels after 24 h IFN-γ incubation. The outward progression of the inflammatory signalling cascade over time suggests sequential cellular propagation of these markers in response to IFN-γ stimulation. In other words, as with IL-1R1 and iNOS activation, their delayed induction may reflect the dependence on prior signalling cascades, such as the IL-1β production, or the acquisition of adaptive mechanisms. Besides, NLRP3 is not limited to the NF-κB-dependent transcriptional upregulation, suggesting IFN-γ-mediated activation via alternative pathways, resulting in autocrine IL-1β-mediated increases in CHME3 microglia. We must consider that the mechanisms leading to the metabolic regulation of IFN-γ are complex and usually culminate in adaptive mechanisms when the cell is not chronically dysregulated.

Of the 3 VS hit compounds studied, two elicited significant mRNA expression changes in the inflammatory-associated genes that were examined. Noteworthy, **NCM-V14** altered mRNA expression to a greater extent than the **NCM-V16**. In addition, these two molecules supressed the IFN-γ-evoked upregulation of NF-κB activation and IL-1R1, NLRP3 and iNOS protein levels. Of note, **NCM-V08** was efficient at decreasing IL-1R1 and iNOS production. Amongst the three compounds, **NCM-V14** was the strongest immunomodulator. Interestingly, some studies have demonstrated that the IL-1R1/Myd88/NF-κB signalling pathway is involved in regulating NLRP3 inflammasome expression (Xing et al., 2017; Swanson et al., 2019). Since the expression and protein levels of key pro-inflammatory mediators, directly or indirectly related to the IL-1 system, were all increased in IFN-γ induced microglia, we hypothesize that **NCM-V14** and **NCM-V16** supressed the upregulation of the NLRP3 inflammasome via inhibition of the IL-1R1/Myd88/NF-κB signalling pathway in IFN-γ induced CHME3 microglia (**Figure VI.8**). However, further studies are required to confirm if the above effects of **NCM-V14** and **NCM-V16** also involve other intracellular and extracellular-mediated mechanisms, before

testing their effects *in vivo* models of CNS disorders associated to increased and dysregulated neuroinflammatory processes.

Our search for potential neuroinflammatory modulators in a suitable human microglial *in vitro* model yielded two promising molecular entities. Still, future studies should validate and challenge our screening cellular model. Indeed, it would be interesting to confirm the modulatory effects of **NCM-V14** and **NCM-V16** in primary cultures of microglia and in co-cultures of primary microglia with neurons or astrocytes. The use of different models will strengthen the effects of the two compounds to be tested in the modulation of microglia neuroinflammatory responses linked to neurodegeneration. Furthermore, the exact knowledge of the mechanism of the two compounds, **NCM-V14** and **NCM-V16,** may be crucial for the success of efficient therapeutics. Thus, it would be important to evaluate more pro-inflammatory components associated with microglial activation to further unravel and dissect which inflammatory pathways the compounds specifically target. Time and money are important constraints in every project and, unfortunately, we had to focus our efforts on the selection of the three compounds holding the best physiochemical features to be tested in microglia, discarding some compounds without getting a fair experimental hearing. However, despite these limitations, I personally believe that the results achieved in this chapter provide a meaningful and promising baseline toward the identification of novel of novel modulators of pro-inflammatory conditions.

To sum up, these data confirm the modulatory activity of **NCM-V14** and **NCM-V16** on the IL-1R1 signalling pathway. Although further studies are required to better understand such effects, the modulation of specific IL-1R1 related pro-inflammatory markers in IFN-γ-activated microglia indicate that **NCM-V14** and **NCM-V16** can counteract the polarized pro-inflammatory activated microglia. From the Medicinal Chemistry viewpoint, these findings indicate that **NCM-V14** and **NCM-V16** can be valuable strategies for modulating the IL-1R1 signalling pathway specifically related with microglial pro-inflammatory phenotypes and unbalanced neuroinflammatory processes.

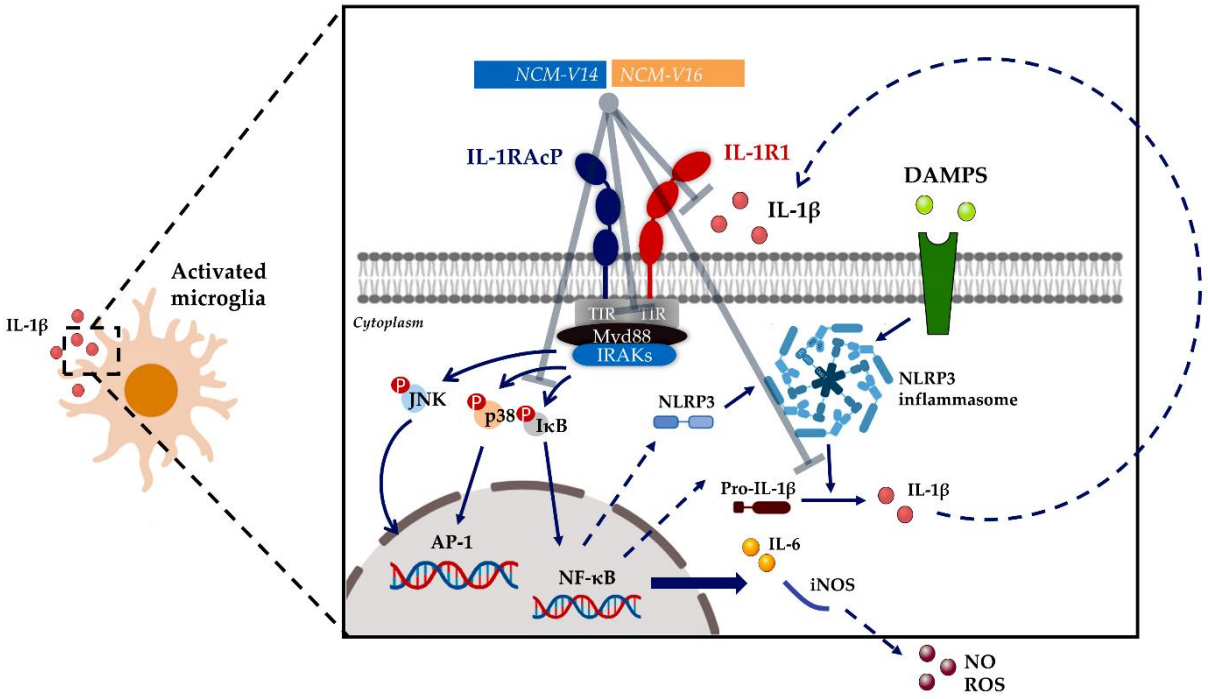

Figure VI. 8 - Schematic representation proposing that NCM-V14 modulates the IL-1R1/Myd88/NF-κB signalling pathway. Compounds NCM-V14 and NCMV-16 attenuate the IL-1R1/Myd88/NF-κB inflammatory response, resulting in the downregulation of pro-inflammatory NLRP3, IL-6, IL-1β and iNOS in response to IL-1β induced IL-1R1 activation, in immunostimulatory conditions as those produced by pathogen-associated molecular patterns (PAMPs), such as lipopolysaccharide and interferon-gamma, or damage-associated molecular patterns (DAMPs), like alarmins. *Figure abbreviations: interleukin-1 receptor type 1, IL-1R1; interleukin-1 receptor accessory protein, IL-1RAcP; interleukin-1β, IL-1β; interleukin-6, IL-6; myeloid differentiation primary response 88, MYD88; the toll-interleukin-1 receptor homology domain, TIR domain; interleukin-1 receptor-associated kinases, IRAKs; activator protein, AP-1; NLR family pyrin domain containing 3, NLRP3; nitric oxide, NO; reactive oxygen species, ROS.*

Epilogue

"Encumbered forever by desire and ambition
There's a hunger still unsatisfied
Our weary eyes still stray to the horizon
Though down this road we've been so many times

The grass was greener
The light was brighter
The taste was sweeter
The nights of wonder
With friends surrounded
The dawn mist glowing
The water flowing
The endless river

Forever and ever"

Pink Floyd, *High Hopes*

1. In search of modulators of neuroinflammation: a 3-year project in a nutshell

Is neuroinflammation a malicious driver of neurodegenerative diseases? Could the modulation of neuroinflammatory responses be an effective neuroprotective therapeutic strategy? Is there any existing evidence for disease-modifying effects of immunotherapies in neurodegeneration? Could an immunomodulatory small molecule set the brakes on neurodegeneration processes? What's on the horizon to ameliorate neurodegenerative diseases? These are the sort of questions that burned in my brain before, during and even after the conclusion of the work carried out in this project. The immune system has a tremendous power, that spreads in all sorts of directions, revealing layers upon layers of insane complexity, with an astonishing number of potential targets to think about. This project, strongly rooted in molecular modelling approaches closely followed by confirmatory biological experiments, exploits the identification and prioritization of promising new modulators using a well-established target in immune and inflammation pathways.

The focus of this project was the modulation of pro-inflammatory signalling pathways linked to disease states of the central nervous system (CNS) and associated with exuberant neuroinflammatory responses. Within the complex neuroinflammatory landscape, we prioritized interleukin-1 receptor type 1 (IL-1R1) as a target for modulating neuroinflammatory responses, since the regulatory role of this receptor in the innate immune system activation renders it an ideal candidate to block downstream effects of the IL-1 pathway. Although the crystal structure of IL-1R1 has been solved more than two decades ago, no small molecules targeting this receptor have been reported to date. Thus, to identify competitive and selective IL-1R1 modulators, we decided to undertake a virtual screening (VS) approach combined with *in vitro* phenotypic experiments. First, the druggability of IL-1R1 was studied by applying three different computational algorithms to map the IL-1R1 surface for putative small-molecule binding sites holding suitable drug-like physicochemical properties. A putative binding site located at the D1-D2 interface, which is of central importance for cytokine binding, was prioritized for the assembly of structure-based VS experiments. Different binding site detection methods offered consistent predictions on this IL-1R1 region.

To probe the dynamic behaviour and the interdomain conformational flexibility of IL-1R1, molecular dynamics (MD) simulations of the soluble and membrane-bound IL-1R1 were performed. The soluble form of this cytokine receptor is a rather dynamic and flexible protein whose activity has been structurally linked to the interdomain flexibility of the D2-D3 linker. In the presence of a biological membrane, the rotational motions of the globular domains are more restrained, likely contributing to different functional properties. These MD simulations

were further exploited to gain insights into the stability and conformational flexibility of the predicted binding sites on both IL-1R1 forms, revealing similar physicochemical features for the binding pockets of the soluble and membrane-bound forms of the IL-1R1 ectodomain. Additionally, cluster analysis of the large collection of structures sampled by the MD simulations allowed the identification of distinct binding pocket conformations that were used in virtual screening (VS) campaigns.

With the aim of discovering novel neuroinflammatory modulators with selectivity for IL-1R1, an innovative VS workflow was devised, consisting of MD simulations for sampling, receptor-based pharmacophore modelling for building three-dimensional (3D) predictive models characterising the structural determinants for ligand binding to IL-1R1, maximum common substructure (MCS) clustering, molecular docking and 3D-shape similarity for filtering. Accordingly, receptor-based pharmacophore hypotheses devised for IL-1R1 allowed the retrieval of 27.206 virtual hit compounds from a CNS-tailored library of 19.3 million compounds. This subset of molecules was clustered by MCS to ensure chemical diversity and structural insight in the selection procedure and docked in the predicted binding region of IL-1R1. Given that the values output by docking scoring functions are, at best, approximations and often not reliable to discriminate between active and inactive ligands, VS hits were ranked by quantitative analysis of protein-ligand interactions and pharmacophore model compliance. The use of 3D similarity allowed the prioritization of compounds against a small molecule dataset holding relevant bioactivity signatures.

Thus far, amongst the top VS hits retrieved by the structure-based VS protocol, 21 structurally distinct compounds were purchased from various chemical suppliers to be experimentally tested. At an initial stage, the compounds were evaluated for their aqueous (kinetic) solubility and screened for *in vitro* cytotoxic activity using a human cancer cell line (HepG2) and a human microglial cell line (CHME3). Of these, three promising compounds were selected for *in vitro* phenotypic assays, of which two revealed to be active at decreasing IFN-γ-driven CHME3 microglial pro-inflammatory levels of IL-1R1, IL-1β, IL-6, NRLP3 and iNOS, as well as reducing IFN-γ-induced activation of NF-κB. Though it can be easy to slip into a mind-set of compartmentalization - where inflammatory mediators do not act as an interacting network of molecular partners but rather as individual factors - we need to keep in mind that these factors may very well have very different outcomes on a microenvironment composed of different cell populations acting synergistically. Hence, our promising data call for further investigation into the details of the molecular mechanism of action of the selected hit compounds, and their action on the combined activities of different inflammatory cells, cytokines and chemokines occurring in the CNS cellular milieu in a state of neuroinflammation.

On one hand, the results presented here are a promising starting point in the ongoing development of a candidate molecule to target disease states that trigger or are a consequence of neuroinflammatory processes. On the other hand, we have expanded the understanding of the structural features of IL-1R1, which can be exploited in other drug discovery settings targeting this receptor. This work has been carried out taking advantage of a multidisciplinary approach combining computational methodologies, such as molecular dynamics simulations and virtual screening, with experimental toxicity and drug screening cell assays. On a personal level, this project was an exciting challenge, with much brainstorming and troubleshooting throughout the three years. More important than the results obtained is the collective sum of life experiences, knowledge, creativity, innovation, self-expression and scientific thinking that was learnt throughout this work.

2. Perspectives

The complex nature of neurodegenerative diseases is well reflected in the clinical failures of therapeutic approaches for these diseases. The search for disease-modifying treatments will likely depend on the willingness to explore uncharted territories and/or apply an "outside-the-box" line of thinking – towards the development of innovative and more effective therapeutic strategies to solve the neurodegeneration puzzle. Undoubtedly, one of the most critical aspects facing neurodegenerative diseases is the development of community-wide efforts to prepare and share large databases, harbouring statistical analyses, data files and clinical study reports, and to implement multidisciplinary collaborations that brings together diverse ideas and people into the field. From this perspective, Medicinal Chemistry stands as a rapidly evolving field intersecting important scientific areas - from organic chemistry and chemical biology, through pharmacology, to computational chemistry - providing ample networking opportunities to novel developments and hopefully bring us closer to developing effective treatments for these diseases. With this in mind, the application of computational methodologies in medicinal chemistry is well illustrated in this thesis, despite all of its limitations. In an era of data and informatics, the field of computational medicinal chemistry is expanding and will continue to do so if it stays closely intertwined with other disciplines in the medicinal chemistry toolkit.

Dysregulated and exuberant neuroinflammatory responses associated with several neurological disorders and ageing are currently an exciting proving ground for new therapeutic ideas and new modes of action to act on neurodegenerative diseases. Even after the discovery of potential small molecule modulators of neuroinflammatory responses directed to an upstream target like IL-1R1, covered in this thesis, it is still a distant hope to have a small molecule effective in slowing progression of a neurodegenerative disease. First, whether the observed effects are a direct result of action on signal transduction events initiated

by IL-1R1 or a downstream dependent on other cytokine (or other gene) expression resulting from IL-1R1 initiated signalling remains to be determined. Second, the implementation and application of VS endeavours is still underway for other protein targets involved not only in neuroinflammation but also being at the core of neurodegeneration. With this, I firmly believe that in the future one may need to abandon the "one target – one solution" philosophy. Instead, one type of a lead molecule acting specifically against a particular target, may be effective only in a particular cellular environment, whereas another molecule against the same target could be efficient in another environment. In other words, we need to leave behind the illusion that a single bullet can fix the problem and adopt a systems biology approach. Within that complex mainframe, combination therapies consisting of chemical entities targeting both protein aggregation and neuroinflammation may be a way to substantially delay progression of the disease.

As a young medicinal chemistry scientist with a project research on drug discovery for neuroinflammation-associated neurodegenerative diseases, I am aware of the many obstacles and unknowns associated with this field, and that only a small number of projects truly go "all the way". Still, the novelty of this project employing an innovative VS framework that could be extended and tested in many other inflammatory proteins, as well as the experimental validation approach incorporating solely human cell lines into the phenotypic screening process – allowing target validation with disease-relevant *in vitro* assays that confirm cellular activity – represents an *in progress* thrilling playground to be explored in the near future. The current limitations, like lack of reference ligand(s), the use of a single docking program with respect to pose prediction, or the uncertainties in predicting biological activities, only to name a few, present valid starting points for further improvements to enhance the full potential of these project. In the end, the results provided initial identification of key compounds that modulate pro-inflammatory markers and provided the rationale for future medicinal chemistry studies based on their chemical structures.

Appendix

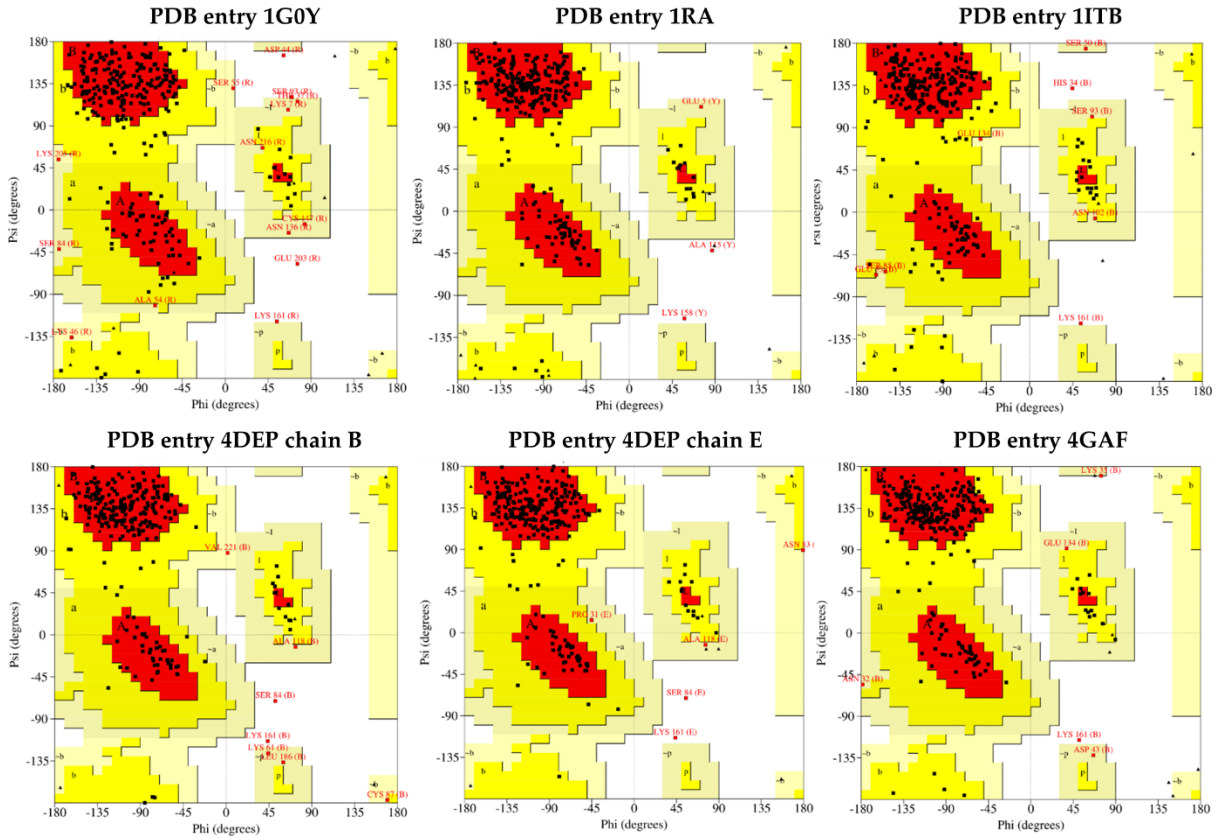

Figure A.1. Ramachandran plots for the crystallographic structures of the extracellular domain of interleukin-1 receptor type 1 (IL-1R1-ECD) available in the PDB. The red regions in the plots indicate the most allowed regions, whereas the yellow regions represent allowed regions. Glycine is represented by triangles and other residues are represented by squares.

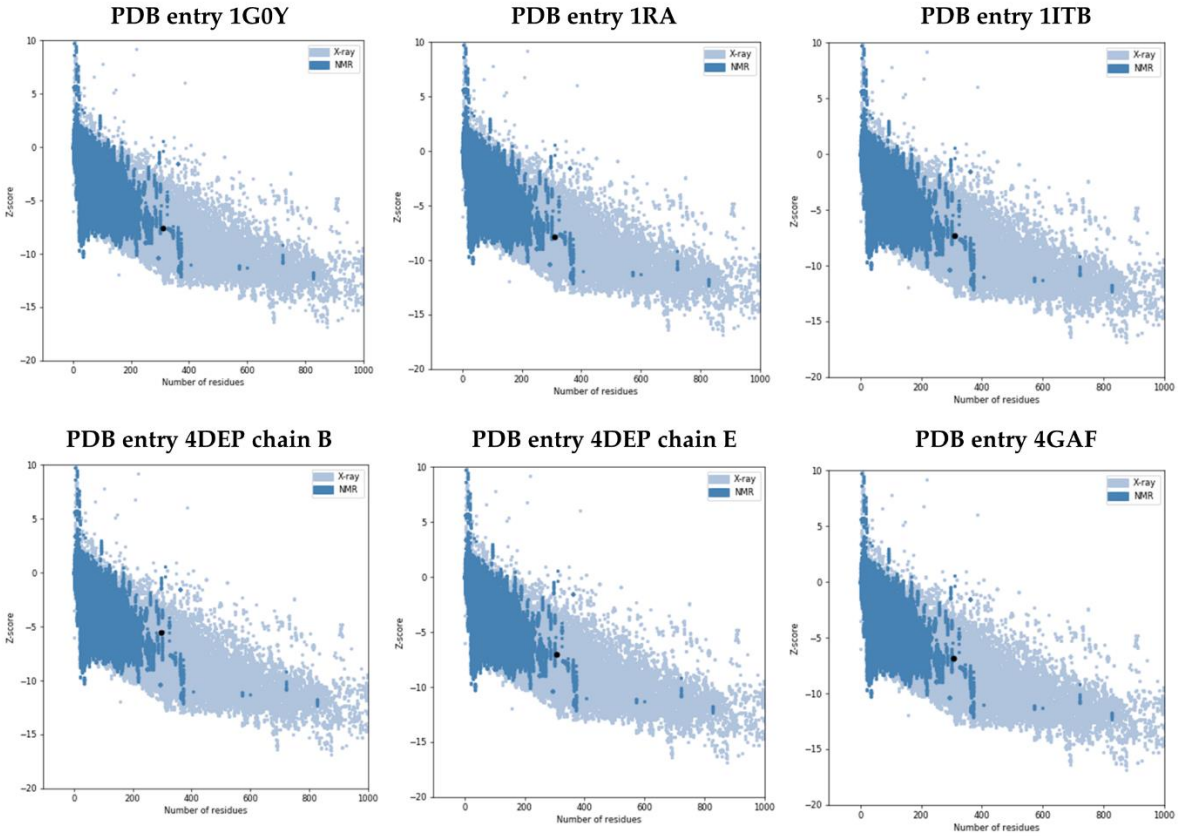

Figure A.2. *Z*-plots for the for the crystallographic structures of the extracellular domain of interleukin-1 receptor type 1 (IL-1R1-ECD) available in the PDB. Z-scores for all structures (represented as black dots) were found to be within the range observed for proteins determined by X-ray crystallography (light blue) and NMR spectroscopy (dark blue).

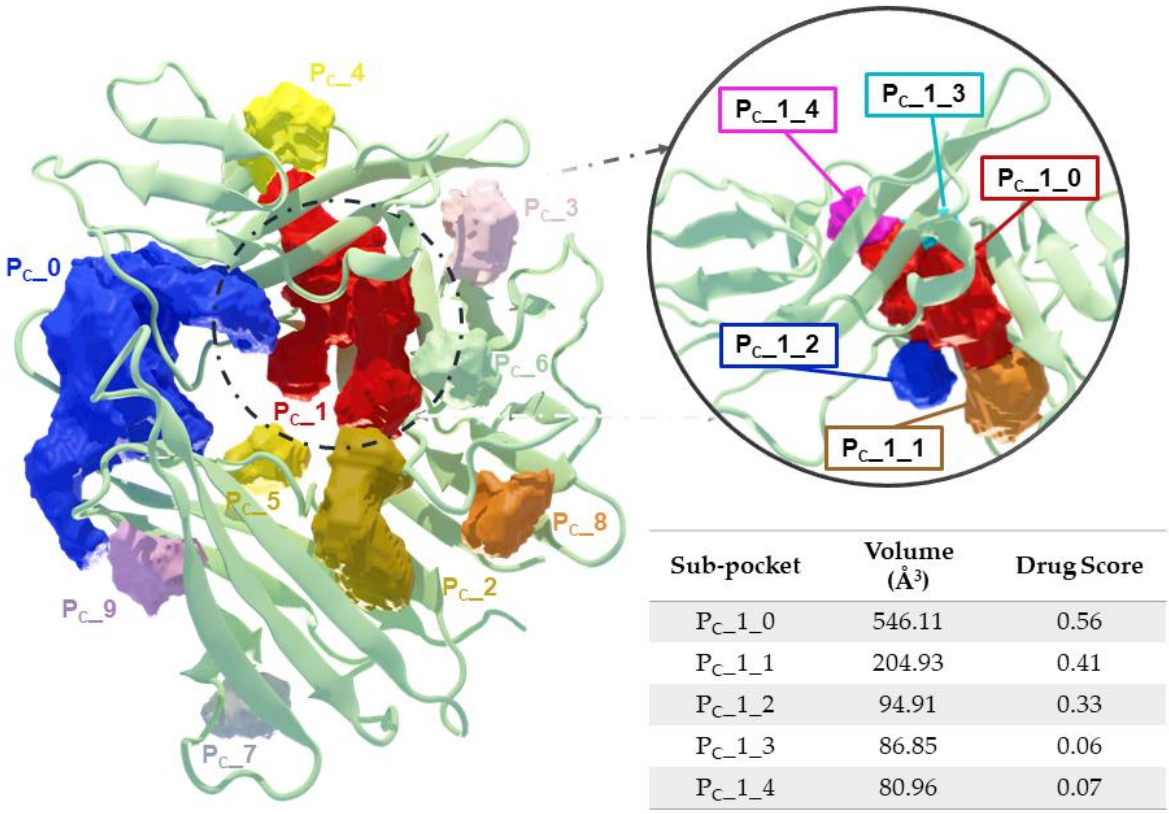

Sub-pocket	Volume (Å³)	Drug Score
Pc_1_0	546.11	0.56
Pc_1_1	204.93	0.41
Pc_1_2	94.91	0.33
Pc_1_3	86.85	0.06
Pc_1_4	80.96	0.07

Figure A-3: Binding pocket prediction on the extracellular domain of interleukin-1 receptor type 1 (PDB entry 1G0Y), using the DoGSiteScorer tool. **(A)** Ten binding pockets are shown: Pc_0 (blue); Pc_1 (red); Pc_2 (brown); Pc_3 (mauve); Pc_4 (yellow); Pc_5 (dark yellow); Pc_6 (lime); Pc_7 (grey); Pc_8 (orange); Pc_9 (purple). **(B)** The sub-pockets composing Pc_1 are illustrated in detail, with respective volume and druggability scores. Five sub-pockets are shown: Pc_1_0 (red); Pc_1_1 (orange); Pc_1_2 (blue); Pc_1_3 (cyan); Pc_1_4 (pink).

Table A-1. Predicted pockets by DoGSiteScorer on the IL-1R1-ECD surface (PDB entry 1G0Y).

Pocket	Volume (Å³)	Surface (Å²)	Depth (Å)	Nº residues	Hydrophobicity ratio	HBA /HBD	Drug Score
Pc_0	1288.51	2094.76	28.36	42	0.42	86/44	0.81
Pc_1	1013.76	1151.38	18.88	39	0.35	74/27	0.81
Pc_2	386.56	517.85	11.74	18	0.39	25/8	0.61
Pc_3	187.71	381.02	12.35	11	0.53	10/8	0.44
Pc_4	173.89	371.96	9.72	12	0.39	14/9	0.35
Pc_5	153.09	304.38	8.39	10	0.41	14/5	0.3
Pc_6	126.66	250.77	7.78	11	0.50	8/3	0.23
Pc_7	124.42	230.08	7.48	12	0.27	12/4	0.23
Pc_8	123.71	206.71	8.85	11	0.42	12/3	0.24
Pc_9	123.39	209.34	7.35	10	0.41	16/3	0.22

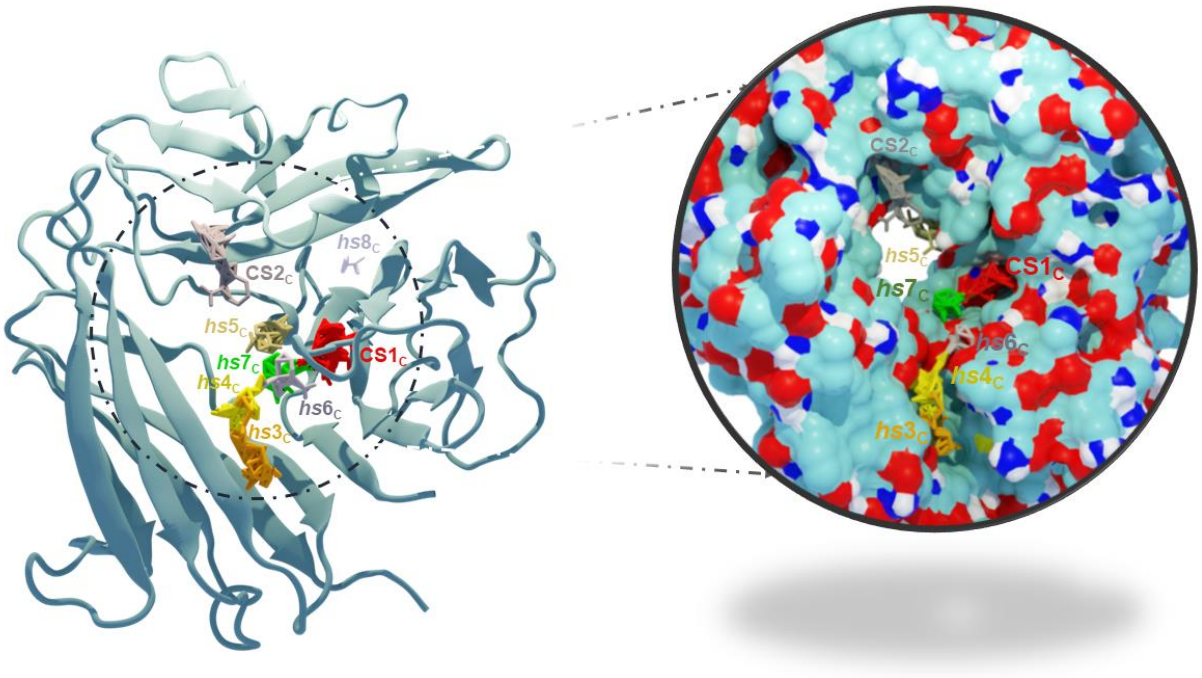

Figure A-4 - Binding pocket prediction and druggability assessment on the extracellular domain of interleukin-1 receptor type 1 (PDB entry 1G0Y), using the FTMap tool. The D1-D2 surface representation enclosed by the black line is illustrated in detail. Eight binding *hot-spots* are shown: CS1C (red); CS2C (mauve); *hs*3C (orange); *hs*4C (yellow); *hs*5C (beige); *hs*6C (grey); *hs*7C (green) and *hs*8C (light grey). Consensus sites (CS) denote regions binding 16 or more probes. *Hot-spots* (*hs*) denote regions binding less than 15 probes.

Table A-2. Summary of FTMap druggability mapping on the IL-1R1-ECD surface (PDB entry 1G0Y).

Hot-spot	**Probe clusters**	**Probe composition**	**Key IL-1R1-ECD residues**
CS1C	24	ACD, ACN, ACT, ADY, AMN, BDY, BEN, BUT, CHX, DFO, DME, ETH, EOL, PHN, THS, URE	Glu11, Ile13, Leu15, Arg25, Pro26, Pro28, Ile92, Tyr127
CS2C	17	ACD, ACN, ACT, ADY, AMN, BDY, BEN, BUT, CHX, DFO, DME, ETH, EOL, PHN, THS, URE	Phe111, Gln113, Val124, Pro126, Tyr127, Ile196
*hs*3C	14	ACD, ACT, ADY, AMN, BDY, BEN, BUT, CHX, DFO, DME, ETH, URE	Arg9, Glu217, Met219, Leu229, Ile230, Ile308, Leu310
*hs*4C	14	ACD, ACT, ADY, BDY, BEN, BUT, DFO, DME, EOL, PHN, THS, URE	Arg9, Glu11, Ser213, Pro214, Glu217, Ile230
*hs*5C	11	ACN, ACT, ADY, BDY, BEN, BUT, CHX, DFO, DME, ETH	Leu15, Val16, Ser18, Gln108, Ala109, Phe111, Tyr127
*hs*6C	5	BUT, EOL, PHN, THS, URE	Pro28, Leu29, Asn30, Ala215
*hs*7C	4	EOL, PHN, THS, URE	Glu11, Lys12, Ile13, Ala215
*hs*8C	2	AMN, ETH	Asp23, Val24, Phe131, Arg194

Tabble abreviations: acetamide (ACD), acetonitrile (ACN), acetone (ACT), acetaldehyde (ADY), methylamine (AMN), benzaldehyde (BDY), benzene (BEN), isobutanol (BUT), cyclohexane (CHX), N,N-dimethylformamide (DFO), dimethyl ether (DME), ethane (ETH), ethanol (EOL), phenol (PHN), isopropanol (THS), urea (URE).

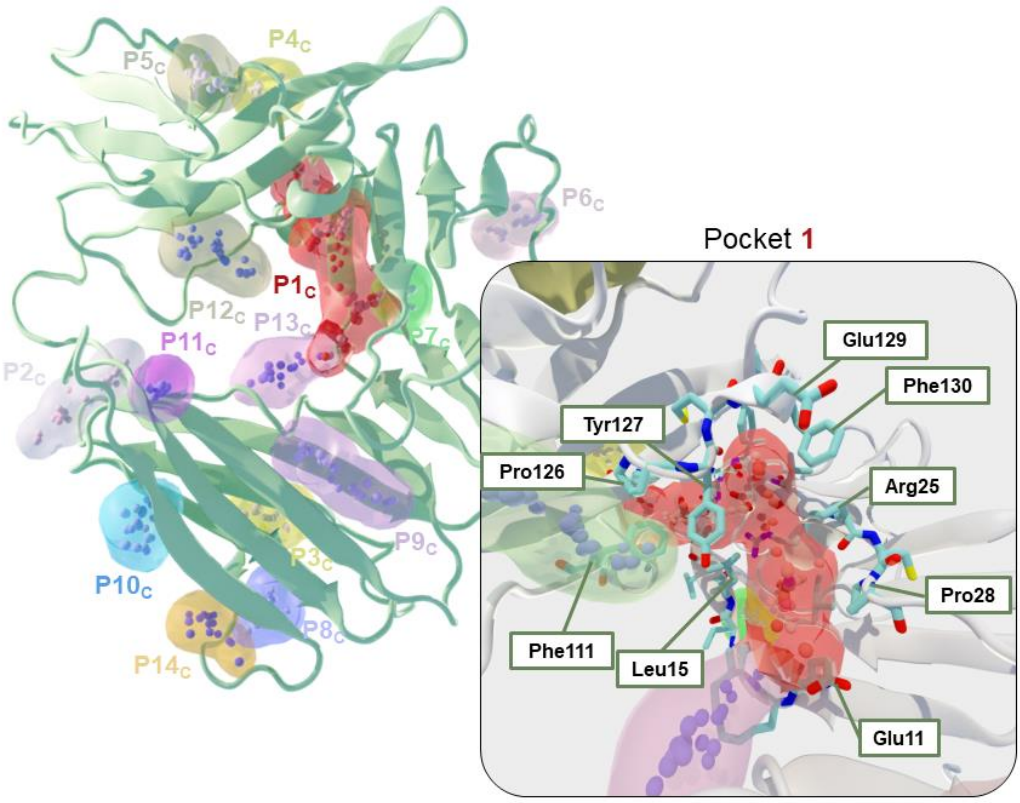

Figure A-5 - Structural pockets identified by Fpocket, on the extracellular domain of interleukin-1 receptor type 1 (IL-1R1-ECD) surface (PDB entry 1G0Y). Fourteen binding pockets are shown: P1c (red); P2c (light grey); P3c (yellow); P4c (dark yellow); P5c (lime); P6c (grey); P7c (green); P8c (blue); P9c (mauve); P10c (cyan); P11c (purple); P12c (green); and P13c (violet). Expanded views are provided for P1c.

Table A-3. Summary of Fpocket druggability mapping on the IL-1R1-ECD surface (PDB entry 1G0Y).

Pocket	Volume (Å³)	Total SASA (nm²)	Mean local hydrophobic density	Druggability score	Key residues IL-1R1-ECD
P1c	865.72	280.859	31.908	0.997	Glu11, Ile13, Leu15, Val16, Ser17, Ser18, Asp23, Val24, Arg25, Pro26, Pro28, Ile92, Asn99, Cys104, Tyr105, Asn106, Ala109, Phe111, Tyr127, Glu129, Phe130, Phe131, Arg194
P2c	268.728	97.638	0.000	0.001	Leu115, Lys205, Thr207, Arg208, Gln236, Ser238, Asn299, His301
P3c	281.001	72.736	9.000	0.003	Lys244, Trp245, Asn246, His291, Pro292, Phe296
P4c	162.784	42.662	18.000	0.008	Cys104, Tyr144, Thr178, His180, Thr193

P5C	201.919	75.774	1.000	0.000	Glu137, Leu138, Pro139, Lys140, Leu141, Gly159, Lys161
P6C	295.761	90.403	3.000	0.000	Lys42, Val49, Ser50, Ile57, Glu72, Asp73
P7C	208.133	48.898	6.000	0.001	Ser74, Gly75, His76, Ser93, Ala94, Lys95
P8C	300.794	84.257	8.000	0.001	Tr+245, Asn246, Ser248, Val249, Ile250, Asp251, Asp254, Leu257, Arg287
P9C	481.155	149.716	12.909	0.014	Arg9, Asn30, Pro31, Ser213, Met219, Val221, Ile227, Gln228, Leu229, Ile230, Ile308
P10C	404.495	108.172	11.846	0.013	Leu237, Asp239, Ile240, Ala241, Tyr242, Tyr261, Tyr262, Ser263, Leu275, Thr277
P11C	157.070	52.279	2.000	0.000	Val264, Asn266, Arg272, Ser273, Thr274
P12C	331.278	109.455	15.000	0.014	Phe111, Lys112, Gln113, Leu115, Val124, Pro126, Tyr127, Ile196
P13C	262.396	104.894	9.000	0.002	Glu11, Ile13, Ile211, Pro214, Ala215, Asn216, Asp304, Ala306
P14C	237.413	101.694	0.000	0.000	Ile250, Asp251, Glu252, Asp254, Leu257, Glu259, Tyr261

Section B *(chapter 3)*

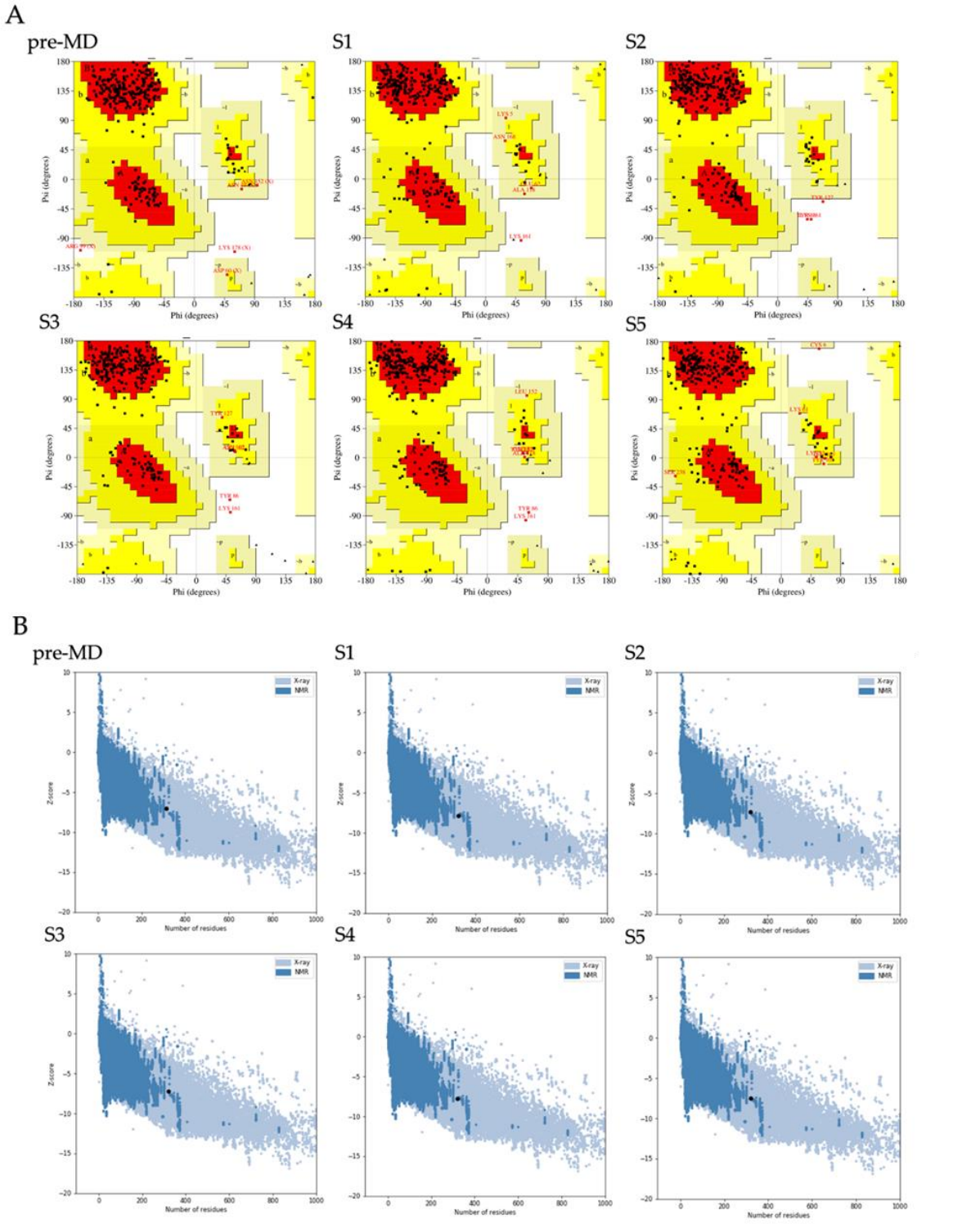

Figure B-1 - (A) Ramachandran plot for the pre-MD model and the final snapshots of the S1, S2, S3, S4 and S5 trajectories of the soluble IL-1R1. (B) Z-plot for the pre-MD model and the final snapshots of the S1, S2, S3, S4 and S5 trajectories of the soluble IL-1R1. Z-scores for all models (represented as black dots) were found to be within the range observed for proteins determined by X-ray crystallography (light blue) and NMR spectroscopy (dark blue).

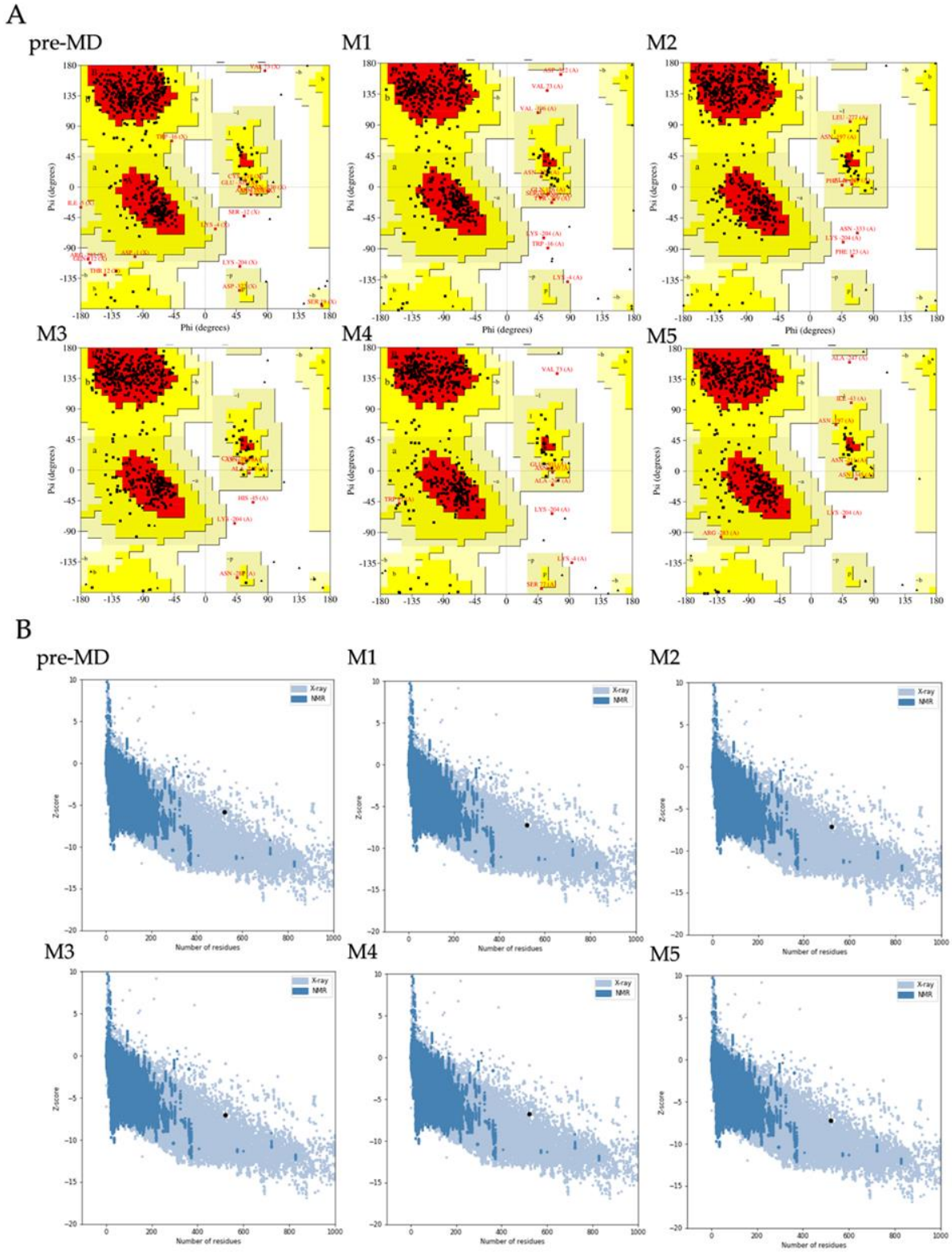

Figure B-2 - (A) Ramachandran plot for the pre-MD model and the final snapshots of the M1, M2, M3, M4 and M5 trajectories of the membrane-bound full-length IL-1R1. (B) Z-plot for the pre-MD model and the final snapshots of the M1, M2, M3, M4 and M5 trajectories of the membrane-bound full-length IL-1R1. *Z*-scores for all models (represented as black dots) were found to be within the range observed for proteins determined by X-ray crystallography (light blue) and NMR spectroscopy (dark blue).

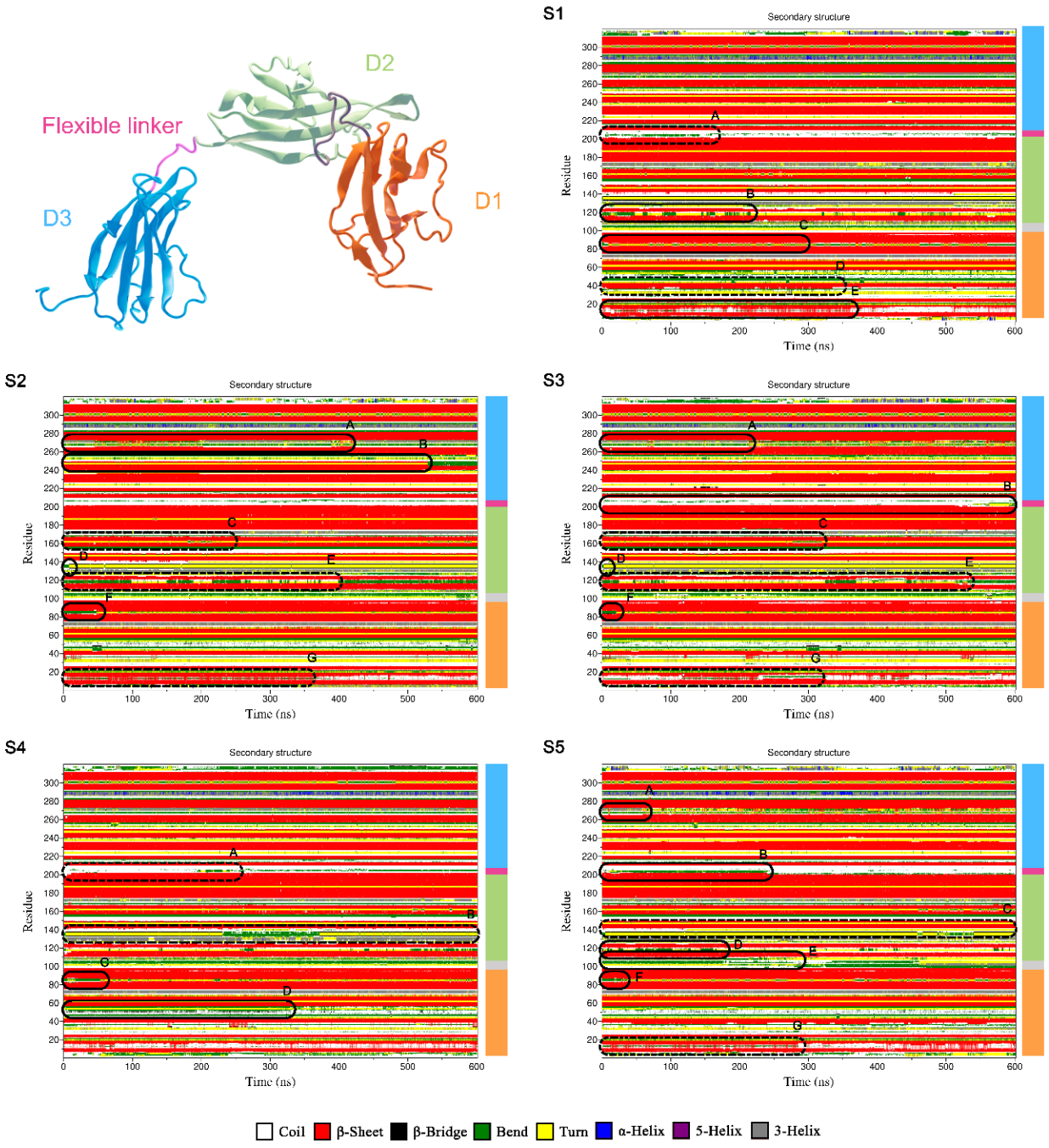

Figure B-3 - Secondary structure assignment according to DSSP, throughout the whole simulation length for the soluble extracellular domain of interleukin-1 receptor type 1 (IL-1R1-ECD) – trajectories S1, S2, S3, S4, and S5. Significant variations are circled in black: solid lines represent relevant changes in the secondary structure; dashed lines indicate smaller variations that tend to reset to the original secondary structure.

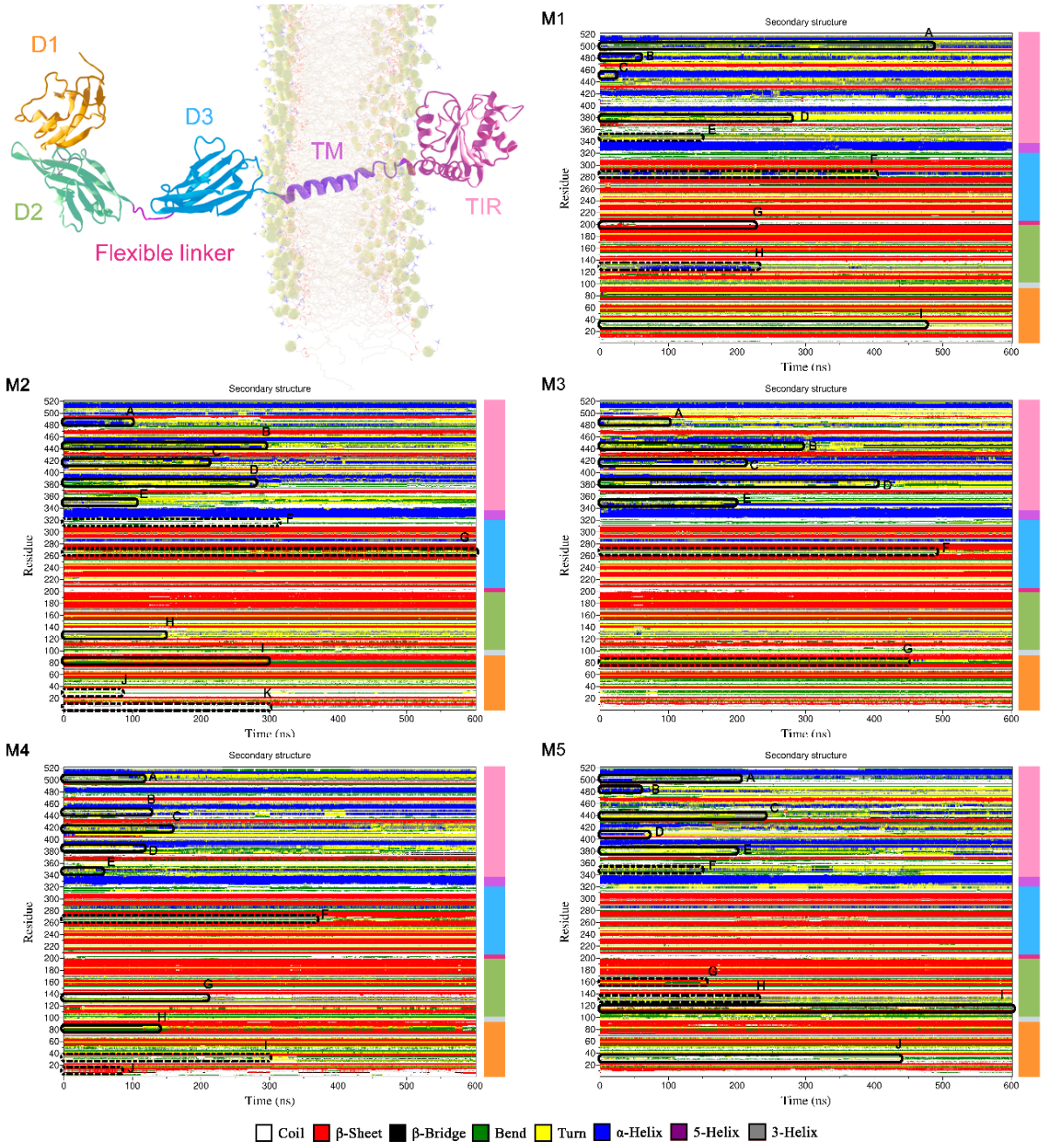

Figure B-4 - Secondary structure assignment according to DSSP, throughout the whole simulation length for the extracellular domain (ECD), transmembrane (TM) and TIR domains of full-length IL-1R1 - trajectories M1, M2, M3, M4, and M5. Significant variations are circled in black: solid lines represent relevant changes in the secondary structure; dashed lines indicate smaller variations that tend to reset to the original secondary structure.

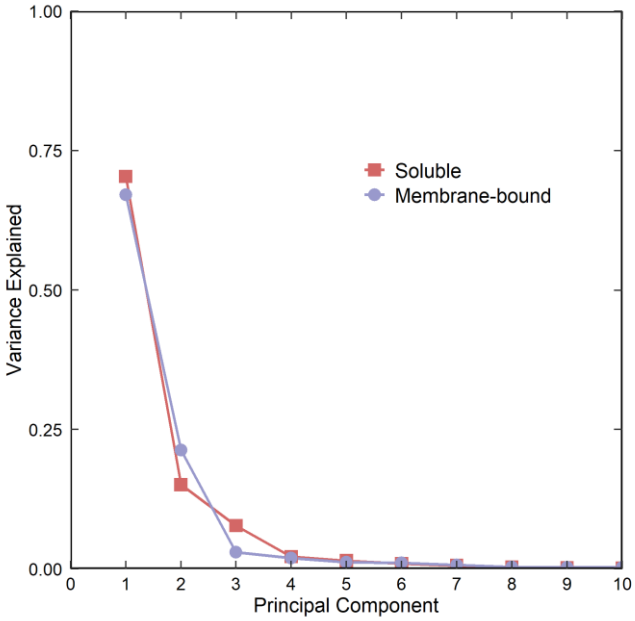

Figure B-5 - Scree plot representing the proportion of variance explained for the first 10 principal components, determined by principal component analysis (PCA) on the trajectories of (A) soluble (red line) and (B) membrane-bound (purple line) extracellular domains of interleukin-1 receptor type 1 (IL-1R1-ECD).

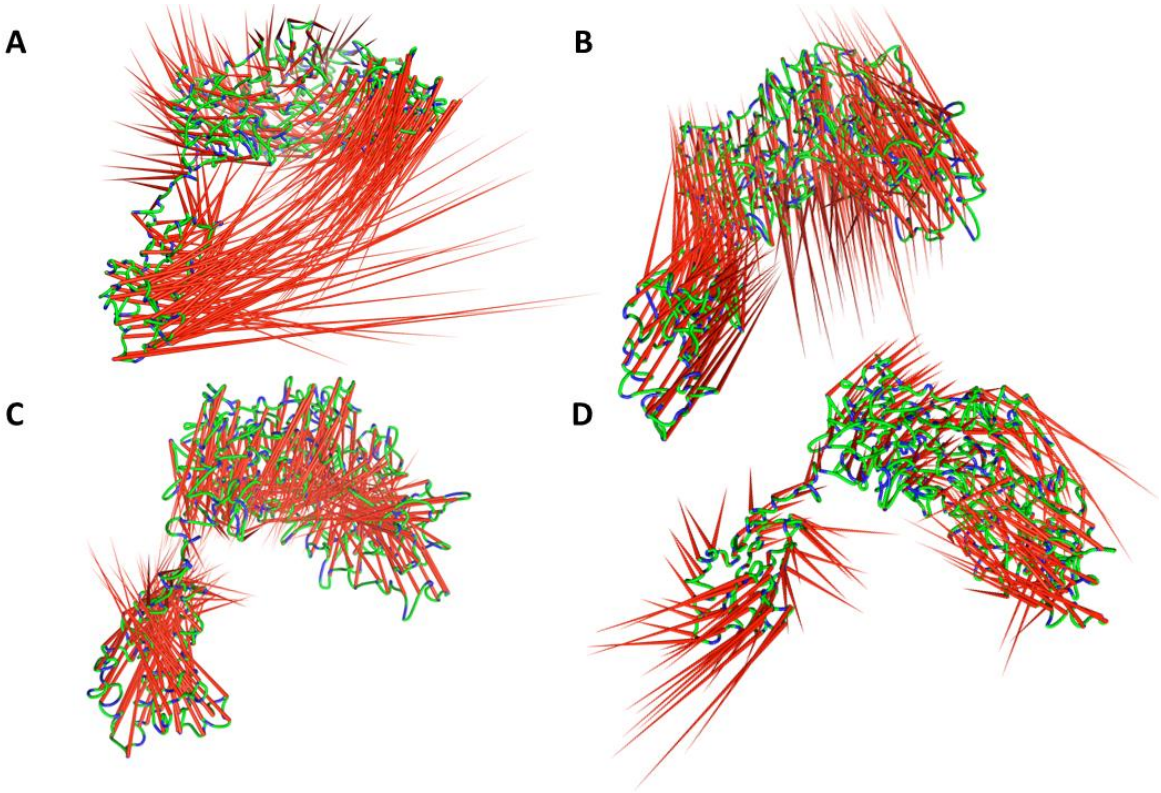

Figure B-6 - Porcupine plots showing the significant motion across the principal components (PCs) (A) PC1; (B) PC2; (C) PC3; and (D) PC4, in the IL-1R1-ECD. The arrows indicate the direction of correlated motion.

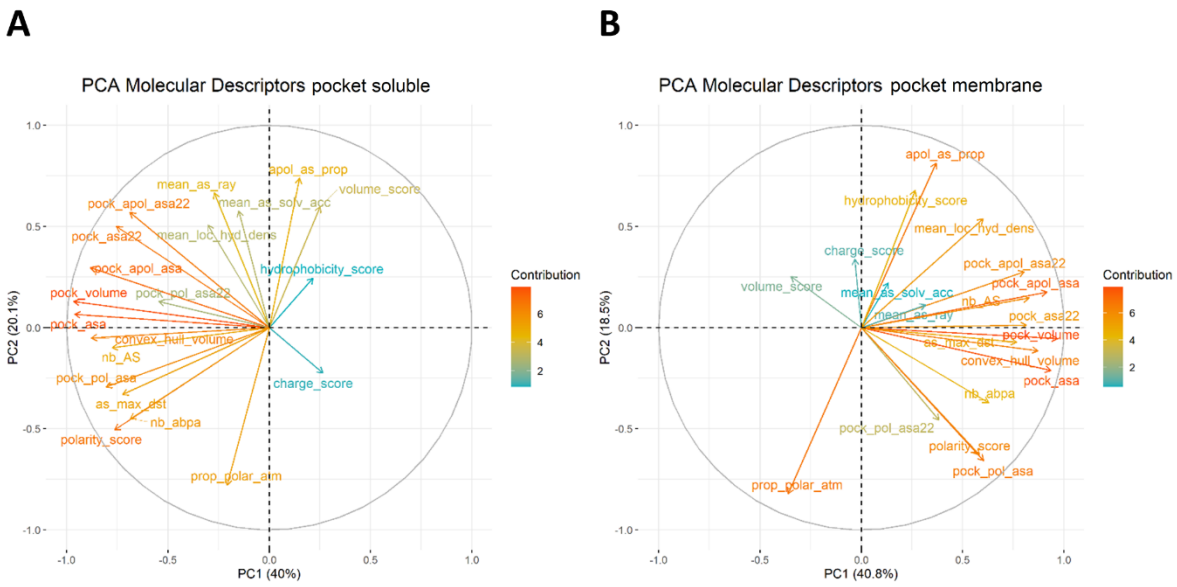

Figure B-7 - Principal component analysis (PCA) of the molecular descriptor space explored by the pocket on (A) the soluble and (B) membrane-bound extracellular domains of interleukin-1 receptor type 1 (IL-1R1-ECD). Twenty MDPocket descriptors characterizing the binding pocket were projected onto the first two PCA axes. *pock_volume*: Volume of the pocket; *pock_asa*: solvent accessible surface area of the pocket; *pock_pol_asa*: polar solvent accessible surface area of the pocket; *pock_apol_asa*: apolar solvent accessible surface area of the pocket; *pock_asa22*: accessible surface area using a probe of 2.2Å; *pock_pol_asa22*: polar accessible surface area using a probe of 2.2Å; *pock_apol_asa22*: apolar accessible surface area using a probe of 2.2Å; *nb_AS*: number of alpha spheres; *mean_as_ray*: mean alpha sphere radius; *mean_as_solv_acc*: mean alpha sphere solvent accessibility; *apol_as_prop*: proportion of apolar alpha spheres in the pocket; *mean_loc_hyd_dens*: mean local hydrophobic density; *hydrophobicity_score*: residue based hydrophobicity; *volume_score*: mean volume score of all amino acids in contact with at least one alpha sphere; *polarity_score*: ; *charge_score*: mean charge for all amino acids in contact with at least one alpha sphere; *prop_polar_atm*: proportion of polar atoms; *as_density*: alpha sphere density; *as_max_dst*: maximum distance between the center of mass and all alpha spheres;

Table B-1 - Contribution of MDPocket's molecular descriptors to the first two principal components (PC1 and PC2) describing the putative pocket evolution during the MD simulations.

	Soluble		**Membrane-bound**	
Descriptor	*PC1*	*PC2*	*PC1*	*PC2*
pock_volume	-0.34111643	0.06420109	0.33835757	-0.02848370
pock_asa	-0.33962947	0.03258052	0.32717103	-0.11027587
pock_apol_asa	-0.31204565	0.14801511	0.32064194	0.09151747
convex_hull_volume	-0.31042248	-0.02578107	0.30444671	-0.05997160
nb_AS	-0.27402834	-0.04978003	0.28950969	0.07593383
pock_asa22	-0.26647090	0.24890560	0.28493483	0.00583966
pock_apol_asa22	-0.24333145	0.28416856	0.28110819	0.14343235
as_max_dst	-0.25591587	-0.16508785	0.26795163	-0.03783970
nb_abpa	-0.24246494	-0.22493053	0.21995738	-0.19326309
pock_pol_asa	-0.28448823	-0.14620821	0.21096821	-0.34234371
mean_loc_hyd_dens	-0.10702266	0.25267690	0.21053245	0.27984039
polarity_score	-0.26965289	-0.25204615	0.20359585	-0.32743996
pock_pol_asa22	-0.19288472	0.06415194	0.13375016	-0.23777941

apol_as_prop	0.05278602	0.36862932	0.12888394	0.42330385
prop_polar_atm	-0.07366071	-0.38856500	-0.12622681	-0.42712468
volume_score	0.08856685	0.29815099	-0.12165946	0.13101572
mean_as_ray	-0.09596384	0.33209349	0.11115458	0.05821154
hydrophobicity_score	0.07608753	0.12197551	0.09278400	0.35262229
mean_as_solv_acc	-0.05329298	0.28778344	0.04648431	0.11508175
charge_score	0.09363060	-0.11224556	-0.01127742	0.17570732

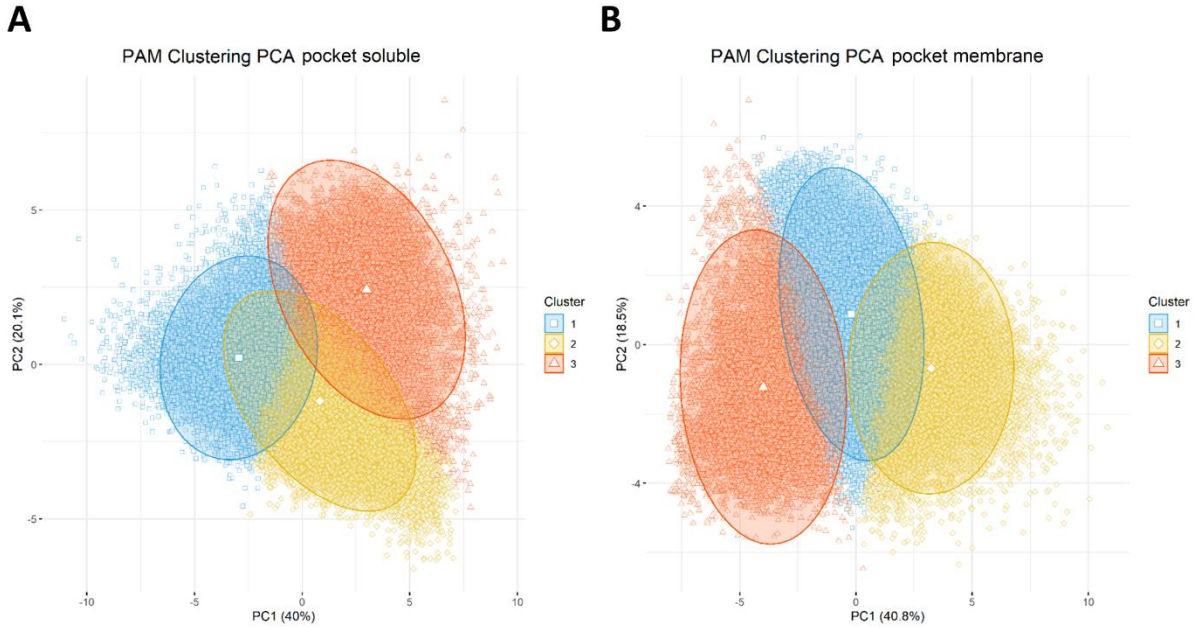

Figure B-8 - Bi-plots of principal components derived from the PAM clustering analysis on the putative binding pocket of (A) soluble and (B) membrane-bound extracellular domains of interleukin-1 receptor type 1 (IL-1R1-ECD).

Section D *(chapter 5)*

Table D-1 - *In vitro* toxicity of the virtual screening (VS) hits in HepG2 cells.

NCM	Viability (%) HepG2 cells – group 1							
	5 μM	**10 μM**	**20 μM**	**50 μM**	**100 μM**	**150 μM**	**200 μM**	**300 μM**
V02	99.7±4.51	106.5±1.88	103.6±2.07	100.5±4.67	102.1±5.02	97.1±9.72	90.0±0.86	85.5±2.91
V04	93.7±7.57	88.4±1.46	77.2±6.00	51.5±9.30	0.66±0.66	0.1±0.09	0	0
V06	96.6±1.16	99.7±0.55	97.3±2.63	92.9±4.01	80.2±3.83	38.3±12.50	12.3±10.91	0
V08	104.9±2.61	104.7±0.77	105.7±6.51	102.0±6.25	91.9±3.72	77.7±4.32	72.1±1.69	59.5±1.09
V10	96.0±11.78	105.6±6.98	104.9±5.69	88.9±11.35	69.7±7.15	53.9±4.55	40.5±9.05	23.9±6.86
V11	93.5±0.25	96.5±1.57	95.2±4.54	97.1±3.39	103.6±2.24	91.5±8.78	91.0±6.00	91.6±15.21
V12	102.6±5.57	104.1±3.72	104.3±6.70	102.2±0.17	106.7±6.96	111.8±1.62	108.4±0.11	110.3±6.19
V13	100.5±0.47	100.1±5.85	102.5±2.82	80.1±3.58	24.3±10.74	0	0	0
V14	110.7±0.22	110.3±5.32	108.0±5.44	105.4±0.26	109.0±1.45	110.7±3.38	111.9±2.48	111.6±4.32
V16	117.1±2.13	115.1±2.12	104.2±4.23	104.1±2.88	99.4±0.65	93.0±2.65	83.2±2.2	41.4±0.95
V17	0	0	0	0	0	0	0	0
NCM	**Viability (%) HepG2 cells – group 2**							
	2.5 μM	**5 μM**	**10 μM**	**20 μM**	**40 μM**	**60 μM**	**80 μM**	**100 μM**
V01	98.9±3.44	100.3±1.05	104.8±1.61	104.4±2.03	97.3±0.78	81.0±4.48	67.4±6.27	48.7±4.14
V07	105.3±3.14	108.5±10.51	109.4±7.59	74.2±1.51	58.4±5.23	76.0±6.64	34.5±5.50	18.1±6.93
V15	100.8±1.60	99.9±0.69	99.9±0.34	100.2±6.29	98.0±2.74	93.3±0.05	91.4±6.14	84.4±4.36
V18	96.1±4.17	96.8±5.84	98.9±4.36	104.8±1.83	99.6±2.38	95.2±10.18	96.3±10.58	94.6±6.98
V19	N.D.	98.1±7.44	98.1±10.64	81.9±6.09	78.4±1.64	75.1±5.00	77.0±3.92	72.2±7.20
V20	N.D.	102.5±2.48	95.0±5.04	93.4±4.84	88.2±7.29	81.5±0.02	77.5±0.84	77.4±4.14
V21	95.3±6.58	92.4±1.37	83.0±0.44	80.0±9.34	70.4±10.02	47.5±21.64	28.3±26.8	13.2±5.7
NCM	**Viability (%) HepG2 cells – group 3**							
	2.5 μM	**5 μM**	**10 μM**	**15 μM**	**20 μM**	**50 μM**		
V03	74.8±5.17	54.2±9.02	33.3±20.8	8.9±7.74	3.8±3.83	0		
V05	17.4±1.48	16.0±3.53	12.5±4.53	6.4±4.95	0	0		
V09	N.D.	N.D.	N.D.	N.D.	N.D.	N.D.		

Cell viability was measured as rezasurin reduction. Data are expressed as the mean±SEM of triplicate of three independent experiments. N.D. – not determined.

Table D-2 - *In vitro* toxicity of the virtual screening (VS) hits in CHME3 microglial cells.

NCM	Viability (%) CHME3 microglia – group 1		
	20 μM	**50 μM**	**100 μM**
V04	53.1±7.11	29.0±0.80	18.9±3.36
V06	86.0±0.62	61.2±2.57	33.1±2.56
V08	98.9±6.24	91.1±2.58	76.5±2.70
V10	105.4±6.55	110.4±3.92	69.4±4.29
V11	105.0±1.73	90.8±2.97	60.2±3.64
V13	79.0±3.99	40.4±10.0	0
V14	106.2±2.08	105.5±7.41	95.4±9.28
V16	93.5±3.78	89.2±9.19	86.5±8.65
NCM	**Viability (%) CHME3 cells – group 2**		
	20 μM	**50 μM**	**100 μM**
V01	79.3±11.46	60.7±15.22	35.6±8.35
V07	75.9±3.45	67.1±1.01	12.3±3.41
V15	85.8±2.86	71.4±2.53	31.3±13.02
V19	108.3±9.53	96.2±2.78	66.8±4.58
V21	40.5±1.62	27.1±3.29	12.8±2.40

Cell viability was measured as MTS reduction. Data are expressed as the mean±SEM of triplicate of three independent experiments.

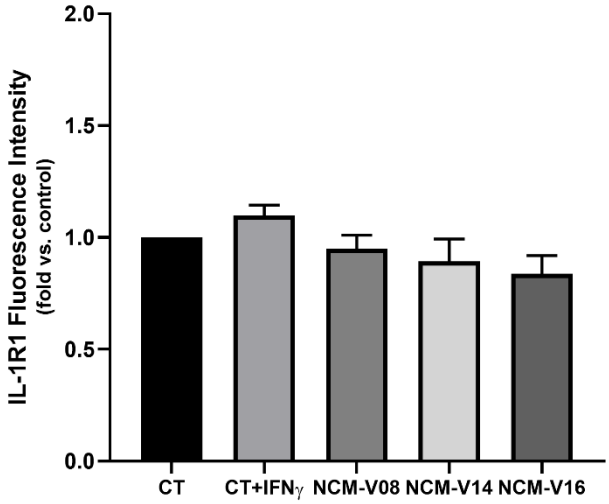

Figure E-1 - Quantification of IL-1R1 mean fluorescence intensity, at 12h incubation. Results are mean ± SEM fold change vs. respective controls (untreated cells) from 5 independent experiments. No significant differences were found between the control cells and IFN-γ-stimulated microglial cells either untreated or treated with compounds NCM-V08, NCM-V14 and NCM-V16.

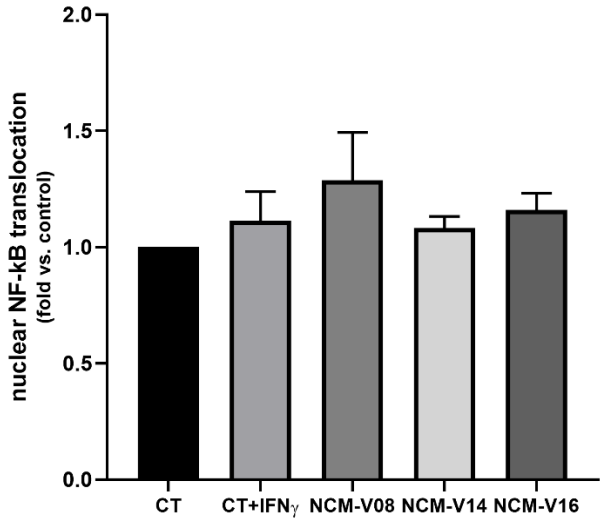

Figure E-2 - Quantification of nuclear NF-κB p65 subunit translocation, at 24h incubation. Results are mean ± SEM fold change vs. respective controls (untreated cells) from 5 independent experiments. No significant differences were found between the control cells and IFN-γ-stimulated microglial cells either untreated or treated with compounds NCM-V08, NCM-V14 and NCM-V16.

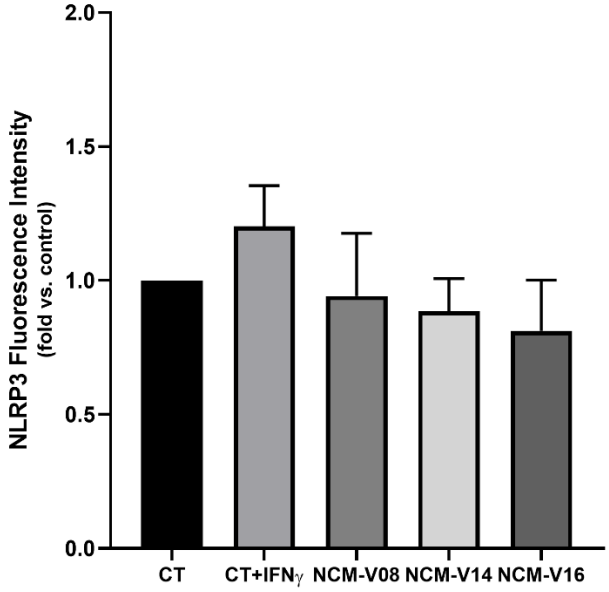

Figure E-3 - Quantification of NLRP3 mean fluorescence intensity, at 24h incubation. Results are mean ± SEM fold change vs. respective controls (untreated cells) from 5 independent experiments. No significant differences were found between the control cells and IFN-γ-stimulated microglial cells either untreated or treated with compounds NCM-V08, NCM-V14 and NCM-V16.

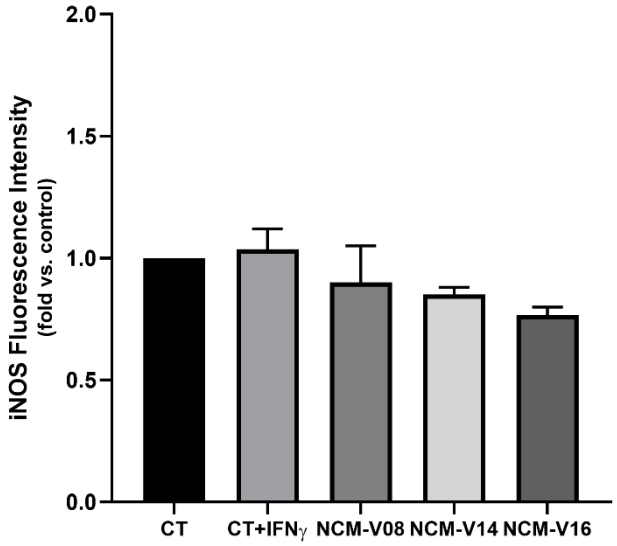

Figure E-4 - Quantification of iNOS mean fluorescence intensity, at 12h incubation. Results are mean ± SEM fold change vs. respective controls (untreated cells) from 5 independent experiments. No significant differences were found between the control cells and IFN-γ-stimulated microglial cells either untreated or treated with compounds NCM-V08, NCM-V14 and NCM-V16.

References

Abbate, A., Van Tassell, B. W., Biondi-Zoccai, G., Kontos, M. C., Grizzard, J. D., Spillman, D. W., et al. (2013). Effects of Interleukin-1 Blockade With Anakinra on Adverse Cardiac Remodeling and Heart Failure After Acute Myocardial Infarction [from the Virginia Commonwealth University-Anakinra Remodeling Trial (2) (VCU-ART2) Pilot Study]. *Am. J. Cardiol.* 111, 1394–1400. doi:10.1016/j.amjcard.2013.01.287.

Abraham, M. J., Murtola, T., Schulz, R., Páll, S., Smith, J. C., Hess, B., et al. (2015). GROMACS: High performance molecular simulations through multi-level parallelism from laptops to supercomputers. *SoftwareX* 1–2, 19–25. doi:10.1016/j.softx.2015.06.001.

Abraham, M., van der Spoel, D., Lindahl, E., Hess, B., and and the GROMACS development Team (2019). GROMACS User Manual version 2019.3.

Acharya, C., Coop, A., E. Polli, J., and D. MacKerell, A. (2011). Recent Advances in Ligand-Based Drug Design: Relevance and Utility of the Conformationally Sampled Pharmacophore Approach. *Curr. Comput. Aided-Drug Des.* 7, 10–22. doi:10.2174/157340911793743547.

Acuña, Hamadat, Corbalán, González-Lizárraga, dos-Santos-Pereira, Rocca, et al. (2019). Rifampicin and Its Derivative Rifampicin Quinone Reduce Microglial Inflammatory Responses and Neurodegeneration Induced In Vitro by α-Synuclein Fibrillary Aggregates. *Cells* 8, 776. doi:10.3390/cells8080776.

Agamah, F. E., Mazandu, G. K., Hassan, R., Bope, C. D., Thomford, N. E., Ghansah, A., et al. (2020). Computational/in silico methods in drug target and lead prediction. *Brief. Bioinform.* 21, 1663–1675. doi:10.1093/bib/bbz103.

Agoni, C., Olotu, F. A., Ramharack, P., and Soliman, M. E. (2020). Druggability and drug-likeness concepts in drug design: are biomodelling and predictive tools having their say? *J. Mol. Model.* 26, 120. doi:10.1007/s00894-020-04385-6.

Allen, D. D., Caviedes, R., Cárdenas, A. M., Shimahara, T., Segura-Aguilar, J., and Caviedes, P. A. (2005). Cell Lines as In Vitro Models for Drug Screening and Toxicity Studies. *Drug Dev. Ind. Pharm.* 31, 757–768. doi:10.1080/03639040500216246.

Alokam, R., Singhal, S., Srivathsav, G. S., Garigipati, S., Puppala, S., Sriram, D., et al. (2015). Design of dual inhibitors of ROCK-I and NOX2 as potential leads for the treatment of neuroinflammation associated with various neurological diseases including autism spectrum disorder. *Mol. Biosyst.* 11, 607–617. doi:10.1039/C4MB00570H.

Altschul, S. F., Gish, W., Miller, W., Myers, E. W., and Lipman, D. J. (1990). Basic local alignment search tool. *J. Mol. Biol.* 215, 403–410. doi:10.1016/S0022-2836(05)80360-2.

Alzheimer, A. (1907). Über eine eigenartige Erkrankung der Hirnrinde. *Allg. Zeitschrift fur Psychiatr. und Psych. Medizin*, 64():146–8.

Anderson, A. C. (2003). The Process of Structure-Based Drug Design. *Chem. Biol.* 10, 787–797. doi:10.1016/j.chembiol.2003.09.002.

Anderson, F. L., von Herrmann, K. M., Andrew, A. S., Kuras, Y. I., Young, A. L., Scherzer, C. R., et al. (2021). Plasma-borne indicators of inflammasome activity in Parkinson's disease patients. *npj Park. Dis.* 7, 2. doi:10.1038/s41531-020-00147-6.

Ardura-Fabregat, A., Boddeke, E. W. G. M., Boza-Serrano, A., Brioschi, S., Castro-Gomez, S., Ceyzériat, K., et al. (2017). Targeting Neuroinflammation to Treat Alzheimer's Disease. *CNS Drugs* 31, 1057–1082. doi:10.1007/s40263-017-0483-3.

Arend, W. P., Malyak, M., Guthridge, C. J., and Gabay, C. (1998). INTERLEUKIN-1 RECEPTOR ANTAGONIST: Role in Biology. *Annu. Rev. Immunol.* 16, 27–55. doi:10.1146/annurev.immunol.16.1.27.

Aytan, N., Choi, J.-K., Carreras, I., Brinkmann, V., Kowall, N. W., Jenkins, B. G., et al. (2016). Fingolimod modulates multiple neuroinflammatory markers in a mouse model of Alzheimer's disease. *Sci. Rep.* 6, 24939. doi:10.1038/srep24939.

Baell, J., and Walters, M. A. (2014). Chemistry: Chemical con artists foil drug discovery. *Nature* 513, 481–483. doi:10.1038/513481a.

Bamborough, P., Hedgecock, C. J., and Richards, W. G. (1994). The interleukin-2 and interleukin-4 receptors studied by molecular modelling. *Structure* 2, 839–851. doi:10.1016/S0969-2126(94)00085-9.

Barateiro, A., Afonso, V., Santos, G., Cerqueira, J. J., Brites, D., van Horssen, J., et al. (2016). S100B as a Potential Biomarker and Therapeutic Target in Multiple Sclerosis. *Mol. Neurobiol.* 53, 3976–3991. doi:10.1007/s12035-015-9336-6.

Barbosa, M., Gomes, C., Sequeira, C., Gonçalves-Ribeiro, J., Pina, C. C., Carvalho, L. A., et al. (2021). Recovery of Depleted miR-146a in ALS Cortical Astrocytes Reverts Cell Aberrancies and Prevents Paracrine Pathogenicity on Microglia and Motor Neurons. *Front. Cell Dev. Biol.* 9. doi:10.3389/fcell.2021.634355.

Barducci, A., Bonomi, M., and Parrinello, M. (2011). Metadynamics. *WIREs Comput. Mol. Sci.* 1, 826–843. doi:10.1002/wcms.31.

Barkholt, P., Sanchez-Guajardo, V., Kirik, D., and Romero-Ramos, M. (2012). Long-term polarization of microglia upon α-synuclein overexpression in nonhuman primates. *Neuroscience* 208, 85–96. doi:10.1016/j.neuroscience.2012.02.004.

Barnum, D., Greene, J., Smellie, A., and Sprague, P. (1996). Identification of Common Functional Configurations Among Molecules. *J. Chem. Inf. Comput. Sci.* 36, 563–571. doi:10.1021/ci950273r.

Barros, C., and Fernandes, A. (2021). Linking Cognitive Impairment to Neuroinflammation in Multiple Sclerosis using neuroimaging tools. *Mult. Scler. Relat. Disord.* 47, 102622. doi:10.1016/j.msard.2020.102622.

Basu, A., Krady, J. K., O'Malley, M., Styren, S. D., DeKosky, S. T., and Levison, S. W. (2002). The Type 1 Interleukin-1 Receptor Is Essential for the Efficient Activation of Microglia and the Induction of Multiple Proinflammatory Mediators in Response to Brain Injury. *J. Neurosci.* 22, 6071–6082. doi:10.1523/JNEUROSCI.22-14-06071.2002.

Bauernfeind, F. G., Horvath, G., Stutz, A., Alnemri, E. S., MacDonald, K., Speert, D., et al. (2009). Cutting Edge: NF-κB Activating Pattern Recognition and Cytokine Receptors License NLRP3 Inflammasome Activation by Regulating NLRP3 Expression. *J. Immunol.* 183, 787–791. doi:10.4049/jimmunol.0901363.

Bellucci, A., Bubacco, L., Longhena, F., Parrella, E., Faustini, G., Porrini, V., et al. (2020). Nuclear Factor-κB Dysregulation and α-Synuclein Pathology: Critical Interplay in the Pathogenesis of Parkinson's Disease. *Front. Aging Neurosci.* 12. doi:10.3389/fnagi.2020.00068.

Benner, C., van der Meulen, T., Cacéres, E., Tigyi, K., Donaldson, C. J., and Huising, M. O. (2014). The transcriptional landscape of mouse beta cells compared to human beta cells reveals notable species differences in long non-coding RNA and protein-coding gene expression. *BMC Genomics* 15, 620. doi:10.1186/1471-2164-15-620.

Béraud, D., Hathaway, H. A., Trecki, J., Chasovskikh, S., Johnson, D. A., Johnson, J. A., et al. (2013). Microglial Activation and Antioxidant Responses Induced by the Parkinson's Disease Protein α-Synuclein. *J. Neuroimmune Pharmacol.* 8, 94–117. doi:10.1007/s11481-012-9401-0.

Berendsen, H. J. C., Grigera, J. R., and Straatsma, T. P. (1987). The missing term in effective pair potentials. *J. Phys. Chem.* 91, 6269–6271. doi:10.1021/j100308a038.

Berendsen, H. J. C., Postma, J. P. M., van Gunsteren, W. F., DiNola, A., and Haak, J. R. (1984). Molecular dynamics with coupling to an external bath. *J. Chem. Phys.* 81, 3684–3690. doi:10.1063/1.448118.

Berendsen, H. J. C., van der Spoel, D., and van Drunen, R. (1995). GROMACS: A message-passing parallel molecular dynamics implementation. *Comput. Phys. Commun.* 91, 43–56. doi:10.1016/0010-4655(95)00042-E.

Berger, O., Edholm, O., and Jähnig, F. (1997). Molecular dynamics simulations of a fluid bilayer of dipalmitoylphosphatidylcholine at full hydration, constant pressure, and constant temperature. *Biophys. J.* 72, 2002–2013. doi:10.1016/S0006-3495(97)78845-3.

Bergholdt, R., Larsen, Z., Andersen, N., Johannesen, J., Kristiansen, O., Mandrup-Poulsen, T., et al. (2000). Characterization of new polymorphisms in the 5′UTR of the human interleukin-1 receptor type 1 (IL1R1) gene: linkage to type 1 diabetes and correlation to IL-1RI plasma level. *Genes Immun.* 1, 495–500. doi:10.1038/sj.gene.6363719.

Berman, H. M., Westbrook, J., Feng, Z., Gilliland, G., Bhat, T. N., Weissig, H., et al. (2000). The Protein Data Bank. *Nucleic Acids Res.* 28, 235–242. doi:10.1093/nar/28.1.235.

Bertani, I., Iori, V., Trusel, M., Maroso, M., Foray, C., Mantovani, S., et al. (2017). Inhibition of IL-1β Signaling Normalizes NMDA-Dependent Neurotransmission and Reduces Seizure Susceptibility in a Mouse Model of Creutzfeldt–Jakob Disease. *J. Neurosci.* 37, 10278–10289. doi:10.1523/JNEUROSCI.1301-17.2017.

Berthold, M. R., Cebron, N., Dill, F., Gabriel, T. R., Kötter, T., Meinl, T., et al. (2008). "KNIME: The Konstanz Information Miner," in, 319–326. doi:10.1007/978-3-540-78246-9_38.

Bhaskar, K., Konerth, M., Kokiko-Cochran, O. N., Cardona, A., Ransohoff, R. M., and Lamb, B. T. (2010). Regulation of Tau Pathology by the Microglial Fractalkine Receptor. *Neuron* 68, 19–31. doi:10.1016/j.neuron.2010.08.023.

Biber, K., Bhattacharya, A., Campbell, B. M., Piro, J. R., Rohe, M., Staal, R. G. W., et al. (2019). Microglial Drug Targets in AD: Opportunities and Challenges in Drug Discovery and

Development. *Front. Pharmacol.* 10. doi:10.3389/fphar.2019.00840.

Bidula, S. M., Cromer, B. A., Walpole, S., Angulo, J., and Stokes, L. (2019). Mapping a novel positive allosteric modulator binding site in the central vestibule region of human P2X7. *Sci. Rep.* 9, 3231. doi:10.1038/s41598-019-39771-5.

Bieber, T. (2021). Atopic dermatitis: an expanding therapeutic pipeline for a complex disease. *Nat. Rev. Drug Discov.* doi:10.1038/s41573-021-00266-6.

Bjelobaba, I., Savic, D., and Lavrnja, I. (2017). Multiple Sclerosis and Neuroinflammation: The Overview of Current and Prospective Therapies. *Curr. Pharm. Des.* 23, 693–730. doi:10.2174/1381612822666161214153108.

Björkqvist, M., Wild, E. J., Thiele, J., Silvestroni, A., Andre, R., Lahiri, N., et al. (2008). A novel pathogenic pathway of immune activation detectable before clinical onset in Huntington's disease. *J. Exp. Med.* 205, 1869–1877. doi:10.1084/jem.20080178.

Blank, T., and Prinz, M. (2013). Microglia as modulators of cognition and neuropsychiatric disorders. *Glia* 61, 62–70. doi:10.1002/glia.22372.

Blum-Degena, D., Müller, T., Kuhn, W., Gerlach, M., Przuntek, H., and Riederer, P. (1995). Interleukin-1β and interleukin-6 are elevated in the cerebrospinal fluid of Alzheimer's and de novo Parkinson's disease patients. *Neurosci. Lett.* 202, 17–20. doi:10.1016/0304-3940(95)12192-7.

Boraschi, D., Italiani, P., Weil, S., and Martin, M. U. (2018). The family of the interleukin-1 receptors. *Immunol. Rev.* 281, 197–232. doi:10.1111/imr.12606.

Borgelt, C., Meinl, T., and Berthold, M. (2005). MoSS. in *Proceedings of the 1st international workshop on open source data mining frequent pattern mining implementations - OSDM '05* (New York, New York, USA: ACM Press), 6–15. doi:10.1145/1133905.1133908.

Bowers, K. J., Sacerdoti, F. D., Salmon, J. K., Shan, Y., Shaw, D. E., Chow, E., et al. (2006). Molecular dynamics---Scalable algorithms for molecular dynamics simulations on commodity clusters. in *Proceedings of the 2006 ACM/IEEE conference on Supercomputing - SC '06* (New York, New York, USA: ACM Press), 84. doi:10.1145/1188455.1188544.

Braga, C., and Travis, K. P. (2005). A configurational temperature Nosé-Hoover thermostat. *J. Chem. Phys.* 123, 134101. doi:10.1063/1.2013227.

Brambilla, R. (2019). Neuroinflammation, the thread connecting neurological disease. *Acta Neuropathol.* 137, 689–691. doi:10.1007/s00401-019-02009-9.

Braun, E., Gilmer, J., Mayes, H. B., Mobley, D. L., Monroe, J. I., Prasad, S., et al. (2019). Best Practices for Foundations in Molecular Simulations [Article v1.0]. *Living J. Comput. Mol. Sci.* 1. doi:10.33011/livecoms.1.1.5957.

Breitner, J. C., Baker, L. D., Montine, T. J., Meinert, C. L., Lyketsos, C. G., Ashe, K. H., et al. (2011). Extended results of the Alzheimer's disease anti-inflammatory prevention trial. *Alzheimer's Dement.* 7, 402–411. doi:10.1016/j.jalz.2010.12.014.

Brites, D. (2015). Cell ageing: a flourishing field for neurodegenerative diseases. *AIMS Mol. Sci.* 2, 225–258. doi:10.3934/molsci.2015.3.225.

Brites, D. (2020). Regulatory function of <scp>microRNAs</scp> in microglia. *Glia* 68, 1631–1642. doi:10.1002/glia.23846.

Brites, D., and Fernandes, A. (2015). Neuroinflammation and Depression: Microglia Activation, Extracellular Microvesicles and microRNA Dysregulation. *Front. Cell. Neurosci.* 9. doi:10.3389/fncel.2015.00476.

Brites, D., and Vaz, A. R. (2014). Microglia centered pathogenesis in ALS: insights in cell interconnectivity. *Front. Cell. Neurosci.* 8, 1–24. doi:10.3389/fncel.2014.00117.

Brooijmans, N., and Kuntz, I. D. (2003). Molecular Recognition and Docking Algorithms. *Annu. Rev. Biophys. Biomol. Struct.* 32, 335–373. doi:10.1146/annurev.biophys.32.110601.142532.

Brooks, B. R., Brooks, C. L., Mackerell, A. D., Nilsson, L., Petrella, R. J., Roux, B., et al. (2009). CHARMM: The biomolecular simulation program. *J. Comput. Chem.* 30, 1545–1614. doi:10.1002/jcc.21287.

Brosseron, F., Krauthausen, M., Kummer, M., and Heneka, M. T. (2014). Body Fluid Cytokine Levels in Mild Cognitive Impairment and Alzheimer's Disease: a Comparative Overview. *Mol. Neurobiol.* 50, 534–544. doi:10.1007/s12035-014-8657-1.

Brown, D. G., and Wobst, H. J. (2020). Opportunities and Challenges in Phenotypic Screening for Neurodegenerative Disease Research. *J. Med. Chem.* 63, 1823–1840. doi:10.1021/acs.jmedchem.9b00797.

Bruttger, J., Karram, K., Wörtge, S., Regen, T., Marini, F., Hoppmann, N., et al. (2015). Genetic Cell Ablation Reveals Clusters of Local Self-Renewing Microglia in the Mammalian Central Nervous System. *Immunity* 43, 92–106. doi:10.1016/j.immuni.2015.06.012.

Brylinski, M., and Skolnick, J. (2008). A threading-based method (FINDSITE) for ligand-binding site prediction and functional annotation. *Proc. Natl. Acad. Sci.* 105, 129–134. doi:10.1073/pnas.0707684105.

Burm, S. M., Peferoen, L. A. N., Zuiderwijk-Sick, E. A., Haanstra, K. G., 't Hart, B. A., van der Valk, P., et al. (2016). Expression of IL-1β in rhesus EAE and MS lesions is mainly induced in the CNS itself. *J. Neuroinflammation* 13, 138. doi:10.1186/s12974-016-0605-8.

Bussi, G., Donadio, D., and Parrinello, M. (2007). Canonical sampling through velocity rescaling. *J. Chem. Phys.* 126, 014101. doi:10.1063/1.2408420.

Butovsky, O., and Weiner, H. L. (2018). Microglial signatures and their role in health and disease. *Nat. Rev. Neurosci.* 19, 622–635. doi:10.1038/s41583-018-0057-5.

Caldeira, C., Oliveira, A. F., Cunha, C., Vaz, A. R., FalcÃ£o, A. S., Fernandes, A., et al. (2014). Microglia change from a reactive to an age-like phenotype with the time in culture. *Front. Cell. Neurosci.* 8. doi:10.3389/fncel.2014.00152.

Calverley, P. M. A., Sethi, S., Dawson, M., Ward, C. K., Finch, D. K., Penney, M., et al. (2017). A randomised, placebo-controlled trial of anti–interleukin-1 receptor 1 monoclonal antibody MEDI8968 in chronic obstructive pulmonary disease. *Respir. Res.* 18, 153. doi:10.1186/s12931-017-0633-7.

Cappoli, N., Mezzogori, D., Tabolacci, E., Coletta, I., Navarra, P., Pani, G., et al. (2019). The mTOR kinase inhibitor rapamycin enhances the expression and release of pro-inflammatory cytokine interleukin 6 modulating the activation of human microglial cells. *EXCLI J.* 18, 779–798. doi:10.17179/excli2019-1715.

Cardona, A. E., Pioro, E. P., Sasse, M. E., Kostenko, V., Cardona, S. M., Dijkstra, I. M., et al. (2006). Control of microglial neurotoxicity by the fractalkine receptor. *Nat. Neurosci.* 9, 917–924. doi:10.1038/nn1715.

Case, D. A., Cheatham, T. E., Darden, T., Gohlke, H., Luo, R., Merz, K. M., et al. (2005). The Amber biomolecular simulation programs. *J. Comput. Chem.* 26, 1668–1688. doi:10.1002/jcc.20290.

Chauhan, D., Vande Walle, L., and Lamkanfi, M. (2020). Therapeutic modulation of inflammasome pathways. *Immunol. Rev.* 297, 123–138. doi:10.1111/imr.12908.

Chen, K., Mizianty, M. J., Gao, J., and Kurgan, L. (2011). A Critical Comparative Assessment of Predictions of Protein-Binding Sites for Biologically Relevant Organic Compounds. *Structure* 19, 613–621. doi:10.1016/j.str.2011.02.015.

Chen, Q., Zhang, H., Li, Q., An, Y., Herkenham, M., Lai, W., et al. (2009). Three Promoters Regulate Tissue- and Cell Type-specific Expression of Murine Interleukin-1 Receptor Type I. *J. Biol. Chem.* 284, 8703–8713. doi:10.1074/jbc.M808261200.

Chow, B. W., and Gu, C. (2015). The Molecular Constituents of the Blood–Brain Barrier. *Trends Neurosci.* 38, 598–608. doi:10.1016/j.tins.2015.08.003.

Chung, J. Y., Krapp, N., Wu, L., Lule, S., McAllister, L. M., Edmiston, W. J., et al. (2019). Interleukin-1 Receptor 1 Deletion in Focal and Diffuse Experimental Traumatic Brain Injury in Mice. *J. Neurotrauma* 36, 370–379. doi:10.1089/neu.2018.5659.

Chung, Y., Chang, S. H., Martinez, G. J., Yang, X. O., Nurieva, R., Kang, H. S., et al. (2009). Critical Regulation of Early Th17 Cell Differentiation by Interleukin-1 Signaling. *Immunity* 30, 576–587. doi:10.1016/j.immuni.2009.02.007.

Clausen, B. H., Lambertsen, K. L., Dagnæs-Hansen, F., Babcock, A. A., von Linstow, C. U., Meldgaard, M., et al. (2016). Cell therapy centered on IL-1Ra is neuroprotective in experimental stroke. *Acta Neuropathol.* 131, 775–791. doi:10.1007/s00401-016-1541-5.

Cohen, P. (2014). The TLR and IL-1 signalling network at a glance. *J. Cell Sci.* 127, 2383–2390. doi:10.1242/jcs.149831.

Cohen, S. B., Proudman, S., Kivitz, A. J., Burch, F. X., Donohue, J. P., Burstein, D., et al. (2011). A randomized, double-blind study of AMG 108 (a fully human monoclonal antibody to IL-1R1) in patients with osteoarthritis of the knee. *Arthritis Res. Ther.* 13, R125. doi:10.1186/ar3430.

Coll, R. C., Hill, J. R., Day, C. J., Zamoshnikova, A., Boucher, D., Massey, N. L., et al. (2019). MCC950 directly targets the NLRP3 ATP-hydrolysis motif for inflammasome inhibition. *Nat. Chem. Biol.* 15, 556–559. doi:10.1038/s41589-019-0277-7.

Coll, R. C., Robertson, A. A. B., Chae, J. J., Higgins, S. C., Muñoz-Planillo, R., Inserra, M. C., et al. (2015). A small-molecule inhibitor of the NLRP3 inflammasome for the treatment

of inflammatory diseases. *Nat. Med.* 21, 248–255. doi:10.1038/nm.3806.

Copeland, N. G., Silan, C. M., Kingsley, D. M., Jenkins, N. A., Cannizzaro, L. A., Croce, C. M., et al. (1991). Chromosomal location of murine and human IL-1 receptor genes. *Genomics* 9, 44–50. doi:10.1016/0888-7543(91)90219-5.

Corti, D. S., and Soto-Campos, G. (1998). Deriving the isothermal–isobaric ensemble: The requirement of a "shell" molecule and applicability to small systems. *J. Chem. Phys.* 108, 7959–7966. doi:10.1063/1.476236.

Cozzini, P., Kellogg, G. E., Spyrakis, F., Abraham, D. J., Costantino, G., Emerson, A., et al. (2008). Target Flexibility: An Emerging Consideration in Drug Discovery and Design †. *J. Med. Chem.* 51, 6237–6255. doi:10.1021/jm800562d.

Craft, J. M., Watterson, D. M., and Van Eldik, L. J. (2005). Neuroinflammation: a potential therapeutic target. *Expert Opin. Ther. Targets* 9, 887–900. doi:10.1517/14728222.9.5.887.

Cuendet, M. A., and van Gunsteren, W. F. (2007). On the calculation of velocity-dependent properties in molecular dynamics simulations using the leapfrog integration algorithm. *J. Chem. Phys.* 127, 184102. doi:10.1063/1.2779878.

Cunha, C., Gomes, C., Vaz, A. R., and Brites, D. (2016). Exploring New Inflammatory Biomarkers and Pathways during LPS-Induced M1 Polarization. *Mediators Inflamm.* 2016. doi:10.1155/2016/6986175.

Cunha, C., Santos, C., Gomes, C., Fernandes, A., Correia, A. M., Sebastião, A. M., et al. (2017). Downregulated Glia Interplay and Increased miRNA-155 as Promising Markers to Track ALS at an Early Stage. *Mol. Neurobiol.* doi:10.1007/s12035-017-0631-2.

Cunningham, E., Wada, E., Carter, D., Tracey, D., Battey, J., and De Souza, E. (1992). In situ histochemical localization of type I interleukin-1 receptor messenger RNA in the central nervous system, pituitary, and adrenal gland of the mouse. *J. Neurosci.* 12, 1101–1114. doi:10.1523/JNEUROSCI.12-03-01101.1992.

D'Anna, L., Abu-Rumeileh, S., Fabris, M., Pistis, C., Baldi, A., Sanvilli, N., et al. (2017). Serum Interleukin-10 Levels Correlate with Cerebrospinal Fluid Amyloid Beta Deposition in Alzheimer Disease Patients. *Neurodegener. Dis.* 17, 227–234. doi:10.1159/000474940.

Dabouz, R., Cheng, C. W. H., Abram, P., Omri, S., Cagnone, G., Sawmy, K. V., et al. (2020). An allosteric interleukin-1 receptor modulator mitigates inflammation and photoreceptor toxicity in a model of retinal degeneration. *J. Neuroinflammation* 17, 359. doi:10.1186/s12974-020-02032-8.

Dale, M., and Nicklin, M. J. H. (1999). Interleukin-1 Receptor Cluster: Gene Organization ofIL1R2, IL1R1, IL1RL2(IL-1Rrp2),IL1RL1(T1/ST2), andIL18R1(IL-1Rrp) on Human Chromosome 2q. *Genomics* 57, 177–179. doi:10.1006/geno.1999.5767.

Damisah, E. C., Hill, R. A., Rai, A., Chen, F., Rothlin, C. V., Ghosh, S., et al. (2020). Astrocytes and microglia play orchestrated roles and respect phagocytic territories during neuronal corpse removal in vivo. *Sci. Adv.* 6, eaba3239. doi:10.1126/sciadv.aba3239.

Dar, K. B., Bhat, A. H., Amin, S., Hamid, R., Anees, S., Anjum, S., et al. (2019). Modern Computational Strategies for Designing Drugs to Curb Human Diseases: A Prospect.

Curr. Top. Med. Chem. 18, 2702–2719. doi:10.2174/1568026619666190119150741.

De Leo, F., Quilici, G., De Marchis, F., Mantonico, M. V., Bianchi, M. E., and Musco, G. (2020). Discovery of 5,5′-Methylenedi-2,3-Cresotic Acid as a Potent Inhibitor of the Chemotactic Activity of the HMGB1·CXCL12 Heterocomplex Using Virtual Screening and NMR Validation. *Front. Chem.* 8. doi:10.3389/fchem.2020.598710.

De Schepper, S., Crowley, G., and Hong, S. (2020). Understanding microglial diversity and implications for neuronal function in health and disease. *Dev. Neurobiol.*, dneu.22777. doi:10.1002/dneu.22777.

De Vivo, M., Masetti, M., Bottegoni, G., and Cavalli, A. (2016). Role of Molecular Dynamics and Related Methods in Drug Discovery. *J. Med. Chem.* 59, 4035–4061. doi:10.1021/acs.jmedchem.5b01684.

Deczkowska, A., Keren-Shaul, H., Weiner, A., Colonna, M., Schwartz, M., and Amit, I. (2018). Disease-Associated Microglia: A Universal Immune Sensor of Neurodegeneration. *Cell* 173, 1073–1081. doi:10.1016/j.cell.2018.05.003.

Dello Russo, C., Cappoli, N., Coletta, I., Mezzogori, D., Paciello, F., Pozzoli, G., et al. (2018). The human microglial HMC3 cell line: where do we stand? A systematic literature review. *J. Neuroinflammation* 15, 259. doi:10.1186/s12974-018-1288-0.

Deng, W., Breneman, C., and Embrechts, M. J. (2004). Predicting protein-ligand binding affinities using novel geometrical descriptors and machine-learning methods. *J. Chem. Inf. Comput. Sci.* 44, 699–703. doi:10.1021/ci034246+.

Deora, V., Lee, J. D., Albornoz, E. A., McAlary, L., Jagaraj, C. J., Robertson, A. A. B., et al. (2020). The microglial NLRP3 inflammasome is activated by amyotrophic lateral sclerosis proteins. *Glia* 68, 407–421. doi:10.1002/glia.23728.

Depino, A. M., Alonso, M., Ferrari, C., del Rey, A., Anthony, D., Besedovsky, H., et al. (2004). Learning modulation by endogenous hippocampal IL-1: Blockade of endogenous IL-1 facilitates memory formation. *Hippocampus* 14, 526–535. doi:10.1002/hipo.10164.

Dileep, K. V., Remya, C., Tintu, I., and Sadasivan, C. (2013). Designing of multi-target-directed ligands against the enzymes associated with neuroinflammation: an in silico approach. *Front. Life Sci.* 7, 174–185. doi:10.1080/21553769.2014.901924.

Dinarello, C. A. (1998). Interleukin-1, Interleukin-1 Receptors and Interleukin-1 Receptor Antagonist. *Int. Rev. Immunol.* 16, 457–499. doi:10.3109/08830189809043005.

Dinarello, C. A. (2018). Overview of the IL-1 family in innate inflammation and acquired immunity. *Immunol. Rev.* 281, 8–27. doi:10.1111/imr.12621.

Dinarello, C. A., Simon, A., and van der Meer, J. W. M. (2012). Treating inflammation by blocking interleukin-1 in a broad spectrum of diseases. *Nat. Rev. Drug Discov.* 11, 633–652. doi:10.1038/nrd3800.

Dinarello, C. A., and van der Meer, J. W. M. (2013). Treating inflammation by blocking interleukin-1 in humans. *Semin. Immunol.* 25, 469–484. doi:10.1016/j.smim.2013.10.008.

Dixon, S. L., Smondyrev, A. M., Knoll, E. H., Rao, S. N., Shaw, D. E., and Friesner, R. A.

(2006). PHASE: a new engine for pharmacophore perception, 3D QSAR model development, and 3D database screening: 1. Methodology and preliminary results. *J. Comput. Aided. Mol. Des.* 20, 647–671. doi:10.1007/s10822-006-9087-6.

Do, P.-C., Lee, E. H., and Le, L. (2018). Steered Molecular Dynamics Simulation in Rational Drug Design. *J. Chem. Inf. Model.* 58, 1473–1482. doi:10.1021/acs.jcim.8b00261.

Donato, M. T., Tolosa, L., and Gómez-Lechón, M. J. (2015). "Culture and Functional Characterization of Human Hepatoma HepG2 Cells," in, 77–93. doi:10.1007/978-1-4939-2074-7_5.

Donzis, E. J., and Tronson, N. C. (2014). Modulation of learning and memory by cytokines: Signaling mechanisms and long term consequences. *Neurobiol. Learn. Mem.* 115, 68–77. doi:10.1016/j.nlm.2014.08.008.

Dower, S. K., Kronheim, S. R., March, C. J., Conlon, P. J., Hopp, T. P., Gillis, S., et al. (1985). Detection and characterization of high affinity plasma membrane receptors for human interleukin 1. *J. Exp. Med.* 162, 501–515. doi:10.1084/jem.162.2.501.

Dripps, D. J., Brandhuber, B. J., Thompson, R. C., and Eisenberg, S. P. (1991). Interleukin-1 (IL-1) receptor antagonist binds to the 80-kDa IL-1 receptor but does not initiate IL-1 signal transduction. *J. Biol. Chem.* 266, 10331–6. doi:1828071.

Duffy, J. P., Harrington, E. M., Salituro, F. G., Cochran, J. E., Green, J., Gao, H., et al. (2011). The Discovery of VX-745: A Novel and Selective p38α Kinase Inhibitor. *ACS Med. Chem. Lett.* 2, 758–763. doi:10.1021/ml2001455.

Durrant, J. D. (2019). BlendMol: advanced macromolecular visualization in Blender. *Bioinformatics* 35, 2323–2325. doi:10.1093/bioinformatics/bty968.

Durrant, J. D., and McCammon, J. A. (2011). BINANA: A novel algorithm for ligand-binding characterization. *J. Mol. Graph. Model.* 29, 888–893. doi:10.1016/j.jmgm.2011.01.004.

Durrenberger, P. F., Fernando, F. S., Kashefi, S. N., Bonnert, T. P., Seilhean, D., Nait-Oumesmar, B., et al. (2015). Common mechanisms in neurodegeneration and neuroinflammation: a BrainNet Europe gene expression microarray study. *J. Neural Transm.* 122, 1055–1068. doi:10.1007/s00702-014-1293-0.

Edelsbrunner, H., and Mücke, E. P. (1994). Three-dimensional alpha shapes. *ACM Trans. Graph.* 13, 43–72. doi:10.1145/174462.156635.

Edfors, F., Danielsson, F., Hallström, B. M., Käll, L., Lundberg, E., Pontén, F., et al. (2016). Gene-specific correlation of <scp>RNA</scp> and protein levels in human cells and tissues. *Mol. Syst. Biol.* 12, 883. doi:10.15252/msb.20167144.

Eggen, B. J. L., Raj, D., Hanisch, U.-K., and Boddeke, H. W. G. M. (2013). Microglial Phenotype and Adaptation. *J. Neuroimmune Pharmacol.* 8, 807–823. doi:10.1007/s11481-013-9490-4.

Elzinga, B. M., Twomey, C., Powell, J. C., Harte, F., and McCarthy, J. V. (2009). Interleukin-1 receptor type 1 is a substrate for γ-secretase- dependent regulated intramembrane proteolysis. *J. Biol. Chem.* 284, 1394–1409. doi:10.1074/jbc.M803108200.

Emsley, H. C., Smith, C. J., Georgiou R. F., Vail, A., Hopkins, S. J., Rothwell, N. J., et al. (2005). A randomised phase II study of interleukin-1 receptor antagonist in acute stroke patients. *J. Neurol. Neurosurg. Psychiatry* 76, 1366–1372. doi:10.1136/jnnp.2004.054882.

Essmann, U., Perera, L., Berkowitz, M. L., Darden, T., Lee, H., and Pedersen, L. G. (1995). A smooth particle mesh Ewald method. *J. Chem. Phys.* 103, 8577–8593. doi:10.1063/1.470117.

Evans, L. P., Woll, A. W., Wu, S., Todd, B. P., Hehr, N., Hedberg-Buenz, A., et al. (2020). Modulation of Post-Traumatic Immune Response Using the IL-1 Receptor Antagonist Anakinra for Improved Visual Outcomes. *J. Neurotrauma* 37, 1463–1480. doi:10.1089/neu.2019.6725.

Evans, R. J., Bray, J., Childs, J. D., Vigers, G. P. A., Brandhuber, B. J., Thompson, R. C., et al. (1995). Mapping Receptor Binding Sites in Interleukin (IL)-1 Receptor Antagonist and IL-1β by Site-directed Mutagenesis. *J. Biol. Chem.* 270, 11477–11483. doi:10.1074/jbc.270.19.11477.

Eyrisch, S., and Helms, V. (2007). Transient pockets on protein surfaces involved in protein-protein interaction. *J. Med. Chem.* 50, 3457–3464. doi:10.1021/jm070095g.

Fang, Y., and Eglen, R. M. (2017). Three-Dimensional Cell Cultures in Drug Discovery and Development. *SLAS Discov. Adv. Sci. Drug Discov.* 22, 456–472. doi:10.1177/1087057117696795.

Fauman, E. B., Rai, B. K., and Huang, E. S. (2011). Structure-based druggability assessment—identifying suitable targets for small molecule therapeutics. *Curr. Opin. Chem. Biol.* 15, 463–468. doi:10.1016/j.cbpa.2011.05.020.

Feller, S. E., Zhang, Y., Pastor, R. W., and Brooks, B. R. (1995). Constant pressure molecular dynamics simulation: The Langevin piston method. *J. Chem. Phys.* 103, 4613–4621. doi:10.1063/1.470648.

Felsky, D., Roostaei, T., Nho, K., Risacher, S. L., Bradshaw, E. M., Petyuk, V., et al. (2019). Neuropathological correlates and genetic architecture of microglial activation in elderly human brain. *Nat. Commun.* 10, 409. doi:10.1038/s41467-018-08279-3.

Feng, T., and Barakat, K. (2018). "Molecular Dynamics Simulation and Prediction of Druggable Binding Sites," in, 87–103. doi:10.1007/978-1-4939-7756-7_6.

Feng, Z., Pearce, L. V., Xu, X., Yang, X., Yang, P., Blumberg, P. M., et al. (2015). Structural Insight into Tetrameric hTRPV1 from Homology Modeling, Molecular Docking, Molecular Dynamics Simulation, Virtual Screening, and Bioassay Validations. *J. Chem. Inf. Model.* 55, 572–588. doi:10.1021/ci5007189.

Fengler, A., and Brandt, W. (2000). "Development and Validation of Homology Models of Human Cathepsins K, S, H, and F," in *Cellular Peptidases in Immune Functions and Diseases 2* (Boston: Kluwer Academic Publishers), 255–260. doi:10.1007/0-306-46826-3_27.

Fernandes, A., Ribeiro, A. R., Monteiro, M., Garcia, G., Vaz, A. R., and Brites, D. (2018). Secretome from SH-SY5Y APPSwe cells trigger time-dependent CHME3 microglia

activation phenotypes, ultimately leading to miR-21 exosome shuttling. *Biochimie* 155, 67–82. doi:10.1016/j.biochi.2018.05.015.

Ferreira, T. M., Coreta-Gomes, F., Ollila, O. H. S., Moreno, M. J., Vaz, W. L. C., and Topgaard, D. (2013). Cholesterol and POPC segmental order parameters in lipid membranes: solid state 1 H– 13 C NMR and MD simulation studies. *Phys. Chem. Chem. Phys.* 15, 1976–1989. doi:10.1039/C2CP42738A.

Fields, J. K., Günther, S., and Sundberg, E. J. (2019). Structural basis of IL-1 family cytokine signaling. *Front. Immunol.* 10, 1–20. doi:10.3389/fimmu.2019.01412.

Fiser, A. (2010). Template-Based Protein Structure Modeling. *Methods Mol Biol.* 673, 73–94. doi:10.1007/978-1-60761-842-3_6.

Fletcher, R. (1964). Function minimization by conjugate gradients. *Comput. J.* 7, 149–154. doi:10.1093/comjnl/7.2.149.

Frakes, A. E., Ferraiuolo, L., Haidet-Phillips, A. M., Schmelzer, L., Braun, L., Miranda, C. J., et al. (2014). Microglia Induce Motor Neuron Death via the Classical NF-κB Pathway in Amyotrophic Lateral Sclerosis. *Neuron* 81, 1009–1023. doi:10.1016/j.neuron.2014.01.013.

French, R. A., VanHoy, R. W., Chizzonite, R., Zachary, J. F., Dantzer, R., Parnet, P., et al. (1999). Expression and localization of p80 and p68 interleukin-1 receptor proteins in the brain of adult mice. *J. Neuroimmunol.* 93, 194–202. doi:10.1016/S0165-5728(98)00224-0.

Friedman, W. J. (2001). Cytokines Regulate Expression of the Type 1 Interleukin-1 Receptor in Rat Hippocampal Neurons and Glia. *Exp. Neurol.* 168, 23–31. doi:10.1006/exnr.2000.7595.

Friesner, R. A., Banks, J. L., Murphy, R. B., Halgren, T. A., Klicic, J. J., Mainz, D. T., et al. (2004). Glide: A New Approach for Rapid, Accurate Docking and Scoring. 1. Method and Assessment of Docking Accuracy. *J. Med. Chem.* 47, 1739–1749. doi:10.1021/jm0306430.

Frost, J. L., and Schafer, D. P. (2016). Microglia: Architects of the Developing Nervous System. *Trends Cell Biol.* 26, 587–597. doi:10.1016/j.tcb.2016.02.006.

Fuller, J. C., Burgoyne, N. J., and Jackson, R. M. (2009). Predicting druggable binding sites at the protein-protein interface. *Drug Discov. Today* 14, 155–161. doi:10.1016/j.drudis.2008.10.009.

Furst, D. E. (2004). Anakinra: Review of recombinant human interleukin-I receptor antagonist in the treatment of rheumatoid arthritis. *Clin. Ther.* 26, 1960–1975. doi:10.1016/j.clinthera.2004.12.019.

Galea, J., Ogungbenro, K., Hulme, S., Patel, H., Scarth, S., Hoadley, M., et al. (2018). Reduction of inflammation after administration of interleukin-1 receptor antagonist following aneurysmal subarachnoid hemorrhage: results of the Subcutaneous Interleukin-1Ra in SAH (SCIL-SAH) study. *J. Neurosurg.* 128, 515–523. doi:10.3171/2016.9.JNS16615.

Ganesan, A., Coote, M. L., and Barakat, K. (2017). Molecular dynamics-driven drug discovery: leaping forward with confidence. *Drug Discov. Today* 22, 249–269.

doi:10.1016/j.drudis.2016.11.001.

Gangwal, R. P., Das, N. R., Thanki, K., Damre, M. V., Dhoke, G. V., Sharma, S. S., et al. (2014). Identification of p38α MAP kinase inhibitors by pharmacophore based virtual screening. *J. Mol. Graph. Model.* 49, 18–24. doi:10.1016/j.jmgm.2014.01.002.

Garlanda, C., Dinarello, C. A., and Mantovani, A. (2013a). The Interleukin-1 Family: Back to the Future. *Immunity* 39, 1003–1018. doi:10.1016/j.immuni.2013.11.010.

Garlanda, C., Riva, F., Bonavita, E., Gentile, S., and Mantovani, A. (2013b). Decoys and regulatory "receptors" of the il-1/toll-like receptor superfamily. *Front. Immunol.* 4, 1–13. doi:10.3389/fimmu.2013.00180.

Gattorno, M., Obici, L., Cattalini, M., Tormey, V., Abrams, K., Davis, N., et al. (2017). Canakinumab treatment for patients with active recurrent or chronic TNF receptor-associated periodic syndrome (TRAPS): an open-label, phase II study. *Ann. Rheum. Dis.* 76, 173–178. doi:10.1136/annrheumdis-2015-209031.

Gaulton, A., Bellis, L. J., Bento, A. P., Chambers, J., Davies, M., Hersey, A., et al. (2012). ChEMBL: a large-scale bioactivity database for drug discovery. *Nucleic Acids Res.* 40, D1100–D1107. doi:10.1093/nar/gkr777.

Ge, J., Remesh, S. G., Hammel, M., Pan, S., Mahan, A. D., Wang, S., et al. (2019). Functional Relevance of Interleukin-1 Receptor Inter-domain Flexibility for Cytokine Binding and Signaling. *Structure* 27, 1296-1307.e5. doi:10.1016/j.str.2019.05.011.

Gehrke, L., Jobling, S. A., Paik, L. S., McDonald, B., Rosenwasser, L. J., and Auron, P. E. (1990). A point mutation uncouples human interleukin-1 beta biological activity and receptor binding. *J. Biol. Chem.* 265, 5922–5925. doi:10.1016/S0021-9258(19)39265-8.

Geloso, M. C., Corvino, V., Marchese, E., Serrano, A., Michetti, F., and D'Ambrosi, N. (2017). The Dual Role of Microglia in ALS: Mechanisms and Therapeutic Approaches. *Front. Aging Neurosci.* 9. doi:10.3389/fnagi.2017.00242.

Genheden, S., Reymer, A., Saenz-Méndez, P., and Eriksson, L. A. (2017). "Chapter 1. Computational Chemistry and Molecular Modelling Basics," in *Computational Tools for Chemical Biology*, 1–38. doi:10.1039/9781788010139-00001.

Gerber, Y. N., Sabourin, J.-C., Rabano, M., Vivanco, M. d M., and Perrin, F. E. (2012). Early Functional Deficit and Microglial Disturbances in a Mouse Model of Amyotrophic Lateral Sclerosis. *PLoS One* 7, e36000. doi:10.1371/journal.pone.0036000.

Gerets, H. H. J., Hanon, E., Cornet, M., Dhalluin, S., Depelchin, O., Canning, M., et al. (2009). Selection of cytotoxicity markers for the screening of new chemical entities in a pharmaceutical context: A preliminary study using a multiplexing approach. *Toxicol. Vitr.* 23, 319–332. doi:10.1016/j.tiv.2008.11.012.

Ghasemi, F., Bagheri, H., Barreto, G. E., Read, M. I., and Sahebkar, A. (2019). Effects of Curcumin on Microglial Cells. *Neurotox. Res.* 36, 12–26. doi:10.1007/s12640-019-00030-0.

Gimeno, A., Ojeda-Montes, M., Tomás-Hernández, S., Cereto-Massagué, A., Beltrán-Debón, R., Mulero, M., et al. (2019). The Light and Dark Sides of Virtual Screening: What Is There to Know? *Int. J. Mol. Sci.* 20, 1375. doi:10.3390/ijms20061375.

Glaser, F., Pupko, T., Paz, I., Bell, R. E., Bechor-Shental, D., Martz, E., et al. (2003). ConSurf: Identification of Functional Regions in Proteins by Surface-Mapping of Phylogenetic Information. *Bioinformatics* 19, 163–164. doi:10.1093/bioinformatics/19.1.163.

Goldstein, M. H., Martel, J. R., Sall, K., Goldberg, D. F., Abrams, M., Rubin, J., et al. (2017). Multicenter Study of a Novel Topical Interleukin-1 Receptor Inhibitor, Isunakinra, in Subjects With Moderate to Severe Dry Eye Disease. *Eye Contact Lens Sci. Clin. Pract.* 43, 287–296. doi:10.1097/ICL.0000000000000276.

Goodford, P. J. (1985). A computational procedure for determining energetically favorable binding sites on biologically important macromolecules. *J. Med. Chem.* 28, 849–857. doi:10.1021/jm00145a002.

Gordon, R., Albornoz, E. A., Christie, D. C., Langley, M. R., Kumar, V., Mantovani, S., et al. (2018). Inflammasome inhibition prevents α-synuclein pathology and dopaminergic neurodegeneration in mice. *Sci. Transl. Med.* 10, eaah4066. doi:10.1126/scitranslmed.aah4066.

Gough, D. J., Levy, D. E., Johnstone, R. W., and Clarke, C. J. (2008). IFNγ signaling—Does it mean JAK–STAT? *Cytokine Growth Factor Rev.* 19, 383–394. doi:10.1016/j.cytogfr.2008.08.004.

Grabert, K., Michoel, T., Karavolos, M. H., Clohisey, S., Baillie, J. K., Stevens, M. P., et al. (2016). Microglial brain region−dependent diversity and selective regional sensitivities to aging. *Nat. Neurosci.* 19, 504–516. doi:10.1038/nn.4222.

Graeber, M. B., Li, W., and Rodriguez, M. L. (2011). Role of microglia in CNS inflammation. *FEBS Lett.* 585, 3798–3805. doi:10.1016/j.febslet.2011.08.033.

Greene, J., Kahn, S., Savoj, H., Sprague, P., and Teig, S. (1994). Chemical Function Queries for 3D Database Search. *J. Chem. Inf. Comput. Sci.* 34, 1297–1308. doi:10.1021/ci00022a012.

Griffin, W. S., Stanley, L. C., Ling, C., White, L., MacLeod, V., Perrot, L. J., et al. (1989). Brain interleukin 1 and S-100 immunoreactivity are elevated in Down syndrome and Alzheimer disease. *Proc. Natl. Acad. Sci.* 86, 7611–7615. doi:10.1073/pnas.86.19.7611.

Guedes, I. A., Pereira, F. S. S., and Dardenne, L. E. (2018). Empirical Scoring Functions for Structure-Based Virtual Screening: Applications, Critical Aspects, and Challenges. *Front. Pharmacol.* 9. doi:10.3389/fphar.2018.01089.

Guerreiro, R., Wojtas, A., Bras, J., Carrasquillo, M., Rogaeva, E., Majounie, E., et al. (2013). TREM2 Variants in Alzheimer's Disease. *N. Engl. J. Med.* 368, 117–127. doi:10.1056/NEJMoa1211851.

Gui, W.-S., Wei, X., Mai, C.-L., Murugan, M., Wu, L.-J., Xin, W.-J., et al. (2016). Interleukin-1β overproduction is a common cause for neuropathic pain, memory deficit, and depression following peripheral nerve injury in rodents. *Mol. Pain* 12, 174480691664678. doi:10.1177/1744806916646784.

Günther, S., Deredge, D., Bowers, A. L., Luchini, A., Bonsor, D. A., Beadenkopf, R., et al. (2017). IL-1 Family Cytokines Use Distinct Molecular Mechanisms to Signal through Their Shared Co-receptor. *Immunity* 47, 510-523.e4. doi:10.1016/j.immuni.2017.08.004.

Guo, D.-H., Yamamoto, M., Hernandez, C. M., Khodadadi, H., Baban, B., and Stranahan, A. M. (2020). Visceral adipose NLRP3 impairs cognition in obesity via IL-1R1 on CX3CR1+ cells. *J. Clin. Invest.* 130, 1961–1976. doi:10.1172/JCI126078.

Guo, Z., Li, B., Cheng, L. T., Zhou, S., McCammon, J. A., and Che, J. (2015). Identification of protein-ligand binding sites by the level-set variational implicit-solvent approach. *J. Chem. Theory Comput.* 11, 753–765. doi:10.1021/ct500867u.

Gustafson, M. P., Staff, N. P., Bornschlegl, S., Butler, G. W., Maas, M. L., Kazamel, M., et al. (2017). Comprehensive immune profiling reveals substantial immune system alterations in a subset of patients with amyotrophic lateral sclerosis. *PLoS One* 12, e0182002. doi:10.1371/journal.pone.0182002.

Guvench, O., and MacKerell, A. D. (2008). "Comparison of Protein Force Fields for Molecular Dynamics Simulations," in, 63–88. doi:10.1007/978-1-59745-177-2_4.

Guzman-Martinez, L., Maccioni, R. B., Andrade, V., Navarrete, L. P., Pastor, M. G., and Ramos-Escobar, N. (2019). Neuroinflammation as a Common Feature of Neurodegenerative Disorders. *Front. Pharmacol.* 10. doi:10.3389/fphar.2019.01008.

Ha, H., Debnath, B., Odde, S., Bensman, T., Ho, H., Beringer, P. M., et al. (2015). Discovery of Novel CXCR2 Inhibitors Using Ligand-Based Pharmacophore Models. *J. Chem. Inf. Model.* 55, 1720–1738. doi:10.1021/acs.jcim.5b00181.

Haasen, D., Schopfer, U., Antczak, C., Guy, C., Fuchs, F., and Selzer, P. (2017). How Phenotypic Screening Influenced Drug Discovery: Lessons from Five Years of Practice. *Assay Drug Dev. Technol.* 15, 239–246. doi:10.1089/adt.2017.796.

Halgren, T. A. (1996). Merck molecular force field. I. Basis, form, scope, parameterization, and performance of MMFF94. *J. Comput. Chem.* 17, 490–519. doi:10.1002/(SICI)1096-987X(199604)17:5/6<490::AID-JCC1>3.0.CO;2-P.

Halgren, T. A. (2009). Identifying and Characterizing Binding Sites and Assessing Druggability. *J. Chem. Inf. Model.* 49, 377–389. doi:10.1021/ci800324m.

Hauser, S. L., Doolittle, T. H., Lincoln, R., Brown, R. H., and Dinarello, C. A. (1990). Cytokine accumulations in CSF of multiple sclerosis patients. *Neurology* 40, 1735–1735. doi:10.1212/WNL.40.11.1735.

Hawkins, P. C. D., Skillman, A. G., Warren, G. L., Ellingson, B. A., and Stahl, M. T. (2010). Conformer Generation with OMEGA: Algorithm and Validation Using High Quality Structures from the Protein Databank and Cambridge Structural Database. *J. Chem. Inf. Model.* 50, 572–584. doi:10.1021/ci100031x.

Hayashida, K., Bartlett, A. H., Chen, Y., and Park, P. W. (2010). Molecular and Cellular Mechanisms of Ectodomain Shedding. *Anat. Rec. Adv. Integr. Anat. Evol. Biol.* 293, 925–937. doi:10.1002/ar.20757.

Heneka, M. T., Carson, M. J., Khoury, J. El, Landreth, G. E., Brosseron, F., Feinstein, D. L., et al. (2015). Neuroinflammation in Alzheimer's disease. *Lancet Neurol.* 14, 388–405. doi:10.1016/S1474-4422(15)70016-5.

Heneka, M. T., Kummer, M. P., Stutz, A., Delekate, A., Schwartz, S., Vieira-Saecker, A., et al.

(2013). NLRP3 is activated in Alzheimer's disease and contributes to pathology in APP/PS1 mice. *Nature* 493, 674–678. doi:10.1038/nature11729.

Henrich, S., Salo-Ahen, O. M. H., Huang, B., Rippmann, F. F., Cruciani, G., and Wade, R. C. (2009). Computational approaches to identifying and characterizing protein binding sites for ligand design. *J. Mol. Recognit.*, n/a-n/a. doi:10.1002/jmr.984.

Henzler-Wildman, K., and Kern, D. (2007). Dynamic personalities of proteins. *Nature* 450, 964–972. doi:10.1038/nature06522.

Heo, L., and Feig, M. (2018). Experimental accuracy in protein structure refinement via molecular dynamics simulations. *Proc. Natl. Acad. Sci.* 115, 13276–13281. doi:10.1073/pnas.1811364115.

Heppner, F. L., Ransohoff, R. M., and Becher, B. (2015). Immune attack: the role of inflammation in Alzheimer disease. *Nat. Rev. Neurosci.* 16, 358–372. doi:10.1038/nrn3880.

Hess, B., Bekker, H., Berendsen, H. J. C., and Fraaije, J. G. E. M. (1997). LINCS: A linear constraint solver for molecular simulations. *J. Comput. Chem.* 18, 1463–1472. doi:10.1002/(SICI)1096-987X(199709)18:12<1463::AID-JCC4>3.0.CO;2-H.

Hickman, S. E., Kingery, N. D., Ohsumi, T. K., Borowsky, M. L., Wang, L., Means, T. K., et al. (2013). The microglial sensome revealed by direct RNA sequencing. *Nat. Neurosci.* 16, 1896–1905. doi:10.1038/nn.3554.

Hickman, S., Izzy, S., Sen, P., Morsett, L., and El Khoury, J. (2018). Microglia in neurodegeneration. *Nat. Neurosci.* 21, 1359–1369. doi:10.1038/s41593-018-0242-x.

Hirsch, E. C., and Hunot, S. (2009). Neuroinflammation in Parkinson's disease: a target for neuroprotection? *Lancet Neurol.* 8, 382–397. doi:10.1016/S1474-4422(09)70062-6.

Hitchcock, S. A., and Pennington, L. D. (2006). Structure−Brain Exposure Relationships. *J. Med. Chem.* 49, 7559–7583. doi:10.1021/jm060642i.

Hjorth, E., Frenkel, D., Weiner, H., and Schultzberg, M. (2010). Effects of immunomodulatory substances on phagocytosis of ABeta(1-42) by human microglia. *Int. J. Alzheimers. Dis.* 2010, 1–18. doi:10.4061/2010/798424.

Hoffman, H. M. (2009). Rilonacept for the treatment of cryopyrin-associated periodic syndromes (CAPS). *Expert Opin. Biol. Ther.* 9, 519–531. doi:10.1517/14712590902875518.

Holmes, C., El-Okl, M., Williams, A. L., Cunningham, C., Wilcockson, D., and Perry, V. H. (2003). Systemic infection, interleukin 1beta, and cognitive decline in Alzheimer's disease. *J. Neurol. Neurosurg. Psychiatry* 74, 788–789. doi:10.1136/jnnp.74.6.788.

Hou, J., Townson, S. A., Kovalchin, J. T., Masci, A., Kiner, O., Shu, Y., et al. (2013). Design of a superior cytokine antagonist for topical ophthalmic use. *Proc. Natl. Acad. Sci.* 110, 3913–3918. doi:10.1073/pnas.1217996110.

Hu, S. J., Calippe, B., Lavalette, S., Roubeix, C., Montassar, F., Housset, M., et al. (2015). Upregulation of P2RX7 in Cx3cr1-Deficient Mononuclear Phagocytes Leads to Increased Interleukin-1 Secretion and Photoreceptor Neurodegeneration. *J. Neurosci.* 35, 6987–6996. doi:10.1523/JNEUROSCI.3955-14.2015.

Hu, Y., Cao, C., Qin, X.-Y., Yu, Y., Yuan, J., Zhao, Y., et al. (2017). Increased peripheral blood inflammatory cytokine levels in amyotrophic lateral sclerosis: a meta-analysis study. *Sci. Rep.* 7, 9094. doi:10.1038/s41598-017-09097-1.

Huang, B., and Schroeder, M. (2006). LIGSITEcsc: Predicting ligand binding sites using the Connolly surface and degree of conservation. *BMC Struct. Biol.* 6, 1–11. doi:10.1186/1472-6807-6-19.

Huang, S.-Y. (2018). Comprehensive assessment of flexible-ligand docking algorithms: current effectiveness and challenges. *Brief. Bioinform.* 19, 982–994. doi:10.1093/bib/bbx030.

Hughes, T., Becknell, B., Freud, A. G., McClory, S., Briercheck, E., Yu, J., et al. (2010). Interleukin-1β Selectively Expands and Sustains Interleukin-22+ Immature Human Natural Killer Cells in Secondary Lymphoid Tissue. *Immunity* 32, 803–814. doi:10.1016/j.immuni.2010.06.007.

Humphrey, W., Dalke, A., and Schulten, K. (1996). VMD: Visual molecular dynamics. *J. Mol. Graph.* 14, 33–38. doi:10.1016/0263-7855(96)00018-5.

Ireland, S. F. (2008). The interleukin-1 receptor/ Toll-like receptor superfamily: 10 years of progress. *Immunol. Rev.*, 10–18.

Irwin, J. J., and Shoichet, B. K. (2005). ZINC--a free database of commercially available compounds for virtual screening. *J. Chem. Inf. Model.* 45, 177–82. doi:10.1021/ci049714+.

Ising, C., Venegas, C., Zhang, S., Scheiblich, H., Schmidt, S. V., Vieira-Saecker, A., et al. (2019). NLRP3 inflammasome activation drives tau pathology. *Nature* 575, 669–673. doi:10.1038/s41586-019-1769-z.

Italiani, P., Puxeddu, I., Napoletano, S., Scala, E., Melillo, D., Manocchio, S., et al. (2018). Circulating levels of IL-1 family cytokines and receptors in Alzheimer's disease: new markers of disease progression? *J. Neuroinflammation* 15, 342. doi:10.1186/s12974-018-1376-1.

Jain, A., Song, R., Wakeland, E. K., and Pasare, C. (2018). T cell-intrinsic IL-1R signaling licenses effector cytokine production by memory CD4 T cells. *Nat. Commun.* 9, 3185. doi:10.1038/s41467-018-05489-7.

James, M. L., Wang, H., Cantillana, V., Lei, B., Kernagis, D. N., Dawson, H. N., et al. (2012). TT-301 Inhibits Microglial Activation and Improves Outcome after Central Nervous System Injury in Adult Mice. *Anesthesiology* 116, 1299–1311. doi:10.1097/ALN.0b013e318253a02a.

Jana, M., Palencia, C. A., and Pahan, K. (2008). Fibrillar Amyloid-β Peptides Activate Microglia via TLR2: Implications for Alzheimer's Disease. *J. Immunol.* 181, 7254–7262. doi:10.4049/jimmunol.181.10.7254.

Janabi, N., Peudenier, S., Héron, B., Ng, K. H., and Tardieu, M. (1995). Establishment of human microglial cell lines after transfection of primary cultures of embryonic microglial cells with the SV40 large T antigen. *Neurosci. Lett.* 195, 105–108. doi:10.1016/0304-3940(94)11792-H.

Jansen, I. E., Savage, J. E., Watanabe, K., Bryois, J., Williams, D. M., Steinberg, S., et al. (2019). Genome-wide meta-analysis identifies new loci and functional pathways influencing Alzheimer's disease risk. *Nat. Genet.* 51, 404–413. doi:10.1038/s41588-018-0311-9.

Jiang, S., Feher, M., Williams, C., Cole, B., and Shaw, D. E. (2020). AutoPH4: An Automated Method for Generating Pharmacophore Models from Protein Binding Pockets. *J. Chem. Inf. Model.* 60, 4326–4338. doi:10.1021/acs.jcim.0c00121.

Jiménez, J., Doerr, S., Martínez-Rosell, G., Rose, A. S., and De Fabritiis, G. (2017). DeepSite: protein-binding site predictor using 3D-convolutional neural networks. *Bioinformatics* 33, 3036–3042. doi:10.1093/bioinformatics/btx350.

Jin, M., Günther, R., Akgün, K., Hermann, A., and Ziemssen, T. (2020). Peripheral proinflammatory Th1/Th17 immune cell shift is linked to disease severity in amyotrophic lateral sclerosis. *Sci. Rep.* 10, 5941. doi:10.1038/s41598-020-62756-8.

Johann, S., Heitzer, M., Kanagaratnam, M., Goswami, A., Rizo, T., Weis, J., et al. (2015). NLRP3 inflammasome is expressed by astrocytes in the SOD1 mouse model of ALS and in human sporadic ALS patients. *Glia* 63, 2260–2273. doi:10.1002/glia.22891.

Johnson, M., and Maggiora, G. (1990). *Concepts and Applications of Molecular Similarity*. New York: John Wiley & Sons.

Joosten, R. P., te Beek, T. A. H., Krieger, E., Hekkelman, M. L., Hooft, R. W. W., Schneider, R., et al. (2011). A series of PDB related databases for everyday needs. *Nucleic Acids Res.* 39, D411–D419. doi:10.1093/nar/gkq1105.

Jorgensen, W. L., Chandrasekhar, J., Madura, J. D., Impey, R. W., and Klein, M. L. (1983). Comparison of simple potential functions for simulating liquid water. *J. Chem. Phys.* 79, 926–935. doi:10.1063/1.445869.

Jorgensen, W. L., Maxwell, D. S., and Tirado-Rives, J. (1996). Development and Testing of the OPLS All-Atom Force Field on Conformational Energetics and Properties of Organic Liquids. *J. Am. Chem. Soc.* 118, 11225–11236. doi:10.1021/ja9621760.

Ju Hwang, C., Choi, D.-Y., Park, M. H., and Hong, J. T. (2019). NF-κB as a Key Mediator of Brain Inflammation in Alzheimer's Disease. *CNS Neurol. Disord. - Drug Targets* 18, 3–10. doi:10.2174/1871527316666170807130011.

Kabsch, W., and Sander, C. (1983). Dictionary of protein secondary structure: Pattern recognition of hydrogen-bonded and geometrical features. *Biopolymers* 22, 2577–2637. doi:10.1002/bip.360221211.

Kadukova, M., and Grudinin, S. (2017). Convex-PL: a novel knowledge-based potential for protein-ligand interactions deduced from structural databases using convex optimization. *J. Comput. Aided. Mol. Des.* 31, 943–958. doi:10.1007/s10822-017-0068-8.

Kaiser, C., Knight, A., Nordström, D., Pettersson, T., Fransson, J., Florin-Robertsson, E., et al. (2012). Injection-site reactions upon Kineret (anakinra) administration: experiences and explanations. *Rheumatol. Int.* 32, 295–299. doi:10.1007/s00296-011-2096-3.

Kamei, H., Ishihara, Y., Fuma, D., Niwa, T., Kamiya, Y., Yokoi, T., et al. (2014). Interleukin-1 receptor gene variants are associated with aggressive periodontitis in the Japanese.

Arch. Oral Biol. 59, 756–763. doi:10.1016/j.archoralbio.2014.04.006.

Kamo, H., Haebara, H., Akiguchi, I., Kameyama, M., Kimura, H., and McGeer, P. L. (1987). A distinctive distribution of reactive astroglia in the precentral cortex in amyotrophic lateral sclerosis. *Acta Neuropathol.* 74, 33–38. doi:10.1007/BF00688335.

Karpenko, M. N., Vasilishina, A. A., Gromova, E. A., Muruzheva, Z. M., and Bernadotte, A. (2018). Interleukin-1β, interleukin-1 receptor antagonist, interleukin-6, interleukin-10, and tumor necrosis factor-α levels in CSF and serum in relation to the clinical diversity of Parkinson's disease. *Cell. Immunol.* 327, 77–82. doi:10.1016/j.cellimm.2018.02.011.

Kästner, J. (2011). Umbrella sampling. *Wiley Interdiscip. Rev. Comput. Mol. Sci.* 1, 932–942. doi:10.1002/wcms.66.

Katsila, T., Spyroulias, G. A., Patrinos, G. P., and Matsoukas, M.-T. (2016). Computational approaches in target identification and drug discovery. *Comput. Struct. Biotechnol. J.* 14, 177–184. doi:10.1016/j.csbj.2016.04.004.

Kaufman, L., and Rousseeuw, P. J. (1990). *Finding Groups in Data*. Hoboken, NJ, USA: John Wiley & Sons, Inc. doi:10.1002/9780470316801.

Kelley, L. A., Mezulis, S., Yates, C. M., Wass, M. N., and Sternberg, M. J. E. (2015). The Phyre2 web portal for protein modeling, prediction and analysis. *Nat. Protoc.* 10, 845–858. doi:10.1038/nprot.2015.053.

Kent, B. R. (2015). *3D Scientific Visualization with Blender*. Morgan & Claypool Publishers doi:10.1088/978-1-6270-5612-0.

Keren-Shaul, H., Spinrad, A., Weiner, A., Matcovitch-Natan, O., Dvir-Szternfeld, R., Ulland, T. K., et al. (2017). A Unique Microglia Type Associated with Restricting Development of Alzheimer's Disease. *Cell* 169, 1276-1290.e17. doi:10.1016/j.cell.2017.05.018.

Kerns, E., Di, L., and Carter, G. (2008). In Vitro Solubility Assays in Drug Discovery. *Curr. Drug Metab.* 9, 879–885. doi:10.2174/138920008786485100.

Khan, J. A., Brint, E. K., O'Neill, L. A. J., and Tong, L. (2004). Crystal Structure of the Toll/Interleukin-1 Receptor Domain of Human IL-1RAPL. *J. Biol. Chem.* 279, 31664–31670. doi:10.1074/jbc.M403434200.

Khanfar, M. A., and Alqtaishat, S. (2019). Discovery of potent IRAK-4 inhibitors as potential anti-inflammatory and anticancer agents using structure-based exploration of IRAK-4 pharmacophoric space coupled with QSAR analyses. *Comput. Biol. Chem.* 79, 147–154. doi:10.1016/j.compbiolchem.2019.02.005.

Kim, H.-J., Choo, H., Cho, Y. S., No, K. T., and Pae, A. N. (2008). Novel GSK-3β inhibitors from sequential virtual screening. *Bioorg. Med. Chem.* 16, 636–643. doi:10.1016/j.bmc.2007.10.047.

Kim, S., Thiessen, P. A., Bolton, E. E., Chen, J., Fu, G., Gindulyte, A., et al. (2016). PubChem Substance and Compound databases. *Nucleic Acids Res.* 44, D1202–D1213. doi:10.1093/nar/gkv951.

Kirschner, K. N., Yongye, A. B., Tschampel, S. M., González-Outeiriño, J., Daniels, C. R.,

Foley, B. L., et al. (2008). GLYCAM06: A generalizable biomolecular force field. Carbohydrates. *J. Comput. Chem.* 29, 622–655. doi:10.1002/jcc.20820.

Kitazawa, M., Cheng, D., Tsukamoto, M. R., Koike, M. A., Wes, P. D., Vasilevko, V., et al. (2011). Blocking IL-1 Signaling Rescues Cognition, Attenuates Tau Pathology, and Restores Neuronal β-Catenin Pathway Function in an Alzheimer's Disease Model. *J. Immunol.* 187, 6539–6549. doi:10.4049/jimmunol.1100620.

Kitchen, D. B., Decornez, H., Furr, J. R., and Bajorath, J. (2004). Docking and scoring in virtual screening for drug discovery: methods and applications. *Nat. Rev. Drug Discov.* 3, 935–949. doi:10.1038/nrd1549.

Klarnet, J. P., Kern, D. E., Dower, S. K., Matis, L. A., Cheever, M. A., and Greenberg, P. D. (1989). Helper-independent CD8+ cytotoxic T lymphocytes express IL-1 receptors and require IL-1 for secretion of IL-2. *J. Immunol.* 142, 2187–91. Available at: http://www.ncbi.nlm.nih.gov/pubmed/2466890.

Klein, A. L., Imazio, M., Cremer, P., Brucato, A., Abbate, A., Fang, F., et al. (2021). Phase 3 Trial of Interleukin-1 Trap Rilonacept in Recurrent Pericarditis. *N. Engl. J. Med.* 384, 31–41. doi:10.1056/NEJMoa2027892.

Klementiev, B., Li, S., Korshunova, I., Dmytriyeva, O., Pankratova, S., Walmod, P. S., et al. (2014). Anti-inflammatory properties of a novel peptide interleukin 1 receptor antagonist. *J. Neuroinflammation* 11, 27. doi:10.1186/1742-2094-11-27.

Knapp, B., Ospina, L., and Deane, C. M. (2018). Avoiding False Positive Conclusions in Molecular Simulation: The Importance of Replicas. *J. Chem. Theory Comput.* 14, 6127–6138. doi:10.1021/acs.jctc.8b00391.

Kobayashi, K., Imagama, S., Ohgomori, T., Hirano, K., Uchimura, K., Sakamoto, K., et al. (2013). Minocycline selectively inhibits M1 polarization of microglia. *Cell Death Dis.* 4, e525–e525. doi:10.1038/cddis.2013.54.

Koné-Paut, I., and Galeotti, C. (2014). Anakinra for cryopyrin-associated periodic syndrome. *Expert Rev. Clin. Immunol.* 10, 7–18. doi:10.1586/1744666X.2014.861325.

Kong, W.-L., Peng, Y.-Y., and Peng, B.-W. (2017). Modulation of neuroinflammation: Role and therapeutic potential of TRPV1 in the neuro-immune axis. *Brain. Behav. Immun.* 64, 354–366. doi:10.1016/j.bbi.2017.03.007.

Koo, J. W., and Duman, R. S. (2008). IL-1 is an essential mediator of the antineurogenic and anhedonic effects of stress. *Proc. Natl. Acad. Sci.* 105, 751–756. doi:10.1073/pnas.0708092105.

Koonin, E. V., Wolf, Y. I., and Karev, G. P. (2002). The structure of the protein universe and genome evolution. *Nature* 420, 218–223. doi:10.1038/nature01256.

Kopf, M., Bachmann, M. F., and Marsland, B. J. (2010). Averting inflammation by targeting the cytokine environment. *Nat. Rev. Drug Discov.* 9, 703–718. doi:10.1038/nrd2805.

Kopitar-Jerala, N. (2017). The Role of Interferons in Inflammation and Inflammasome Activation. *Front. Immunol.* 8. doi:10.3389/fimmu.2017.00873.

Kortagere, S., Krasowski, M. D., and Ekins, S. (2009). The importance of discerning shape in molecular pharmacology. *Trends Pharmacol. Sci.* 30, 138–147. doi:10.1016/j.tips.2008.12.001.

Koscielny, G., An, P., Carvalho-Silva, D., Cham, J. A., Fumis, L., Gasparyan, R., et al. (2017). Open Targets: a platform for therapeutic target identification and validation. *Nucleic Acids Res.* 45, D985–D994. doi:10.1093/nar/gkw1055.

Kozakov, D., Grove, L. E., Hall, D. R., Bohnuud, T., Mottarella, S. E., Luo, L., et al. (2015). The FTMap family of web servers for determining and characterizing ligand-binding hot spots of proteins. *Nat. Protoc.* 10, 733–755. doi:10.1038/nprot.2015.043.

Krasnow, S. M., Knoll, J. G., Verghese, S. C., Levasseur, P. R., and Marks, D. L. (2017). Amplification and propagation of interleukin-1β signaling by murine brain endothelial and glial cells. *J. Neuroinflammation* 14, 133. doi:10.1186/s12974-017-0908-4.

Krivák, R., and Hoksza, D. (2018). P2Rank: machine learning based tool for rapid and accurate prediction of ligand binding sites from protein structure. *J. Cheminform.* 10, 39. doi:10.1186/s13321-018-0285-8.

Kroemer, R. T., and Richards, W. G. (1996). Homology modeling study of the human interleukin-7 receptor complex. *"Protein Eng. Des. Sel.* 9, 1135–1142. doi:10.1093/protein/9.12.1135.

Kron, J., Crawford, T., Mihalick, V., Bogun, F., Jordan, J. H., Koelling, T., et al. (2021). Interleukin-1 blockade in cardiac sarcoidosis: study design of the multimodality assessment of granulomas in cardiac sarcoidosis: Anakinra Randomized Trial (MAGiC-ART). *J. Transl. Med.* 19, 460. doi:10.1186/s12967-021-03130-8.

Krueger, J. M., Fang, J., Taishi, P., Chen, Z., Kushikata, T., and Gardi, J. (1998). Sleep: A Physiologic Role for IL-1β and TNF-α a. *Ann. N. Y. Acad. Sci.* 856, 148–159. doi:10.1111/j.1749-6632.1998.tb08323.x.

Krumm, B., Xiang, Y., and Deng, J. (2014). Structural biology of the IL-1 superfamily: Key cytokines in the regulation of immune and inflammatory responses. *Protein Sci.* 23, 526–538. doi:10.1002/pro.2441.

Kubarenko, A. V., Ranjan, S., Colak, E., George, J., Frank, M., and Weber, A. N. R. (2010). Comprehensive modeling and functional analysis of Toll-like receptor ligand-recognition domains. *Protein Sci.* 19, 558–569. doi:10.1002/pro.333.

Kuenemann, M. A., Labbé, C. M., Cerdan, A. H., and Sperandio, O. (2016). Imbalance in chemical space: How to facilitate the identification of protein-protein interaction inhibitors. *Sci. Rep.* 6, 1–17. doi:10.1038/srep23815.

Kumar, A., and Zhang, K. Y. J. (2018). Advances in the Development of Shape Similarity Methods and Their Application in Drug Discovery. *Front. Chem.* 6. doi:10.3389/fchem.2018.00315.

Kuntz, I. D., Blaney, J. M., Oatley, S. J., Langridge, R., and Ferrin, T. E. (1982). A geometric approach to macromolecule-ligand interactions. *J. Mol. Biol.* 161, 269–288. doi:10.1016/0022-2836(82)90153-X.

Labadorf, A., Hoss, A. G., Lagomarsino, V., Latourelle, J. C., Hadzi, T. C., Bregu, J., et al. (2015). RNA Sequence Analysis of Human Huntington Disease Brain Reveals an Extensive Increase in Inflammatory and Developmental Gene Expression. *PLoS One* 10, e0143563. doi:10.1371/journal.pone.0143563.

Lachmann, H. J., Kone-Paut, I., Kuemmerle-Deschner, J. B., Leslie, K. S., Hachulla, E., Quartier, P., et al. (2009). Use of Canakinumab in the Cryopyrin-Associated Periodic Syndrome. *N. Engl. J. Med.* 360, 2416–2425. doi:10.1056/NEJMoa0810787.

Lai, J., Hu, M., Wang, H., Hu, M., Long, Y., Miao, M., et al. (2014). Montelukast targeting the cysteinyl leukotriene receptor 1 ameliorates Aβ1-42-induced memory impairment and neuroinflammatory and apoptotic responses in mice. *Neuropharmacology* 79, 707–714. doi:10.1016/j.neuropharm.2014.01.011.

Lam, S. D., Das, S., Sillitoe, I., and Orengo, C. (2017). An overview of comparative modelling and resources dedicated to large-scale modelling of genome sequences. *Acta Crystallogr. Sect. D Struct. Biol.* 73, 628–640. doi:10.1107/S2059798317008920.

Lan, X., Han, X., Li, Q., Yang, Q.-W., and Wang, J. (2017). Modulators of microglial activation and polarization after intracerebral haemorrhage. *Nat. Rev. Neurol.* 13, 420–433. doi:10.1038/nrneurol.2017.69.

Langer, T., and Hoffmann, R. D. eds. (2006). *Pharmacophores and Pharmacophore Searches*. Wiley doi:10.1002/3527609164.

Larsen, C. M., Faulenbach, M., Vaag, A., Vølund, A., Ehses, J. A., Seifert, B., et al. (2007). Interleukin-1–Receptor Antagonist in Type 2 Diabetes Mellitus. *N. Engl. J. Med.* 356, 1517–1526. doi:10.1056/NEJMoa065213.

Laskowski, R. A. (1995). SURFNET: A program for visualizing molecular surfaces, cavities, and intermolecular interactions. *J. Mol. Graph.* 13, 323–330. doi:10.1016/0263-7855(95)00073-9.

Laskowski, R. A., MacArthur, M. W., Moss, D. S., and Thornton, J. M. (1993). PROCHECK: a program to check the stereochemical quality of protein structures. *J. Appl. Crystallogr.* 26, 283–291. doi:10.1107/S0021889892009944.

Latiano, A., Palmieri, O., Pastorelli, L., Vecchi, M., Pizarro, T. T., Bossa, F., et al. (2013). Associations between Genetic Polymorphisms in IL-33, IL1R1 and Risk for Inflammatory Bowel Disease. *PLoS One* 8, e62144. doi:10.1371/journal.pone.0062144.

Laurie, A. T. R., and Jackson, R. M. (2005). Q-SiteFinder: an energy-based method for the prediction of protein-ligand binding sites. *Bioinformatics* 21, 1908–1916. doi:10.1093/bioinformatics/bti315.

Lauro, C., and Limatola, C. (2020). Metabolic Reprograming of Microglia in the Regulation of the Innate Inflammatory Response. *Front. Immunol.* 11. doi:10.3389/fimmu.2020.00493.

Lavecchia, A., and Giovanni, C. (2013). Virtual Screening Strategies in Drug Discovery: A Critical Review. *Curr. Med. Chem.* 20, 2839–2860. doi:10.2174/09298673113209990001.

Le Guilloux, V., Schmidtke, P., and Tuffery, P. (2009). Fpocket: An open source platform for ligand pocket detection. *BMC Bioinformatics* 10, 168. doi:10.1186/1471-2105-10-168.

Leach, A. R., Shoichet, B. K., and Peishoff, C. E. (2006). Prediction of Protein−Ligand Interactions. Docking and Scoring: Successes and Gaps. *J. Med. Chem.* 49, 5851–5855. doi:10.1021/jm060999m.

Lee, D. H., Kim, M., Kim, M., Lee, Y. J., Yoo, H. J., Lee, S.-H., et al. (2017). Age-dependent alterations in serum cytokines, peripheral blood mononuclear cell cytokine production, natural killer cell activity, and prostaglandin F2α. *Immunol. Res.* 65, 1009–1016. doi:10.1007/s12026-017-8940-0.

Lee, Y. B., Nagai, A., and Kim, S. U. (2002). Cytokines, chemokines, and cytokine receptors in human microglia. *J. Neurosci. Res.* 69, 94–103. doi:10.1002/jnr.10253.

Leng, F., and Edison, P. (2020). Neuroinflammation and microglial activation in Alzheimer disease: where do we go from here? *Nat. Rev. Neurol.* doi:10.1038/s41582-020-00435-y.

Li, D., Song, X., Huang, H., Huang, H., and Ye, Z. (2018). Association of Parkinson's disease-related pain with plasma interleukin-1, interleukin-6, interleukin-10, and tumour necrosis factor-α. *Neurosci. Lett.* 683, 181–184. doi:10.1016/j.neulet.2018.07.027.

Li, J., Fu, A., and Zhang, L. (2019). An Overview of Scoring Functions Used for Protein–Ligand Interactions in Molecular Docking. *Interdiscip. Sci. Comput. Life Sci.* 11, 320–328. doi:10.1007/s12539-019-00327-w.

Liang, J., Woodward, C., and Edelsbrunner, H. (1998). Anatomy of protein pockets and cavities: Measurement of binding site geometry and implications for ligand design. *Protein Sci.* 7, 1884–1897. doi:10.1002/pro.5560070905.

Licastro, F., Pedrini, S., Caputo, L., Annoni, G., Davis, L. J., Ferri, C., et al. (2000). Increased plasma levels of interleukin-1, interleukin-6 and α-1-antichymotrypsin in patients with Alzheimer's disease: peripheral inflammation or signals from the brain? *J. Neuroimmunol.* 103, 97–102. doi:10.1016/S0165-5728(99)00226-X.

Lin, H.-W., Basu, A., Druckman, C., Cicchese, M., Krady, J. K., and Levison, S. W. (2006). Astrogliosis is delayed in type 1 interleukin-1 receptor-null mice following a penetrating brain injury. *J. Neuroinflammation* 3, 15. doi:10.1186/1742-2094-3-15.

Lindberg, C., Hjorth, E., Post, C., Winblad, B., and Schultzberg, M. (2005). Cytokine production by a human microglial cell line: Effects of ßamyloid and α-melanocyte-stimulating hormone. *Neurotox. Res.* 8, 267–276. doi:10.1007/BF03033980.

Lindestam Arlehamn, C. S., Dhanwani, R., Pham, J., Kuan, R., Frazier, A., Rezende Dutra, J., et al. (2020). α-Synuclein-specific T cell reactivity is associated with preclinical and early Parkinson's disease. *Nat. Commun.* 11, 1875. doi:10.1038/s41467-020-15626-w.

Lindorff-Larsen, K., Piana, S., Palmo, K., Maragakis, P., Klepeis, J. L., Dror, R. O., et al. (2010). Improved side-chain torsion potentials for the Amber ff99SB protein force field. *Proteins Struct. Funct. Bioinforma.*, NA-NA. doi:10.1002/prot.22711.

Lipinski, C. A., Lombardo, F., Dominy, B. W., and Feeney, P. J. (2001). Experimental and computational approaches to estimate solubility and permeability in drug discovery and development settings 1PII of original article: S0169-409X(96)00423-1. The article was originally published in Advanced Drug Delivery Reviews 23 (1997). *Adv. Drug Deliv.*

Rev. 46, 3–26. doi:10.1016/S0169-409X(00)00129-0.

Liu, J., and Wang, R. (2015). Classification of Current Scoring Functions. *J. Chem. Inf. Model.* 55, 475–482. doi:10.1021/ci500731a.

Liu, X., Nemeth, D. P., McKim, D. B., Zhu, L., DiSabato, D. J., Berdysz, O., et al. (2019). Cell-Type-Specific Interleukin 1 Receptor 1 Signaling in the Brain Regulates Distinct Neuroimmune Activities. *Immunity* 50, 317-333.e6. doi:10.1016/j.immuni.2018.12.012.

Liu, X., and Quan, N. (2018). Microglia and CNS Interleukin-1: Beyond Immunological Concepts. *Front. Neurol.* 9, 1–11. doi:10.3389/fneur.2018.00008.

Liu, Y., Ho, R. C.-M., and Mak, A. (2012). Interleukin (IL)-6, tumour necrosis factor alpha (TNF-α) and soluble interleukin-2 receptors (sIL-2R) are elevated in patients with major depressive disorder: A meta-analysis and meta-regression. *J. Affect. Disord.* 139, 230–239. doi:10.1016/j.jad.2011.08.003.

Livingston, G., Huntley, J., Sommerlad, A., Ames, D., Ballard, C., Banerjee, S., et al. (2020). Dementia prevention, intervention, and care: 2020 report of the Lancet Commission. *Lancet* 396, 413–446. doi:10.1016/S0140-6736(20)30367-6.

Lobsiger, C. S., and Cleveland, D. W. (2007). Glial cells as intrinsic components of non-cell-autonomous neurodegenerative disease. *Nat. Neurosci.* 10, 1355–1360. doi:10.1038/nn1988.

Loddick, S. A., and Rothwell, N. J. (1996). Neuroprotective Effects of Human Recombinant Interleukin-1 Receptor Antagonist in Focal Cerebral Ischaemia in the Rat. *J. Cereb. Blood Flow Metab.* 16, 932–940. doi:10.1097/00004647-199609000-00017.

Lonnemann, N., Hosseini, S., Marchetti, C., Skouras, D. B., Stefanoni, D., D'Alessandro, A., et al. (2020). The NLRP3 inflammasome inhibitor OLT1177 rescues cognitive impairment in a mouse model of Alzheimer's disease. *Proc. Natl. Acad. Sci.* 117, 32145–32154. doi:10.1073/pnas.2009680117.

Lucin, K. M., and Wyss-Coray, T. (2009). Immune Activation in Brain Aging and Neurodegeneration: Too Much or Too Little? *Neuron* 64, 110–122. doi:10.1016/j.neuron.2009.08.039.

Lv, R., Du, L., Liu, X., Zhou, F., Zhang, Z., and Zhang, L. (2019). Rosmarinic acid attenuates inflammatory responses through inhibiting HMGB1/TLR4/NF-κB signaling pathway in a mouse model of Parkinson's disease. *Life Sci.* 223, 158–165. doi:10.1016/j.lfs.2019.03.030.

MacDonald, H. R., Wingfield, P., Schmeissner, U., Shaw, A., Clore, G. M., and Gronenborn, A. M. (1986). Point mutations of human interleukin-1 with decreased receptor binding affinity. *FEBS Lett.* 209, 295–298. doi:10.1016/0014-5793(86)81130-9.

MacKerell, A. D., Bashford, D., Bellott, M., Dunbrack, R. L., Evanseck, J. D., Field, M. J., et al. (1998). All-Atom Empirical Potential for Molecular Modeling and Dynamics Studies of Proteins †. *J. Phys. Chem. B* 102, 3586–3616. doi:10.1021/jp973084f.

Mahdaviani, S. A., Rezaei, N., Moradi, B., Dorkhosh, S., Amirzargar, A. A., and Movahedi, M. (2009). Proinflammatory Cytokine Gene Polymorphisms among Iranian Patients

with Asthma. *J. Clin. Immunol.* 29, 57–62. doi:10.1007/s10875-008-9232-1.

Maihofner, C., Probst-Cousin, S., Bergmann, M., Neuhuber, W., Neundorfer, B., and Heuss, D. (2003). Expression and localization of cyclooxygenase-1 and -2 in human sporadic amyotrophic lateral sclerosis. *Eur. J. Neurosci.* 18, 1527–1534. doi:10.1046/j.1460-9568.2003.02879.x.

Majumdar, I., Nagpal, I., and Paul, J. (2017). Homology modeling and in silico prediction of Ulcerative colitis associated polymorphisms of NOD1. *Mol. Cell. Probes* 35, 8–19. doi:10.1016/j.mcp.2017.05.009.

Makin, S. (2018). The amyloid hypothesis on trial. *Nature* 559, S4–S7. doi:10.1038/d41586-018-05719-4.

Mancuso, R., Fryatt, G., Cleal, M., Obst, J., Pipi, E., Monzón-Sandoval, J., et al. (2019). CSF1R inhibitor JNJ-40346527 attenuates microglial proliferation and neurodegeneration in P301S mice. *Brain* 142, 3243–3264. doi:10.1093/brain/awz241.

Mantovani, A., Dinarello, C. A., Molgora, M., and Garlanda, C. (2019). Interleukin-1 and Related Cytokines in the Regulation of Inflammation and Immunity. *Immunity* 50, 778–795. doi:10.1016/j.immuni.2019.03.012.

Markt, P., Petersen, R. K., Flindt, E. N., Kristiansen, K., Kirchmair, J., Spitzer, G., et al. (2008). Discovery of Novel PPAR Ligands by a Virtual Screening Approach Based on Pharmacophore Modeling, 3D Shape, and Electrostatic Similarity Screening. *J. Med. Chem.* 51, 6303–6317. doi:10.1021/jm800128k.

Maroso, M., Balosso, S., Ravizza, T., Iori, V., Wright, C. I., French, J., et al. (2011). Interleukin-1β Biosynthesis Inhibition Reduces Acute Seizures and Drug Resistant Chronic Epileptic Activity in Mice. *Neurotherapeutics* 8, 304–315. doi:10.1007/s13311-011-0039-z.

Martin, M. U., and Wesche, H. (2002). Summary and comparison of the signaling mechanisms of the Toll/interleukin-1 receptor family. *Biochim. Biophys. Acta - Mol. Cell Res.* 1592, 265–280. doi:10.1016/S0167-4889(02)00320-8.

Martin, P., Goldstein, J. D., Mermoud, L., Diaz-Barreiro, A., and Palmer, G. (2021). IL-1 Family Antagonists in Mouse and Human Skin Inflammation. *Front. Immunol.* 12. doi:10.3389/fimmu.2021.652846.

Martínez, H. R., Escamilla-Ocañas, C. E., Tenorio-Pedraza, J. M., Gómez-Almaguer, D., Jaime-Perez, J. C., Olguín-Ramírez, L. A., et al. (2017). Altered CSF cytokine network in amyotrophic lateral sclerosis patients: A pathway-based statistical analysis. *Cytokine* 90, 1–5. doi:10.1016/j.cyto.2016.09.022.

McCammon, J. A., Gelin, B. R., and Karplus, M. (1977). Dynamics of folded proteins. *Nature* 267, 585–590. doi:10.1038/267585a0.

McCauley, M. E., and Baloh, R. H. (2019). Inflammation in ALS/FTD pathogenesis. *Acta Neuropathol.* 137, 715–730. doi:10.1007/s00401-018-1933-9.

McColl, B. W., Rothwell, N. J., and Allan, S. M. (2007). Systemic Inflammatory Stimulus Potentiates the Acute Phase and CXC Chemokine Responses to Experimental Stroke and Exacerbates Brain Damage via Interleukin-1- and Neutrophil-Dependent

Mechanisms. *J. Neurosci.* 27, 4403–4412. doi:10.1523/JNEUROSCI.5376-06.2007.

McGeer, P. L., Itagaki, S., Boyes, B. E., and McGeer, E. G. (1988). Reactive microglia are positive for HLA-DR in the substantia nigra of Parkinson's and Alzheimer's disease brains. *Neurology* 38, 1285–1285. doi:10.1212/WNL.38.8.1285.

McGuinness, M. ., Powers, J. ., Bias, W. ., Schmeckpeper, B. ., Segal, A. ., Gowda, V. ., et al. (1997). Human leukocyte antigens and cytokine expression in cerebral inflammatory demyelinative lesions of X-linked adrenoleukodystrophy and multiple sclerosis. *J. Neuroimmunol.* 75, 174–182. doi:10.1016/S0165-5728(97)00020-9.

McMahan, C. J., Slack, J. L., Mosley, B., Cosman, D., Lupton, S. D., Brunton, L. L., et al. (1991). A novel IL-1 receptor, cloned from B cells by mammalian expression, is expressed in many cell types. *EMBO J.* 10, 2821–32. doi:1833184.

Meissner, F., Molawi, K., and Zychlinsky, A. (2010). Mutant superoxide dismutase 1-induced IL-1 accelerates ALS pathogenesis. *Proc. Natl. Acad. Sci.* 107, 13046–13050. doi:10.1073/pnas.1002396107.

Mekni, N., De Rosa, M., Cipollina, C., Gulotta, M. R., De Simone, G., Lombino, J., et al. (2019). In Silico Insights towards the Identification of NLRP3 Druggable Hot Spots. *Int. J. Mol. Sci.* 20, 4974. doi:10.3390/ijms20204974.

Mering, C. v. (2003). STRING: a database of predicted functional associations between proteins. *Nucleic Acids Res.* 31, 258–261. doi:10.1093/nar/gkg034.

Metcalfe, M. J., and Figueiredo-Pereira, M. E. (2010). Relationship Between Tau Pathology and Neuroinflammation in Alzheimer's Disease. *Mt. Sinai J. Med. A J. Transl. Pers. Med.* 77, 50–58. doi:10.1002/msj.20163.

Migheli, A., Cordera, S., Bendotti, C., Atzori, C., Piva, R., and Schiffer, D. (1999). S-100β protein is upregulated in astrocytes and motor neurons in the spinal cord of patients with amyotrophic lateral sclerosis. *Neurosci. Lett.* 261, 25–28. doi:10.1016/S0304-3940(98)01001-5.

Mikitsh, J. L., and Chacko, A.-M. (2014). Pathways for Small Molecule Delivery to the Central Nervous System across the Blood-Brain Barrier. *Perspect. Medicin. Chem.* 6, PMC.S13384. doi:10.4137/PMC.S13384.

Minami, M., Kuraishi, Y., Yabuuchi, K., Yamazaki, A., and Satoh, M. (1992). Induction of Interleukin-1β mRNA in Rat Brain After Transient Forebrain Ischemia. *J. Neurochem.* 58, 390–392. doi:10.1111/j.1471-4159.1992.tb09324.x.

Miret, S., De Groene, E. M., and Klaffke, W. (2006). Comparison of In Vitro Assays of Cellular Toxicity in the Human Hepatic Cell Line HepG2. *J. Biomol. Screen.* 11, 184–193. doi:10.1177/1087057105283787.

Mishra, P.-S., Vijayalakshmi, K., Nalini, A., Sathyaprabha, T. N., Kramer, B. W., Alladi, P. A., et al. (2017). Etiogenic factors present in the cerebrospinal fluid from amyotrophic lateral sclerosis patients induce predominantly pro-inflammatory responses in microglia. *J. Neuroinflammation* 14, 251. doi:10.1186/s12974-017-1028-x.

Miyata, T., Ikuta, Y., and Hirata, F. (2010). Free energy calculation using molecular dynamics

simulation combined with the three dimensional reference interaction site model theory. I. Free energy perturbation and thermodynamic integration along a coupling parameter. *J. Chem. Phys.* 133, 044114. doi:10.1063/1.3462276.

Mizuno, T. (2012). The Biphasic Role of Microglia in Alzheimer's Disease. *Int. J. Alzheimers. Dis.* 2012, 1–9. doi:10.1155/2012/737846.

Mogi, M., Harada, M., Narabayashi, H., Inagaki, H., Minami, M., and Nagatsu, T. (1996). Interleukin (IL)-1β, IL-2, IL-4, IL-6 and transforming growth factor-α levels are elevated in ventricular cerebrospinal fluid in juvenile parkinsonism and Parkinson's disease. *Neurosci. Lett.* 211, 13–16. doi:10.1016/0304-3940(96)12706-3.

Mogi, M., Harada, M., Riederer, P., Narabayashi, H., Fujita, K., and Nagatsu, T. (1994). Tumor necrosis factor-α (TNF-α) increases both in the brain and in the cerebrospinal fluid from parkinsonian patients. *Neurosci. Lett.* 165, 208–210. doi:10.1016/0304-3940(94)90746-3.

Mohan, R. R., Wilson, M., Gorham, R. D., Harrison, R. E. S., Morikis, V. A., Kieslich, C. A., et al. (2018). Virtual Screening of Chemical Compounds for Discovery of Complement C3 Ligands. *ACS Omega* 3, 6427–6438. doi:10.1021/acsomega.8b00606.

Moll, J., and Carotta, S. eds. (2019). *Target Identification and Validation in Drug Discovery*. New York, NY: Springer New York doi:10.1007/978-1-4939-9145-7.

Monsonego, A., Zota, V., Karni, A., Krieger, J. I., Bar-Or, A., Bitan, G., et al. (2003). Increased T cell reactivity to amyloid β protein in older humans and patients with Alzheimer disease. *J. Clin. Invest.* 112, 415–422. doi:10.1172/JCI18104.

Moritz, C. P., Mühlhaus, T., Tenzer, S., Schulenborg, T., and Friauf, E. (2019). Poor transcript-protein correlation in the brain: negatively correlating gene products reveal neuronal polarity as a potential cause. *J. Neurochem.* 149, 582–604. doi:10.1111/jnc.14664.

Moritz, K. E., McCormack, N. M., Abera, M. B., Viollet, C., Yauger, Y. J., Sukumar, G., et al. (2017). The role of the immunoproteasome in interferon-γ-mediated microglial activation. *Sci. Rep.* 7, 9365. doi:10.1038/s41598-017-09715-y.

Morris, G. M., Goodsell, D. S., Halliday, R. S., Huey, R., Hart, W. E., Belew, R. K., et al. (1998). Automated docking using a Lamarckian genetic algorithm and an empirical binding free energy function. *J. Comput. Chem.* 19, 1639–1662. doi:10.1002/(SICI)1096-987X(19981115)19:14<1639::AID-JCC10>3.0.CO;2-B.

Morris, G. M., Huey, R., Lindstrom, W., Sanner, M. F., Belew, R. K., Goodsell, D. S., et al. (2009). AutoDock4 and AutoDockTools4: Automated docking with selective receptor flexibility. *J. Comput. Chem.* 30, 2785–2791. doi:10.1002/jcc.21256.

Müller, N., Weidinger, E., Leitner, B., and Schwarz, M. J. (2015). The role of inflammation in schizophrenia. *Front. Neurosci.* 9. doi:10.3389/fnins.2015.00372.

Müller, S. I., Friedl, A., Aschenbrenner, I., Esser-von Bieren, J., Zacharias, M., Devergne, O., et al. (2019). A folding switch regulates interleukin 27 biogenesis and secretion of its α-subunit as a cytokine. *Proc. Natl. Acad. Sci.* 116, 1585–1590. doi:10.1073/pnas.1816698116.

Murgolo, N. J., Windsor, W. T., Hruza, A., Reichert, P., Tsarbopoulos, A., Baldwin, S., et al.

(1993). A homology model of human interferon α-2. *Proteins Struct. Funct. Genet.* 17, 62–74. doi:10.1002/prot.340170109.

Murgueitio, M. S., Henneke, P., Glossmann, H., Santos-Sierra, S., and Wolber, G. (2014). Prospective Virtual Screening in a Sparse Data Scenario: Design of Small-Molecule TLR2 Antagonists. *ChemMedChem* 9, 813–822. doi:10.1002/cmdc.201300445.

Nakano-Kobayashi, A., Fukumoto, A., Morizane, A., Nguyen, D. T., Le, T. M., Hashida, K., et al. (2020). Therapeutics potentiating microglial p21-Nrf2 axis can rescue neurodegeneration caused by neuroinflammation. *Sci. Adv.* 6, eabc1428. doi:10.1126/sciadv.abc1428.

Nakashima, T., Hori, T., Mori, T., Kuriyama, K., and Mizuno, K. (1989). Recombinant human interleukin-1 β alters the activity of preoptic thermosensitive neurons in vitro. *Brain Res. Bull.* 23, 209–213. doi:10.1016/0361-9230(89)90149-4.

Näkki, A., Kouhia, S. T., Saarela, J., Harilainen, A., Tallroth, K., Videman, T., et al. (2010). Allelic variants of IL1R1gene associate with severe hand osteoarthritis. *BMC Med. Genet.* 11, 50. doi:10.1186/1471-2350-11-50.

Narayanan, K. B., and Park, H. H. (2015). Toll/interleukin-1 receptor (TIR) domain-mediated cellular signaling pathways. *Apoptosis* 20, 196–209. doi:10.1007/s10495-014-1073-1.

Newell, E. A., Todd, B. P., Mahoney, J., Pieper, A. A., Ferguson, P. J., and Bassuk, A. G. (2018). Combined Blockade of Interleukin-1 α and β Signaling Protects Mice from Cognitive Dysfunction after Traumatic Brain Injury. 10, 385–17. doi:10.1523/ENEURO.0385-17.2018.

Ng, A., Tam, W. W., Zhang, M. W., Ho, C. S., Husain, S. F., McIntyre, R. S., et al. (2018). IL-1β, IL-6, TNF- α and CRP in Elderly Patients with Depression or Alzheimer's disease: Systematic Review and Meta-Analysis. *Sci. Rep.* 8, 12050. doi:10.1038/s41598-018-30487-6.

Ngan, C. H., Bohnuud, T., Mottarella, S. E., Beglov, D., Villar, E. A., Hall, D. R., et al. (2012). FTMAP: Extended protein mapping with user-selected probe molecules. *Nucleic Acids Res.* 40, 271–275. doi:10.1093/nar/gks441.

Nguyen, V. T., and Benveniste, E. N. (2002). Critical Role of Tumor Necrosis Factor-α and NF-κB in Interferon-γ-induced CD40 Expression in Microglia/Macrophages. *J. Biol. Chem.* 277, 13796–13803. doi:10.1074/jbc.M111906200.

Nimmerjahn, A. (2005). Resting Microglial Cells Are Highly Dynamic Surveillants of Brain Parenchyma in Vivo. *Science (80-.).* 308, 1314–1318. doi:10.1126/science.1110647.

Nissl, F. (1899). Über einige Beziehungen zwischen Nervenzellerkrankungen und gliösen Erscheinungen bei verschiedenen Psychosen. *Arch Psychiatr*, 32:656–76.

Noha, S. M., Atanasov, A. G., Schuster, D., Markt, P., Fakhrudin, N., Heiss, E. H., et al. (2011). Discovery of a novel IKK-β inhibitor by ligand-based virtual screening techniques. *Bioorg. Med. Chem. Lett.* 21, 577–583. doi:10.1016/j.bmcl.2010.10.051.

O'Brien, P. J. (2014). High-Content Analysis in Toxicology: Screening Substances for Human Toxicity Potential, Elucidating Subcellular Mechanisms and In Vivo Use as

Translational Safety Biomarkers. *Basic Clin. Pharmacol. Toxicol.* 115, 4–17. doi:10.1111/bcpt.12227.

Olah, M., Menon, V., Habib, N., Taga, M. F., Ma, Y., Yung, C. J., et al. (2020). Single cell RNA sequencing of human microglia uncovers a subset associated with Alzheimer's disease. *Nat. Commun.* 11, 6129. doi:10.1038/s41467-020-19737-2.

OpenEye Scientific Software (2013). QUACPAC v.1.7.0.2. Available at: https://www.eyesopen.com/quacpac.

OpenEye Scientific Software (2018). ROCS v.3.2.2.2. Available at: https://www.eyesopen.com/rocs.

OpenEye Scientific Software (2019). Omega v.3.0.0.1. Available at: https://www.eyesopen.com/omega.

Owens, J. (2007). Determining druggability. *Nat. Rev. Drug Discov.* 6, 187–187. doi:10.1038/nrd2275.

Paik, S., Kim, J. K., Silwal, P., Sasakawa, C., and Jo, E.-K. (2021). An update on the regulatory mechanisms of NLRP3 inflammasome activation. *Cell. Mol. Immunol.* 18, 1141–1160. doi:10.1038/s41423-021-00670-3.

Palomer, A., Cabré, F., Pascual, J., Campos, J., Trujillo, M. A., Entrena, A., et al. (2002). Identification of Novel Cyclooxygenase-2 Selective Inhibitors Using Pharmacophore Models. *J. Med. Chem.* 45, 1402–1411. doi:10.1021/jm010458r.

Pantsar, T., and Poso, A. (2018). Binding Affinity via Docking: Fact and Fiction. *Molecules* 23, 1899. doi:10.3390/molecules23081899.

Paramo, T., East, A., Garzón, D., Ulmschneider, M. B., and Bond, P. J. (2014). Efficient Characterization of Protein Cavities within Molecular Simulation Trajectories: trj_cavity. *J. Chem. Theory Comput.* 10, 2151–2164. doi:10.1021/ct401098b.

Pardridge, W. M. (2007). Blood–brain barrier delivery. *Drug Discov. Today* 12, 54–61. doi:10.1016/j.drudis.2006.10.013.

Parisi, C., Arisi, I., D'Ambrosi, N., Storti, A. E., Brandi, R., D'Onofrio, M., et al. (2013). Dysregulated microRNAs in amyotrophic lateral sclerosis microglia modulate genes linked to neuroinflammation. *Cell Death Dis.* 4, e959–e959. doi:10.1038/cddis.2013.491.

Park, M. H., Lee, M., Nam, G., Kim, M., Kang, J., Choi, B. J., et al. (2019). N , N ′-Diacetyl- p -phenylenediamine restores microglial phagocytosis and improves cognitive defects in Alzheimer's disease transgenic mice. *Proc. Natl. Acad. Sci.* 116, 23426–23436. doi:10.1073/pnas.1916318116.

Parrinello, M., and Rahman, A. (1981). Polymorphic transitions in single crystals: A new molecular dynamics method. *J. Appl. Phys.* 52, 7182–7190. doi:10.1063/1.328693.

Patas, K., Willing, A., Demiralay, C., Engler, J. B., Lupu, A., Ramien, C., et al. (2018). T Cell Phenotype and T Cell Receptor Repertoire in Patients with Major Depressive Disorder. *Front. Immunol.* 9. doi:10.3389/fimmu.2018.00291.

Pence, H. E., and Williams, A. (2010). ChemSpider: An Online Chemical Information

Resource. *J. Chem. Educ.* 87, 1123–1124. doi:10.1021/ed100697w.

Pérez-Regidor, L., Zarioh, M., Ortega, L., and Martín-Santamaría, S. (2016). Virtual Screening Approaches towards the Discovery of Toll-Like Receptor Modulators. *Int. J. Mol. Sci.* 17, 1508. doi:10.3390/ijms17091508.

Pérot, S., Sperandio, O., Miteva, M. A., Camproux, A.-C., and Villoutreix, B. O. (2010). Druggable pockets and binding site centric chemical space: a paradigm shift in drug discovery. *Drug Discov. Today* 15, 656–667. doi:10.1016/j.drudis.2010.05.015.

Petrova, S. S., and Solov'ev, A. D. (1997). The Origin of the Method of Steepest Descent. *Hist. Math.* 24, 361–375. doi:10.1006/hmat.1996.2146.

Pettersen, E. F., Goddard, T. D., Huang, C. C., Couch, G. S., Greenblatt, D. M., Meng, E. C., et al. (2004). UCSF Chimera?A visualization system for exploratory research and analysis. *J. Comput. Chem.* 25, 1605–1612. doi:10.1002/jcc.20084.

Phillips, J. C., Braun, R., Wang, W., Gumbart, J., Tajkhorshid, E., Villa, E., et al. (2005). Scalable molecular dynamics with NAMD. *J. Comput. Chem.* 26, 1781–1802. doi:10.1002/jcc.20289.

Piggot, T. J., Allison, J. R., Sessions, R. B., and Essex, J. W. (2017). On the Calculation of Acyl Chain Order Parameters from Lipid Simulations. *J. Chem. Theory Comput.* 13, 5683–5696. doi:10.1021/acs.jctc.7b00643.

Pinteaux, E., Parker, L. C., Rothwell, N. J., and Luheshi, G. N. (2002). Expression of interleukin-1 receptors and their role in interleukin-1 actions in murine microglial cells. *J. Neurochem.* 83, 754–763. doi:10.1046/j.1471-4159.2002.01184.x.

Pinteaux, E., Trotter, P., and Simi, A. (2009). Cell-specific and concentration-dependent actions of interleukin-1 in acute brain inflammation. *Cytokine* 45, 1–7. doi:10.1016/j.cyto.2008.10.008.

Pinto, S., Cunha, C., Barbosa, M., Vaz, A. R., and Brites, D. (2017). Exosomes from NSC-34 cells transfected with hSOD1-G93A are enriched in mir-124 and drive alterations in microglia phenotype. *Front. Neurosci.* 11. doi:10.3389/fnins.2017.00273.

Poger, D., Caron, B., and Mark, A. E. (2016). Validating lipid force fields against experimental data: Progress, challenges and perspectives. *Biochim. Biophys. Acta - Biomembr.* 1858, 1556–1565. doi:10.1016/j.bbamem.2016.01.029.

Poger, D., and Mark, A. E. (2010). On the Validation of Molecular Dynamics Simulations of Saturated and cis -Monounsaturated Phosphatidylcholine Lipid Bilayers: A Comparison with Experiment. *J. Chem. Theory Comput.* 6, 325–336. doi:10.1021/ct900487a.

Pradillo, J. M., Murray, K. N., Coutts, G. A., Moraga, A., Oroz-Gonjar, F., Boutin, H., et al. (2017). Reparative effects of interleukin-1 receptor antagonist in young and aged/co-morbid rodents after cerebral ischemia. *Brain. Behav. Immun.* 61, 117–126. doi:10.1016/j.bbi.2016.11.013.

Priller, J., and Prinz, M. (2019). Targeting microglia in brain disorders. *Science (80-.).* 365, 32–33. doi:10.1126/science.aau9100.

Procacci, P., and Marchi, M. (1996). Taming the Ewald sum in molecular dynamics simulations of solvated proteins via a multiple time step algorithm. *J. Chem. Phys.* 104, 3003–3012. doi:10.1063/1.471067.

Qin, X.-Y., Zhang, S.-P., Cao, C., Loh, Y. P., and Cheng, Y. (2016). Aberrations in Peripheral Inflammatory Cytokine Levels in Parkinson Disease. *JAMA Neurol.* 73, 1316. doi:10.1001/jamaneurol.2016.2742.

Quéméner, A., Maillasson, M., Arzel, L., Sicard, B., Vomiandry, R., Mortier, E., et al. (2017). Discovery of a Small-Molecule Inhibitor of Interleukin 15: Pharmacophore-Based Virtual Screening and Hit Optimization. *J. Med. Chem.* 60, 6249–6272. doi:10.1021/acs.jmedchem.7b00485.

Quiniou, C., Sapieha, P., Lahaie, I., Hou, X., Brault, S., Beauchamp, M., et al. (2008). Development of a Novel Noncompetitive Antagonist of IL-1 Receptor. *J. Immunol.* 180, 6977–6987. doi:10.4049/jimmunol.180.10.6977.

Rankovic, Z. (2015). CNS Drug Design: Balancing Physicochemical Properties for Optimal Brain Exposure. *J. Med. Chem.* 58, 2584–2608. doi:10.1021/jm501535r.

Ransohoff, R. M. (2016). A polarizing question: do M1 and M2 microglia exist? *Nat. Neurosci.* 19, 987–991. doi:10.1038/nn.4338.

Rapaport, D. C. (2004). *The Art of Molecular Dynamics Simulation*. Cambridge University Press doi:10.1017/CBO9780511816581.

Raymond, J. W., and Willett, P. (2002). Maximum common subgraph isomorphism algorithms for the matching of chemical structures. *J. Comput. Aided. Mol. Des.* 16, 521–33. doi:10.1023/a:1021271615909.

Read, R. J., Adams, P. D., Arendall, W. B., Brunger, A. T., Emsley, P., Joosten, R. P., et al. (2011). A New Generation of Crystallographic Validation Tools for the Protein Data Bank. *Structure* 19, 1395–1412. doi:10.1016/j.str.2011.08.006.

Reale, M., Iarlori, C., Thomas, A., Gambi, D., Perfetti, B., Di Nicola, M., et al. (2009). Peripheral cytokines profile in Parkinson's disease. *Brain. Behav. Immun.* 23, 55–63. doi:10.1016/j.bbi.2008.07.003.

Reed-Geaghan, E. G., Savage, J. C., Hise, A. G., and Landreth, G. E. (2009). CD14 and Toll-Like Receptors 2 and 4 Are Required for Fibrillar A -Stimulated Microglial Activation. *J. Neurosci.* 29, 11982–11992. doi:10.1523/JNEUROSCI.3158-09.2009.

Reker, D., Bernardes, G. J. L., and Rodrigues, T. (2019). Computational advances in combating colloidal aggregation in drug discovery. *Nat. Chem.* 11, 402–418. doi:10.1038/s41557-019-0234-9.

Reynolds, A. P., Richards, G., de la Iglesia, B., and Rayward-Smith, V. J. (2006). Clustering Rules: A Comparison of Partitioning and Hierarchical Clustering Algorithms. *J. Math. Model. Algorithms* 5, 475–504. doi:10.1007/s10852-005-9022-1.

Richardson, J. M., and Brinkley, S. R. (1960). Cell Method in Grand Canonical Ensemble. *J. Chem. Phys.* 33, 1467–1478. doi:10.1063/1.1731428.

Rio-Hortega, P. (1939). THE MICROGLIA. *Lancet* 233, 1023–1026. doi:10.1016/S0140-6736(00)60571-8.

Rissanen, A., Howard, C. P., Botha, J., and Thuren, T. (2012). Effect of anti-IL-1β antibody (canakinumab) on insulin secretion rates in impaired glucose tolerance or type 2 diabetes: results of a randomized, placebo-controlled trial. *Diabetes, Obes. Metab.* 14, 1088–1096. doi:10.1111/j.1463-1326.2012.01637.x.

Rivers-Auty, J., Daniels, M. J. D., Colliver, I., Robertson, D. L., and Brough, D. (2018). Redefining the ancestral origins of the interleukin-1 superfamily. *Nat. Commun.* 9, 1156. doi:10.1038/s41467-018-03362-1.

Rock, R. B., Hu, S., Deshpande, A., Munir, S., May, B. J., Baker, C. A., et al. (2005). Transcriptional response of human microglial cells to interferon-γ. *Genes Immun.* 6, 712–719. doi:10.1038/sj.gene.6364246.

Rost, B. (1999). Twilight zone of protein sequence alignments. *Protein Eng. Des. Sel.* 12, 85–94. doi:10.1093/protein/12.2.85.

Roy, E. R., Wang, B., Wan, Y., Chiu, G., Cole, A., Yin, Z., et al. (2020). Type I interferon response drives neuroinflammation and synapse loss in Alzheimer disease. *J. Clin. Invest.* 130, 1912–1930. doi:10.1172/JCI133737.

Roy, S. M., Minasov, G., Arancio, O., Chico, L. W., Van Eldik, L. J., Anderson, W. F., et al. (2019). A Selective and Brain Penetrant p38αMAPK Inhibitor Candidate for Neurologic and Neuropsychiatric Disorders That Attenuates Neuroinflammation and Cognitive Dysfunction. *J. Med. Chem.* 62, 5298–5311. doi:10.1021/acs.jmedchem.9b00058.

RStudio Team (2020). RStudio: Integrated Development for R. Available at: https://www.rstudio.com.

Rush, T. S., Grant, J. A., Mosyak, L., and Nicholls, A. (2005). A Shape-Based 3-D Scaffold Hopping Method and Its Application to a Bacterial Protein−Protein Interaction. *J. Med. Chem.* 48, 1489–1495. doi:10.1021/jm040163o.

Ryckaert, J.-P., Ciccotti, G., and Berendsen, H. J. . (1977). Numerical integration of the cartesian equations of motion of a system with constraints: molecular dynamics of n-alkanes. *J. Comput. Phys.* 23, 327–341. doi:10.1016/0021-9991(77)90098-5.

Saha, R. N., and Pahan, K. (2006). Regulation of Inducible Nitric Oxide Synthase Gene in Glial Cells. *Antioxid. Redox Signal.* 8, 929–947. doi:10.1089/ars.2006.8.929.

Sali, A. (2008). Make alpha helix - Modeller Wiki. Available at: https://salilab.org/modeller/wiki/Make alpha helix [Accessed January 3, 2020].

Šali, A., and Blundell, T. L. (1993). Comparative Protein Modelling by Satisfaction of Spatial Restraints. *J. Mol. Biol.* 234, 779–815. doi:10.1006/jmbi.1993.1626.

Salmaso, V., and Moro, S. (2018). Bridging Molecular Docking to Molecular Dynamics in Exploring Ligand-Protein Recognition Process: An Overview. *Front. Pharmacol.* 9. doi:10.3389/fphar.2018.00923.

Salo-Ahen, O. M. H., Alanko, I., Bhadane, R., Bonvin, A. M. J. J., Honorato, R. V., Hossain, S.,

et al. (2020). Molecular Dynamics Simulations in Drug Discovery and Pharmaceutical Development. *Processes* 9, 71. doi:10.3390/pr9010071.

Samson, J. M., Ravindran Menon, D., Vaddi, P. K., Kalani Williams, N., Domenico, J., Zhai, Z., et al. (2020). Computational Modeling of NLRP3 Identifies Enhanced ATP Binding and Multimerization in Cryopyrin-Associated Periodic Syndromes. *Front. Immunol.* 11. doi:10.3389/fimmu.2020.584364.

Sánchez-Manubens, J., Iglesias, E., and Anton, J. (2019). Canakinumab for the treatment of hyperimmunoglobulin D syndrome. *Expert Rev. Clin. Immunol.* 15, 215–220. doi:10.1080/1744666X.2019.1571410.

Sassa, S., Sugita, O., Galbraith, R. A., and Kappas, A. (1987). Drug metabolism by the human hepatoma cell, Hep G2. *Biochem. Biophys. Res. Commun.* 143, 52–57. doi:10.1016/0006-291X(87)90628-0.

Sato, A., Ohtaki, H., Tsumuraya, T., Song, D., Ohara, K., Asano, M., et al. (2012). Interleukin-1 participates in the classical and alternative activation of microglia/macrophages after spinal cord injury. *J. Neuroinflammation* 9, 553. doi:10.1186/1742-2094-9-65.

Schaller, D., Šribar, D., Noonan, T., Deng, L., Nguyen, T. N., Pach, S., et al. (2020). Next generation 3D pharmacophore modeling. *WIREs Comput. Mol. Sci.* 10. doi:10.1002/wcms.1468.

Scheiblich, H., Schlütter, A., Golenbock, D. T., Latz, E., Martinez-Martinez, P., and Heneka, M. T. (2017). Activation of the NLRP3 inflammasome in microglia: the role of ceramide. *J. Neurochem.* 143, 534–550. doi:10.1111/jnc.14225.

Schenone, M., Dančík, V., Wagner, B. K., and Clemons, P. A. (2013). Target identification and mechanism of action in chemical biology and drug discovery. *Nat. Chem. Biol.* 9, 232–240. doi:10.1038/nchembio.1199.

Schlüter, T., Schelmbauer, C., Karram, K., and Mufazalov, I. A. (2018). Regulation of IL-1 signaling by the decoy receptor IL-1R2. *J. Mol. Med.* 96, 983–992. doi:10.1007/s00109-018-1684-z.

Schmidtke, P., and Barril, X. (2010). Understanding and Predicting Druggability. A High-Throughput Method for Detection of Drug Binding Sites. *J. Med. Chem.* 53, 5858–5867. doi:10.1021/jm100574m.

Schmidtke, P., Bidon-Chanal, A., Luque, F. J., and Barril, X. (2011). MDpocket: open-source cavity detection and characterization on molecular dynamics trajectories. *Bioinformatics* 27, 3276–3285. doi:10.1093/bioinformatics/btr550.

Schneider, C. A., Rasband, W. S., and Eliceiri, K. W. (2012). NIH Image to ImageJ: 25 years of image analysis. *Nat. Methods* 9, 671–675. doi:10.1038/nmeth.2089.

Schreuder, H., Tardif, C., Trump-Kallmeyer, S., Soffientini, A., Sarubbi, E., Akeson, A., et al. (1997). A new cytokine-receptor binding mode revealed by the crystal structure of the IL-1 receptor with an antagonist. *Nature* 386, 194–200. doi:10.1038/386194a0.

Schrödinger LLC (2020). The PyMOL Molecular Graphics System, Version 2.4.1. *PyMOL Mol. Graph. Syst. Version 2.4.1*.

Schuler, L. D., Daura, X., and van Gunsteren, W. F. (2001). An improved GROMOS96 force field for aliphatic hydrocarbons in the condensed phase. *J. Comput. Chem.* 22, 1205–1218. doi:10.1002/jcc.1078.

Schwede, T. (2003). SWISS-MODEL: an automated protein homology-modeling server. *Nucleic Acids Res.* 31, 3381–3385. doi:10.1093/nar/gkg520.

Sciacca, F. ., Ferri, C., Licastro, F., Veglia, F., Biunno, I., Gavazzi, A., et al. (2003). Interleukin-1B polymorphism is associated with age at onset of Alzheimer's disease. *Neurobiol. Aging* 24, 927–931. doi:10.1016/S0197-4580(03)00011-3.

Scott, D. E., Bayly, A. R., Abell, C., and Skidmore, J. (2016). Small molecules, big targets: drug discovery faces the protein–protein interaction challenge. *Nat. Rev. Drug Discov.* 15, 533–550. doi:10.1038/nrd.2016.29.

Selmaj, K., Brosnan, C. F., and Raine, C. S. (1991). Colocalization of lymphocytes bearing gamma delta T-cell receptor and heat shock protein hsp65+ oligodendrocytes in multiple sclerosis. *Proc. Natl. Acad. Sci.* 88, 6452–6456. doi:10.1073/pnas.88.15.6452.

Seppi, D., Puthenparampil, M., Federle, L., Ruggero, S., Toffanin, E., Rinaldi, F., et al. (2014). Cerebrospinal fluid IL-1β correlates with cortical pathology load in multiple sclerosis at clinical onset. *J. Neuroimmunol.* 270, 56–60. doi:10.1016/j.jneuroim.2014.02.014.

Seto, M. H., Harkins, R. N., Adler, M., Whitlow, M., Croze, E., and Bret Church, W. (2008). Homology model of human interferon-α8 and its receptor complex. *Protein Sci.* 4, 655–670. doi:10.1002/pro.5560040406.

Sfriso, P., Bindoli, S., Doria, A., Feist, E., and Galozzi, P. (2020). Canakinumab for the treatment of adult-onset Still's disease. *Expert Rev. Clin. Immunol.* 16, 129–138. doi:10.1080/1744666X.2019.1707664.

Shahane, G., Ding, W., Palaiokostas, M., and Orsi, M. (2019). Physical properties of model biological lipid bilayers: insights from all-atom molecular dynamics simulations. *J. Mol. Model.* 25, 76. doi:10.1007/s00894-019-3964-0.

Shaw, D. E., Maragakis, P., Lindorff-Larsen, K., Piana, S., Dror, R. O., Eastwood, M. P., et al. (2010). Atomic-Level Characterization of the Structural Dynamics of Proteins. *Science (80-.).* 330, 341–346. doi:10.1126/science.1187409.

Sheehan, D. (2011). Introduction to Proteins: Structure, Function and Motion. *ChemBioChem* 12, 1603–1604. doi:10.1002/cbic.201100254.

Shen, M., and Sali, A. (2006). Statistical potential for assessment and prediction of protein structures. *Protein Sci.* 15, 2507–2524. doi:10.1110/ps.062416606.

Sheridan, C. (2009). J&J's billion dollar punt on anti-amyloid antibody. *Nat. Biotechnol.* 27, 679–681. doi:10.1038/nbt0809-679.

Sheridan, R. P., Maiorov, V. N., Holloway, M. K., Cornell, W. D., and Gao, Y.-D. (2010). Drug-like Density: A Method of Quantifying the "Bindability" of a Protein Target Based on a Very Large Set of Pockets and Drug-like Ligands from the Protein Data Bank. *J. Chem. Inf. Model.* 50, 2029–2040. doi:10.1021/ci100312t.

Shi, H., Zheng, K., Su, Z., Su, H., Zhong, M., He, X., et al. (2016). Sinomenine enhances microglia M2 polarization and attenuates inflammatory injury in intracerebral hemorrhage. *J. Neuroimmunol.* 299, 28–34. doi:10.1016/j.jneuroim.2016.08.010.

Shi, Y., and Holtzman, D. M. (2018). Interplay between innate immunity and Alzheimer disease: APOE and TREM2 in the spotlight. *Nat. Rev. Immunol.* 18, 759–772. doi:10.1038/s41577-018-0051-1.

Shoichet, B. K. (2004). Virtual screening of chemical libraries. *Nature* 432, 862–865. doi:10.1038/nature03197.

Shrivastava, K., Gonzalez, P., and Acarin, L. (2012). The immune inhibitory complex CD200/CD200R is developmentally regulated in the mouse brain. *J. Comp. Neurol.* 520, 2657–2675. doi:10.1002/cne.23062.

Sievers, F., and Higgins, D. G. (2018). Clustal Omega for making accurate alignments of many protein sequences. *Protein Sci.* 27, 135–145. doi:10.1002/pro.3290.

Silvestroni, A., Faull, R. L. M., Strand, A. D., and Möller, T. (2009). Distinct neuroinflammatory profile in post-mortem human Huntington's disease. *Neuroreport* 20, 1098–1103. doi:10.1097/WNR.0b013e32832e34ee.

Simões, T., Lopes, D., Dias, S., Fernandes, F., Pereira, J., Jorge, J., et al. (2017). Geometric Detection Algorithms for Cavities on Protein Surfaces in Molecular Graphics: A Survey. *Comput. Graph. Forum* 36, 643–683. doi:10.1111/cgf.13158.

Simon, D. W., McGeachy, M. J., Baylr, H., Clark, R. S. B., Loane, D. J., and Kochanek, P. M. (2017). The far-reaching scope of neuroinflammation after traumatic brain injury. *Nat. Rev. Neurol.* 13, 171–191. doi:10.1038/nrneurol.2017.13.

Sims, J. E., Gayle, M. A., Slack, J. L., Alderson, M. R., Bird, T. A., Giri, J. G., et al. (1993). Interleukin 1 signaling occurs exclusively via the type I receptor. *Proc. Natl. Acad. Sci.* 90, 6155–6159. doi:10.1073/pnas.90.13.6155.

Sims, J. E., Painter, S. L., and Gow, I. R. (1995). Genomic organization ot the type I and type II IL-1 receptors. *Cytokine* 7, 483–490. doi:10.1006/cyto.1995.0066.

Sims, J. E., and Smith, D. E. (2010). The IL-1 family: Regulators of immunity. *Nat. Rev. Immunol.* 10, 89–102. doi:10.1038/nri2691.

Sims, J., March, C., Cosman, D., Widmer, M., MacDonald, H., McMahan, C., et al. (1988). cDNA expression cloning of the IL-1 receptor, a member of the immunoglobulin superfamily. *Science (80-.).* 241, 585–589. doi:10.1126/science.2969618.

Sjöström, E. O., Culot, M., Leickt, L., Åstrand, M., Nordling, E., Gosselet, F., et al. (2021). Transport study of interleukin-1 inhibitors using a human in vitro model of the blood-brain barrier. *Brain, Behav. Immun. - Heal.* 16, 100307. doi:10.1016/j.bbih.2021.100307.

Śledź, P., and Caflisch, A. (2018). Protein structure-based drug design: from docking to molecular dynamics. *Curr. Opin. Struct. Biol.* 48, 93–102. doi:10.1016/j.sbi.2017.10.010.

Sliwoski, G., Kothiwale, S., Meiler, J., and Lowe, E. W. (2014). Computational Methods in Drug Discovery. *Pharmacol. Rev.* 66, 334–395. doi:10.1124/pr.112.007336.

Sloan-Lancaster, J., Abu-Raddad, E., Polzer, J., Miller, J. W., Scherer, J. C., De Gaetano, A., et al. (2013). Double-Blind, Randomized Study Evaluating the Glycemic and Anti-inflammatory Effects of Subcutaneous LY2189102, a Neutralizing IL-1 Antibody, in Patients With Type 2 Diabetes. *Diabetes Care* 36, 2239–2246. doi:10.2337/dc12-1835.

Smith, A. J. P., Keen, L. J., Billingham, M. J., Perry, M. J., Elson, C. J., Kirwan, J. R., et al. (2004). Extended haplotypes and linkage disequilibrium in the IL1R1–IL1A–IL1B–IL1RN gene cluster: association with knee osteoarthritis. *Genes Immun.* 5, 451–460. doi:10.1038/sj.gene.6364107.

Smith, C. J., Hulme, S., Vail, A., Heal, C., Parry-Jones, A. R., Scarth, S., et al. (2018). SCIL-STROKE (Subcutaneous Interleukin-1 Receptor Antagonist in Ischemic Stroke). *Stroke* 49, 1210–1216. doi:10.1161/STROKEAHA.118.020750.

Smith, D. E., Hanna, R., Friend, D., Moore, H., Chen, H., Farese, A. M., et al. (2003). The Soluble Form of IL-1 Receptor Accessory Protein Enhances the Ability of Soluble Type II IL-1 Receptor to Inhibit IL-1 Action. *Immunity* 18, 87–96. doi:10.1016/S1074-7613(02)00514-9.

So, A., De Smedt, T., Revaz, S., and Tschopp, J. (2007). A pilot study of IL-1 inhibition by anakinra in acute gout. *Arthritis Res. Ther.* 9, R28. doi:10.1186/ar2143.

Sochocka, M., Diniz, B. S., and Leszek, J. (2017). Inflammatory Response in the CNS: Friend or Foe? *Mol. Neurobiol.* 54, 8071–8089. doi:10.1007/s12035-016-0297-1.

Sonar, S. A., and Lal, G. (2019). The iNOS Activity During an Immune Response Controls the CNS Pathology in Experimental Autoimmune Encephalomyelitis. *Front. Immunol.* 10. doi:10.3389/fimmu.2019.00710.

Song, A., Zhu, L., Gorantla, G., Berdysz, O., Amici, S. A., Guerau-de-Arellano, M., et al. (2018). Salient type 1 interleukin 1 receptor expression in peripheral non-immune cells. *Sci. Rep.* 8, 723. doi:10.1038/s41598-018-19248-7.

Spencer, N. G., Schilling, T., Miralles, F., and Eder, C. (2016). Mechanisms Underlying Interferon-γ-Induced Priming of Microglial Reactive Oxygen Species Production. *PLoS One* 11, e0162497. doi:10.1371/journal.pone.0162497.

Šribar, D., Grabowski, M., Murgueitio, M. S., Bermudez, M., Weindl, G., and Wolber, G. (2019). Identification and characterization of a novel chemotype for human TLR8 inhibitors. *Eur. J. Med. Chem.* 179, 744–752. doi:10.1016/j.ejmech.2019.06.084.

Stelmasiak, Z., Kozioł-Montewka, M., Dobosz, B., Rejdak, K., Bartosik-Psujek, H., Mitosek-Szewczyk, K., et al. (2000). Interleukin-6 concentration in serum and cerebrospinal fluid in multiple sclerosis patients. *Med. Sci. Monit.* 6, 1104–8. Available at: http://www.ncbi.nlm.nih.gov/pubmed/11208463.

Stephenson, J., Nutma, E., van der Valk, P., and Amor, S. (2018). Inflammation in CNS neurodegenerative diseases. *Immunology* 154, 204–219. doi:10.1111/imm.12922.

Stork, C., Chen, Y., Šícho, M., and Kirchmair, J. (2019). Hit Dexter 2.0: Machine-Learning Models for the Prediction of Frequent Hitters. *J. Chem. Inf. Model.* 59, 1030–1043. doi:10.1021/acs.jcim.8b00677.

Stroemer, R. P., and Rothwell, N. J. (1998). Exacerbation of Ischemic Brain Damage by Localized Striatal Injection of Interleukin-1β in the Rat. *J. Cereb. Blood Flow Metab.* 18, 833–839. doi:10.1097/00004647-199808000-00003.

Stylianou, E., O'Neill, L. A., Rawlinson, L., Edbrooke, M. R., Woo, P., and Saklatvala, J. (1992). Interleukin 1 induces NF-kappa B through its type I but not its type II receptor in lymphocytes. *J. Biol. Chem.* 267, 15836–41. doi:1386364.

Sulzer, D., Alcalay, R. N., Garretti, F., Cote, L., Kanter, E., Agin-Liebes, J., et al. (2017). T cells from patients with Parkinson's disease recognize α-synuclein peptides. *Nature* 546, 656–661. doi:10.1038/nature22815.

Sunseri, J., and Koes, D. R. (2016). Pharmit: interactive exploration of chemical space. *Nucleic Acids Res.* 44, W442–W448. doi:10.1093/nar/gkw287.

Swanson, K. V., Deng, M., and Ting, J. P.-Y. (2019). The NLRP3 inflammasome: molecular activation and regulation to therapeutics. *Nat. Rev. Immunol.* 19, 477–489. doi:10.1038/s41577-019-0165-0.

Swinney, D. C., and Lee, J. A. (2020). Recent advances in phenotypic drug discovery. *F1000Research* 9, 944. doi:10.12688/f1000research.25813.1.

Sydow, D. (2015). Dynophores: Novel dynamic pharmacophores (Master Thesis). Humboldt-Universität zu Berlin.

Sydow, D., Burggraaff, L., Szengel, A., van Vlijmen, H. W. T., IJzerman, A. P., van Westen, G. J. P., et al. (2019). Advances and Challenges in Computational Target Prediction. *J. Chem. Inf. Model.* 59, 1728–1742. doi:10.1021/acs.jcim.8b00832.

Symons, J. A., Eastgate, J. A., and Duff, G. W. (1991). Purification and characterization of a novel soluble receptor for interleukin 1. *J. Exp. Med.* 174, 1251–1254. doi:10.1084/jem.174.5.1251.

Symons, J. A., Young, P. R., and Duff, G. W. (1995). Soluble type II interleukin 1 (IL-1) receptor binds and blocks processing of IL-1 beta precursor and loses affinity for IL-1 receptor antagonist. *Proc. Natl. Acad. Sci.* 92, 1714–1718. doi:10.1073/pnas.92.5.1714.

Ta, T.-T., Dikmen, H. O., Schilling, S., Chausse, B., Lewen, A., Hollnagel, J.-O., et al. (2019). Priming of microglia with IFN-γ slows neuronal gamma oscillations in situ. *Proc. Natl. Acad. Sci.* 116, 4637–4642. doi:10.1073/pnas.1813562116.

Takata, K., Kitamura, Y., Tsuchiya, D., Kawasaki, T., Taniguchi, T., and Shimohama, S. (2004). High mobility group box protein-1 inhibits microglial A? clearance and enhances A? neurotoxicity. *J. Neurosci. Res.* 78, 880–891. doi:10.1002/jnr.20340.

Tanaka, S., Ishii, A., Ohtaki, H., Shioda, S., Yoshida, T., and Numazawa, S. (2013). Activation of microglia induces symptoms of Parkinson's disease in wild-type, but not in IL-1 knockout mice. *J. Neuroinflammation* 10, 907. doi:10.1186/1742-2094-10-143.

Tansey, M. G., and Romero-Ramos, M. (2018). Immune system responses in Parkinson's disease: Early and dynamic. *Eur. J. Neurosci.*, ejn.14290. doi:10.1111/ejn.14290.

Tavares-Gomes, L., Monney, C., Neuhaus, G., Francisco, D., Solis, D., Summerfield, A., et al.

(2021). Transcriptome of microglia reveals a species-specific expression profile in bovines with conserved and new signature genes. *Glia* 69, 1932–1949. doi:10.1002/glia.24002.

Temml, V., Garscha, U., Romp, E., Schubert, G., Gerstmeier, J., Kutil, Z., et al. (2017). Discovery of the first dual inhibitor of the 5-lipoxygenase-activating protein and soluble epoxide hydrolase using pharmacophore-based virtual screening. *Sci. Rep.* 7, 42751. doi:10.1038/srep42751.

Terkeltaub, R., Sundy, J. S., Schumacher, H. R., Murphy, F., Bookbinder, S., Biedermann, S., et al. (2009). The interleukin 1 inhibitor rilonacept in treatment of chronic gouty arthritis: results of a placebo-controlled, monosequence crossover, non-randomised, single-blind pilot study. *Ann. Rheum. Dis.* 68, 1613–1617. doi:10.1136/ard.2009.108936.

Thomas, C., Bazan, J. F., and Garcia, K. C. (2012). Structure of the activating IL-1 receptor signaling complex. *Nat. Struct. Mol. Biol.* 19, 455–457. doi:10.1038/nsmb.2260.

Tian, W., Chen, C., Lei, X., Zhao, J., and Liang, J. (2018). CASTp 3.0: computed atlas of surface topography of proteins. *Nucleic Acids Res.* 46, W363–W367. doi:10.1093/nar/gky473.

Tomasoni, R., Morini, R., Lopez-Atalaya, J. P., Corradini, I., Canzi, A., Rasile, M., et al. (2017). Lack of IL-1R8 in neurons causes hyperactivation of IL-1 receptor pathway and induces MECP2-dependent synaptic defects. *Elife* 6. doi:10.7554/eLife.21735.

Toshchakov, V. Y., and Neuwald, A. F. (2020). A survey of TIR domain sequence and structure divergence. *Immunogenetics* 72, 181–203. doi:10.1007/s00251-020-01157-7.

Toulmond, S., and Rothwell, N. J. (1995). Interleukin-1 receptor antagonist inhibits neuronal damage caused by fluid percussion injury in the rat. *Brain Res.* 671, 261–266. doi:10.1016/0006-8993(94)01343-G.

Troncoso-Escudero, P., Parra, A., Nassif, M., and Vidal, R. L. (2018). Outside in: Unraveling the role of neuroinflammation in the progression of Parkinson's disease. *Front. Neurol.* 9, 1–15. doi:10.3389/fneur.2018.00860.

Trott, O., and Olson, A. J. (2009). AutoDock Vina: Improving the speed and accuracy of docking with a new scoring function, efficient optimization, and multithreading. *J. Comput. Chem.*, NA-NA. doi:10.1002/jcc.21334.

Tsutsumi, N., Kimura, T., Arita, K., Ariyoshi, M., Ohnishi, H., Yamamoto, T., et al. (2014). The structural basis for receptor recognition of human interleukin-18. *Nat. Commun.* 5, 5340. doi:10.1038/ncomms6340.

Tugal-Tutkun, I., Pavesio, C., De Cordoue, A., Bernard-Poenaru, O., and Gül, A. (2018). Use of Gevokizumab in Patients with Behçet's Disease Uveitis: An International, Randomized, Double-Masked, Placebo-Controlled Study and Open-Label Extension Study. *Ocul. Immunol. Inflamm.* 26, 1023–1033. doi:10.1080/09273948.2017.1421233.

Vainchtein, I. D., and Molofsky, A. V. (2020). Astrocytes and Microglia: In Sickness and in Health. *Trends Neurosci.* 43, 144–154. doi:10.1016/j.tins.2020.01.003.

van der Meer, J. W. M., and Simon, A. (2010). Blocking IL-1 to slow down progression of

ALS? *Proc. Natl. Acad. Sci.* 107, 12741–12742. doi:10.1073/pnas.1007946107.

Van Eldik, L. J., Sawaki, L., Bowen, K., Laskowitz, D. T., Noveck, R. J., Hauser, B., et al. (2020). First-in-Human Studies of MW01-6-189WH, a Brain-Penetrant, Antineuroinflammatory Small-Molecule Drug Candidate: Phase 1 Safety, Tolerability, Pharmacokinetic, and Pharmacodynamic Studies in Healthy Adult Volunteers. *Clin. Pharmacol. Drug Dev.*, cpdd.795. doi:10.1002/cpdd.795.

Varadi, M., Anyango, S., Deshpande, M., Nair, S., Natassia, C., Yordanova, G., et al. (2021). AlphaFold Protein Structure Database: massively expanding the structural coverage of protein-sequence space with high-accuracy models. *Nucleic Acids Res.* doi:10.1093/nar/gkab1061.

Vasilyev, F., Silkov, A., and Sennikov, S. (2015). Relationship between interleukin-1 type 1 and 2 receptor gene polymorphisms and the expression level of membrane-bound receptors. *Cell. Mol. Immunol.* 12, 222–230. doi:10.1038/cmi.2014.43.

Vawter, M. P., Dillon-Carter, O., Tourtellotte, W. W., Carvey, P., and Freed, W. J. (1996). TGFβ1 and TGFβ2 Concentrations Are Elevated in Parkinson's Disease in Ventricular Cerebrospinal Fluid. *Exp. Neurol.* 142, 313–322. doi:10.1006/exnr.1996.0200.

Vaz, A. R., Pinto, S., Ezequiel, C., Cunha, C., Carvalho, L. A., Moreira, R., et al. (2019). Phenotypic Effects of Wild-Type and Mutant SOD1 Expression in N9 Murine Microglia at Steady State, Inflammatory and Immunomodulatory Conditions. *Front. Cell. Neurosci.* 13. doi:10.3389/fncel.2019.00109.

Vaz, A. R., Vizinha, D., Morais, H., Colaço, A. R., Loch-Neckel, G., Barbosa, M., et al. (2021). Overexpression of miR-124 in Motor Neurons Plays a Key Role in ALS Pathological Processes. *Int. J. Mol. Sci.* 22, 6128. doi:10.3390/ijms22116128.

Verlet, L. (1967). Computer "Experiments" on Classical Fluids. I. Thermodynamical Properties of Lennard-Jones Molecules. *Phys. Rev.* 159, 98–103. doi:10.1103/PhysRev.159.98.

Vigers, G. P. A., Anderson, L. J., Caffes, P., and Brandhuber, B. J. (1997). Crystal structure of the type-I interleukin-1 receptor complexed with interleukin-1β. *Nature* 386, 190–194. doi:10.1038/386190a0.

Vigers, G. P. A., Dripps, D. J., Edwards, C. K., and Brandhuber, B. J. (2000). X-ray crystal structure of a small antagonist peptide bound to interleukin-1 receptor type 1. *J. Biol. Chem.* 275, 36927–36933. doi:10.1074/jbc.M006071200.

Volkamer, A., Kuhn, D., Grombacher, T., Rippmann, F., and Rarey, M. (2012a). Combining Global and Local Measures for Structure-Based Druggability Predictions. *J. Chem. Inf. Model.* 52, 360–372. doi:10.1021/ci200454v.

Volkamer, A., Kuhn, D., Rippmann, F., and Rarey, M. (2012b). DoGSiteScorer: a web server for automatic binding site prediction, analysis and druggability assessment. *Bioinformatics* 28, 2074–2075. doi:10.1093/bioinformatics/bts310.

Voronoi, G. (1908). Nouvelles applications des paramètres continus à la théorie des formes quadratiques. Premier mémoire. Sur quelques propriétés des formes quadratiques

positives parfaites. *J. für die reine und Angew. Math. (Crelles Journal)* 1908, 97–102. doi:10.1515/crll.1908.133.97.

Vroon, A., Drukarch, B., Bol, J. G. J. M., Cras, P., Brevé, J. J. P., Allan, S. M., et al. (2007). Neuroinflammation in Parkinson's patients and MPTP-treated mice is not restricted to the nigrostriatal system: Microgliosis and differential expression of interleukin-1 receptors in the olfactory bulb. *Exp. Gerontol.* 42, 762–771. doi:10.1016/j.exger.2007.04.010.

Wager, T. T., Hou, X., Verhoest, P. R., and Villalobos, A. (2010). Moving beyond Rules: The Development of a Central Nervous System Multiparameter Optimization (CNS MPO) Approach To Enable Alignment of Druglike Properties. *ACS Chem. Neurosci.* 1, 435–449. doi:10.1021/cn100008c.

Wagner, B. K. (2016). The resurgence of phenotypic screening in drug discovery and development. *Expert Opin. Drug Discov.* 11, 121–125. doi:10.1517/17460441.2016.1122589.

Wakefield, A. E., Yueh, C., Beglov, D., Castilho, M. S., Kozakov, D., Keserű, G. M., et al. (2020). Benchmark Sets for Binding Hot Spot Identification in Fragment-Based Ligand Discovery. *J. Chem. Inf. Model.* 60, 6612–6623. doi:10.1021/acs.jcim.0c00877.

Waltenberger, B., Wiechmann, K., Bauer, J., Markt, P., Noha, S. M., Wolber, G., et al. (2011). Pharmacophore Modeling and Virtual Screening for Novel Acidic Inhibitors of Microsomal Prostaglandin E 2 Synthase-1 (mPGES-1). *J. Med. Chem.* 54, 3163–3174. doi:10.1021/jm101309g.

Walters, W. P., and Wang, R. (2020). New Trends in Virtual Screening. *J. Chem. Inf. Model.* 60, 4109–4111. doi:10.1021/acs.jcim.0c01009.

Wang, J., Wolf, R. M., Caldwell, J. W., Kollman, P. A., and Case, D. A. (2004). Development and testing of a general amber force field. *J. Comput. Chem.* 25, 1157–1174. doi:10.1002/jcc.20035.

Wang, K., Xiao, J., Liu, X., Jiang, Z., Zhan, Y., Yin, T., et al. (2019). AICD: an integrated anti-inflammatory compounds database for drug discovery. *Sci. Rep.* 9, 7737. doi:10.1038/s41598-019-44227-x.

Wang, S., Mustafa, M., Yuede, C. M., Salazar, S. V., Kong, P., Long, H., et al. (2020). Anti-human TREM2 induces microglia proliferation and reduces pathology in an Alzheimer's disease model. *J. Exp. Med.* 217. doi:10.1084/jem.20200785.

Wang, X.-F., Huang, L.-D., Yu, P.-P., Hu, J.-G., Yin, L., Wang, L., et al. (2006). Upregulation of type I interleukin−1 receptor after traumatic spinal cord injury in adult rats. *Acta Neuropathol.* 111, 220–228. doi:10.1007/s00401-005-0016-x.

Wang, Y., Xiao, J., Suzek, T. O., Zhang, J., Wang, J., Zhou, Z., et al. (2012). PubChem's BioAssay Database. *Nucleic Acids Res.* 40, D400–D412. doi:10.1093/nar/gkr1132.

Wang, Z., Vilekar, P., Huang, J., and Weaver, D. F. (2020). Furosemide as a Probe Molecule for the Treatment of Neuroinflammation in Alzheimer's Disease. *ACS Chem. Neurosci.* 11, 4152–4168. doi:10.1021/acschemneuro.0c00445.

Wannamaker, W., Davies, R., Namchuk, M., Pollard, J., Ford, P., Ku, G., et al. (2007). (S)-1-((

S)-2-{[1-(4-Amino-3-chloro-phenyl)-methanoyl]-amino}-3,3-dimethyl-butanoyl)-pyrrolidine-2-carboxylic acid ((2 R ,3 S)-2-ethoxy-5-oxo-tetrahydro-furan-3-yl)-amide (VX-765), an Orally Available Selective Interleukin (IL)-Converting Enzyme/Caspa. *J. Pharmacol. Exp. Ther.* 321, 509–516. doi:10.1124/jpet.106.111344.

Warchal, S. J., Unciti-Broceta, A., and Carragher, N. O. (2016). Next-generation phenotypic screening. *Future Med. Chem.* 8, 1331–1347. doi:10.4155/fmc-2016-0025.

Warren, G. L., Andrews, C. W., Capelli, A.-M., Clarke, B., LaLonde, J., Lambert, M. H., et al. (2006). A Critical Assessment of Docking Programs and Scoring Functions. *J. Med. Chem.* 49, 5912–5931. doi:10.1021/jm050362n.

Wei, T., Gong, J., Jamitzky, F., Heckl, W. M., Stark, R. W., and Rössle, S. C. (2009). Homology modeling of human Toll-like receptors TLR7, 8, and 9 ligand-binding domains. *Protein Sci.* 18, 1684–1691. doi:10.1002/pro.186.

Whiting, C. C., Siebert, J., Newman, A. M., Du, H., Alizadeh, A. A., Goronzy, J., et al. (2015). Large-Scale and Comprehensive Immune Profiling and Functional Analysis of Normal Human Aging. *PLoS One* 10, e0133627. doi:10.1371/journal.pone.0133627.

Wiedemann, J., Rashid, K., and Langmann, T. (2018). Resveratrol induces dynamic changes to the microglia transcriptome, inhibiting inflammatory pathways and protecting against microglia-mediated photoreceptor apoptosis. *Biochem. Biophys. Res. Commun.* 501, 239–245. doi:10.1016/j.bbrc.2018.04.223.

Wieder, M., Garon, A., Perricone, U., Boresch, S., Seidel, T., Almerico, A. M., et al. (2017). Common Hits Approach: Combining Pharmacophore Modeling and Molecular Dynamics Simulations. *J. Chem. Inf. Model.* 57, 365–385. doi:10.1021/acs.jcim.6b00674.

Wieder, M., Perricone, U., Boresch, S., Seidel, T., and Langer, T. (2016). Evaluating the stability of pharmacophore features using molecular dynamics simulations. *Biochem. Biophys. Res. Commun.* 470, 685–689. doi:10.1016/j.bbrc.2016.01.081.

Wiederstein, M., and Sippl, M. J. (2007). ProSA-web: interactive web service for the recognition of errors in three-dimensional structures of proteins. *Nucleic Acids Res.* 35, W407–W410. doi:10.1093/nar/gkm290.

Wishart, D. S., Feunang, Y. D., Guo, A. C., Lo, E. J., Marcu, A., Grant, J. R., et al. (2018). DrugBank 5.0: a major update to the DrugBank database for 2018. *Nucleic Acids Res.* 46, D1074–D1082. doi:10.1093/nar/gkx1037.

Wohleb, E. S., Patterson, J. M., Sharma, V., Quan, N., Godbout, J. P., and Sheridan, J. F. (2014). Knockdown of Interleukin-1 Receptor Type-1 on Endothelial Cells Attenuated Stress-Induced Neuroinflammation and Prevented Anxiety-Like Behavior. 34, 2583–2591. doi:10.1523/JNEUROSCI.3723-13.2014.

Wolber, G., and Langer, T. (2005). LigandScout: 3-D Pharmacophores Derived from Protein-Bound Ligands and Their Use as Virtual Screening Filters. *J. Chem. Inf. Model.* 45, 160–169. doi:10.1021/ci049885e.

Wolf, M. G., Hoefling, M., Aponte-Santamaría, C., Grubmüller, H., and Groenhof, G. (2010). g_membed: Efficient insertion of a membrane protein into an equilibrated lipid bilayer

with minimal perturbation. *J. Comput. Chem.* 31, 2169–2174. doi:10.1002/jcc.21507.

Wu, Y.-Y., Hsu, J.-L., Wang, H.-C., Wu, S.-J., Hong, C.-J., and Cheng, I. H.-J. (2015). Alterations of the Neuroinflammatory Markers IL-6 and TRAIL in Alzheimer's Disease. *Dement. Geriatr. Cogn. Dis. Extra* 5, 424–434. doi:10.1159/000439214.

Xiao, S., Chan, P., Wang, T., Hong, Z., Wang, S., Kuang, W., et al. (2021). A 36-week multicenter, randomized, double-blind, placebo-controlled, parallel-group, phase 3 clinical trial of sodium oligomannate for mild-to-moderate Alzheimer's dementia. *Alzheimers. Res. Ther.* 13, 62. doi:10.1186/s13195-021-00795-7.

Xie, Z.-R., and Hwang, M.-J. (2015). "Methods for Predicting Protein–Ligand Binding Sites," in, 383–398. doi:10.1007/978-1-4939-1465-4_17.

Xing, Y., Yao, X., Li, H., Xue, G., Guo, Q., Yang, G., et al. (2017). Cutting Edge: TRAF6 Mediates TLR/IL-1R Signaling–Induced Nontranscriptional Priming of the NLRP3 Inflammasome. *J. Immunol.* 199, 1561–1566. doi:10.4049/jimmunol.1700175.

Xu, L.-L., Zhu, J.-F., Xu, X.-L., Zhu, J., Li, L., Xi, M.-Y., et al. (2015). Discovery and Modification of in Vivo Active Nrf2 Activators with 1,2,4-Oxadiazole Core: Hits Identification and Structure–Activity Relationship Study. *J. Med. Chem.* 58, 5419–5436. doi:10.1021/acs.jmedchem.5b00170.

Yamanaka, G., Ishida, Y., Kanou, K., Suzuki, S., Watanabe, Y., Takamatsu, T., et al. (2021). Towards a Treatment for Neuroinflammation in Epilepsy: Interleukin-1 Receptor Antagonist, Anakinra, as a Potential Treatment in Intractable Epilepsy. *Int. J. Mol. Sci.* 22, 6282. doi:10.3390/ijms22126282.

Yamanaka, K., Chun, S. J., Boillee, S., Fujimori-Tonou, N., Yamashita, H., Gutmann, D. H., et al. (2008). Astrocytes as determinants of disease progression in inherited amyotrophic lateral sclerosis. *Nat. Neurosci.* 11, 251–253. doi:10.1038/nn2047.

Yang, C.-Y. (2020). Comparative Analyses of the Conformational Dynamics Between the Soluble and Membrane-Bound Cytokine Receptors. *Sci. Rep.* 10, 7399. doi:10.1038/s41598-020-64034-z.

Yang, C. Y. (2015). Identification of potential small molecule allosteric modulator sites on IL-1R1 ectodomain using accelerated conformational sampling method. *PLoS One* 10, 1–25. doi:10.1371/journal.pone.0118671.

Yang, H., Wang, H., and Andersson, U. (2020). Targeting Inflammation Driven by HMGB1. *Front. Immunol.* 11. doi:10.3389/fimmu.2020.00484.

Yang, Z., Liu, Y., Yuan, F., Li, Z., Huang, S., Shen, H., et al. (2014). Sinomenine inhibits microglia activation and attenuates brain injury in intracerebral hemorrhage. *Mol. Immunol.* 60, 109–114. doi:10.1016/j.molimm.2014.03.005.

Yanofsky, S. D., Baldwin, D. N., Butler, J. H., Holden, F. R., Jacobs, J. W., Balasubramanian, P., et al. (1996). High affinity type I interleukin 1 receptor antagonists discovered by screening recombinant peptide libraries. *Proc. Natl. Acad. Sci.* 93, 7381–7386. doi:10.1073/pnas.93.14.7381.

Ye, K., Vannier, E., Clark, B. D., Sims, J. E., and Dinarello, C. A. (1996). Three distinct

promoters direct transcription of different 5′ untranslated regions of the Human Interleukin 1 Type I Receptor: a possible mechanism for control of translation. *Cytokine* 8, 421–429. doi:10.1006/cyto.1996.0058.

Yuskaitis, C. J., and Jope, R. S. (2009). Glycogen synthase kinase-3 regulates microglial migration, inflammation, and inflammation-induced neurotoxicity. *Cell. Signal.* 21, 264–273. doi:10.1016/j.cellsig.2008.10.014.

Zhang, C.-J., Jiang, M., Zhou, H., Liu, W., Wang, C., Kang, Z., et al. (2018a). TLR-stimulated IRAKM activates caspase-8 inflammasome in microglia and promotes neuroinflammation. *J. Clin. Invest.* 128, 5399–5412. doi:10.1172/JCI121901.

Zhang, C., Griciuc, A., Hudry, E., Wan, Y., Quinti, L., Ward, J., et al. (2018b). Cromolyn Reduces Levels of the Alzheimer's Disease-Associated Amyloid β-Protein by Promoting Microglial Phagocytosis. *Sci. Rep.* 8, 1144. doi:10.1038/s41598-018-19641-2.

Zhang, G., Li, J., Purkayastha, S., Tang, Y., Zhang, H., Yin, Y., et al. (2013). Hypothalamic programming of systemic ageing involving IKK-β, NF-κB and GnRH. *Nature* 497, 211–216. doi:10.1038/nature12143.

Zhang, M., Luo, G., Zhou, Y., Wang, S., and Zhong, Z. (2014). Phenotypic Screens Targeting Neurodegenerative Diseases. *J. Biomol. Screen.* 19, 1–16. doi:10.1177/1087057113499777.

Zhang, Y., and He, M. (2017). Deferoxamine enhances alternative activation of microglia and inhibits amyloid beta deposits in APP/PS1 mice. *Brain Res.* 1677, 86–92. doi:10.1016/j.brainres.2017.09.019.

Zhao, J., Cao, Y., and Zhang, L. (2020). Exploring the computational methods for protein-ligand binding site prediction. *Comput. Struct. Biotechnol. J.* 18, 417–426. doi:10.1016/j.csbj.2020.02.008.

Zhao, M.-L., Kim, M.-O., Morgello, S., and Lee, S. C. (2001). Expression of inducible nitric oxide synthase, interleukin-1 and caspase-1 in HIV-1 encephalitis. *J. Neuroimmunol.* 115, 182–191. doi:10.1016/S0165-5728(00)00463-X.

Zhao, W., Beers, D. R., and Appel, S. H. (2013). Immune-mediated Mechanisms in the Pathoprogression of Amyotrophic Lateral Sclerosis. *J. Neuroimmune Pharmacol.* 8, 888–899. doi:10.1007/s11481-013-9489-x.

Zhao, W., Xie, W., Le, W., Beers, D. R., He, Y., Henkel, J. S., et al. (2004). Activated Microglia Initiate Motor Neuron Injury by a Nitric Oxide and Glutamate-Mediated Mechanism. *J. Neuropathol. Exp. Neurol.* 63, 964–977. doi:10.1093/jnen/63.9.964.

Zhao, Z., Wang, Y., Zhou, R., Li, Y., Gao, Y., Tu, D., et al. (2020). A novel role of NLRP3-generated IL-1β in the acute-chronic transition of peripheral lipopolysaccharide-elicited neuroinflammation: implications for sepsis-associated neurodegeneration. *J. Neuroinflammation* 17, 64. doi:10.1186/s12974-020-1728-5.

Zhong, Z., Liu, L.-J., Dong, Z.-Q., Lu, L., Wang, M., Leung, C.-H., et al. (2015). Structure-based discovery of an immunomodulatory inhibitor of TLR1–TLR2 heterodimerization from a natural product-like database. *Chem. Commun.* 51, 11178–11181. doi:10.1039/C5CC02728D.

Zhou, K., Shi, L., Wang, Y., Chen, S., and Zhang, J. (2016). Recent Advances of the NLRP3 Inflammasome in Central Nervous System Disorders. *J. Immunol. Res.* 2016. doi:10.1155/2016/9238290.

Zhou, L., Wang, K., Li, L., Li, H., and Geng, M. (2015). Pinocembrin inhibits lipopolysaccharide-induced inflammatory mediators production in BV2 microglial cells through suppression of PI3K/Akt/NF-κB pathway. *Eur. J. Pharmacol.* 761, 211–216. doi:10.1016/j.ejphar.2015.06.003.

Zusso, M., Lunardi, V., Franceschini, D., Pagetta, A., Lo, R., Stifani, S., et al. (2019). Ciprofloxacin and levofloxacin attenuate microglia inflammatory response via TLR4/NF-kB pathway. *J. Neuroinflammation* 16, 148. doi:10.1186/s12974-019-1538-9.

List of Publications

João P. Luís, Ana I. Mata, Carlos J. V. Simões, Rui M. M. Brito. Analysis of the Conformational Dynamics of the Apo forms of Soluble and Membrane-Bound Interleukin-1 Receptor Type-1: insights into linker flexibility. 2021 (submitted for publication)

João P. Luís, Carlos J. V. Simões, Rui M. M. Brito. The therapeutic prospects of targeting IL-1R1 for the modulation of neuroinflammation in central nervous system disorders. 2021 (submitted for publication)

Alves, N. G, Mata, A. I., Luís, J. P., Brito, R. M. M., Simões, C. J. V. An Innovative Sequence-to-Structure-Based Approach to Drug Resistance Interpretation and Prediction: The Use of Molecular Interaction Fields to Detect HIV-1 Protease Binding-Site Dissimilarities, Front. Chem., 8, pp 243, 2020.DOI: 10.3389/fchem.2020.00243

Communications in scientific meetings

João P. Luís, Carlos J. V. Simões, Rui M. M. Brito. "Targeting Neuroinflammation: Integrating Molecular Dynamics in a Virtual Screening protocol for Interleukin-1 Receptor type I (IL-1R1)". 13th National Organic Chemistry Meeting - 6th National Medicinal Chemistry Meeting; Universidade de Aveiro.

João P. Luís, Carlos J. V. Simões, Rui M. M. Brito. "Targeting Neuroinflammation: a combined Virtual Screening protocol towards the discovery of Interleukin-1 Receptor type I (IL-1R1) modulators". 7º Encontro de Jovens Investigadores de Biologia Computacional e Estrutural (EJIBCE 2019); Faculdade de Ciências da Universidade de Lisboa.

João P. Luís, Carlos J. V. Simões, Rui M. M. Brito. "Targeting neuroinflammation: inclusion of interleukin-1 receptor type I dynamics towards the design of potent modulators". BioExcel Summer school on Biomolecular Simulations; Science and Technology Park of Sardinia, Italy.

João P. Luís, Nuno G. Alves, Carlos J. V. Simões, João Pereira-Vaz, Daniela C. Vaz, Vítor Duque, Rui M. M. Brito. "A new structure-based anti-viral resistance prediction algorithm: HIV-1 protease as a case study". 12th National Organic Chemistry Meeting - 5th National Medicinal Chemistry Meeting; Faculdade de Ciências e Tecnologias da Universidade de Coimbra.

João P. Luís, Nuno G. Alves, Carlos J. V. Simões, João Pereira-Vaz, Daniela C. Vaz, Vítor Duque, Rui M. M. Brito. "Influence of codon 35 amino acid insertion in HIV-1 protease: insights from Molecular Dynamics". 6º Encontro de Jovens Investigadores de Biologia Computacional e Estrutural (EJIBCE 2018); Faculdade de Medicina da Universidade do Porto.